

AD_____

AWARD NUMBER: W81XWH-05-1-0291

TITLE: A Partnership Training Program In Breast Cancer Research Using Molecular Imaging Techniques

PRINCIPAL INVESTIGATOR: Paul C. Wang, Ph.D.

CONTRACTING ORGANIZATION: Howard University
Washington, DC 20059

REPORT DATE: July 2009

TYPE OF REPORT: Final

PREPARED FOR: U.S. Army Medical Research and Materiel Command
Fort Detrick, Maryland 21702-5012

DISTRIBUTION STATEMENT: Approved for Public Release;
Distribution Unlimited

The views, opinions and/or findings contained in this report are those of the author(s) and should not be construed as an official Department of the Army position, policy or decision unless so designated by other documentation.

REPORT DOCUMENTATION PAGE				Form Approved OMB No. 0704-0188	
Public reporting burden for this collection of information is estimated to average 1 hour per response, including the time for reviewing instructions, searching existing data sources, gathering and maintaining the data needed, and completing and reviewing this collection of information. Send comments regarding this burden estimate or any other aspect of this collection of information, including suggestions for reducing this burden to Department of Defense, Washington Headquarters Services, Directorate for Information Operations and Reports (0704-0188), 1215 Jefferson Davis Highway, Suite 1204, Arlington, VA 22202-4302. Respondents should be aware that notwithstanding any other provision of law, no person shall be subject to any penalty for failing to comply with a collection of information if it does not display a currently valid OMB control number. PLEASE DO NOT RETURN YOUR FORM TO THE ABOVE ADDRESS.					
1. REPORT DATE 1 July 2009		2. REPORT TYPE Final		3. DATES COVERED 1 Jul 2005 – 30 Jun 2009	
4. TITLE AND SUBTITLE A Partnership Training Program In Breast Cancer Research Using Molecular Imaging Techniques				5a. CONTRACT NUMBER	
				5b. GRANT NUMBER W81XWH-05-1-0291	
				5c. PROGRAM ELEMENT NUMBER	
6. AUTHOR(S) Paul C. Wang, Ph.D. E-Mail: pwang@howard.edu				5d. PROJECT NUMBER	
				5e. TASK NUMBER	
				5f. WORK UNIT NUMBER	
7. PERFORMING ORGANIZATION NAME(S) AND ADDRESS(ES) Howard University Washington, DC 20059				8. PERFORMING ORGANIZATION REPORT NUMBER	
9. SPONSORING / MONITORING AGENCY NAME(S) AND ADDRESS(ES) U.S. Army Medical Research and Materiel Command Fort Detrick, Maryland 21702-5012				10. SPONSOR/MONITOR'S ACRONYM(S)	
				11. SPONSOR/MONITOR'S REPORT NUMBER(S)	
12. DISTRIBUTION / AVAILABILITY STATEMENT Approved for Public Release; Distribution Unlimited					
13. SUPPLEMENTARY NOTES					
14. ABSTRACT This partnership training program is between Howard University and the Johns Hopkins University to pursue breast cancer research using molecular imaging techniques. The program has two components: a research component and a broad training component. Six Howard faculty members and two research assistants were trained. Two collaborative research projects have completed: (1) Magnetic Resonance Imaging Enhancement by Tumor Cell Targeted Immunoliposome Complex Delivered Contrast Agent, and (2) Imaging the Effects of Macrophage Function on Tumor Progression. The broad training program includes: mentoring research, seminars, workshops, and laboratory internships. A Molecular Imaging Lab at Howard has been established and an optical imaging equipment was acquired. The lab has offered journal club, seminars and workshops on MRI and optical imaging. The Molecular Imaging Lab became a synergic center for promoting molecular imaging research on campus. New research collaborations were established among the faculty at Howard and scientists from Georgetown and Children's Hospital. We have recruited a new faculty member and supported one undergraduate student. We published 15 papers and gave 40 presentations. We have submitted 24 grants, and we received three new grants from DoD, NIH, and Latham Foundation. We have achieved the goals of our program: to offer training opportunities for new researchers and Howard community, to establish a Molecular Imaging Lab, and to secure external funding.					
15. SUBJECT TERMS raining, molecular imaging, breast cancer, optical imaging, magnetic resonance imaging					
16. SECURITY CLASSIFICATION OF:			17. LIMITATION OF ABSTRACT	18. NUMBER OF PAGES	19a. NAME OF RESPONSIBLE PERSON
a. REPORT	b. ABSTRACT	c. THIS PAGE			USAMRMC
U	U	U	UU	156	19b. TELEPHONE NUMBER (include area code)

Table of Contents

Introduction.....	4
Body.....	5
Key Research Accomplishments.....	10
Reportable Outcomes.....	12
Conclusions.....	18
References.....	20
Appendices.....	21

A Partnership Training Program In Breast Cancer Research Using Molecular Imaging Techniques

I. INTRODUCTION

Advances in molecular and cell biology techniques in recent years have had a marked effect on our understanding of the cellular and molecular mechanisms of cancers, including breast cancer. Significant strides have also been made in the development of a noninvasive, high-resolution, in vivo imaging technology such as positron emission tomography (PET), magnetic resonance imaging (MRI), and optical imaging techniques for better imaging of tumors. In vivo molecular imaging, which utilizes these two fronts, opens up an extraordinary opportunity for studying diseases noninvasively, and in many cases, quantitatively at the molecular level (1-4). Molecular imaging is a growing research discipline aimed at developing and testing novel tools, reagents, and methods to image specific molecular pathways in vivo, particularly those that are key targets in disease processes.

The current assessment of breast cancer depends on anatomic and physiological changes of the disease. These changes are a late manifestation of the molecular changes that truly underlie the disease. If imaging of these early molecular changes is possible, it will directly affect patient care by allowing much earlier detection of the disease. Potentially, clinicians may be able to image molecular changes that currently are defined as “predisease states”. This will allow intervention at a time when the outcome will be most likely affected. In addition, by directly imaging the underlying alterations of disease, the effects of therapy may be monitored shortly after therapy has been initiated in contrast to the many months often required(5).

In this proposed training program, a partnership between Howard University (HU) and the In Vivo Cellular Molecular Imaging Center (ICMIC) at Johns Hopkins University (JHU) was established to pursue the molecular imaging research of breast cancer. At Howard University, this partnership involves a multidisciplinary consortium of five departments. The program is composed of two components: a research component and a broad training component. Howard University faculty have obtained training through conducting collaborative research and by participating in a broad based training program. Experts from Johns Hopkins have participated in training by offering laboratory internships, mentoring research efforts, and conducting seminars and workshops. Through this program, a core facility will be established to support sustainable long-term molecular imaging research at Howard University.

Our goal for this program is to provide faculty trainees at Howard University with basic and updated molecular imaging techniques that they can employ while conducting breast cancer research. The program objectives are:

1. Train new researchers in the breast cancer imaging using molecular imaging techniques.
2. Offer molecular imaging and breast cancer-related lectures, seminars, workshops, and laboratory internships.
3. Conduct two proposed research projects:
 - a. Magnetic resonance (MR) image enhancement by tumor cell targeted immunoliposome complex delivered contrast agent.
 - b. Imaging the effects of macrophage function on tumor progression.
4. Establish a molecular imaging core to support long-term sustainable research.
5. Research concept development and submit grants in breast cancer imaging.

II. BODY

This training program consists of two components: a research component and a broad based training component. The research component includes research in molecular imaging of breast cancer and the establishment of a molecular imaging core facility at Howard University.

II.1 Research Projects

(a) Research Projects:

Project 1: MR Image Enhancement by Tumor Cell Targeted Immunoliposome Complex Delivered Contrast Agent

Contrast-enhanced MRI is one of the best noninvasive methodologies available today in clinical medicine for assessing anatomy and function of tissues (6). High spatial resolution and high soft tissue contrast are desirable features of noninvasive MRI. However, due to intrinsically low sensitivity, a large amount of CA has to be used due to the non-specific uptake by tumors *in vivo*. In recent years, targeted CA delivery systems have been developing based on the concept that molecular imaging can increase the signal to noise ratio by detecting the difference in 'molecular properties' between cancer and normal tissues (7-9). This should, in theory, allow for detection of smaller tumors. As one strategy, monoclonal antibodies or antibody fragments have been coupled with CA directly or linked with CA through liposome (Lip) carriers. High concentrations of antibody-mediated CA such as Gd provides high T1 positive contrast *in vivo*, but insufficient direct linkage of Gd with antibodies or the large molecular size of antibody-Lip-Gd particles may limit its use for imaging cell-surface receptors in solid tumors because of inefficient extravasation and very slow diffusion in the interstitial compartment (10,11). Furthermore, antibody immunogenicity, poor stability of the conjugates and a potential change of the antibody binding ability due to changes in surface antigens are still problematic for *in vivo* applications. A ligand with less toxic, high binding specificity for tumors, relative small size and without immunogenicity is required to target the CA to tumors.

Optical imaging offers several advantages over other imaging techniques. Among these are simplicity of technique, high sensitivity and absence of ionizing radiation. There is a general increase in the development of techniques for *in vivo* evaluation of gene expression, monitoring of gene delivery and real-time intraoperative visualization of tumor margins and metastatic lesions to improve surgical outcomes (12-14). Limited depth of light penetration and lack of tomographic information prevent *in vivo* efficiency of optical imaging. In order to overcome the limitations of various imaging modalities, multimodal probes have been developed for detection using multiple imaging devices (15-17).

Transferrin receptor (TfR) is a cell-surface internalizing receptor responsible for almost all iron sequestration in mammalian cells. Overexpression of TfR is reported on human cancers from various tissues including breast and is of great value in grading tumors and determining prognosis (18). TfR has been successfully applied as a molecular target to direct therapeutic agents to tumor cells (19). Transferrin (Tf), the TfR ligand, is a monomeric glycoprotein that binds Fe^{3+} atoms for delivery to vertebrate cells through receptor-mediated endocytosis. Fluorescently labeled Tf has greatly aided the investigation of endocytosis *in vitro*. *In vivo* use of the physiological serum protein Tf is less likely to cause adverse reactions. Indeed, Tf has been

successfully used in targeted gene therapy (20, 21). We hypothesized that near-infrared dye (NIR) labeled Tf (Tf^{NIR}) would be an ideal ligand and would selectively increase the cellular uptake of MRI and optical reporters *in vivo*, resulting in contrast-enhanced MRI and NIR-based optical detection.

We have first developed a Tf- and Lip-mediated dual molecular probe with both fluorescent and magnetic reporter groups (Tf^{NIR}-Lip^{NBD}-CA). The nanoparticles were constructed with Tf on the surface of Lip as a ligand for specific targeting and CA (Magnevist) inside as the payload. These components together formed a liposomal nanocomplex, Tf^{NIR}-Lip^{NBD}-CA, with a diameter less than 100 nm. The feasibility of the nanoparticles was tested both *in vitro* and in animal models. *In vitro* analysis demonstrated that the Tf^{NIR}-Lip^{NBD}-CA nanocomplex dramatically improved the uptake of CA in monolayer cultures of MDA-MB-231-luc human breast cancer cells through both receptor- and Lip-mediated endocytosis. *In vivo*, the probe significantly enhanced the MRI signals, and was superior to the use of clinical MRI CA alone. The DCE-MRI exhibited heterogeneous signal enhancement by the liposomal nanocomplex probe and was correlated well with the pathology of the tumors.

To visualize tumors using the optical imaging technique, the Tf was labeled with NIR fluorescent dye (Tf^{NIR}). NIR dyes were encapsulated in the Lip, instead of MRI CA, to yield targeted fluorescent liposome nanoparticles (Tf^{NIR}-Lip^{NBD}-dye) in some experiments. Confocal microscopy showed endocytosis of the fluorescent reporters from Tf, liposome particles and encapsulated dyes, separately, following incubation of the MDA-MB-231-luc cells with the nanoparticles. Pretreatment with Tf blocked the cellular uptake of the reporters indicating the importance and specificity of the Tf moiety for targeting. Quantification using flow cytometry revealed a 1.8, 7.0 and 16 fold higher fluorescence intensity in cells incubated for 1 hour with Tf^{NIR}, Lip^{NBD}-dye, and Tf^{NIR}-Lip^{NBD}-dye, separately, than in control cells without probes (all $p < 0.05$). Systemic administration of Tf^{NIR} alone showed a preferential accumulation of the fluorescent signal in tumor xenografts in nude mice. The fluorescent signal was clearly detectable at 10 min in tumors and reached the maximum intensity at 90-120 min after injection. The ratio of the signal from tumor to background from muscle ranged from 1.64 to 3.14, depending on the tumor sizes. Application of the Tf^{NIR}-Lip^{NBD}-dye nanoparticles further increased the signal from tumor to background ratio by up to 30 % compared to Tf^{NIR} alone. Importantly, Tf^{NIR}-Lip^{NBD}-dye system is superior to Tf^{NIR} alone for imaging small tumors (<3 mm in diameter).

To increase the sensitivity of optical imaging in early diagnosis of cancers, we have further designed QDs conjugated with Tf as an optical imaging agent. QD is chosen to improve detection sensitivity due to its great extinction coefficient and emission of bright light in comparison to the organic fluorescent dyes. Two-step carbodiimide chemistry process was used to obtain the QDs-transferrin conjugation. First, Carboxylated QDs were activated by excess EDC and sulfo-NHS at pH 6.5. Then the excess EDC and sulfo-NHS was removed by Sephadex™. Later, the activated QDs were conjugated with transferrin at pH 8.3, and further purified by gel filtration. A controlled experiment from Tf-Alexa Fluor conjugate was used to confirm the conjugation. The successful linkage of transferrin to QDs was demonstrated by SDS-PAGE gel electrophoresis. *In vitro* uptake of QDs-Tf by MDA-MB-231 cells was confirmed by cellular labeling combined with flow cytometry. In addition, to further stabilize quantum dots, a novel kind of tri-block copolymer as a multi-dentate ligand has been successfully synthesized. The block copolymer has a polycarboxylic acid and polythiol block at both ends and an intermediate poly(styrene/divinyl benzene) block. The multiple mercapto groups of polythiol

block will act as multi-dentate ligands to stabilize quantum dots nanoparticles, while the polycarboxylic acid block offers reaction sites to modify or conjugate quantum dots with biomolecules. The densely compacted hydrophobic intermediate shell formed from cross-linked poly(styrene/divinyl benzene) block will efficiently prohibit the diffusion of other molecules through the macromolecular shell, resulting in decomposition of quantum dots. The QDs can be coated and stabilized with this multi-dentate block copolymer in water. It is expected that the novel multi-dentate ligand can improve the stability and biocompatibility of QDs under harsh in vivo conditions.

In addition, we have also developed a bioluminescence assay system for rapid measurement of tumor cell death using Xenogen IVIS digital camera system and luciferase-transfected MDA-MB-231-luc cells. The system was tested when cells were subjected to 43 °C hyperthermia and compared with traditional methods including MTT and colony formation assays. The luminescence using the bioluminescence assay system was related to the number of viable cells over a wide range (10^2 to 10^5 cells per well). The decrease in luminescence was detectable immediately after heat treatment. This decrease was related to the duration of heating at 43°C. Relative to the gold standard of clonogenic assay, MTT assay overestimated viability, while bioluminescence underestimated viability of cells subjected to hyperthermia. Bioluminescence assay of response to hyperthermia is rapid in bioluminescent cells, but is not closely related to the clonogenic potential. This suggests that other ATP based assays of cell viability will also overestimate cytotoxicity when compared to clonogenicity assays. Nonetheless bioluminescence estimate of ATP in cells can be used for rapid screening of cytotoxic regimens.

Project 2: Imaging the Effects of Macrophage Function on Tumor Promotion

Accumulating evidence implicates tumor-associated macrophages (TAMs) in tumor progression. Recent reports indicate that key modifier genes of tumor progression are expressed in TAMs. Macrophage ablation has been proposed as a therapeutic strategy; however, context-specific targeting of TAMs would be preferable. We used a pathway-focused gene array, RT-PCR, and Western blot analyses of inflammation- and angiogenesis-related gene expression in co-cultured MCF-7 cells and macrophages, to determine how interactions between the two cell types are affected by tamoxifen and aspirin. We also sought to identify phenotypic changes that may render TAMs selectively vulnerable to pharmacological agents.

THP-1 (human monocytic leukemia), MCF-10A (nontumorigenic mammary epithelial), MCF-7 (mammary adenocarcinoma) and MDA-MB-231 (mammary adenocarcinoma) were used in this study. THP-1 monocytes were differentiated to macrophages with PMA (100 nM) for 3 d; differentiated macrophages were activated with LPS (20 ng/ml) for 5 h. THP-1 were cultured in RPMI medium 1640 supplemented with 7.5% FBS, 100 U/ml penicillin, 100 µg/ml streptomycin, and 50 µM 2-mercaptoethanol. Breast cell lines were propagated in MEM supplemented with 8% FBS and antibiotics. 1×10^6 THP-1 cells/well were seeded in the inserts (3-µm pore size) of 6-well Transwell™ chambers, and differentiated 1 d later with PMA, and then activated with LPS. 2.5×10^5 MCF-7 cells/ml were seeded in a 2-ml volume in lower wells (separately) 2 d after THP-1 cells were seeded. The medium of both cell types was changed and inserts (activated macrophages) were placed in the lower wells. Chambers were incubated for 3 d. Tamoxifen, aspirin, and rhMIF were used at final concentrations of 10 µM (24 h), 1 mM (24 h), and 10 ng/ml (6 h), respectively. The results showed that all cells expressed MIF RNA. In culture, *MIF* expression was upregulated in MCF-7, but downregulated in macrophages. MCF-7-

induced reduction of MIF expression in TAMs may be associated with partial M2 polarization; therefore, co-culture produced macrophage phenotypes that were intermediate between M1 and M2. Reduction of MIF expression may also produce context-specific vulnerability of macrophages to therapeutic agents. Aspirin induced *IL-10* expression in both macrophages and MCF-7 grown separately. MCF-7 cells did not express *IL-10* when grown separately or in co-culture. However, aspirin induced *IL-10* expression in MCF-7 and in tamoxifen-pretreated MCF-7. Moreover, aspirin-pretreated macrophages potently induced *IL-10* expression in MCF-7 cells and pretreatment of MCF-7 with tamoxifen did not prevent this induction. Two molecular variants of MIF were identified: a larger, macrophage-type and a smaller, MCF-7-type; both variants were present in co-cultured MCF-7 cells. Co-culture of MCF-7 with LPS-activated THP-1 macrophages induced a change in MCF-7 morphology reminiscent of an epithelial-to-mesenchymal transition.

(b) Establish a Molecular Imaging Core Facility

It is essential for Howard to establish a basic infrastructure that is capable of supporting a sustainable long-term research program in the field of molecular imaging of breast cancer after this training program. This infrastructure is necessary in order to provide the researchers with tools to perform the proposed researched projects as well as to provide a broader research training experience. The core of the infrastructure is built upon the existing Biomedical NMR Laboratory in the Howard University Cancer Center. The newly established Molecular Imaging Laboratory has two NMR machines capable of imaging small animals. Through this program, a fluorescent and luminescence imaging instrument (Xenogen IVIS 200) was acquired, which enables us to study stromal inflammation and the internalization of contrast agent in tumor. This new optical imaging instrument has significantly enhanced the molecular imaging capabilities of the research core at Howard University. This has complemented the existing NMR imaging facility on campus. The core facility in the Molecular Imaging Laboratory also includes other optical instruments such as a fluorescent microscope, a confocal microscope, and a SEM. The staff of the Molecular Imaging Lab includes two imaging scientists, a molecular biologist, a chemist, and a research assistant. The lab becomes a synergistic center on campus for promoting molecular imaging research. New research collaborations were established among the faculty at Howard as well as with the external scientists from Georgetown University and the Children's National Medical Center. Currently, there are fourteen projects using the lab imaging facility conducting research on a variety of topics including breast cancer research.

II.2 Broad Based Training Components

The Molecular Imaging Lab has regular bi-weekly group meetings, journal club, and seminars. Many outside speakers were invited to give seminars. The faculty trainees have also attended special workshops on molecular imaging and imaging instrumentation. There were at least three workshops on molecular imaging and imaging techniques each year. The trainees have also attended weekly seminars at JHU ICMIC. The trainees have in-depth group meetings with faculty from JHU to exchange ideas and discussing various aspects of the research. The PI and the partnership leader at JHU have been coordinating the training efforts through meetings and emails. The PI and faculty trainees have submitted grants to NIH and CDMRP together with the partnership leader at JHU.

II.3 Statement of Work

All the tasks listed in the Statement of Work have been accomplished.

Task 1. To conduct the study “MR Image Enhancement by Tumor Cell Targeted immunoliposome Complex Delivered Contrast Agent”

- a. Purchase supplies for cell culture and materials for construction of liposome (Mon 1-2)
- b. Construct and measure the size of liposome (Months 3-4)
- c. Attach ligands (single chain variable fragment of transferring antibody) to liposome (TfR-scFv-Lip) (Months 5-8)
- d. Make TfR-scFv-Lip-contrast agent complex. Measure the size of complex and amount of contrast agent encapsulated in the liposome (Month 9-12)
- e. In vitro imaging of transfected MDA-MB-231 breast cancer cells in pellet (Month 13-24)
- f. Verify the transfection efficiency by MRI and optical imaging (Month 19-24)
- g. Animal Study: Grow tumor xenografts on nude mice. In vivo MRI imaging of 120 tumor-bearing mice administered TfR-scFv-Lip-CA, Lip-CA, and CA only, using T1 and T2 weighted MRI imaging techniques (Months 27-45)
- h. Quantify the contrast enhancement. Image data analysis (Months 27-45).

Task 2. To conduct the study “Imaging the Effects of Macrophage Function on Tumor Promotion”

- Determine the effects of macrophages on metastasis-related gene expression in breast cancer cells (Months 1 – 24)
 - a. Measure migratory and invasive properties of breast cell lines that are co-cultured with macrophages: changes in anchorage-dependent cell growth, invasion through matrigel (Months 1 – 12)
 - b. Isolate RNA for gene expression analysis using gene arrays. Monitor expression of proinvasive integrins, MMPs, and TIMPs, etc. (Months 6 – 18)
 - c. Transfect MCF-12A (mammary epithelial cells), MDA-MB-231, and MDA-MB-468 cancer cells with luciferase construct. Screen luciferase-expressing cells and isolate stable clones by limiting dilution (Months 8 – 24)
- Determine the effects of co-culture with macrophages on the growth of Luc⁺ mammary co-culture with macrophages on the growth of Luc⁺ mammary epithelial cells and breast cancer cells in 20 athymic nu/nu mice (Months 24 – 48)
 - a. Luc⁺ MCF-7 cells (in development) and MDA-MB-231 cells will be obtained from Xenogen. Luc⁺ mammary epithelial and breast cancer cells co-cultured with macrophages (LPS activated or unactivated). Inject breast cells into athymic mice and monitor with the Xenogen IVIS™ Imaging System. (Month 24-48)
 - b. Repeat gene expression experiments in Luc⁺ cells to correlate gene expression patterns with *in vivo* growth (Months 36 – 48)

Task 3. To establish a molecular imaging core facility

- a. Purchase laboratory supplies (months 1-4)
- b. Purchase Xenogen IVIS imaging system (months 3-9)
- c. Establish the designated Molecular Imaging Core Facility in Cancer Center (Rm B103). Install incubator and hood. (Months 3-9)
- d. Relocate/centralize all the molecular biology instruments to the Molecular Imaging Core Facility (Months 3-9)
- e. Training on Xenogen IVIS imaging system (Month 10)
- f. Molecular Imaging Core Facility open house (Month 10)

Task 4. To train faculty trainees in molecular imaging research.

- a. Biweekly group meetings (organized by research leaders) (Months 1-48)
- b. Monthly journal clubs (Months 1-48)
- c. Seminar series (nine seminars each year) (Months 1-48)
- d. Six workshops (chaired by Dr. Wang and Dr. Bhujwalla) (months 1-18)
- e. Laboratory Internships (2 days to one week each) (Months 1-18)
- f. Research concepts development
- g. Research grants submission

Task 5. Administrative and communication affairs

- a. Status reports (monthly, quarterly, and annual reports).
- b. Research progress review (quarterly).
- c. Administrative meetings (biannually meetings).
- d. Coordination of seminars, workshops, and laboratory internships.

III. KEY RESEARCH ACCOMPLISHMENTS

Project 1: MR Image Enhancement by Tumor Cell Targeted Immunoliposome Complex Delivered Contrast Agent

- We have successfully constructed a dual imaging probe for MRI and fluorescent imaging by linkage of near-infrared (NIR) fluorescently labeled transferrin (Tf^{NIR}) on the surface of contrast agent (CA)-encapsulated cationic liposomes (Tf^{NIR} -Lip^{NBD}-CA).
- The size of dual probe is controlled by gel filtration and its size (~80 nm) was determined by laser light scattering technique. The amount of MR contrast agent encapsulated in the liposome was measured by the atomic absorption spectroscopy.
- Using confocal microscopy, fluorescent imaging, and MRI, we have confirmed that the cellular uptake of both fluorescent and magnetic reporter groups in monolayer cultures of MDA-MB-231-luc human breast cancer cells significantly increased compared to that of fluorescent dye or MR contrast agent alone.
- In vivo, the probe significantly enhanced the MRI signals, and was superior to the use of clinical MRI CA alone. The contrast enhancement in MRI by the Tf^{NIR} -Lip^{NBD}-CA probe showed a heterogeneous pattern within tumors, which reflected the tumor morphological

heterogeneity. The heterogeneous signal enhancement by the liposomal nanocomplex probe correlates well with the pathology of the tumors.

- Dynamic contrast enhancement MRI (DCE-MRI) imaging shows the MRI image intensities increase initially and later decrease at various rates for different regions in the tumor using either Tf-Lip-Mag liposomal nanocomplex or Magnevist. These distinct differences are due to the specific targeting and prolong retention of the Tf-Lip-Mag liposomal nanocomplex in the tumor.
- A much higher contrast in viable cells in the periphery of tumors was observed at the initial stage of the targeted DCE-MRI. The image intensity was persistently higher compared to the DCE-MRI of free CA and lasts for several hours.
- Quantitative analysis of Gd concentration from muscle, necrotic areas and area of viable cells of the tumor reveal that after 120 min of i.v. administration of the nanocomplex the Gd concentrations are about ~2.5 times higher in the samples collected from the mice injected with Tf-Lip-Mag than the mice injected with contrast agent, Magnevist, only.
- The highest Gd concentration ratio of 2.8 was observed in the samples collected in the region of viable cells in the tumor.
- The dual probe not only enhances the tumor MR image contrast but also is an excellent probe for NIR optical imaging. The probe is also superior to the MR contrast agent for identifying the tumor pathology.
- Three human breast cancer models including subcutaneous tumor xenografts, mammary gland xenografts and lung metastasis in nude mice were also established using luciferase-expressing MDA-MB-231-luc cells. The MDA-MB-231-luc cell line has been transfected with the luciferase gene for bioluminescent optical imaging.
- For optical imaging of human breast cancers, we have constructed targeted fluorescent liposome nanoparticles using near-infrared (NIR) fluorescent transferrin conjugate (Tf^{NIR}), NIR fluorescent dyes and fluorescently labeled (NBD) cationic liposomes (Lip^{NBD}) ($\text{Tf}^{\text{NIR}}\text{-Lip}^{\text{NBD}}\text{-dye}$). *In vitro* and *in vivo* analysis indicates that both Tf^{NIR} and $\text{Tf}^{\text{NIR}}\text{-Lip}^{\text{NBD}}\text{-dye}$ are potentially useful for visualizing human breast cancer in clinic. $\text{Tf}^{\text{NIR}}\text{-Lip}^{\text{NBD}}\text{-dye}$ is superior to Tf^{NIR} alone for imaging small tumors because of better delivery of fluorescent contrast agents to the tumors.
- Dynamic optical imaging of MDA-MB-231-luc tumors growing on the mouse's back or on the mammary gland fat pad showed the luminescent image intensity increased to its peak in ~ 20 minutes and gradually diminished about one hour after intraperitoneal injection of D-luciferin.
- A significant correlation between tumor volume and optical signal intensity of luminescent images in tumor was established. Metastatic lesion of 0.3-0.5 mm in diameter could be clearly detected *in vivo*.
- To increase the sensitivity of optical detection of breast cancer, we have synthesized QDs and conjugated QDs with Tf as an optical imaging agent. *In vitro* targeted uptake of QDs-Tf by MDA-MB-231 cells was confirmed using flow cytometry. In addition, to further stabilize QDs, a novel kind of tri-block copolymer as a multi-dentate ligand has been successfully synthesized. It is expected that the novel multi-dentate ligand can improve the stability and biocompatibility of QDs under harsh *in vivo* conditions.
- We have also developed a bioluminescence assay for rapid measurement of cell death using Xenogen Optical Imaging System and luciferase transfected MDA-MB-231-luc human breast cancer cells. The assay was tested when cells were subjected to 43°C

hyperthermia and compared with traditional methods including MTT and colony formation assays. The results indicate that this assay may be used for rapid screening of cytotoxic regimens.

Project 2: Imaging the Effects of Macrophages on Breast Cancer Metastasis

- MCF-7-Luc-F5 cells grown in RPMI Medium 1640 supplemented with 10% FBS and 10 g/ml bovine insulin, sodium pyruvate and non-essential amino acids, showed significant differences in the growth patterns, compared with the parent MCF-7 cells grown in MEM without insulin, non-essential amino acids, sodium pyruvate and phenol red.
- MCF-7-Luc-F5 cells have a doubling time of 22 hours as compared to the parental MCF-7 cell line which takes 40 hours.
- MCF-10A (immortalized mammary epithelial) cells have the highest levels of phosphatase and tensin homology gene PTEN mRNA compared to MCF-7 and MDA-MB-231, which is consistent to their non-tumorigenic characteristic.
- Co-culture of MCF-7 with activated human monocytic leukemia, THP-1, derived macrophages caused an increase in PTEN expression.
- Migration inhibitory factor (MIF) expression is dramatically induced in MCF-7 cells when they are co-cultured with macrophages.
- We have analyzed how interactions between the MCF-7 and macrophages are affected by tamoxifen and aspirin, and the phenotypic changes that may render TAMs selectively vulnerable to pharmacological agents.
- All cells expressed MIF RNA. In co-culture, *MIF* expression was upregulated in MCF-7, but downregulated in macrophages. MCF-7-induced reduction of MIF expression in TAMs may be associated with partial M2 polarization; therefore, co-culture produced macrophage phenotypes that were intermediate between M1 and M2. Reduction of MIF expression may also produce context-specific vulnerability of macrophages to therapeutic agents.
- Aspirin induced *IL-10* expression in both macrophages and MCF-7 grown separately. MCF-7 cells did not express *IL-10* when grown separately or in co-culture. However, aspirin induced *IL-10* expression in MCF-7 and in tamoxifen-pretreated MCF-7. Moreover, aspirin-pretreated macrophages potently induced *IL-10* expression in MCF-7 cells and pretreatment of MCF-7 with tamoxifen did not prevent this induction.
- Two molecular variants of MIF were identified: a larger, macrophage-type and a smaller, MCF-7-type; both variants were present in co-cultured MCF-7 cells. Co-culture of MCF-7 with LPS-activated THP-1 macrophages induced a change in MCF-7 morphology reminiscent of an epithelial-to-mesenchymal transition.

IV. REPORTABLE OUTCOMES

Publications

1. Pirollo K, Dagata J, Wang PC, Freedman M, Vladar A, Fricke S, Ileva L, Zhou Q, Chang EH. A Tumor-Targeted Nanodelivery System to Improve Early MRI Detection of Cancer. *Molecular Imaging* 5(1):41-52, 2006

2. Shan L, Wang S, Sridhar R, Bhujwalla ZM, Wang PC. Dual Probe with Fluorescent and Magnetic Properties for Imaging Solid Tumor Xenografts. *Molecular Imaging* 6(2):85-95, 2007.
3. Chang YJ, Hsu HY, Hsu J, Yao WC, Hsu MS, Chen MC, Lee SC, Hsu C, Miao L, Byrd K, Chouikha M, Gu XB, Wang PC, Szu H. Non-invasive methodology for wellness baseline profiling. *Proceedings of SPIE "Independent Component Analyses, Wavelets, Unsupervised Nano-Biomimetic Sensors, and Neural Networks V"*, vol. 6576:OR1-17, 2007.
4. Manaye KF, Wang PC, O'Neil JN, Tizabi Y, Lei D, Xu T, Huang SY, Ottinger MA, Ingram DK, Mouton PR. Neuropathological Quantification of Dtg APP/PS1: Neuroimaging, Stereology, and Biochemistry. *AGE* (29):87-96, 2007.
5. Ross, S, Ejofodomi O, Jendoubi A, Kinnard L, Chouikha M, Lo B, Wang P, Zheng J. A Mammography Database and View System for the African American Patients. *J Digital Imaging* 21(1):18-26, 2008.
6. Cheng KT, Wang PC, and Shan L. Alexa Fluor 680-labeled transferrin- cationic (NBD-labeled DOPE-DOTAP) liposome-encapsulated gadopentetate dimeglumine complex (Abbreviated name: Tf^{NIR}-Lip^{NBD}-CA complex) targeting to transferrin receptors (TfR). In: *Molecular Imaging and Contrast Agent Database (MICAD)* [database online]. Bethesda (MD): National Library of Medicine (US), NCBI; 2008. <http://micad.nih.gov>.
7. Burnett GT, Wathersby DC, Taylor TE, Bremner TA. Regulation of Inflammation- and Angiogenesis-related Gene Expression in Breast Cancer and Co-Cultured Macrophage. *AntiCancer Res.* 28(4B): 2093-2100, 2008
8. Shan L, Hao YB, Wang SP, Korotcov A, Zhang RS, Wang TX, Califano J, Gu XB, Sridhar R, Bhujwalla ZM, Wang PC. Visualizing Head and Neck Tumors In Vivo Using Near-infrared Fluorescent Transferrin Conjugate. *Molecular Imaging* 7(1):42-49, 2008.
9. Shan L, Wang SP, Zhou YF, Korotcov A, Sridhar R, Wang PC. Bioluminescent Animal Models of Human Breast Cancer for Tumor Biomass Evaluation and Metastasis Detection. *Ethnicity and Disease* 18(S2):65-69, 2008.
10. Yin JJ, Lao F, Meng J, Fu PP, Zhao YL, Xing GM, Gao XY, Sun BY, Wang PC, Chen CY, and Liang XJ. Inhibition of Tumor Growth by Endohedral Metallofullerenol Nanoparticles Optimized as Reactive Oxygen Species Scavenger. *Mol Pharmacol.* Vol 74(4):1132-1140, 2008
11. Shan L, Zhang RS, Zhang WH, Lee E, Sridhar R, Snyderwine EG, Wang PC. Image-based Real-time Evaluation of the Molecular Events Underlying HC11 Mammary Epithelial Cell Differentiation, *Anal Biochem* vol 382:122-128, 2008.
12. Wang PC, Shan L, Wang SP, Korotcov A, Liang XJ. Transferrin Liposome Nanoparticle (Tf^{NIR}-Lip^{NBD}-Magnevist) – A Tumor Targeting MRI Contrast Agent. *Acta Biophysica Sinica* 24(4):315-322, 2008
13. Liang XJ, Chen CY, Zhao YL, Jia L, Wang PC. Biopharmaceutics and Therapeutic Potential of Engineered Nanoparticles. *Curr Drug Metab* vol 9(8):697-709, 2008

14. Yin JJ, Lao F, Fu PP, Wamer WG, Zhao YL, Wang PC, Han D , Qin Y, Sun BY, Xing GM, Dong JQ, Liang XJ, Chen CY. The Scavenging of Reactive Oxygen Species and the Potential for Cell Protection by Functionalized Fullerene Materials. *Biomaterials*. 30(4):611-621, 2009.
15. Wang PC, Blumenthal RP, Zhao YL, Schneider JA, Miller N, Grodzinski P, Gottesman MM, Tinkle S, Wang K, Wang C, Liang XJ. Building Scientific Progress Without Borders: Nanobiology and Nanomedicine in China and the U.S. *Cancer Res* 69(13):5294-5295, 2009

Meeting Abstracts

1. Wang PC, Pirollo K, Song HF, Shan L, Bhujwalla Z, Chang E. Evaluation of Transferrin Receptor Targeted Immunoliposome Contrast Agent Delivery System for In Vivo MR Imaging in Solid Tumor Xenografts. The Society of Molecular Imaging 4th Annual Meeting, September 7-10, 2005, Cologne, Germany.
2. Freedman M, Pirollo K, Fricke S, Wang PC, Chang E. Imaging of pancreatic carcinoma xenografts in athymic nude mice with carcinoma selective transferrin receptor targeting gadopentetate dimeglumine contrast agent. Radiological Society of North America 2005 Annual Meeting, Chicago, IL, Nov 27- Dec 2, 2005.
3. Zhao A, Teos LY, Wang PC, Blackwell KN, Haddad GE. Alterations in ANGII and IGF-1 signaling pathways during eccentric cardiac hypertrophy. *FASEB J*, 19(4): A557, 2005
4. Zhao A, Wang PC, Wang S, Li C, Laurence GG, Teos L, Haddad GE. Effects of ACE-Inhibition on ANG II and IGF-1 signaling during development and regression of eccentric cardiac hypertrophy. *FASEB J*. 495.3,.A834, 2006
5. Wang PC, Shan L, Wang S, Sridhar R, Bhujwalla Z, A Dual Probe with both Fluorescent and MR Reporters for Imaging Solid Tumor Xenografts. The Society of Molecular Imaging 5th Annual Meeting, August 29-September 2, 2006, Big Island, HI.
6. Shan L, Wang SP, Zhou YF, Wang PC. In Vivo Optical Imaging of Transferrin Receptors: Visualization of Tumor Biomarkers. 5th Asia Pacific Organization of Cell Biology, Oct 27-30, 2006, Beijing, China.
7. Wang PC, Shan L, Wang SP, Sridhar R, Bhujwalla ZM. Molecular Imaging of Solid Tumor Xenografts Using a Dual Fluorescent and MR Probe. 10th RCMI International Symposium, Dec 13-16, 2006, San Juan, Puerto Rico.
8. Chang, Hon-Yen Hsu, James Hsu, Wei-Cheng Yao, Ming-Sin Hsu, Ming-Chung Chen, Shi-Chen Lee, Charles Hsu, Lidan Miao, Kenny Byrd, Mohamed F. Chouikha, Xin-Bin Gu, Paul C. Wang, Harold Szu. Nonintrusive methodology for wellness baseline profiling. SPIE Defense and Security Symposium, "Independent Component Analyses, Wavelets, Unsupervised Nano-Biomimetic Sensors, and Neural Networks V", April 9-13, 2007, Orlando, FL.

9. Zhang R, Shan L, Zhou YF, Wang PC, Sridhar R. Rapid detection of cell death in a bioluminescent human breast cancer cell line subjected to hyperthermia. American Association for Cancer Research. April 14-18, 2007. Los Angeles, CA.
10. Wang PC, Shan L, Hao Y, Zhang D, Zhang R, Korotcov A, Wang TX, Califano J, Gu X. Optical Imaging of Head and Neck Squamous Cell Carcinoma Xenografts Using Near-infrared Fluorescent Transferrin Conjugate. Joint Molecular Imaging Conference, pp.318, Providence, RI, Sep 8-11, 2007
11. Wang PC. Molecular Imaging of Solid Tumor Xenografts Using a Dual Fluorescent and MR Probe. Progress in Biochemistry and Biophysics. vol 34(1):95, YiChang, China, Oct 12-15, 2007.
12. Liang XJ, Wang PC. Circumventing Malignant Tumors by Innovative and Effective Nanoparticle as Novel Chemotherapeutic Agent. Progress in Biochemistry and Biophysics. Vol 34(1):104, YiChang, China, Oct 12-15, 2007.
13. Wang PC. Molecular Imaging of Solid Tumor Xenografts Using a Dual Fluorescent and MR Probe, National Center for Nanoscience and Technology, Beijing, China. Oct 9, 2007.
14. Wang PC. Molecular Imaging of Tumor in Small Animals. NanChang, JiangXi, China. Oct 12, 2007.
15. Wang PC. Molecular Imaging of Solid Tumor Xenografts Using a Dual Fluorescent and MRI Probe. Fu Jen Catholic University, Taipei, Taiwan. Oct 24, 2007.
16. Wang PC. Studying of Solid Tumor in Small Animals Using Various Imaging Modalities. National Chung Shing University, TaiChung, Taiwan. Oct 26, 2007.
17. Wang PC. Molecular Imaging Laboratory. Howard University Nanotechnology Symposium. Nov 5-6, 2007.
18. Wang PC. Howard University Molecular Imaging Laboratory, National Children's Hospital, Washington, DC, January 9, 2008.
19. Wang PC. Molecular Imaging of Solid Tumor Xenografts Using a Dual Fluorescent and MRI Probe. Howard University Biochemistry and Molecular Biology Department, February 14, 2008.
20. Wang PC, Wang TX, Shan L, Wang SP, Korotcov A. Molecular Imaging of Solid Tumor in Small Animal Using a Dual Fluorescent and MRI Probe. BIROW, Rockville, MD, Jan 17-19, 2008.
21. Shan L, Korotcov A, Wang SP, Wang TX, Wang PC. Molecular Imaging of Solid Tumor in Small Animal Using a Dual Fluorescent and MRI Probe. Cancer Nanobiology Think Tank, NCI, Fredrick, MD, May 24, 2008.
22. Wang PC. Molecular Imaging Laboratory at Howard University. Era of Hope: Building Networks Symposium. Baltimore, MD, June 24-25, 2008
23. Wang TX, Shan L, Korotcov A, Wang SP, Zhou YF, Wang PC. Surface Coating and Bioconjugating of Quantum Dots for Non-invasive Detection of Breast Cancer. Era of Hope. Baltimore, MD, June 25-28, 2008.

24. Shan L, Wang SP, Zhou YF, Korotcov A, Zhang RS, Wang TX, Sridhar R, Bhujwalla ZM, Wang PC. Targeted Fluorescent Liposome Nanoparticles for Molecular Imaging of Breast Cancer Xenografts in Mouse. Era of Hope. Baltimore, MD, June 25-28, 2008.
25. Korotcov A, Shan L, Wang SP, Wang TX, Sridhar R, Bhujwalla ZM, Wang PC. Targeted DCE-MRI for Imaging and Characterization of Solid Tumor Xenografts. Era of Hope. Baltimore, MD, June 25-28, 2008.
26. Burnett G, Bremner T. Breast Cancer Cells Down-regulate Tristetraprolin in Co-cultured Macrophages: A Possible Mechanism for Sustaining Inflammation and Angiogenesis in the Tumor Microenvironment. Era of Hope. June 25-28, 2008, Baltimore, MD
27. Burnett GT, Weathersby DC, Taylor TE, Bremner TA. MCF-7 breast cancer cells down-regulate macrophage migration inhibitory factor in co-cultured macrophages: Implications for context-specific modulation of tumor-associated macrophages. Era of Hope. June 25-28, 2008, Baltimore, MD
28. Sridhar R, Beyene D, Zhou Y, Kassa A, Zhang R, Ashayeri E. Cytotoxicity, cell cycle effects and mutagenicity of etidronic acid towards MCF-7 human breast cancer cells. Era of Hope. June 25-28, 2008, Baltimore, MD
29. Sridhar R, Zhang R, Zhou Y, Shan L, Ashayeri E, Wang PC. Bioluminescence Imaging for Monitoring the Response of a Luciferase Transfected Human Breast Cancer Cell Line Subjected to Hyperthermia. Era of Hope. June 25-28, 2008, Baltimore, MD
30. Wang PC, Zhang RS, Sridhar R, Shan L. Imaging Molecular Events Underlying HC11 Mammary Epithelial Cell Differentiation. World Molecular Imaging Congress. Nice, France, September 10-13, 2008.
31. Wang PC. Molecular Imaging of Solid Tumor Xenografts Using a Dual Fluorescent and MRI Probe. Xiamen, China, October 6, 2008.
32. Wang PC. Lecture Series: Nuclear Magnetic Resonance Imaging. Chinese National Center for Nanosciences and Technology. Beijing, China, October 8, 10, 12 and 14, 2008.
33. Wang PC. Howard University Molecular Imaging Laboratory. Howard University Nanotechnology Symposium. Nov 11, 2008.
34. Korotcov AV, Shan L, Wang SP, Wang T, Chen Y, Sridhar R, Bhujwalla ZM, Wang PC. Dynamic Contrast Enhanced MRI of Solid Tumor Xenografts using Transferrin-conjugated Liposomal Nanocomplex. Howard University Nanotechnology Symposium. Nov 11, 2008.
35. Shan L. A Cell-based Imaging Technique for High Throughput Screening of Disruptors of Mammary Gland Differentiation. Howard University Nanotechnology Symposium. Nov 11, 2008.
36. Wang T, Sridhar R, Ting AH, Francis K, Mitchell J, Wang PC. Synthesis of Amphiphilic Triblock Copolymers as Multidentate Ligands for Surface Coating of Quantum Dots. Howard University Nanotechnology Symposium. Nov 11, 2008.

37. Wang PC. Dual Fluorescent and MR Probe and High Throughput Screening Using Optical Imaging Method. Institute of High Energy Physics, Beijing, China. February 13, 2009.
38. Wang PC. Visualizing head and neck tumors in vivo using near-infrared fluorescent transferrin conjugate. Metropolitan Biophotonics Symposium, Washington DC April 6, 2009.
39. Korotcov A, Shan L, Wang PC. A Nanocomplex System as Targeted Contrast Agent Delivery Vehicle for MRI Dynamic-Contrast-Enhancement Study. ChinaNANO 2009, Beijing, China, Sep 1-3, 2009.
40. Wang TX, Wang PC. Synthesis of Amphiphilic Triblock Copolymers with Multidentate Ligands for Surface Coating of Quantum Dots. 2009 World Molecular Imaging Congress. Montreal, Canada, Sep 23-26, 2009.

Degree Obtained

Giselle Burnett, a research assistant supported by this grant received B.S. degree in Biology at Howard University, in June, 2007. She is a medical student at the Howard University Medical School now. She has worked with Dr. Bremner on the Project 2 “Imaging the Effects of Macrophage Function on Tumor Promotion”. She gave a presentation in an international meeting and published a paper in Cancer Research.

Personnel Received Financial Support

- Howard University

Paul C. Wang, Ph.D. (Principal Investigator)
 Theodore A. Bremner, Ph.D. (Faculty Trainee)
 Liang Shan, M.D., Ph.D. (Faculty Trainee)
 James W. Mack, Ph.D. (Faculty Trainee)
 Rajagopalan Sridhar, Ph.D. (Faculty Trainee)
 Xingjie Liang, Ph.D. (Faculty Trainee)
 Songping Wang, Ph.D. (Research Assistant)
 Giselle Burnett, B.S. (Undergraduate Student Trainee)

- Johns Hopkins University

Zaver M. Bhujwalla, Ph.D. (Principle Investigator at Collaborating Institute)
 Dmitri Artemov, Ph.D. (Mentor)
 Arvind P. Pathak, Ph.D. (Mentor)
 Michael A. Jacobs, Ph.D. (Mentor)
 Kristine Glunde, Ph.D. (Mentor)
 Ellen Ackerstaff, Ph.D. (Mentor)

Grants

- Received Grants
 1. Biomedical Imaging Core Facility
NIH/NCRR/RCMI, 06/09-05/14, Paul Wang (PI)
 2. Tumor-targeted MR Contrast Enhancement Using Molecular Imaging Techniques
NIH 2U54CA091431-06A1, 05/07-04/10, Paul Wang (PI)
 3. Targeted Fluorescent Microspheres for Noninvasive Optical Detection of Tumors
Charles & Mary Latham Foundation, 01/07-12/07, Liang Shan (PI)
- Pending Grants
 1. A Partnership Training Program –Studying Targeted Drug Delivery Using Nanoparticles In Breast Cancer Diagnosis and Therapy, DoD CDMRP, Paul Wang (PI), Zaver Bhujwalla (co-PI), 04/09 submitted
 2. In Vivo NMR Spectroscopy for Therapeutic Drug Monitoring
DoD CDMRP, Raj Sridhar (PI), 04/09 submitted
 3. A Mammographic Image Searching System for African-American Women’s Breast Cancer Diagnosis, NIH Challenge Grant, Paul Wang (PI), 04/09 submitted

(Additional 18 unsuccessful grant applications)

V. CONCLUSION

In this four year training program , six Howard University faculty members and two research assistants from the Departments of Radiology, Radiation Oncology, and Biology were trained with the faculty at IC MIC at the Johns Hopkins University In Vivo Cellular Molecular Imaging Center (JHU ICMIC) in conducting molecular imaging research of breast cancer. The program is composed of two components: a research component and a broad training component.

The research training component has supported two collaborative research projects:

(1) *Magnetic Resonance Imaging Enhancement by Tumor Cell Targeted Immunoliposome Complex Delivered Contrast Agent*. We have successfully constructed a dual imaging probe for MRI and fluorescent imaging studies. MRI contrast agent (CA), Magnevist (Mag), was encapsulated inside cationic liposomes (Lip) and near-infrared (NIR) fluorescently labeled transferrin (Tf^{NIR}) was attached to the surface of liposomes to make the probe (Tf^{NIR} -Lip^{NBD}-CA). Using confocal microscopy, fluorescent imaging, and MRI we have confirmed that the cellular uptake of both fluorescent and magnetic reporter groups of the probe were significantly increased compared to that of fluorescent dye or MR contrast agent used alone in monolayer cultures of MDA-MB-231-human breast cancer cells. In vivo, the probe significantly enhanced the MRI signals, and was superior to the use of clinical MRI contrast agent alone. The distinct image enhancement is due to the specific targeting and prolonged retention of the Tf-Lip-Mag liposomal nanocomplex in the tumor. The MRI image contrast enhancement shows a distinct heterogeneous pattern within tumors, which reflects the tumor morphological heterogeneity and correlates well with the pathology of the tumors. It may be used to provide pathological information noninvasively. The superior image enhancement capability of the nanocomplex can also be used to increase the sensitivity of detecting small tumors. In the future,

special ligand attached nanocomplex CA can be used for quantifying the specific biomarkers expressed in tumors, which will be very useful for determining the patient's prognosis and response to treatment. (2) *Imaging the Effects of Macrophage Function on Tumor Progression*. We have shown that non-tumorigenic mammary epithelial MCF-10A cells have the highest levels of PTEN mRNA compared to MCF7 and MDA-MB-231 cells. When MCF-7 co-cultured with activated THP-1 macrophages, it caused an increase in PTEN expression. We also found that recombinant human migration inhibitory factor suppressed p53 expression in all three cell types tested. MIF expression is dramatically induced in MCF-7 cells when they are co-cultured with macrophages. We have determined how the interactions between MCF-7 cells and macrophages are affected by tamoxifen and aspirin. We have also identified the phenotypic changes that may render TAMs selectively vulnerable to pharmacological agents.

For the broad training component, experts from Johns Hopkins have participated in training through mentoring research, seminars, workshops, and offering laboratory internships. The Howard trainees have regularly attended weekly seminars and annual retreats at JHU. One of the trainees has been working with a JHU mentor in the mentor's lab to conduct the MRI dynamic contrast enhancement study and later transferred the technique to the Howard instrument. The PI and the partnership leader at JHU have been coordinating the training efforts through periodic meetings and emails.

We have established the Molecular Imaging Laboratory at the Howard University that serves as a university core facility. A major optical imaging equipment, Xenogen IVIS 200, was acquired through this funding. The Molecular Imaging Laboratory is staffed with an imaging scientist, a molecular biologist, a pharmacologic chemist, and a research assistant. The lab has regular bi-weekly group meetings, a journal club, and seminars. In addition, many guest seminars and workshops on MRI and optical imaging were organized. The Molecular Imaging Lab is continuously becoming a synergistic center on campus for promoting molecular imaging research. New research collaborations were established among the faculty at Howard, as well as with the external scientists from Georgetown University and Children's National Medical Center. Currently, there are fourteen projects using the imaging facilities in the lab conducting research on a variety of topics including breast cancer research.

During the funding period, we have published 15 papers and given 40 presentations in the local and international meetings. The Howard trainees have submitted 24 grants, to DoD CDMRP, NIH, and other funding agencies in the last four years. We received three new grants and three other grant applications are pending. We have recruited a new faculty member to join the project. A research assistant supported by this grant received her undergraduate degree in Biology and now is a second year medical student at the Howard University. One faculty trainee has joined NIH continuing pursuing molecular imaging research.

Overall, we have achieved the goals of the program: to train new researchers in breast cancer research using molecular imaging techniques, to offer broad training opportunities for faculty and students at Howard, conducting two basic research projects, establishing the Molecular Imaging Laboratory, promoting multidisciplinary research, and seeking external fundings for supporting sustainable long-term research.

VI. REFERENCES

1. Pautler RG (2004). Mouse MRI: concepts and applications in physiology. *Physiol.* 19:168-175.
2. Artemov D (2003). Molecular magnetic resonance imaging with targeted contrast agent. *J Cell Biochem.* 90: 518-524.
3. Massoud T F, Gambhir SS (2003). Molecular imaging in living subjects: seeing fundamental biological processes in a new light. *Gene Dev.* 17:545-580.
4. Persigehl T, Heindel W, Bremer C (2005). MR and optical approaches to molecular imaging. *Abdom Imaging.* 30:342-354.
5. Blasberg RG (2003). Molecular imaging and cancer. *Mol Cancer Ther.* 2:335-345.
6. Artemov D, Mori N, Okolie B, Bhujwala ZM (2003). MR molecular imaging of HER-2/neu receptor in breast cancer cells using targeted iron oxide nanoparticles, *Magn Reson Med.* 49:403-408.
7. Mulder WJM, Strijkers GJ, Griffioen AW, van Bloois L, Molema G, Storm G, Koning GA, Nicolay K (2004). A liposomal system for contrast-enhanced magnetic resonance imaging of molecular targets. *Bioconjugate Chem.* 15:799-806.
8. Jones DT, Trowbridge IS, Harris AL (2006). Effects of transferrin receptor blockade on cancer cell proliferation and hypoxia-inducible factor function and their differential regulation by ascorbate. *Cancer Res.* 66:2749-2756.
9. Hogemann-Savellano D, Bos E, Blondet C, Sato F, Abe T, Josephson L, Weissleder R, Gaudet J, Sgroi D, Peters PJ, Basilion JP (2003). The transferrin receptor: a potential molecular imaging marker for human cancer. *Neoplasia.* 5:495-506.
10. Batra JK, Fitzgerald DJ, Chaudhary VK, Pastan I (1991). Single-chain immunotoxins directed at the human transferrin receptor containing Pseudomonas exotoxin A or diphtheria toxin: Anti-TFR(Fv)-PE40 and DT 388-anti-TFR(Fv). *MolCellBiol.* 11:2200-2205.
11. Jain RK, Baxter LT (1988). Mechanisms of heterogeneous distribution of monoclonal antibodies and other macromolecules in tumors: Significance of elevated interstitial pressure. *CancerRes.* 48:7022-7032.
12. Xu L, Tang W H, Huang CC, Alexander W, Xiang LM, Pirollo KF, Rait A, Chang EH (2001). Systemic p53 gene therapy of cancer with immunolipoplexes targeted by anti-transferrin receptor scFv. *MolMed.* 7:723-734.
13. Xu L, Huang C-C, Huang W-Q, Tang W-H, Rait A, Yin Y, Cruz I, Xiang L-M, Pirollo K, Chang EH (2002). Systemic tumor-targeted gene delivery by anti-transferrin receptor scFv-immunoliposomes. *MolCancerTher.* 1:337-346.
14. Xu L, Pirollo KF, Tang W h, Rait A, Chang EH (1999). Transferrin-liposome-mediated systemic p53 gene therapy in combination with radiation results in regression of human head and neck cancer xenografts. *Hum Gene Ther.* 10:2941-2952.
15. Schellenberger EA, Sosnovik D, Weissleder R, Josephson L (2004). Magneto/optical annexin V, a multimodal protein. *Bioconjugate Chem.* 15:1062-1067.
16. Blasberg R G (2003). In vivo molecular-genetic imaging: multi-modality nuclear and optical combinations. *Nucl Med Biol.* 30:879-888.

17. Veisheh O, Sun C, Gunn J, Kohler N, Gabikian P, Lee D, Bhattarai N, Ellenbogen R, Sze R, Hallahan A, Olson J, Zhang M (2005). Optical and MRI multifunctional nanoprobe for targeting gliomas. *Nano Lett.* 5:1003-1008.
18. Jones DT, Trowbridge IS, Harris AL (2006). Effects of transferrin receptor blockade on cancer cell proliferation and hypoxia-inducible factor function and their differential regulation by ascorbate. *Cancer Res.* 66:2749-2756.
19. Hogemann-Savellano D, Bos E, Blondet C, Sato F, Abe T, Josephson L, Weissleder R, Gaudet J, Sgroi D, Peters PJ, Basilion JP (2003). The transferrin receptor: a potential molecular imaging marker for human cancer. *Neoplasia.* 5:495-506.
20. Xu L, Pirollo KF, Tang WH, Rait A, Chang EH (1999). Transferrin-liposome-mediated systemic p53 gene therapy in combination with radiation results in regression of human head and neck cancer xenografts. *Hum Gene Ther.* 10:2941-2952.
21. Bellocq NC, Pun SH, Jensen GS, Davis ME (2003). Transferrin-containing, cyclodextrin polymer-based particles for tumor-targeted gene delivery. *Bioconjugate Chem.* 14:1122-1132.

VII. APPENDICES (Reprints of all the published papers)

1. Pirollo K, Dagata J, Wang PC, Freedman M, Vladar A, Fricke S, Ileva L, Zhou Q, Chang EH. A Tumor-Targeted Nanodelivery System to Improve Early MRI Detection of Cancer. *Molecular Imaging* 5(1):41-52, 2006
2. Shan L, Wang S, Sridhar R, Bhujwalla ZM, Wang PC. Dual Probe with Fluorescent and Magnetic Properties for Imaging Solid Tumor Xenografts. *Molecular Imaging* 6(2):85-95, 2007.
3. Chang YJ, Hsu HY, Hsu J, Yao WC, Hsu MS, Chen MC, Lee SC, Hsu C, Miao L, Byrd K, Chouikha M, Gu XB, Wang PC, Szu H. Non-invasive methodology for wellness baseline profiling. *Proceedings of SPIE "Independent Component Analyses, Wavelets, Unsupervised Nano-Biomimetic Sensors, and Neural Networks V"*, vol. 6576:OR1-17, 2007.
4. Manaye KF, Wang PC, O'Neil JN, Tizabi Y, Lei D, Xu T, Huang SY, Ottinger MA, Ingram DK, Mouton PR. Neuropathological Quantification of Dtg APP/PS1: Neuroimaging, Stereology, and Biochemistry. *AGE* (29):87-96, 2007.
5. Ross, S, Ejofodomi O, Jendoubi A, Kinnard L, Chouikha M, Lo B, Wang P, Zheng J. A Mammography Database and View System for the African American Patients. *J Digital Imaging* 21(1):18-26, 2008.
6. Cheng KT, Wang PC, and Shan L. Alexa Fluor 680-labeled transferrin- cationic (NBD-labeled DOPE-DOTAP) liposome-encapsulated gadopentetate dimeglumine complex (Abbreviated name: Tf^{NIR}-Lip^{NBD}-CA complex) targeting to transferrin receptors (TfR). In: *Molecular Imaging and Contrast Agent Database (MICAD)* [database online]. Bethesda (MD): National Library of Medicine (US), NCBI; 2008. <http://micad.nih.gov>.
7. Burnett GT, Wathersby DC, Taylor TE, Bremner TA. Regulation of Inflammation- and Angiogenesis-related Gene Expression in Breast Cancer and Co-Cultured Macrophage. *AntiCancer Res.* 28(4B): 2093-2100, 2008

8. Shan L, Hao YB, Wang SP, Korotcov A, Zhang RS, Wang TX, Califano J, Gu XB, Sridhar R, Bhujwalla ZM, Wang PC. Visualizing Head and Neck Tumors In Vivo Using Near-infrared Fluorescent Transferrin Conjugate. *Molecular Imaging* 7(1):42-49, 2008.
9. Shan L, Wang SP, Zhou YF, Korotcov A, Sridhar R, Wang PC. Bioluminescent Animal Models of Human Breast Cancer for Tumor Biomass Evaluation and Metastasis Detection. *Ethnicity and Disease* 18(S2):65-69, 2008.
10. Yin JJ, Lao F, Meng J, Fu PP, Zhao YL, Xing GM, Gao XY, Sun BY, Wang PC, Chen CY, and Liang XJ. Inhibition of Tumor Growth by Endohedral Metallofullerenol Nanoparticles Optimized as Reactive Oxygen Species Scavenger. *Mol Pharmacol*. Vol 74(4):1132-1140, 2008
11. Shan L, Zhang RS, Zhang WH, Lee E, Sridhar R, Snyderwine EG, Wang PC. Image-based Real-time Evaluation of the Molecular Events Underlying HC11 Mammary Epithelial Cell Differentiation, *Anal Biochem* vol 382:122-128, 2008.
12. Wang PC, Shan L, Wang SP, Korotcov A, Liang XJ. Transferrin Liposome Nanoparticle (Tf^{NIR} -Lip NBD -Magnevist) – A Tumor Targeting MRI Contrast Agent. *Acta Biophysica Sinica* 24(4):315-322, 2008
13. Liang XJ, Chen CY, Zhao YL, Jia L, Wang PC. Biopharmaceutics and Therapeutic Potential of Engineered Nanoparticles. *Curr Drug Metab* vol 9(8):697-709, 2008
14. Yin JJ, Lao F, Fu PP, Wamer WG, Zhao YL, Wang PC, Han D, Qin Y, Sun BY, Xing GM, Dong JQ, Liang XJ, Chen CY. The Scavenging of Reactive Oxygen Species and the Potential for Cell Protection by Functionalized Fullerene Materials. *Biomaterials*. 30(4):611-621, 2009.
15. Wang PC, Blumenthal RP, Zhao YL, Schneider JA, Miller N, Grodzinski P, Gottesman MM, Tinkle S, Wang K, Wang C, Liang XJ. Building Scientific Progress Without Borders: Nanobiology and Nanomedicine in China and the U.S. *Cancer Res* 69(13):5294-5295, 2009

A Tumor-Targeted Nanodelivery System to Improve Early MRI Detection of Cancer

Kathleen F. Pirollo¹, John Dagata², Paul Wang³, Matthew Freedman¹, Andras Vladar², Stanley Fricke¹, Lilia Ileva¹, Qi Zhou¹, and Esther H. Chang¹

¹Georgetown University Medical Center, ²National Institute of Standards and Technology, and ³Howard University

Abstract

The development of improvements in magnetic resonance imaging (MRI) that would enhance sensitivity, leading to earlier detection of cancer and visualization of metastatic disease, is an area of intense exploration. We have devised a tumor-targeting, liposomal nanodelivery platform for use in gene medicine. This systemically administered nanocomplex has been shown to specifically and efficiently deliver both genes and oligonucleotides to primary and metastatic tumor cells, resulting in significant tumor growth inhibition and even tumor regression. Here we examine the effect on MRI of incorporating conventional MRI contrast agent Magnevist[®] into our anti-transferrin receptor single-chain antibody (TfRscFv) liposomal complex. Both in vitro and in an in vivo orthotopic mouse model of pancreatic cancer, we show increased resolution and image intensity with the complexed Magnevist[®]. Using advanced microscopy techniques (scanning electron microscopy and scanning probe microscopy), we also established that the Magnevist[®] is in fact encapsulated by the liposome in the complex and that the complex still retains its nanodimensional size. These results demonstrate that this TfRscFv–liposome–Magnevist[®] nanocomplex has the potential to become a useful tool in early cancer detection. *Mol Imaging* (2006) 5, 41–52.

Keywords: Nanocomplex, tumor targeting, Magnevist[®], MRI, early detection.

Introduction

The ability to detect cancer, both primary and metastatic disease, at an early stage would be a major step toward the goal of ending the pain and suffering from the disease. The development of tumor-targeted delivery systems for gene therapy has opened the potential for delivery of imaging agents more effectively than is currently achievable. Magnetic resonance imaging (MRI) can acquire 3-D anatomical images of organs. Coupling these with paramagnetic images results in the accurate localization of tumors as well as longitudinal and quantitative monitoring of tumor growth and angiogenesis [1,2].

One of the most common paramagnetic imaging agents used in cancer diagnostics is Magnevist[®] (gadopentetate dimeglumine). Gadolinium is a rare earth

element. It shows paramagnetic properties because its ion (Gd^{2+}) has seven unpaired electrons. The contrast enhancement observed in MRI scans is due to the strong effect of Gd^{2+} primarily on the hydrogen-proton spin–lattice relaxation time (T1). Whereas free gadolinium is highly toxic and thus unsuitable for clinical use, chelation with diethylenetriamine pentacetic acid generates a well-tolerated, stable, strongly paramagnetic complex. This metal chelate is metabolically inert. However, after intravenous (iv) injection of gadopentetate dimeglumine, the meglumine ion dissociates from the hydrophobic gadopentetate, which is distributed only in the extracellular water. It cannot cross an intact blood–brain barrier and therefore does not accumulate in normal brain tissue, cysts, postoperative scars, etc, and it is rapidly excreted in the urine. It has a mean half-life of about 1.6 hr. Approximately 80% of the dose is excreted in the urine within 6 hr.

A systemically administered tumor-targeting delivery system has been developed in our laboratory for use in gene medicine [3–8]. This nanosized complex is composed of a cationic liposome encapsulating the nucleic acid payload, which can be either genes [3–6] or oligonucleotides [7,8]. Decorating the surface of the liposome is a targeting molecule that can be a ligand, such as folate or transferrin, or an antibody or an antibody fragment directed against a cell surface receptor. The presence of the ligand/antibody on the liposome facilitates the entry of the complex into the cells through binding of the targeting molecule by its receptor followed by internalization of the bound complex via receptor-mediated endocytosis, a highly efficient

Abbreviations: Lip, liposome; Mag, Magnevist[®] (Gadopentetate Dimeglumine); SEM, scanning electron microscopy; SPM, scanning probe microscopy; STEM, scanning transmission electron microscopy; TfRscFv, anti-transferrin receptor single chain antibody; TfRscFv–Lip–Mag, anti-transferrin receptor single chain antibody–liposome–Magnevist[®] complex.

Corresponding author: Esther H. Chang, PhD, Department of Oncology, Lombardi Comprehensive Cancer Center, Georgetown University Medical Center, 3970 Reservoir Road, NW, The Research Building, TRB E420, Washington, DC 20057-1460; e-mail: change@georgetown.edu. Received 25 February 2005; Received in revised form 8 June 2005; Accepted 17 June 2005. DOI 10.2310/7290.2006.00005

© 2006 BC Decker Inc

internalization pathway [9,10]. This modification of the liposomes results in their being able to not only selectively deliver their payload to tumor cells, but also increases the transfection efficacy of the liposome. Transferrin receptor (TfR) levels are elevated in various types of cancer including oral, prostate, breast, and pancreas [11–16]. Moreover, the TfR recycles during internalization in rapidly developing cells such as cancer cells [16], thus contributing to the uptake of these transferrin-targeted nanocomplexes even in cancer cells where TfR levels are not elevated. The nanocomplex used in the studies described here uses an anti-transferrin receptor single-chain antibody fragment (TfRscFv) as the targeting moiety [17,18]. TfRscFv contains the complete antibody-binding site for the epitope of the TfR recognized by the monoclonal antibody 5E9 [18]. TfRscFv has advantages over the transferrin molecule itself, or an entire monoclonal antibody, in targeting liposomes to cancer cells with elevated TfR levels: (1) The size of the scFv (28 kDa) is much smaller than that of the transferrin molecule (80 kDa) or the parental monoclonal antibody (155 kDa). The scFv liposome–DNA complex may thus exhibit better penetration into small capillaries characteristic of solid tumors. (2) The smaller scFv has a practical advantage related to the scaled-up production necessary for the clinical trials. (3) The scFv is a recombinant molecule and not a blood product like transferrin and thus presents no danger of a potential contamination by blood-borne pathogens. (4) Without the Fc region of the monoclonal antibody, the issue of non-antigen-specific binding through Fc receptors is eliminated [19]. Most importantly, we have already shown that such an anti-TfR single-chain antibody molecule can target an intravenously administered cationic liposome–DNA nanocomplex preferentially to tumors [5,6]. Encapsulating Magnevist[®] within such a tumor-targeted nanocomplex offers potential advantages for enhanced sensitivity, detection of metastases, and diagnosis of cancer.

In this article, using a mouse xenograft model of human pancreatic cancer, we explore the use of this nanocomplex for systemic delivery of the imaging agent Magnevist[®] to tumors. In addition, we used scanning electron microscopy (SEM) and scanning probe microscopy (SPM) [20–25] to examine the physical structure and size of these Magnevist[®]-carrying nanocomplexes. Because gadolinium is a high-atomic-number element and possesses a large magnetic moment, these properties can be exploited in a variety of ways to enhance contrast in both SEM and SPM. The findings presented below demonstrate that our ligand–liposome nanocomplex does indeed encapsulate Magnevist[®] and that iv

administration of this complex results in enhanced tumor imaging.

Materials and Methods

Cell Lines

Human lymphoblastic leukemia cell line K562 was obtained from the Lombardi Comprehensive Cancer Center Tissue Culture core facility (Washington, DC). These suspension cells were maintained in RPMI 1640 supplemented with 10% heat-inactivated fetal bovine serum (FBS) plus 2 mM L-glutamine, and 50 µg/mL each of penicillin, streptomycin, and neomycin. Human pancreatic cancer cell line CaPan-1 (obtained from ATCC, Manassas, VA) was derived from a metastatic adenocarcinoma of the pancreas. It was maintained in Iscove's modified Dulbecco's medium containing 4 mM L-glutamine and sodium bicarbonate, supplemented with 20% non-heat-inactivated FBS, 2 mM L-glutamine, and 50 µg/mL each of penicillin, streptomycin, and neomycin. Human prostate cancer cell line DU145 (ATCC) was originally derived from a lesion in the brain of a patient with widespread metastatic carcinoma of the prostate. It was maintained in minimum essential medium with Earle's salts supplemented with 10% heat-inactivated FBS plus L-glutamine and antibiotics as above.

Nanocomplex Formation

Cationic liposome (DOTAP:DOPE) was prepared by the ethanol injection method as previously described [6]. When delivering plasmid DNA, the full complex was formed in a manner identical to that previously described [26]. To encapsulate the imaging agent, the TfRscFv was mixed with the liposome at a specific ratio (identical to that used with DNA) and incubated at room temperature for 10 min. Magnevist[®] was added to this solution, mixed, and again incubated at room temperature for 10 min. When stored at 2–8°C the complex is stable for at least 8 days, as determined by size measurements using a Malvern Zetasizer 3000H (Malvern, UK). The average of the cumulants (Z average) measurements over this time frame is 112.3 ± 4.67 (SE), whereas the polydispersity (representing the reproducibility of the values during repeat scans) is 0.445 ± 0.03 . For in vitro transfection, 2 mL of serum-free medium was added to the complex before transfection. When prepared for in vivo use, dextrose was added to a final concentration of 5%. For both in vitro and in vivo complex formation, the ratio of Magnevist[®] to liposome was 1:7 (vol/vol).

In Vitro Transfection

To transfect suspension cells K562, 15×10^6 cells in a total volume of 4.0 mL of medium with all supplements except serum (serum-free medium) were placed into a 100-mm² tissue-culture dish. Two milliliters of the transfection solution from above, containing varying amounts of Magnevist[®], was added to the cell suspension. The plate was incubated at 37°C with gentle rocking for the length of time given in the Results section (up to 90 min), after which the cells were gently pelleted ($600 \times g$ for 7 min) at 4°C in 0.5 mL microcentrifuge tubes and washed three times with 10 mL of serum free medium to remove any excess transfection solution and placed on wet ice until imaged.

In Vivo Tumor Targeting

To assess the tumor-selective targeting of the TfRscFv–liposome (TfRscFv–Lip) nanocomplex to primary and metastatic tumors, an orthotopic metastasis model using human pancreatic cancer cell line CaPan-1 was used. Subcutaneous xenograft tumors of CaPan-1 were induced in female athymic nude mice by injection of 1×10^7 CaPan-1 cells suspended in Matrigel collagen basement membrane matrix (BD Biosciences, San Jose, CA). Approximately 8 weeks later, the tumors were harvested and a single-cell suspension of the tumor was prepared. Cells ($1.2\text{--}1.5 \times 10^7$), also suspended in Matrigel were injected into the surgically exposed pancreas of female athymic nude mice as previously described [27]. Five weeks post surgery, the complex carrying the *LacZ* gene was iv injected $3 \times$ over 24 hrs (at 40 μ g DNA per injection). Sixty hours later, the animals were sacrificed and examined for the presence of metastases and organs stained for β -galactosidase expression using a previously described procedure [3].

Magnetic Resonance Imaging

For in vitro MRI, the cell pellets in microcentrifuge tubes were positioned at the center of the magnet. The MRI was performed at Howard University using a 4.7-T horizontal bore NMR machine (Varian Inc, Palo Alto, CA). The imaging protocols consist of a multislice T1-weighted spin–echo imaging sequence and a saturation–recovery sequence. For the T1-weighted imaging technique, the repetition time (TR) was 1000 msec and the echo time (TE) was 13 msec. The T1-weighted spin–echo imaging technique was applied to verify the positive image enhancement. The saturation–recovery MR sequence with variable echo times was used for the T1 measurement. The slice thickness of images was 0.5 mm. The radiofrequency (RF) coil used was a 30-mm single-

loop coil. The RF coil serves as an RF transmitter and receiver. The RF pulse was a selective 5-msec sinc pulse. The number of phase-encoding steps was 256. The field of view was 15×15 mm. The image area chosen in the study was at the center of the RF coil for RF homogeneity. The MR images were taken in the cross-section direction of the microcentrifuge tube. The height of the cell pellet was 12 mm. The range of the multislice images covers the whole pellet. The center slice images, which were not influenced by the image distortion due to the susceptibility effect from the air–pellet boundary, were used for the studies. The image intensity was measured using the Varian Image Browser software. The signal is taken from a region of interest that is big enough to cover two thirds of the image from each microcentrifuge tube. The relative image intensities of the pellets from these tubes were applied for contrast enhancement evaluation and the T1 measurements.

For the in vivo studies, mice bearing CaPan-1 orthotopic tumors or DU145 subcutaneous xenograft tumors were used. The CaPan-1 tumors were induced as described above. DU145 tumors were induced by the subcutaneous inoculation of 7×10^6 cells in Matrigel. These studies were performed at Georgetown University. Animals to be imaged were anesthetized and placed in a proprietary, in-house designed, animal management system. This system incorporates a warm-water heating system that maintains the temperature at 37°C, as well as a four-channel, thermal optical monitoring system used to monitor animals' skin temperature, ambient temperature, and wall temperature of the device. For imaging, anesthesia was induced using isoflurane at 4%, with the remaining gas composed of a 66% oxygen and 30% nitrous oxide mixture. Maintenance of anesthesia was achieved with 1.5% isoflurane under similar gaseous conditions of oxygen and nitrous oxide as noted. The anesthetized animal was positioned inside a cylindrical, variable RF resonant antenna (birdcage resonator volume coil) and tuned to a center frequency of approximately 300 MHz (the resonant frequency of water molecules when subject to a field strength of 7 T). The imaging protocol used was T1-weighted Turbo-RARE (rapid acquisition with rapid enhancement) 3-D imaging sequences performed on a 7T Bruker BioSpin (Billerica, MA) imaging console. The imaging parameters used were as follows: T1-weighted Turbo-RARE 3-D, TE 13.3 msec, TR 229.5 sec, flipback on, four echoes with a field of view of $8.0/3.5/3.5$ cm and a $256 \times 256 \times 256$ matrix. After a baseline image was acquired, the animal was kept immobilized in the animal holder and the Magnevist[®] only [diluted to 400 μ L with $1 \times$ phosphate-

buffered saline (pH = 7.4)] or the TfRscFv–Lip–Mag complex (total volume 400 μ L) was systemically administered using a 27 G needle by iv injection into the tail vein of the animal and the 3-D imaging sequence was immediately initiated. The imaging with the two solutions were performed on sequential days.

Scanning Electron Microscopy

Sample solutions of liposome-encapsulated Magnevist contrast agent and complete nanocomplex consisting of a tumor-targeting single-chain transferrin receptor protein coating the liposome-encapsulated complex, TfRscFv–Lip–Mag, were prepared at Georgetown University Medical Center (GUMC), delivered to National Institute of Standards and Technology (NIST) and were stored under dark and refrigeration. For each imaging session, a fresh dilution 1:3 by volume with deionized water was prepared and a 5- μ L droplet was micropipetted onto a standard 200-mesh transmission electron microscopy grid consisting of 30–60 nm formvar and 15–20 nm carbon. The droplet was allowed to dry on the grid in air for 5 min before being loaded into the vacuum chamber of the microscope. Imaging was performed using a Hitachi S-4800 field-emission microscope at NIST. Of particular interest to applications of SEM to nanocomplex imaging is a comparison of upper and lower secondary electron detectors [SE9(U) and SE(L)]—using the SEM in its usual mode—to the addition of a transmitted electron (TE) detector, transforming the instrument into a low-voltage STEM.

Scanning Probe Microscopy

Sample solutions of liposome-encapsulated Magnevist contrast agent and complete nanocomplex were prepared at GUMC, delivered to NIST, and were stored under dark and refrigeration. For each imaging session, a fresh dilution 1:3 by volume with deionized water was prepared and a 5- μ L droplet was micropipetted onto an ultrasonically cleaned silicon substrate used with native oxide or with a poly-L-lysine coating. SPM imaging were obtained using a Veeco (Santa Barbara, CA) MultiMode microscope with a Nanoscope IV controller. Topography by tapping mode with Z control [Veeco RTESP cantilevers, of approximately 320–360 kHz and k approximately 20–60 N/m], phase imaging, and magnetic force microscopy using magnetic-coated tips (Veeco MESP 68 kHz) were performed in life mode. Dynamic imaging of dewetting and surface energy “phase separation” as the solution evaporates to expose isolated nanoparticles and aggregates were used to understand the consequences of solvent drying on the stability of the particles

and its effect on the various SPM contrast mechanisms available with the SPM system.

Results

Tumor-Specific Targeting by the Ligand–Liposome Nanocomplex Carrying a Reporter Gene

To assess selective targeting of the TfRscFv–LipA nanocomplex to primary tumor and metastases, an orthotopic metastasis model, a closer approximation of the clinical situation, using human PanCa cell line CaPan-1 was used. Surgical orthotopic implantations of CaPan-1 xenograft tumor sections into nude mice have been shown to produce, within 56 days, metastases in liver and spleen [27]. Orthotopic tumors of CaPan-1 were induced in female athymic nude mice as described in Materials and Methods. Approximately 5 weeks later, the animals were euthanized and necropsied to look for tumor in the pancreas and other organs. As shown in Figure 1A, extensive tumor growth is evident throughout the pancreas. Metastases were present in various organs in four of five mice including the spleen, liver, lung, adrenal gland and even within the diaphragm. This experiment was repeated with similar results.

To establish selective targeting tumor and metastasis, before sacrificing the mice, the TfRscFv–LipA complex carrying pSVb (LacZ) plasmid DNA for β -galactosidase expression was iv injected into the mice three times over a 24-hr period (40 μ g of plasmid DNA per injection). All five mice were sacrificed 60 hr after injection and various organs, including the liver, lung, spleen, pancreas and

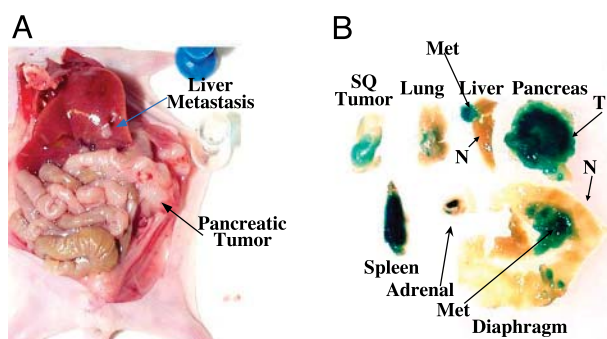


Figure 1. Tumor-specific targeting of a CaPan-1 orthotopic metastasis model by the TfRscFv–Lip–DNA nanocomplex. Subcutaneous CaPan-1 xenograft tumors were induced in female athymic nude mice as described in Materials and Methods. The tumors were harvested and a single-cell suspension in Matrigel was injected into the surgically exposed pancreas. Five weeks post injection, the TfRscFv–Lip complex carrying the LacZ gene for β -galactosidase expression (40 μ g) was iv injected 3 \times over 24 hr. Sixty hours later, the animals were sacrificed and examined for the presence of metastases and the organs stained for β -galactosidase expression. The same tumor nodule in the liver indicated by an arrow in A exhibits intense β -galactosidase expression in B. (A) Gross necropsy; (B) tissues after staining for β -galactosidase.

diaphragm, were harvested and examined for the presence of metastasis and tumor-specific staining. Fresh samples, sliced at 1-mm thickness, were stained with X-gal to produce a blue color where the gene is expressed. The tumor-targeting ability and high transfection efficiency of the complex is demonstrated by the presence of the reporter gene in the various organs from this animal (Figure 1B). In the liver, lung, adrenal gland, and diaphragm, it is clearly shown that the reporter gene is highly expressed only in the metastases, whereas in the adjacent normal tissue, no blue color is evident. The metastasis visible in the liver in Figure 1A (arrow) is the same tumor nodule strongly expressing β -galactosidase in Figure 1B (arrow) confirming the tumor-specific nature of this nanocomplex. In some of the mice, growth of the tumor in pancreas also resulted in extrusion of tumor through the original incision site used for implantation. In Figure 1B, this strongly blue stained subcutaneous tumor, surrounded by normal nonstained skin, is also shown, again showing tumor cell specificity. Similar results were observed in the rest of the mice and in the repeat experiment. Thus, this systemically administered nanocomplex will target tumor cells, both primary and metastatic, wherever they occur in the body, and efficiently deliver plasmid DNA. We wished to expand the potential of this delivery system to include contrast agents. The ability to do so could result in improved imaging and cancer detection.

In Vitro Studies Using TfRscFv–Lip Complex to Deliver Magnevist[®]

As Magnevist[®] is one of the most frequently used contrast agents in the clinic, it was chosen for use in these studies. In our initial experiments, we examined whether the complex could be prepared with Magnevist[®] and if doing so would enhance the MRI signal. Because trypsinization could lead to membrane damage and leakage of contrast agent from the cells, adherent cells were not used in these studies. Instead, a human lymphoblastic leukemia cell line, K562, which grows as a suspension culture was used. Moreover, gentle pelleting and washing of the cells would remove any excess Magnevist[®] or complex before imaging, allowing only cell-associated signal to be detected.

Time-Dependent Image Enhancement by the TfRscFv–Lip–Mag Nanocomplex

We examined the optimal time for transfection of the TfRscFv–Lip–Mag nanocomplex. The suggested clinical dose of Magnevist is 0.1 mmol/kg. In these initial studies, we used a dose of 0.3 mmol/kg (corrected for the smaller weight and blood volume of mouse vs. man)

in the complex per 250 μ L of transfection solution. K562 cells were transfected for times ranging from 20 to 90 min. Twenty minutes showed very low transfection activity based on the image intensity (data not shown). However, as shown in Figure 2A, by 60 min the cells transfected with the complex showed a large increase in intensity as compared to the untreated cells. The intensity of the untreated cells (202 ± 48) was not significantly different from that of an empty marker tube (194 ± 43), indicating that the cells themselves do not contribute to the signal detected. More importantly, the transfection efficiency plateaus at approximately 60 min because the relative intensity of the cells transfected for 60 and 90 min were identical (317 ± 46 and 317 ± 47 , respectively).

Magnevist[®] Dose-Dependent Image Enhancement

Using 60 min as the transfection time, we then assessed the effect of increasing amounts of Magnevist[®] on the TfRscFv–Lip–Mag complex image enhancement. The doses tested were 0.05, 0.3, and 0.9 mmol/kg. Corrected for size and blood volume of the mouse, the volumes of Magnevist[®] used in the complex per 250 μ L of transfection solution were 0.25, 1.5, and 4.5 μ L. As shown in Figure 2B and Table 1, the image intensity increases and the T1 relaxation time shortens as a function of the amount of contrast agent included in the complex.

Image Enhancement by TfRscFv–Lip–Mag as Compared to Free Magnevist[®]

Based on the above experiments it appears that the TfRscFv–Lip can complex with Magnevist[®] and deliver it to the cells for image enhancement. To assess the level of enhancement of the complexed contrast agent as compared to the agent alone and demonstrate that the signal obtained is not due to the presence of unincorporated Magnevist[®], we treated K562 cells with either free Magnevist[®] or the TfRscFv–Lip–Mag nanocomplex. The identical amount of contrast agent (0.3 mmole/kg or 1.5 μ L/250 μ L transfection volume) and transfection time (60 min) was used for both solutions. Whereas free Magnevist[®] showed enhanced contrast relative to the untreated cells as expected, the cells treated with the TfRscFv–Lip–Magnevist complex demonstrated a much greater increase in image intensity and shortened T1 relaxation time compared to both untreated and free-Magnevist[®]-treated cells (Figure 2C, Table 2). These results not only demonstrate the increased efficiency of contrast agent uptake by means of the targeted nanocomplex, but also indicate that the observed signal is

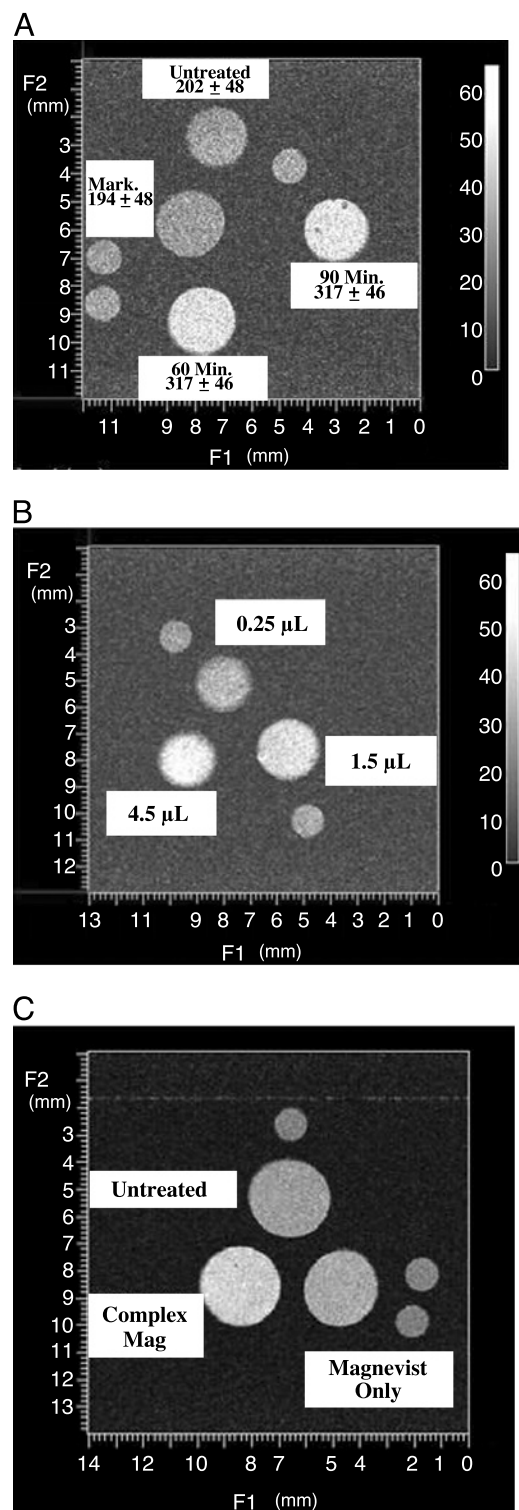


Figure 2. *In vitro* MRI of K564 cells after transfection with the TjRscFv-Lip-Mag nanocomplex. After transfection with either free Magnevist[®] or the noncomplex encapsulating Magnevist[®] the cells were pelleted and washed with serum-free medium, and MRI performed using a 4.7T Varian NMR. The imaging protocol consisted of T1-weighted spin-echo imaging sequences (TR/TE, 1000/13 msec) to verify the image enhancement and a saturation-recovery MR sequence with variable echo times for the T1 measurement. (A) Time-dependent transfection. The values given are relative intensities. (B) Variation in relative intensity with the amount of Magnevist[®] included in the complex (in microliters). (C) Comparison of relative intensity of the TjRscFv-Lip-Mag complex versus free Magnevist[®]. The small circles in all images are markers for sample orientation.

Table 1. Relative Intensity and T1 Relaxation Time as a Function of Magnevist[®] in the Complex

Dose of Contrast Agent (mM/kg)	Relative Intensity	T1 (sec)
0.05 (0.25 µL)	293 ± 50	1.43 ± 0.007
0.3 (1.5 µL)	379 ± 43	1.16 ± 0.004
0.9 (4.5 µL)	454 ± 51	1.01 ± 0.004

likely not due to uncomplexed Magnevist[®]. Further evidence of Magnevist[®] encapsulation is given below.

In Vivo Image Enhancement with TjRscFv-Lip-Mag

The above studies established that the nanocomplex could more efficiently image tumor cells *in vitro* than Magnevist[®] alone. However, to have potential for clinical use, the complex must exhibit a similar effect *in vivo*. We used the same human pancreatic cancer orthotopic mouse model (CaPan-1) for these studies as was used above to demonstrate tumor-specific targeting of the complex carrying a reporter gene. In addition, a second tumor model, a subcutaneous prostate xenograft mouse model (DU145) was also used. Mice bearing CaPan-1 or DU145 tumors were imaged on a 7T Bruker NMR as described in Materials and Methods. Once positioned in the coil, a baseline image was obtained using a T1-weighted Turbo-RARE 3-D imaging sequence. To facilitate image alignment, after baseline acquisition the animal was maintained in the animal holder while the imaging solution was administered via iv injection. Signal acquisition was begun within 3 min of the injection. The amount of Magnevist[®] administered to the mouse, either free (as is performed in the clinic) or included in the complex, was 10 µL. This amount is equivalent to 0.2 mmole/kg or twice that used in humans. This amount was selected because the standard human dose of 0.1 mmole/kg Magnevist[®] alone gave a very poor signal in the mice. The imaging with free Magnevist[®] and the TjRscFv-Lip-Mag complex were performed on two consecutive days. A baseline scan was also performed before administration of nanocomplex to confirm that all of the Magnevist[®] from the previous day had been washed out. MR technique and windows were consistent between the two sets of images with the windows

Table 2. Comparison of the Relative Intensity and T1 Relaxation Time between Free and Complexed Magnevist[®]

Treatment	Relative Intensity	T1 (sec)
Untreated	455 ± 47	1.80 ± 0.009
Free Magnevist [®]	538 ± 50	1.51 ± 0.007
Complexed Magnevist [®]	662 ± 52	1.40 ± 0.004

adjusted to correct for an automatic windowing feature of the scanner.

Images of the Magnevist[®] and nanocomplex–Magnevist in three separate mice are shown in Figure 3. In Figure 3A, 4 months after surgical implantation of the CaPan-1 tumor cells, the animal is carrying a large orthotopic tumor. The increased resolution and signal intensity, as compared to the contrast agent alone is quite evident. Similar results are observed in the second mouse with a CaPan-1 tumor shown in Figure 3B. This animal, only 2 months postsurgery, has a visible subcutaneous tumor growing through the site of the incision. A small abdominal mass was also detected by palpation. Not only is the signal in the subcutaneous tumor more enhanced after administration of the complexed Magnevist[®], but what appears to be the small orthotopic tumor (arrow) is evident in this scan and not in the one in which the animal received the free Magnevist[®]. Similarly, increased definition and contrast are evident in the subcutaneous DU145 tumor (Figure 3C) after

injection with the TfRscFv–Lip–Mag complex as compared to the free Magnevist[®]. Reconstruction and quantitation was performed on the images in Figure 3B and C, representing the two different tumor models, pancreatic cancer (CaPan-1) and prostate cancer (DU145). In both instances, there is an increased intensity (pixels) by the free Magnevist[®] over the baseline, as expected (Table 3). However, delivery of the imaging agent by the tumor-targeting nanocomplex results in an almost three-fold further increase in signal intensity in both of these tumor models. These studies thus demonstrate that when Magnevist[®] is incorporated within the TfRscFv–Lip complex there is an improved tumor visualization in an *in vivo* situation, and they suggest the potential benefit of further developing this means of tumor detection for clinical use.

Physical Characterization Studies

Whereas the *in vitro* studies offered circumstantial evidence that complexed Magnevist[®] is encapsulated

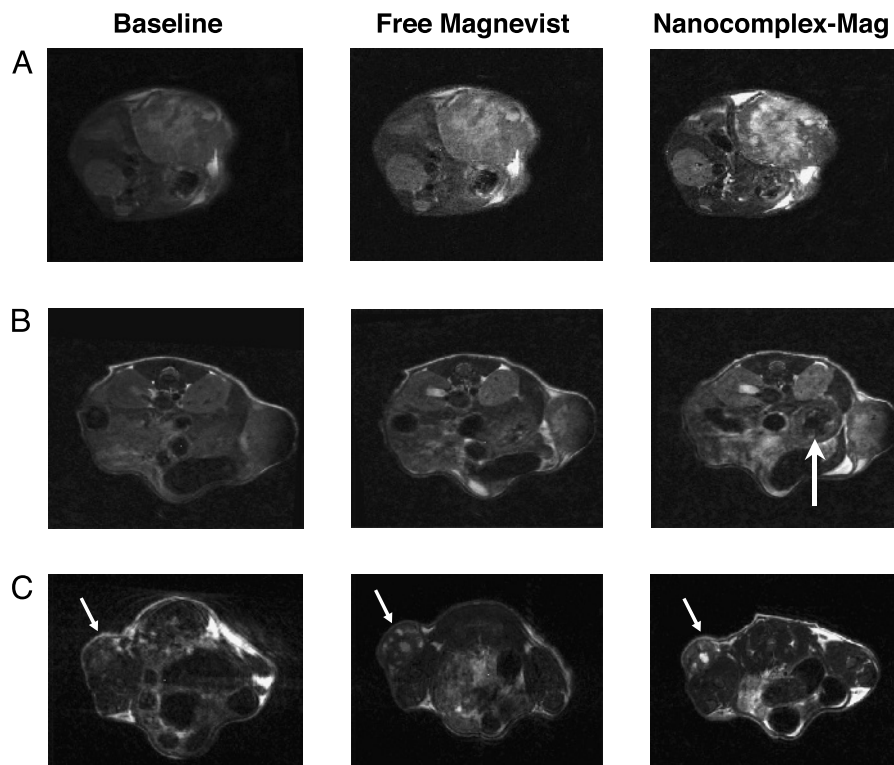


Figure 3. Improved MRI in two different models of cancer using the ligand–liposome–Mag nanocomplex. Human pancreatic cancer cells (CaPan-1) were surgically implanted into the body of the pancreas, and human prostate cancer cells (DU145) were subcutaneously injected on the lower back of female athymic nude mice. Free Magnevist[®] or the TfRscFv–Lip nanocomplex containing the same dose of Magnevist[®] was *iv* injected (via the tail vein) into each of the three mice on two consecutive days. This amount of Magnevist[®] is equivalent to twice the dose that would be administered to a human patient. The total volume of solution administered in all cases was 400 μ L. A baseline scan was performed just before administration of the nanocomplex to confirm that all of the Magnevist[®] from the previous day had been washed out. MR technique and windows were constant between the three sets of images, with the windows adjusted to correct for an automatic windowing feature of the scanner. (A) Differences in MRI signal in a large pancreatic orthotopic tumor (arrow) (4 months after surgical implantation of the tumor) between the *iv*-administered free contrast agent and the TfRscFv–Lip–Mag complex. (B) Similar effect in a second mouse with a subcutaneous pancreatic tumor and a much smaller abdominal pancreatic tumor (arrows). (C) Images of a third animal with a subcutaneous prostate tumor (arrow) in which the same effect is evident.

Table 3. Intensity Increase over Baseline by Free and Complexed Magnevist[®]

	CaPan-1	DU145
	% Increase over Baseline	
Complexed Magnevist [®]	99	215
Free Magnevist [®]	34.5	70

within the liposome, we have used sophisticated microscopy techniques (SEM and SPM) to confirm this fact and further characterize (e.g., complex size) the TfRscFv–Lip–Mag complex.

Imaging of Liposomes without Magnevist. High-resolution imaging implies narrow depth of focus and so requires relatively thin and flat samples. How thin varies with technique, but surface and substrate effects—surface energy and symmetry lowering—often dominate the structural forces typical of biomaterials. This is particularly true for liposomes given their tenuous nature [28]. So an understanding of reliable methods for preparing and characterizing the dimensional and mechanical stability of isolated liposomes is an essential step. The goal of our present characterization efforts is to perform direct sensing of the mechanical stiffness and magnetic properties of nanoparticles to establish that the contrast agent is indeed contained within the nanoparticle and not simply associated externally with the liposomes.

The SPM images surface topography in tapping mode by oscillating the tip and cantilever to which it is attached close to the cantilever resonance frequency. A feedback circuit maintains the oscillation of the cantilever at constant amplitude. This constant amplitude is given by a set point that is somewhat smaller than that of the freely oscillating cantilever. Because the SPM tip interacts with the surface through various small forces, there is a phase shift between the cantilever excitation and its response at a given point on the surface. For an inhomogeneous surface, the tip–surface interactions will vary according to surface charge, steep topographical changes, and mechanical stiffness variations, for example. By changing the set point and observing how certain features respond to softer or harder tapping, we can correlate this with the response expected for a specific structure such as a liposome. (The free oscillation amplitude signal is approximately 1.78 V.) A sequence of SPM phase images of a pair of isolated liposomes without payload is shown in Figure 4. Figure 4A was imaged at a set point of 1.68 V and the corresponding negative phase difference between the substrate and liposome indicates that the tip–sample

interaction is attractive for the liposome, given by a phase value of -3.5° . In the case of an attractive interaction and negative phase, the phase image of the liposome appears dark, except for a topographically keyed ring at the liposome edge. Figure 4B demonstrates the effect of reducing the set point to 1.45 V: The liposome now appears bright because the tip–sample interaction becomes repulsive, and here the phase difference between the liposome and substrate is $+8^\circ$. Finally, Figure 4C shows that the phase difference recorded at a set point of 1.35 V increases further, becoming $+35^\circ$.

Imaging of Liposome-Encapsulated Magnevist. Figure 5 presents SPM and SEM images of isolated lipo-

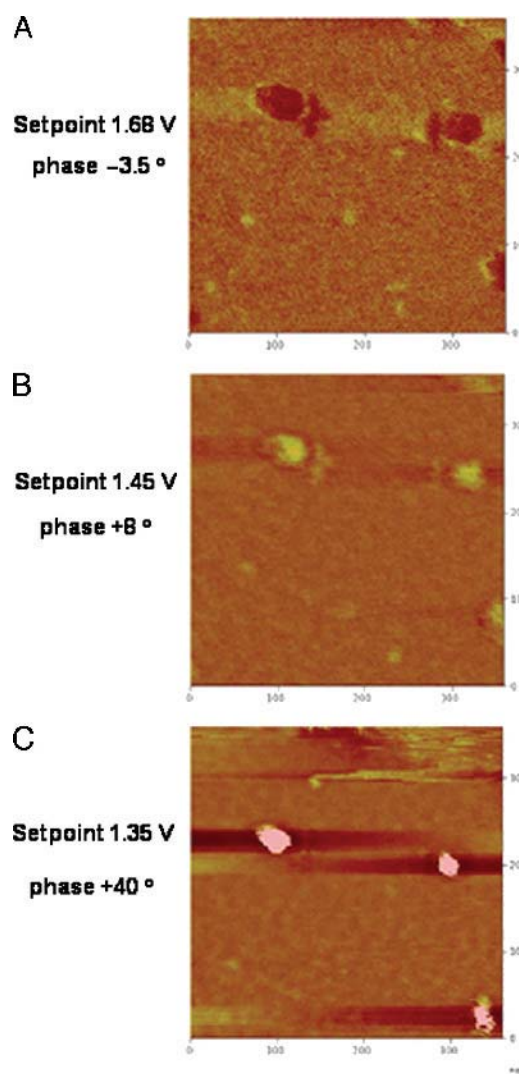


Figure 4. SPM phase images of liposomes without Magnevist[®]. The images appearing in A, B, and C were obtained at set points of 1.68, 1.45, and 1.35 V, respectively. The corresponding phase differences between the noncompliant substrate and the mechanically compliant liposome are -3.5° , $+8^\circ$, and $+40^\circ$. The interaction of the SPM tip and liposome changes from attractive to repulsive as the set point is decreased.

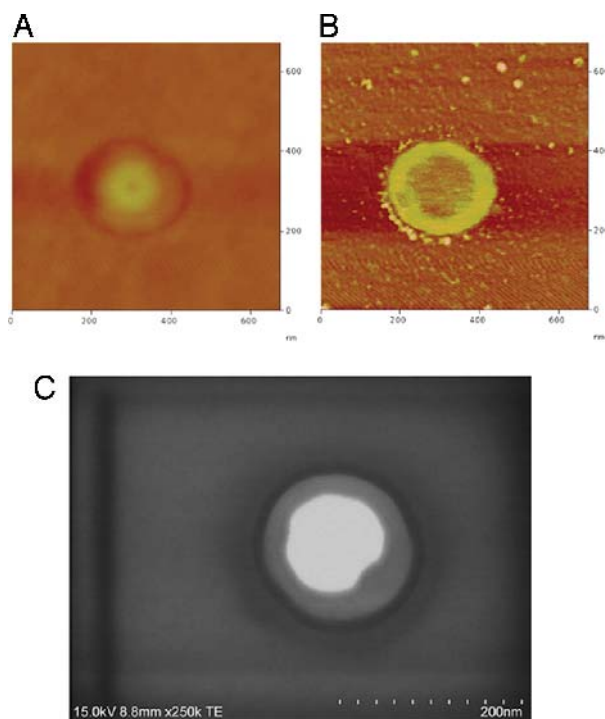


Figure 5. SPM and SEM images of liposome-encapsulated Magnevist[®] (Lip+Mag). (A) Atomic force microscopy topographical image of the liposome-encapsulated Magnevist[®] particle. The SPM phase image (set point = 1.6) (B) and 15 keV SEM (TE) (transmission-mode electron detector) image (C) possess similar contrast, although generated by entirely distinct complementary physical mechanisms.

some-encapsulated Magnevist (Lip+Mag) nanoparticles. The size distribution of single (Lip+Mag) particles is in the diameter range of 100–200 nm and scales according to optical measurements that indicate that payload-encapsulating liposomes are approximately 50% larger than liposomes alone in their spherical state.

The SPM topograph in Figure 5A indicates that liposomes containing Magnevist have a bimodal surface shape after drying that is more complex than that of the simple elliptical surface of a liposome containing no payload (not shown). The SPM phase behavior differs markedly from that of payloadless liposomes, the outer ring is repulsive relative to the center, and a corresponding SPM phase image is shown in Figure 5B. Regions of both attractive and repulsive tip–sample interaction appear at moderate set point values. A correlation between the SPM phase image obtained at a set point of 1.6 and the SEM image in TE mode is evident in Figure 5B and C. Liposomes appear uniformly bright across the entire particle in SEM images (not shown), similar to the uniform phase images we obtain by SPM. Tips and cantilevers change with time and usage. Moreover, it is important to verify that the images produced are not affected by tip instabilities due to

foreign material on the tip. Thus, they are changed frequently. Because each cantilever is somewhat different with respect to its resonance properties, the set points used in Figures 4 and 5 are different.

Imaging of TfRscFv–Lip–Mag Nanocomplex. The complete TfRscFv–Lip–Mag nanocomplex was prepared and imaged by SEM and SPM as described in Materials and Methods. Results, shown in Figure 6 indicate that the solvent film undergoes phase separation; however, examples of isolated NDS can be readily observed on the dried film. Note that the SEM beam clearly causes some damage to the film, but the particles can be repeatedly scanned several times before beam damage becomes significant. The appearance of the full complex is different from that of the (Lip+Mag) only. The shape is less regular and considerable texturing of the liposome surface following drying is consistent with protein denaturation. Also, SEM TE images indicate that the well-defined boundary between the outer ring and center of the liposome seen with the (Lip+Mag) particles is less

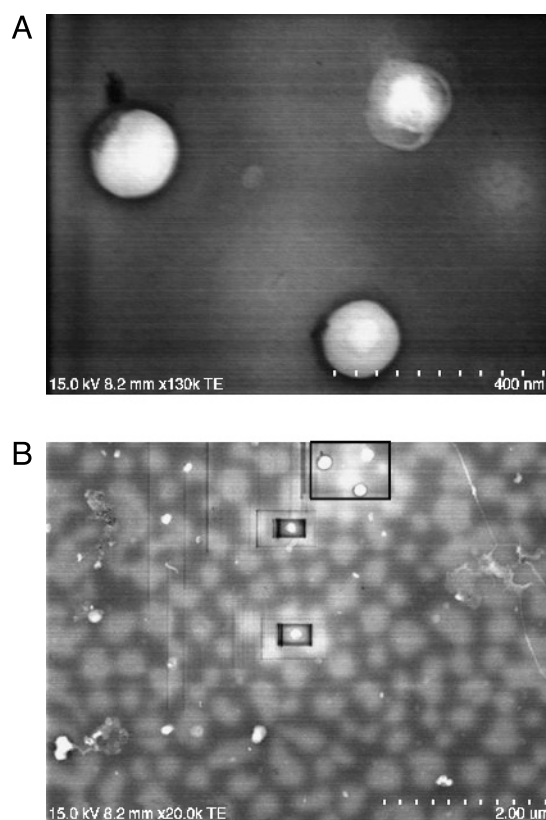


Figure 6. SPM topographic and phase imaging of TfRscFv–Lip–Mag nanocomplex. (A) 15 keV SEM (TE) (transmission-mode electron detector) image of the full nanocomplex. A suitable choice of amplitude set point readily distinguishes intact nanocomplex particles from decomposition products. It is not known if the decomposed material was present in the solution before sample preparation or is the direct result of interaction with the substrate. (B) power image of the field. The boxed area is the image in A.

apparent and the shape much more variable. This is consistent with the view that the presence of protein within the liposome has altered the osmotic outflow across the liposome during film drying.

It is possible to obtain additional information about these NDS particles by using the magnetic force microscopy imaging capabilities of the SPM (MFM). Because the magnetic moment of gadolinium-containing Magnevist is quite large, it should be possible using a magnetized SPM tip to interact with the oriented Magnevist concentrated within the liposomes. This is shown in Figure 7 for MFM of several approximately 100- to 200-nm-diameter nanocomplexes. We establish that, in fact, we are producing an image that is truly magnetic in nature by using the lift-mode capabilities of the SPM: In this mode, a topographic image under normal tapping

mode conditions is obtained. The reference surface information is then used to offset the tip by a specified height away from the surface and the surface is then scanned at this increased height. This removes the influence of topography on the signal. MFM images obtained in lift mode at a height of 15 nm or more from the surface are given by the magnetic phase image. The appearance of a signal confirms the presence of gadolinium encapsulated within the complex.

Discussion

The development of nanoparticle-sized delivery systems that have greater tumor and tissue penetrance is a major direction in medical research in general and cancer research in particular. Combining the capabilities of these small particles with the ability to home specifically to tumor cells wherever they occur in the body could lead to significant advances in cancer treatment and diagnosis. We have previously shown that our ligand-liposome-DNA complex can specifically target and efficiently transfect tumor cells (primary and metastatic) [3–8]. When encapsulating plasmid DNA, this targeted delivery system is truly a nanocomplex, with a uniform size of less than 100 nm [29]. Used in combination with conventional radiation/chemotherapy, delivery of therapeutic genes such as wild-type p53 by means of this nanodelivery system has resulted in tumor growth inhibition and even tumor regression in animal models [3–5,29]. This tumor regression and concomitant decrease in blood flow due to p53-mediated antiangiogenesis have also been demonstrated using Power Doppler ultrasound imaging [30]. Adapting such a tumor-targeted nanocomplex to deliver imaging agents would have the potential to improve early diagnosis as well as detection of metastatic disease. The results described above demonstrate that we can encapsulate and deliver the commonly used MRI agent Magnevist® to tumor cells both in vitro and in an orthotopic animal model and in doing so produce a more defined and intense image than seen with uncomplexed Magnevist®.

Other nanometer-sized delivery systems for contrast agents are being developed. A chylomicron-remnant-like vehicle of approximately 90 nm containing polyiodinated triglyceride analogs in a neutral lipid core has been developed as a hepatocyte-selective contrast agent for computed tomography in animals [31]. A paramagnetic liquid perfluorocarbon nanoparticle of approximately 250 nm to which an anti- $\alpha_v\beta_3$ antibody has been conjugated is being developed for MRI to assess angiogenesis and atherosclerosis [32,33]. However,

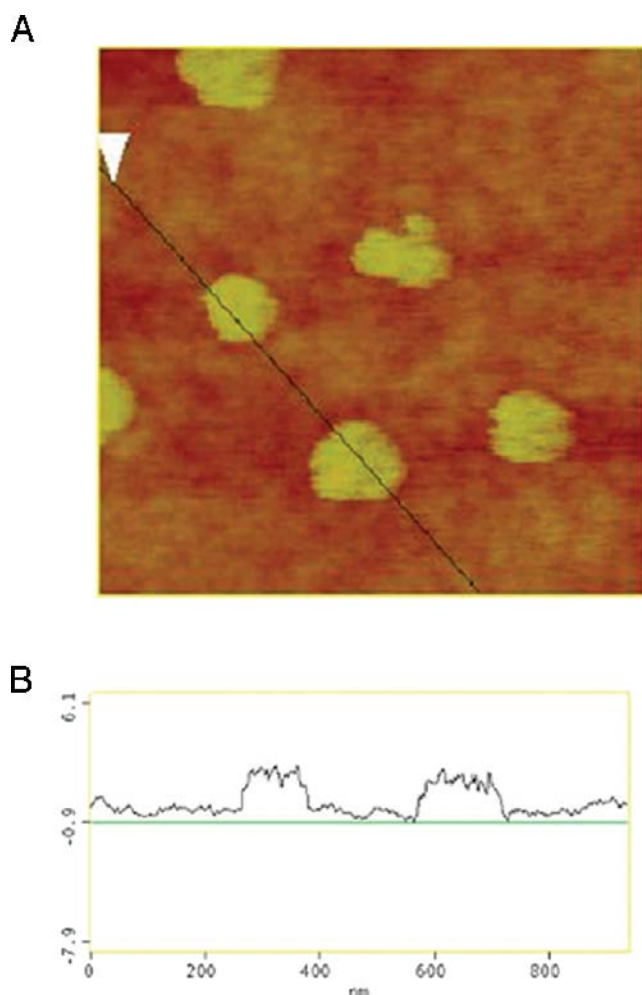


Figure 7. Cross-sectional comparison of SPM topographic and magnetic phase image in lift mode using 25-nm height displacement. (A) SPM topographic/magnetic phase image of the full TfRscFv-Lip-Mag nanocomplex. The appearance of a double dipole-like signal in B consisting of attractive and repulsive in-plane magnetic interactions suggests that the cause of this interaction is the nonuniform toroidal distribution of Magnevist within the NDS, consistent with SEM and nonmagnetic SPM phase images.

none of these are tumor targeting or currently applicable for cancer. However, given, as shown in Figure 1, that our nanocomplex can target metastatic disease it is anticipated that use of the nanocomplexed Magnevist® would also enhance detection sensitivity for metastases. The results shown here are with primary tumors. Studies are currently under way to compare the sensitivity of detection between free Magnevist® and the TfRscFv–Lip–Mag complex in metastases.

Using SEM and SPM we have also shown that the TfRscFv–Lip complex maintains its nanometer size when Magnevist® is encapsulated (particles of approximately 100–200 nm are shown in Figures 6 and 7). We have also demonstrated that the structural and mechanical properties of liposomes containing a payload are sufficiently different from those without one for it to be possible to confirm that Magnevist® is indeed encapsulated with the liposome. This was further confirmed by MFM imaging of the complex.

A tentative explanation for the internal structure of (Lip+Mag) is that the slight bulge in the SPM topographic image, represents a liposome-confined phase separation, that is, formation of a dense Magnevist–lipid toroidal distribution around the periphery of the particle with a preferential aqueous phase at the particle's center. This response is probably attributable to several important factors: First, the properties of Magnevist solution are pH approximately 6.5–8, an osmolality of 1,960, and viscosity of 4.9 at 20°C according to the manufacturer. A plausible chemical basis for this separation of the solution noted in the Magnevist data sheet: The meglumine salts dissociate completely from the complex, so changes in the local osmotic conditions. Coupled with the charge interaction of the gadolinium complex and cationic lipid, these interactions may provide a strong driving force for a hypertonic phase separation within the liposome. The charge distribution between the cationic lipid and Magnevist solution is effective at stabilizing the liposome and at providing structural support in solution and apparently in the bloodstream. This enhanced structural support is an important benefit for our studies because it enables most particles to remain intact during the film-drying process, in contrast to the extensive decomposition observed with the liposome-only solutions.

Therefore, we have been able to successfully encapsulate an MR contrast agent in our tumor-targeted nanodelivery system. The image enhancement demonstrated by the complex over conventionally delivered Magnevist® indicates the potential of this system to improve early detection of cancer via MRI.

Acknowledgments

We thank Ms. Brianna Kalk, Ms. Angelique Forrester, and Mr. Luis Torres for assistance in preparation of this manuscript, as well as the LCCC Animal Research Resource and Tissue Culture Shared Resource Facilities for their assistance in these studies. This work was supported in part by grants from NCI (CA103579-01) and SynerGene Therapeutics Inc (to K. F. P.) and from NRCR (to E. H. C.).

References

- [1] Gillies RJ, Bhujwala ZM, Evelhoch J, Garwood M, Neeman M, Robinson SP, Sotak CH, Van Der SB (2000). Applications of magnetic resonance in model systems: Tumor biology and physiology. *Neoplasia*. **2**:139–151.
- [2] Degani H, Chetrit-Dadiani M, Bogin L, Furman-Haran E (2003). Magnetic resonance imaging of tumor vasculature. *Thromb Haemost*. **89**:25–33.
- [3] Xu L, Pirollo K, Tang W, Rait A, Chang EH (1999). Transferrin–liposome-mediated systemic p53 gene therapy in combination with radiation results in regression of human head and neck cancer xenografts. *Hum Gene Ther*. **10**:2941–2952.
- [4] Xu L, Pirollo K, Chang EH, Murray A (1999). Systemic p53 gene therapy in combination with radiation results in human tumor regression. *Tumor Targeting* **4**:92–104.
- [5] Xu L, Tang WH, Huang CC, Alexander W, Xiang LM, Pirollo KF, Rait A, Chang EH (2001). Systemic p53 gene therapy of cancer with immunolipoplexes targeted by anti-transferrin receptor scFv. *Mol Med*. **7**:723–734.
- [6] Xu L, Huang C-C, Huang W-Q, Tang W-H, Rait A, Yin Y, Cruz I, Xiang L-M, Pirollo K, Chang EH (2002). Systemic tumor-targeted gene delivery by anti-transferrin receptor scFv-immunoliposomes. *Mol Cancer Ther*. **1**:337–346.
- [7] Rait A, Pirollo KF, Xiang LM, Ullick D, Chang EH (2002). Tumor-targeting, systemically delivered antisense HER-2 chemosensitizes human breast cancer xenografts irrespective of HER-2 levels. *Mol Med*. **8**:476–487.
- [8] Rait A, Pirollo KF, Ullick D, Cullen K, Chang EH (2003). HER-2-targeted antisense oligonucleotides result in sensitization of head and neck cancer cells to chemotherapeutic agents. *Ann N Y Acad Sci*. **1002**:1–12.
- [9] Cristiano RJ, Curiel DT (1996). Strategies to accomplish gene delivery via the receptor-mediated endocytosis pathway. *Cancer Gene Ther*. **3**:49–57.
- [10] Cheng PW (1996). Receptor ligand-facilitated gene transfer: Enhancement of liposome-mediated gene transfer and expression by transferrin. *Hum Gene Ther*. **7**:275–282.
- [11] Keer HN, Kozlowski JM, Tsai YC, Lee C, McEwan RN, Grayhack JT (1990). Elevated transferrin receptor content in human prostate cancer cell lines assessed in vitro and in vivo. *J Urol*. **143**:381–385.
- [12] Rossi MC, Zetter BR (1992). Selective stimulation of prostatic carcinoma cell proliferation by transferrin. *Proc Natl Acad Sci USA*. **89**:6197–6201.
- [13] Elliott RL, Elliott MC, Wang F, Head JF (1993). Breast carcinoma and the role of iron metabolism. A cytochemical, tissue culture, and ultrastructural study. *Ann N Y Acad Sci*. **698**:159–166.
- [14] Thorstensen K, Romslo I (1993). The transferrin receptor: Its diagnostic value and its potential as therapeutic target. *Scand J Clin Lab Invest Suppl*. **215**:113–120.
- [15] Miyamoto T, Tanaka N, Eishi Y, Amagasa T (1994). Transferrin receptor in oral tumors. *Int J Oral Maxillofac Surg*. **23**:430–433.
- [16] Ponka P, Lok CN (1999). The transferrin receptor: Role in health and disease. *Int J Biochem Cell Biol*. **31**:1111–1137.

- [17] Haynes BF, Hemler M, Cotner T, Mann DL, Eisenbarth GS, Strominger JL, Fauci AS (1981). Characterization of a monoclonal antibody (5E9) that defines a human cell surface antigen of cell activation. *J Immunol.* **127**:347–351.
- [18] Batra JK, Fitzgerald DJ, Chaudhary VK, Pastan I (1991). Single-chain immunotoxins directed at the human transferrin receptor containing *Pseudomonas* exotoxin A or diphtheria toxin: Anti-TFR(Fv)-PE40 and DT388-anti-TFR(Fv). *Mol Cell Biol.* **11**:2200–2205.
- [19] Jain RK, Baxter LT (1988). Mechanisms of heterogenous distribution of monoclonal antibodies and other macro-molecules in tumors: Significance of elevated interstitial pressure. *Cancer Res.* **48**:7022–7032.
- [20] Wolfert MA, Schacht EH, Toncheva V, Ulbrich K, Nazarova O, Seymour LW (1996). Characterization of vectors for gene therapy formed by self-assembly of DNA with synthetic block copolymers. *Hum Gene Ther.* **7**:2123–2133.
- [21] Dunlap DD, Maggi A, Soria MR, Monaco L (1997). Nanoscopic structure of DNA condensed for gene delivery. *Nucleic Acids Res.* **25**:3095–3101.
- [22] Kawaura C, Noguchi A, Furuno T, Nakanishi M (1998). Atomic force microscopy for studying gene transfection mediated by cationic liposomes with a cationic cholesterol derivative. *FEBS Lett.* **421**:69–72.
- [23] Choi YH, Liu F, Choi JS, Kim SW, Park JS (1999). Characterization of a targeted gene carrier, lactose–polyethylene glycol-grafted poly-L-lysine and its complex with plasmid DNA. *Hum Gene Ther.* **10**:2657–2665.
- [24] Diebel CE, Proksch R, Green CR, Neilson P, Walker MM (2000). Magnetite defines a vertebrate magnetoreceptor. *Nature.* **406**:299–302.
- [25] Rasa M, Kuipers BWM, Philipse AP (2002). Atomic force microscopy and magnetic force microscopy study of model colloids. *J Colloid Interface Sci.* **250**:303–315.
- [26] Yu W, Pirollo KF, Yu B, Rait A, Xiang L, Huang W, Zhou Q, Ertem G, Chang EH (2004). Enhanced transfection efficiency of a systemically delivered tumor-targeting immunolipoplex by inclusion of a pH-sensitive histidylated oligolysine peptide. *Nucleic Acids Res.* **5**.
- [27] Alisauskus R, Wong GY, Gold DV (1995). Initial studies of monoclonal antibody PAM4 targeting to xenografted orthotopic pancreatic cancer. *Cancer Res.* **55**:5743s–5748s.
- [28] Foo JJ, Chan V, Liu KK (2003). Contact deformation of liposome in the presence of osmosis. *Ann Biomed Eng.* **31**:1279–1286.
- [29] Xu L, Frederick P, Pirollo K, Tang W, Rait A, Xiang L, Huang W-Q, Chang EH (2002). Self-assembly of a virus-mimicking nanostructure system for efficient tumor-targeted gene delivery. *Hum Gene Ther.* **13**:469–481.
- [30] Freedman M, Sarcone A, Pirollo KF, Lin C, Chang EH (2001). Ultrasound images of implanted tumors in nude mice using Sono-CT[®] correlated with MRI appearance. *SPIE Medical Imaging: Physiology and Function from Multidimensional Images.* **4321**:163–167.
- [31] Wisner ER, Weichert JP, Longino MA, Counsell RE, Weisbrode SE (2002). A surface-modified chylomicron remnant-like emulsion for percutaneous computed tomography lymphography: Synthesis and preliminary imaging findings. *Invest Radiol.* **37**:232–239.
- [32] Winter PM, Morawski AM, Caruthers SD, Fuhrhop RW, Zhang H, Williams TA, Allen JS, Lacy EK, Robertson JD, Lanza GM, Wickline SA (2003). Molecular imaging of angiogenesis in early-stage atherosclerosis with alpha(v)beta3-integrin-targeted nanoparticles. *Circulation.* **108**:2270–2274.
- [33] Morawski AM, Winter PM, Crowder KC, Caruthers SD, Fuhrhop RW, Scott MJ, Robertson JD, Abendschein DR, Lanza GM, Wickline SA (2004). Targeted nanoparticles for quantitative imaging of sparse molecular epitopes with MRI. *Magn Reson Med.* **51**:480–486.

Dual Probe with Fluorescent and Magnetic Properties for Imaging Solid Tumor Xenografts

Liang Shan, Songping Wang, Rajagopalan Sridhar, Zaver M. Bhujwalla, and Paul C. Wang

Abstract

A dual probe with fluorescent and magnetic reporter groups was constructed by linkage of the near-infrared (NIR) fluorescent transferrin conjugate (Tf^{NIR}) on the surface of contrast agent-encapsulated cationic liposome (Lip-CA). This probe was used for magnetic resonance imaging (MRI) and optical imaging of MDA-MB-231-luc breast cancer cells grown as a monolayer *in vitro* and as solid tumor xenografts in nude mice. Confocal microscopy, optical imaging, and MRI showed a dramatic increase of *in vitro* cellular uptake of the fluorescent and magnetic reporter groups from the probe compared with the uptake of contrast agent or Lip-CA alone. Pretreatment with transferrin (Tf) blocked uptake of the probe reporters, indicating the importance and specificity of the Tf moiety for targeting. Intravenous administration of the dual probe to nude mice significantly enhanced the tumor contrast in MRI, and preferential accumulation of the fluorescent signal was clearly seen in NIR-based optical images. More interestingly, the contrast enhancement in MRI showed a heterogeneous pattern within tumors, which reflected the tumor's morphologic heterogeneity. These results indicate that the newly developed dual probe enhances the tumor image contrast and is superior to contrast agent alone for identifying the tumor pathologic features on the basis of MRI but also is suitable for NIR-based optical imaging.

TUMOR IMAGING exploits the differences in physical properties between malignant and normal tissues. These differences are often insufficient for good contrast resolution.^{1–3} Contrast-enhanced magnetic resonance imaging (MRI) is one of the best noninvasive methodologies available today in clinical medicine for assessing the anatomy and function of tissues.⁴ High spatial resolution and high soft tissue contrast are desirable features of noninvasive MRI. However, owing to intrinsically low sensitivity, high local concentration of contrast agents (CAs) is required to generate detectable magnetic resonance contrast. A large amount of CA has to be used owing to the nonspecific uptake by tumors and other

tissues *in vivo*. In recent years, targeted CA delivery systems have been developing based on the concept that molecular imaging can increase the signal to noise ratio by detecting differences in ‘molecular properties’ between cancer and normal tissues.^{5–7} This should, in theory, allow for detection of smaller tumors. As one strategy, monoclonal antibodies or antibody fragments have been coupled with CA directly or linked with CA through liposome (Lip) carrier. However, insufficient direct linkage of gadolinium (Gd) with antibody or the relatively large molecular size of antibody-Lip-Gd particles may limit its use as a CA for imaging cell surface receptors in solid tumors because of inefficient extravasation and very slow diffusion in the interstitial compartment.^{2,8,9} Furthermore, antibody immunogenicity, poor stability of the conjugates, and potential change of the antibody binding ability owing to changes in surface antigens are still problematic for *in vivo* application. A ligand with less toxic, high binding specificity for tumors and relatively small size and without immunogenicity is required to target the CA to tumors.

Optical imaging offers several advantages over other imaging techniques. Among these are the simplicity of the technique, high sensitivity, and absence of ionizing radiation. There is increasing interest in the development of techniques for *in vivo* evaluation of gene expression, monitoring of gene delivery, and real-time intraoperative

From the Departments of Radiology and Radiation Oncology, Howard University, Washington, DC; and Department of Radiology, Johns Hopkins University School of Medicine, Baltimore, MD.

This study was made possible by grant number 2G12RR003048 from the National Center for Research Resources, a component of the National Institutes of Health (NIH). It was also supported by the following grants: USAMRMC W81XWH-05-1-0291, DAMD17-00-1-0291, DAMD17-03-1-0759, and NIH 5U54CA091431.

Address reprint requests to: Paul C. Wang, PhD, Department of Radiology, Howard University, 2041 Georgia Avenue, NW, Washington, DC 20060; e-mail: pwang@howard.edu.

DOI 10.2310/7290.2007.00006

© 2007 BC Decker Inc

visualization of tumor margins and metastatic lesions to improve surgical outcome.^{10–12} Limited depth of light penetration and a lack of tomographic information prevent in vivo efficiency of optical imaging. To overcome the limitations of various imaging modalities, multimodal probes have been developed for detection using multiple imaging devices.^{13–15}

Transferrin receptor (TfR) is a cell surface internalizing receptor that is responsible for almost all iron sequestration in mammalian cells. TfR is overexpressed in 74% of breast carcinomas, 76% of lung adenocarcinomas, and 93% of lung squamous cell carcinomas. The expression level of TfR receptor is of great value in grading tumors and determining prognosis.^{16,17} TfR has been successfully applied as a molecular target to direct therapeutic agents to tumor cells.¹⁷ Transferrin (Tf), the TfR ligand, is a monomeric glycoprotein that binds Fe^{3+} for delivery to vertebrate cells through receptor-mediated endocytosis. Fluorescently labeled Tf has greatly aided the investigation of endocytosis in vitro. Tf has also been successfully used in targeted gene therapy in vivo.^{18,19} We hypothesized that near-infrared (NIR) dye-labeled Tf (Tf^{NIR}) would be an ideal ligand for targeting MRI and optical reporters to solid tumors, enabling better contrast-enhanced MRI and NIR-based optical detection. We developed a Tf- and Lip-mediated dual molecular probe with both fluorescent and magnetic reporter groups. The Tf^{NIR} was linked on the surface of Lip particles, whereas the MRI CA (Magnevist, obtained from Berlex Laboratories, Wayne, NJ) was encapsulated within the Lip. These components conjugated together and formed small uniform vesicles (less than 100 nm in diameter). In vitro analysis demonstrated that the probe dramatically improved the uptake of CA and NIR dye in monolayer cultures of MDA-MB-231-luc human breast cancer cells through both receptor- and Lip-mediated endocytosis. In vivo, the probe significantly enhanced the magnetic resonance signals from the MDA-MB-231-luc cells grown as solid tumor xenografts in nude mice and was superior to the CA alone for identifying the tumor morphology and infrastructure. Simultaneously, a significant preferential accumulation of fluorescent signal by the tumors was clearly detectable in Tf^{NIR} -based optical imaging.

Materials and Methods

Materials

Cationic lipids including 1,2-dioleoyl-sn-glycero-3-phosphoethanolamine (DOPE), 1,2-dioleoyl-3-trimethylammo-

nium-propane (DOTAP), and fluorescent lipid DOPE-N-(7-nitro-2-1,3-benzoxadiazole-4-yl) (NBD-DOPE) were purchased from Avanti Polar Lipids (Alabaster, AL). They were premixed and dissolved in chloroform in a formula of DOTAP:DOPE (1:1 w/w) (Lip) or in a fluorescent formula of DOTAP:DOPE + 0.1% NBD-DOPE (Lip^{NBD}). Fluorescent Alexa fluor 680 conjugate of human Tf (Tf^{NIR}), a SelectFX nuclear labeling kit, Alexa fluor 680 fluorophore, and enzyme-free phosphate-buffered saline (PBS)-based cell dissociation solution were purchased from Invitrogen (Carlsbad, CA). Holo-transferrin without fluorescent conjugate and MicroSpin G-50 columns were obtained from Sigma (St. Louis, MO) and Amersham Biosciences (Piscataway, NJ), respectively. The SPI-Pore polycarbonate membrane filter and filter holder were from Structure Probe Inc (West Chester, PA).

Preparation of the Molecular Dual Probe: Tf^{NIR} - Lip^{NBD} -CA Complex

The Tf^{NIR} - Lip^{NBD} -CA complex was constructed using Tf^{NIR} , cationic Lip^{NBD} , and Magnevist. Premixed Lip^{NBD} in chloroform (3.607 μL) was dried under a nitrogen stream and hydrated by adding 50 μL of water containing 12 μL of Magnevist. Each microliter of Magnevist contains 469.01 μg of gadopentatate dimeglumine. The hydrated Lip^{NBD} -CA mixture was homogenized using a vortex generator and incubated for 10 minutes. The volume of the mixture was adjusted to 175 μL with water. The mixture was then sequentially downsized by sonication (80–90 W, 10 minutes) in a water bath and by repeatedly passing through polycarbonate filters with decreasing pore diameter 0.2/0.1 μm . Following that, 25 μL of Tf^{NIR} (5 mg/mL) was mixed and incubated for at least 10 minutes. Gel filtration through a Sephadex G-50 column was used to remove unencapsulated CA and free Tf^{NIR} . A freshly prepared probe was used in all analysis. The final volume was 200 μL , and Lip: Tf :Magnevist composition was 10:12.5:0.56 (nmol/ μg /mg). To monitor different components of the probe, nonfluorescent Tf and Lip were used instead of fluorescent Tf^{NIR} and Lip^{NBD} in some experiments.

Cell Culture and Animal Model

The MDA-MB-231-luc human breast cancer cell line (Xenogen, Alameda, CA) was used to test the efficiency of the probe in vitro and in vivo. This cell line is well documented for constitutional overexpression of TfR and has been transfected with the luciferase gene for luciferase-

based optical imaging. (In this study, we did not use luciferase-based imaging.) Cells were routinely maintained in Dulbecco's Modified Eagle's Medium/F-12 medium supplemented with 10% heat-inactivated fetal bovine serum (FBS) and 50 µg/mL each of penicillin, streptomycin, and neomycin (Invitrogen). The solid tumor xenograft model was developed by subcutaneous injection of 1×10^7 subconfluent cells in 100 µL Dulbecco's phosphate-buffered saline (DPBS) in the lower back of female athymic nude mice (8–10 weeks old; Harlan, Indianapolis, IN). The probe was evaluated in a total of 10 nude mice bearing tumors from 0.4 to 1.2 cm in diameter.

Confocal Microscopy

Tumor cells were grown on eight-chamber glass slides. Twenty-four hours later, the cells at 40 to 50% confluence were incubated with 25 µL of one of the following probes in 150 µL of medium without FBS and antibiotics. The probes included Tf^{NIR}-Lip^{NBD}-CA, Tf-Lip^{NBD}-dye, and dye alone. To visualize the cellular uptake of probe reporters, an NIR dye Alexa fluor 680 fluorophore was used to replace the CA in the preparation of Tf-Lip^{NBD}-dye probe at a concentration of 2 µL in a 200 µL total probe. Incubation was carried out for 5, 30, 60, and 120 minutes, separately. After PBS washing (three times), cells were fixed using 10% neutralized formalin for 10 minutes and cell nuclei were counterstained using 4',6-diamidino-2-phenylindole dihydrochloride (DAPI) blue-fluorescence dye. Confocal images were acquired with a Zeiss LSM 510 Confocal Microscopy System (Carl Zeiss Inc, Thornwood, NY) using a 633 nm excitation line and emission LP 650 filter for Tf^{NIR} and Alexa fluor 680 fluorophore (red), 488 nm excitation line and emission BP 505 – 550 filter for Lip^{NBD} (green), and 364 nm excitation line and emission BP 385 – 470 filter for DAPI (blue). Following sequential excitation, red, green, and blue fluorescent images of the same cells were merged using the Zeiss AIM software for colocalization of the probe different reporters within cells.

In Vitro MRI and Optical Imaging

To quantify the cellular uptake of probe reporters, optical imaging and MRI of the cell pellets were performed. Similar numbers of tumor cells were seeded on 10 cm culture dishes for optical imaging and in 150 cm flasks for MRI. Cells grown to subconfluence were incubated with a 200 µL probe (in 3 mL medium) for 10 cm dishes and a 600 µL probe (in 10 mL medium) for 150 cm flasks.

Differently labeled probes, such as Tf^{NIR}-Lip^{NBD}-CA, Tf-Lip^{NBD}-dye, Lip^{NBD}-dye, CA alone, and dye alone, were used. Incubation was carried out for 60 minutes. After PBS washing (three times), cells were collected using enzyme-free cell dissociation solution and adjusted to the same number. Cells were pelleted in microcentrifuge tubes by centrifugation. The cell pellets were quantified with respect to fluorescent intensity (FI) using the Xenogen IVIS 200 imaging system with excitation/emission filters at 679/702 nm for Tf^{NIR} and the Alexa fluor 680 fluorophore and at 464/531 nm for Lip^{NBD} measurement. Statistical analysis (Student's two-tailed *t*-test) of the FI for cells with different treatments was performed using Microsoft Excel. To obtain enough cells for MRI, cell pellets were pooled from five replicates. MRI was acquired using a Bruker 400 MHz NMR machine (Bruker-Biospin, Billerica, MA). A spin-echo (SE) imaging sequence was used to obtain T₁-weighted images. The imaging parameters were as follows: echo time (TE) = 11.416 milliseconds, repetition time (TR) = 500 milliseconds, number of averages = 4, field of view = 20 × 20 mm, matrix size = 256 × 128, and slice thickness = 2 mm. A fast imaging with steady-state precession sequence was used for T₁ measurement. The T₁ measurement parameters were as follows: TE = 1.5 milliseconds, TR = 3 milliseconds, number of averages = 8, number of frames = 16, number of segments = 32, inversion delay = 49.2 milliseconds, and inversion repetition = 2572.3 milliseconds. The MRIs were taken in the cross-sectional view of the microcentrifuge tubes. The central slice image, which was not influenced by the image distortion owing to the susceptibility effect from the air-pellet boundary, was used for signal intensity measurement. All analyses were performed using the Bruker image sequence analysis tools. All experiments were repeated at least three times. The representative data are presented.

In Vivo MRI and Optical Imaging

The animal was anesthetized using 2% isoflurane and positioned with the tumor at the center of the coil. The physiologic condition of the animals was monitored using a respiratory gating device during the scanning. The tumor was scanned in the perpendicular direction of the tumor and animal skin interface using a Bruker 400 MHz, 89 mm NMR spectrometer. After a search for overall image quality, imaging time, and probe- and CA-mediated contrast enhancement using different imaging sequences and parameters, a multislice multiecho T₁-weighted SE sequence was used for imaging studies, with a TR of 800 milliseconds, a TE of 11.4 milliseconds, and a slice

thickness of 1 mm. For each animal, a baseline image was first obtained; the tumors were then sequentially imaged at an interval of 10 minutes until 3 hours following intravenous injection of 200 μ L of Tf^{NIR}-Lip^{NBD}-CA probe (containing 12 μ L of Magnevist) through the tail vein. This was equivalent to two times the Magnevist dosage used in the clinic. For comparative study, the same animals were also imaged following intravenous administration of the same dosage of Lip-CA and CA alone (12 μ L of Magnevist in 200 μ L of pure water). The interval period between the two MRI studies was at least 3 days to avoid any influence of CA from the previous imaging study. The direction of the tumor was marked each time with water-filled small balls and marker pens before imaging. For optical imaging, the FI of tumors was monitored from 10 minutes after administration of the probe to 3 to 5 days using a Xenogen IVIS 200 imaging system.

Pathologic Analysis

After imaging, the mice were autopsied and the tumors were sampled, fixed in 10% neutral buffered formalin, and embedded in paraffin. Tumors were sectioned in the same direction as MRIs based on the markers of the tumor border made before MRI. Hematoxylin-eosin staining was used for pathologic examination. A comparison was performed between the tumor pathology and the image enhancement pattern in MRI.

Results

Visualization of Tf- and Lip-Mediated Cellular Uptake

For confocal microscopic observation of the cellular uptake of the probe reporters, cells were incubated with the probe Tf-Lip^{NBD}-dye or dye alone from 5 minutes to 2 hours. Here the probe was constructed using unlabeled Tf and NIR fluorescent dye instead of CA to visualize the uptake of encapsulated reagents within Lip. Figure 1 shows representative microscopic images. Both Lip^{NBD} (green) and fluorescent dye (red) were observed to be present in the cell cytoplasm as early as 5 minutes after incubation with the probe, and their FI within the cytoplasm increased gradually, reaching a maximum at about 1 hour of incubation (see Figure 1, A–C). Interestingly, the Lip^{NBD} and dye accumulated again, forming multiple endosomes. These endosomes were mainly located at the peripheral area of the cytoplasm and became more evident at 2 hours of incubation (see Figure 1, D–F), suggesting receptor-

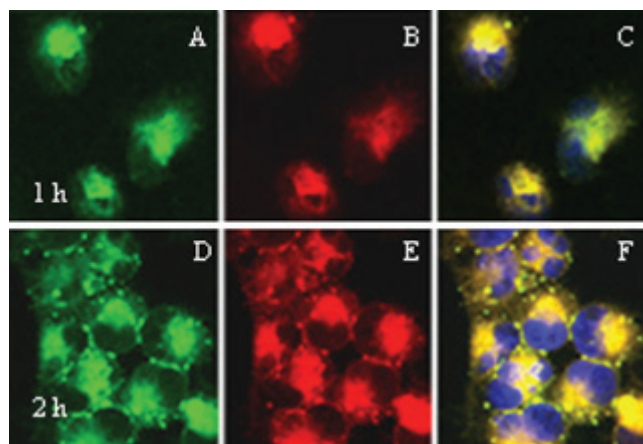


Figure 1. Confocal microscopic observation of cellular uptake of probe reporters. Cells were incubated with the probe transferrin-liposome-nitrobenzoxadiazole (Tf-Lip^{NBD})-dye for 5 minutes to 2 hours. A to C are representative images acquired at the 1 hour of incubation time point showing distribution and colocalization of Lip^{NBD} (A) and near-infrared (NIR) dye (B) in the cytoplasm. D to F are representative images acquired at the 2 hours of incubation time point showing multiple endosomes formed by Lip (D) and NIR dye (E) and colocalized in the peripheral area of the cytoplasm (F). Nuclei were counterstained using 4',6-diamidino-2-phenylindole dihydrochloride (DAPI). Cells were imaged with a 63 \times 1.4 NA Plan-Apochromat oil-immersion objective.

mediated endocytosis and release or degradation of the probe reporters through the action of lysosomal enzymes. Cellular uptake of the dye was not evident in the cells incubated with dye alone.

To visualize whether the Tf and Lip were co-internalized, confocal microscopy and optical imaging were performed for cells incubated with Tf^{NIR}-Lip^{NBD}-CA, Lip^{NBD}-CA, or CA alone. Similarly, from 5 minutes of incubation, the Tf^{NIR} (Figure 2A) and Lip^{NBD} (Figure 2B) were already colocalized within cell cytoplasm (Figure 2C). Optical imaging of the cell pellets further confirmed the uptake of the probe in tumor cells. To avoid membrane damage and probe leakage from cells, enzyme-free PBS-based cell dissociation solution was used instead of trypsin for cell dissociation from culture dishes. As shown in Figure 2D, only cells incubated with Tf^{NIR}-Lip^{NBD}-CA showed a strong fluorescent signal of Tf^{NIR}. Both cells incubated with Tf^{NIR}-Lip^{NBD}-CA and cells incubated with Lip^{NBD}-CA showed strong fluorescent signal of Lip^{NBD} (Figure 2E). Neither Tf^{NIR} nor Lip^{NBD} signal was detectable in cells incubated with CA alone.

We further evaluated whether the CA encapsulated within the probe was internalized into tumor cells using MRI of the cell pellets. A representative MRI of the cell pellets obtained from cells incubated with Tf^{NIR}-Lip^{NBD}-

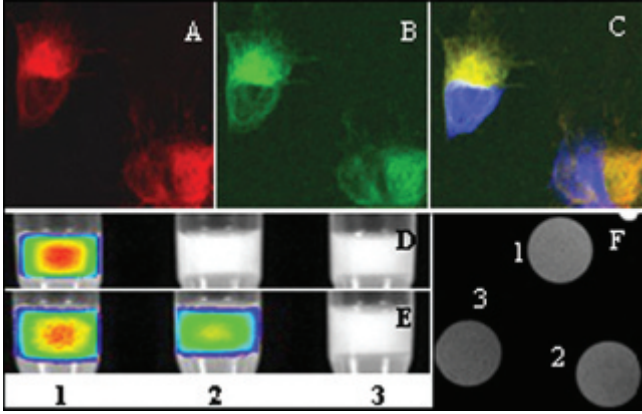


Figure 2. Confocal, optical, and magnetic resonance imaging (MRI) detection of the reporters in cells incubated with the probe near-infrared transferrin-liposome-nitrobenzoxadiazole-contrast agent ($\text{Tf}^{\text{NIR}}\text{-Lip}^{\text{NBD}}\text{-CA}$) for 1 hour. *A* to *C* are representative confocal microscopic images showing distribution and colocalization of Tf^{NIR} (*A*) and Lip^{NBD} (*B*) in cytoplasm. *D* to *E* are optical images of the cell pellets. A strong fluorescent signal of Tf is detected in cells incubated with $\text{Tf}^{\text{NIR}}\text{-Lip}^{\text{NBD}}\text{-CA}$ (*D*, lane 1) but not in cells incubated with $\text{Lip}^{\text{NBD}}\text{-CA}$ or with CA alone (*D*, lanes 2 and 3). Similarly, the strongest signal of Lip^{NBD} is detected in cells incubated with $\text{Tf}^{\text{NIR}}\text{-Lip}^{\text{NBD}}\text{-CA}$ (*E*, lane 1) and less in cells incubated with $\text{Lip}^{\text{NBD}}\text{-CA}$ (*E*, lane 2) but not in cells incubated with CA alone (*E*, lane 3). *F* shows the MRIs of the cell pellets. A stronger signal enhancement and T_1 shortening are obtained in cells incubated with $\text{Tf}^{\text{NIR}}\text{-Lip}^{\text{NBD}}\text{-CA}$ and in cells incubated with $\text{Lip}^{\text{NBD}}\text{-CA}$ (1 and 2) than in cells incubated with CA alone (3). The MRI parameters are as follows: echo time = 11.416 milliseconds, repetition time = 500 milliseconds, number of averages = 4, field of view = 20×20 mm, matrix size = 256×128 , and slice thickness = 2 mm.

CA, $\text{Lip}^{\text{NBD}}\text{-CA}$, or CA alone is shown in Figure 2F. The corresponding signal intensity and T_1 relaxation time are shown in Table 1. Cells incubated with the probe $\text{Tf}^{\text{NIR}}\text{-Lip}^{\text{NBD}}\text{-CA}$ or $\text{Lip}^{\text{NBD}}\text{-CA}$ showed a much greater positive

contrast and T_1 shortening than the cells incubated with CA alone. The T_1 relaxation time shortened from 408 milliseconds for CA alone to 374 milliseconds for $\text{Lip}^{\text{NBD}}\text{-CA}$ and 366 milliseconds for $\text{Tf}^{\text{NIR}}\text{-Lip}^{\text{NBD}}\text{-CA}$ ($p < .05$). The cells incubated with $\text{Tf}^{\text{NIR}}\text{-Lip}^{\text{NBD}}\text{-CA}$ also showed higher signal intensity than the cells incubated with $\text{Lip}^{\text{NBD}}\text{-CA}$. These results highly indicate the importance and specificity of Tf moiety for targeting the probe internalization into tumor cells in vitro. The difference in signal intensity and T_1 relaxation time mediated by $\text{Lip}^{\text{NBD}}\text{-CA}$ and by CA alone might reflect the effective fusion of Lip with tumor cell membrane.

Quantification of Tf- and Lip-Mediated Cellular Uptake

To evaluate the efficiency of Tf- and Lip-mediated cellular uptake, the FI of the Lip^{NBD} and NIR dye within the tumor cells was quantified following 1 hour's incubation of the cells with probes. The FI of NIR dye in the cells incubated with $\text{Tf-Lip}^{\text{NBD}}\text{-dye}$ and with $\text{Lip}^{\text{NBD}}\text{-dye}$ was more than 200-fold higher than that in the cells with dye alone (Table 2). Cells incubated with dye alone showed a similar level of FI to cells without probe and dye exposure (autofluorescence background). Approximately 1.5-fold higher FI of the intracellular NIR dye was observed in cells incubated with $\text{Tf-Lip}^{\text{NBD}}\text{-dye}$ than in cells incubated with $\text{Lip}^{\text{NBD}}\text{-dye}$. Similarly, 2-fold higher FI of Lip^{NBD} was detected in cells incubated with $\text{Tf-Lip}^{\text{NBD}}\text{-dye}$ or $\text{Lip}^{\text{NBD}}\text{-dye}$ than in cells incubated with NIR dye alone (autofluorescent background) (see Table 2). The FI of Lip^{NBD} was 1.3-fold higher in cells incubated with $\text{Tf-Lip}^{\text{NBD}}\text{-dye}$ than in cells incubated with $\text{Lip}^{\text{NBD}}\text{-dye}$. Student's *t*-tests (two-tailed)

Table 1. Comparison between Probe- and Contrast Agent-Mediated Signal Enhancement

MRI Measurement	$\text{Tf}^{\text{NIR}}\text{-Lip}^{\text{NBD}}\text{-CA}$	$\text{Lip}^{\text{NBD}}\text{-CA}$	CA Alone
Relative intensity (10^5)	17.7 ± 0.86	15.33 ± 0.86	13.25 ± 0.78
T_1 relaxation time (ms)	366.7 ± 17.1	374.3 ± 17.3	408.1 ± 13.8

CA = contrast agent; Lip = liposome; NBD = nitrobenzoxadiazole; NIR = near-infrared; Tf = transferrin. $p < .05$ between probe and CA alone for both relative intensity and T_1 .

Table 2. Optical Quantitation of Probe-Mediated Cellular Uptake of Reporters

Reporters	$\text{Tf-Lip}^{\text{NBD}}\text{-Dye}$	$\text{Lip}^{\text{NBD}}\text{-Dye}$	Dye Alone
NIR dye ($\times 10^9$)	6.88 ± 0.59	4.99 ± 0.51	0.23 ± 0.006
Lip^{NBD} ($\times 10^7$)	2.03 ± 0.14	1.64 ± 0.09	1.10 ± 0.13

Lip = liposome; NBD = nitrobenzoxadiazole; NIR = near-infrared; Tf = transferrin. $p < .05$ between probe and dye alone and also between $\text{Tf-Lip}^{\text{NBD}}$ dye and Lip^{NBD} dye for both dye and Lip^{NBD} uptake. Quantitation is based on the fluorescence intensity (p/s/cm²/sr) of cell pellets.

between cells incubated with probe and with dye alone for both intracellular Lip^{NBD} and NIR dye intensity were both significantly different ($p < .05$). The FI in cells incubated with Tf-Lip^{NBD}-dye and in cells incubated with Lip^{NBD}-dye was also significantly different ($p < .05$) for both intracellular Lip^{NBD} and NIR dye uptake.

To further test the specificity of Tf-mediated cellular uptake, cells were first pretreated for 1 hour with unlabeled Tf before incubation with the probes. The amount of Tf was threefold (375 $\mu\text{g}/\text{dish}$) higher than that used in the probe (125 $\mu\text{g}/\text{dish}$). Following incubation with the probe Tf-Lip^{NBD}-dye, the FI of the NIR dye in cells with and without Tf pretreatment was 2.45×10^9 and 3.42×10^9 p/s/cm²/sr, respectively (Table 3). The FI of the Lip^{NBD} in cells with and without Tf pretreatment was 2.57×10^7 and 3.45×10^7 p/s/cm²/sr, respectively. Calculation based on the control cells incubated with Lip^{NBD}-dye revealed a blockage of 65.6% of the dye uptake and 70.97% of the Lip^{NBD} uptake by Tf pretreatment. These results indicate that the probe reporter uptake in vitro was mediated by both Tf and cationic Lip. Tf and Lip have an apparent synergistic effect on the cellular uptake of the probe reporters.

Probe-Mediated Signal Enhancement of the Tumors In Vivo

Signal enhancement was evaluated in 10 athymic nude mice with solid tumor xenografts. The tumor size ranged from 0.4 to 1.2 cm in diameter. To compare the signal enhancement mediated by the probe and mediated by the CA alone, the same mice were used for the probe and CA-alone studies sequentially with an interval of at least 3 days. Intravenous administration of the probe Tf^{NIR}-Lip^{NBD}-CA significantly enhanced the tumor image contrast (Figure 3). The enhancement was observed as early as 10 minutes after administration and increased gradually, reaching the maximum at 90 minutes to 2 hours. After that, a gradual decrease in the signal enhancement was observed. Interestingly, the enhancement was greatly heterogeneous within the tumors (see Figure 3). The enhancement

pattern became relatively consistent from 1 to 3 hours. Some areas of the tumors were strongly enhanced initially, whereas other areas were weakly enhanced. The signals from the strongly enhanced region decreased much more slowly than the signals from the region with weak enhancement. For small tumors, the enhancement was relatively uniform and the enhancement was usually observed starting from the peripheral area. Magnevist alone slightly enhanced the image contrast of tumors compared with the baseline images (Figure 4). The maximum enhancement was usually observed at 30 to 60 minutes after injection. The image contrast enhancement started from the peripheral area to the center of the tumors and was relatively uniform within tumors irrespective of the sizes studied here. The signal enhancement decreased rapidly and returned to baseline within 3 hours. The pharmacokinetics of pure Magnevist was different from that of Tf-labeled Magnevist containing Lip. Magnevist containing Lip without linkage to Tf showed a much weaker signal enhancement than either CA alone or Tf^{NIR}-Lip^{NBD}-CA.

Detection and Dynamic Change of the Fluorescent Signal in Tumors In Vivo

To understand whether the probe was preferentially accumulated in tumors and whether the fluorescent signal was optically detectable in vivo, tumors were monitored using Tf^{NIR}-based optical imaging. The fluorescent signal was clearly detectable as early as 10 minutes and reached the maximum intensity at about 90 minutes to 2 hours after intravenous injection of the probe Tf^{NIR}-Lip^{NBD}-CA (Figure 5). The FI was related to the tumor sizes, and significant FI was still detectable after 2 days for larger tumors (usually > 0.8 cm in diameter). The FI of smaller tumors became very weak at 24 hours. The FI of Lip^{NBD} was too weak to be detectable by optical imaging in vivo, although it was clearly detected ex vivo. High background fluorescence was another reason for the failure to detect Lip^{NBD} in tumors. Following intravenous injection, the probe was rapidly distributed throughout the body and

Table 3. Blockage of Transferrin-Mediated Uptake of Reporters by Transferrin Pretreatment

Reporters	Tf-Lip ^{NBD} -Dye	Tf-Lip ^{NBD} -Dye	Lip ^{NBD} -Dye
NIR dye ($\times 10^9$)	3.42 ± 0.17	2.45 ± 0.21	1.94 ± 0.20
Lip ^{NBD} ($\times 10^7$)	3.45 ± 0.29	2.57 ± 0.21	2.21 ± 0.16

Lip = liposome; NBD = nitrobenzoxadiazole; NIR = near-infrared; Tf = transferrin.

$p < .05$ between pretreated and untreated cells for both dye and Lip^{NBD} uptake. Quantitation is based on the fluorescence intensity (p/s/cm²/sr) of cell pellets.

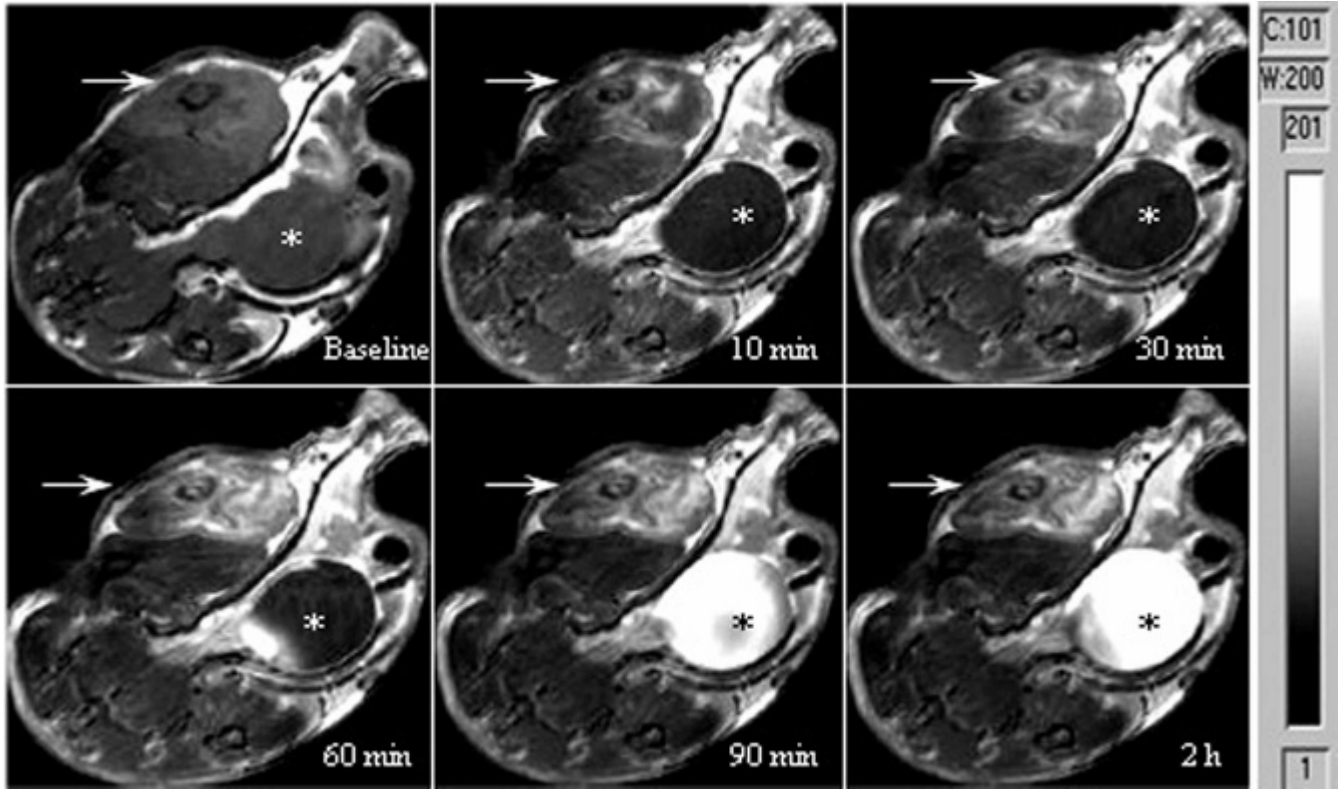


Figure 3. In vivo time course of tumor magnetic resonance imaging (MRI) after intravenous administration of the probe transferrin-liposome-nitrobenzoxadiazole-contrast agent ($\text{Tf}^{\text{NIR}}\text{-Lip}^{\text{NBD}}\text{-CA}$) showing gradually increased enhancement of the tumor signal (arrow) and a heterogeneous enhancement pattern. Gradual accumulation of contrast agent in the urinary bladder is evident (*). The MRI parameters are as follows: echo time = 11.416 milliseconds, repetition time = 800 milliseconds, number of averages = 4, field of view = 28×30 mm, matrix size = 256×192 , and slice thickness = 1.0 mm.

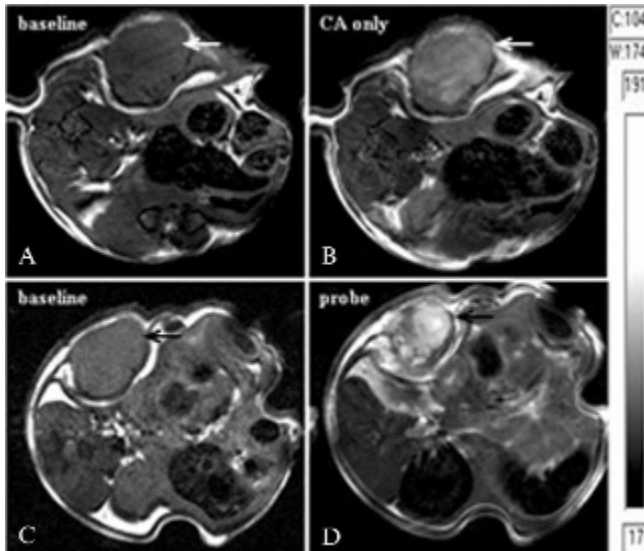


Figure 4. Comparison of the signal enhancement by contrast agent (CA) alone (A–B) and by the probe transferrin-liposome-nitrobenzoxadiazole-contrast agent ($\text{Tf}^{\text{NIR}}\text{-Lip}^{\text{NBD}}\text{-CA}$) (C–D). The magnetic resonance images (MRIs) are from the same tumor, with an interval of 72 hours between studies with the probe and with CA alone. A stronger, heterogeneous signal enhancement is achieved with $\text{Tf}^{\text{NIR}}\text{-Lip}^{\text{NBD}}\text{-CA}$ over CA alone. The MRI parameters are the same as for Figure 3.

was first taken up by the well-perfused organs, such as the liver, spleen, lung, and bone marrow. However, the probe was rapidly washed out from these organs but not from solid tumors. The uptake of the probe in tumors was enhanced because of binding to TfR in the tumor. After the initial rapid increase in the background fluorescence following injection of the probe, the background fluorescence decreased rapidly, as shown in Figure 5H. The tumor to normal (contralateral muscle) ratio varied from 1.3 to 3.4 at the different time points following injection (from 10 minutes to 48 hours), which was related to the tumor sizes. Small tumors (less than 3 mm in diameter) showed less fluorescent signal, perhaps owing to differences in vasculature. Similar to the MRI finding, fluorescent dye containing Lip without Tf linkage failed to induce a preferential increase in fluorescent signal in tumors.

Comparison between MRI Signal Enhancement and Pathologic Findings

To understand the underlying mechanism of heterogeneous contrast enhancement within the tumors by the

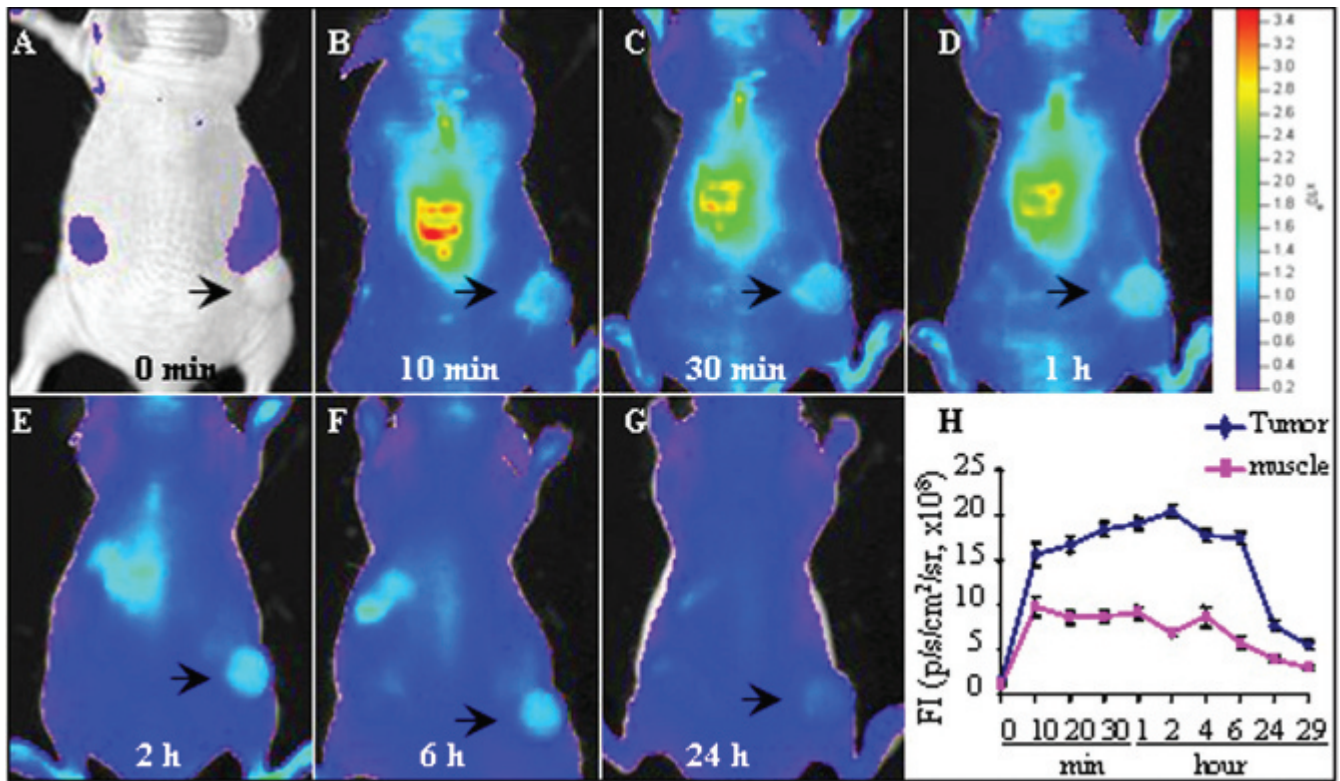


Figure 5. Optical imaging of the tumor after intravenous administration of transferrin-liposome-nitrobenzoxadiazole-contrast agent ($\text{Tf}^{\text{NIR}}\text{-Lip}^{\text{NBD}}\text{-CA}$) showing preferential accumulation of fluorescent signal in tumors (A–G). The fluorescence signal was detectable as early as 10 minutes and reached a maximum at about 2 hours and then deceased gradually. H shows the plot of time versus signal intensity obtained from the tumor and the contralateral muscle. The signal intensity is expressed as $\text{p/s/cm}^2/\text{sr}$.

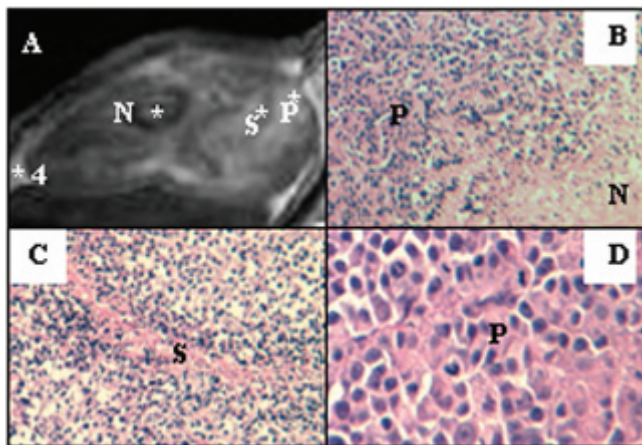


Figure 6. Correlation of magnetic resonance imaging (MRI) with pathologic findings showing high consistency between the probe-mediated enhancement pattern in MRI and pathologic findings (hematoxylin-eosin stain). A is a representative MRI (same as Figure 3) showing a heterogeneous enhancement pattern. B shows a region with high proliferation and necrosis ($\times 250$ original magnification). C shows the stromal tissue ($\times 250$ original magnification), and D shows the proliferating tumor cells with high mitotic activity ($\times 400$ original magnification). N = necrosis; P = proliferating cells; S = stromal tissue.

probe, a comparative analysis was performed between MRI signal enhancement and pathologic findings (Figure 6). Pathologically, the tumor cells in large tumors with heterogeneous enhancement usually presented various stages of growth and necrosis. In some areas, the tumor cells were completely necrotized and became amorphous and liquefied. In some other regions, the tumor cells showed dying features such as condensed or broken nuclei or only shadow cells remaining. The highly enhanced regions of the tumors in MRIs represented the more actively proliferating tumor cells, whereas the weakly enhanced areas contained less active or dying cells. The completely necrotized region showed the least enhancement. The heterogeneous signal enhancement by the probe was well correlated with the in vivo morphologic features of the tumors.

Discussion

The human Tf-targeted cationic Lip–deoxyribonucleic acid (DNA) complex has been used for efficient gene

transfer in animal models recently. The formulation for optimal transfection of cancer cells has been optimized as a DNA:lipid:Tf ratio of 1 μ g:10 nmol:12.5 μ g with Lip composition of DOTAP:DOPE (1:1, w/w). This complex of Tf-Lip-DNA demonstrates a highly compact structure that resembles a virus particle with a dense core enveloped by a membrane coated with Tf molecules spiking the surface.^{20,21} Successful gene delivery using Tf-targeted cationic Lip is based on the fact that TfR is overexpressed in various malignant tumors and Tf-TfR-mediated endocytosis is highly efficient. Furthermore, cationic Lip has many advantages, such as high encapsulation capacity, much less immunogenicity and toxicity, and dramatically increased transfection efficiency through linkage with ligands.²² These characteristics of this system also fulfill the criteria for an ideal system for molecular imaging in vivo. Using the advantages of this system, we developed the probe with both NIR fluorescence and MRI reporters, which is suitable for both optical and nuclear MRI.

Use of the NIR fluorescence molecule minimizes the autofluorescence interference from healthy tissue and allows the visualization of tissues millimeters in depth because of efficient penetration of photons in the NIR range.^{11,12} To encapsulate the CA, we directly hydrated the dried Lip films with concentrated CA solution and downsized the Lip-CA complex by sonication and repeated passing through the membrane before linkage with Tf. The Lip:Tf ratio (10:12.5) used in the probe was optimized as reported previously.^{20–24} The dosage of Magnevist was 0.2 mmol/kg, corresponding to two times the recommended dose for the patient. For this amount of Magnevist (even threefold more), almost all of the Magnevist was found to be encapsulated within the Lip, as estimated by gel filtration and fluorescence study. Our previous study also confirmed Magnevist encapsulation within Lip using scanning electron microscopy and scanning probe microscopy.²⁵ The Tf, cationic Lip, and Gd complex was coupled through charge interaction, which makes the preparation of the probe simple enough to be freshly prepared before use. A concern for Lip carrier, as in the gene delivery, is its size. It has been reported that linkage with Tf condenses the Lip-DNA complex with a uniform size of 50 to 90 nm.^{20,23} After sonication of the probe, we found that repeated passing through 200 and 100 nm polycarbonate membranes resulted only in a loss of less than 10% of the probe and the majority of the probe particles were within 100 nm in size based on the fluorescence measurement of the probe. Transportation of the probe across tumor vessels occurs via open gaps, vesicular vacuoles, and/or fenestrations. A characteristic pore cutoff size is measured

ranging from 200 nm to 1.2 μ m in tumors.²⁶ Another analysis points out that the pore cutoff size is around 400 nm based on in vivo fluorescence microscopy studies of the transportation of sterically stabilized Lip into solid tumors.²⁷ Therefore, the size of our probe should not be a limitation to transport from tumor vasculature into tumor cells.

We first evaluated the probe-mediated uptake efficiency of the reporters in vitro. To visualize and quantify the efficiency, the components of the probe were differentially labeled. On confocal microscopy, Tf^{NIR}, Lip^{NBD}, and the encapsulated NIR dye were clearly codistributed within the cytoplasm of tumor cells. They accumulated and formed endosomes again in the peripheral area of the cytoplasm. In Tf-Lip-mediated plasmid DNA transfection, similar endosome formation has been reported by Lee and Kim.²⁸ They also found nuclear localization of the Tf-Lip. In our system, no nuclear signal of the probe was observed. Quantitative analysis using optical imaging further confirmed the finding of confocal microscopy. The cellular uptake was mediated by both Tf and Lip. Blockage of the TfR with Tf led to significantly decreased uptake. The possibility of nonspecific binding to free NIR dye was excluded because no fluorescent signal of the dye was detected in cells incubated with dye alone. Higher cellular uptake of the Lip and dye in cells incubated with Lip^{NBD}-dye without Tf linkage than in cells incubated with dye alone is not surprising. The probe reporters are taken up in vitro by two different pathways. One is due to Lip-mediated endocytosis and membrane fusion process because Lip is an effective transfection reagent.²² The other is due to binding to TfR. The pretreatment with Tf is not expected to prevent endocytosis of the probe reporters owing to Lip fusion with the cell membrane. Importantly, Tf and Lip showed a synergistic effect on the probe uptake by cells based on our quantitative and blocking analysis. MRI of the cell pellets revealed a similar finding that CA is internalized and the internalization is mediated by both Tf and Lip. The apparent synergistic effect may be explained by a three-step mechanism. The important first step is the specific binding of Tf with TfR on the cell surface followed by the interaction of cationic Lip with anionic cell membrane and finally the receptor- and Lip-membrane fusion-mediated endocytosis.²⁹

For MRI study, a T₁-weighted imaging technique was used to evaluate the positive contrast enhancement mediated by our probe. The actual T₁ shortening in vivo depends on the accumulation of the probe in time, which, in turn, depends on tumor physiology. We have searched the best imaging strategy by using different imaging

sequences and by varying the imaging parameters. The choice of SE sequence with TR = 800 milliseconds and TE = 11.4 milliseconds was based on the consideration of overall image quality, imaging time, and the differences of contrast enhancement between the probe and CA-alone studies. Consistent with our *in vitro* findings, specific targeting of the probe *in vivo* was demonstrated by both optical imaging and MRI. A preferential accumulation of the fluorescent signal in tumors and a significant signal enhancement are clearly achieved with the dual probe but not with CA alone. Time course study revealed a high consistency among confocal images, optical fluorescence, and MRI contrast enhancement. The maximum signal enhancement and FI in tumors are seen at ≈ 90 minutes, and both reach a plateau (which includes the maximum) between 1 and 3 hours after intravenous injection, whereas the maximal magnetic resonance contrast enhancement is achieved at about 45 minutes following administration of CA alone and the enhancement reduces to baseline within 3 hours. The magnetic resonance signal enhancement achieved by the dual probe is much stronger than that achieved by the CA alone. These results are consistent with the finding in gene therapy using a Tf-mediated Lip system that high gene transfection efficiency is observed within tumors.^{23,24} More interestingly, heterogeneous enhancement in MRIs is evident in large tumors, which correlates well with the histologic findings. Within the range of tumor sizes in the present study, CA alone could enhance the image contrast, but the enhancement was weak and relatively uniform. Heterogeneous enhancement that could be correlated with histology may be potentially valuable. It makes it possible to interpret the pathologic features based on specifically enhanced MRI. More information could be provided to the clinician without further invasive procedure of biopsy.^{3,30} *In vivo*, significant uptake of the probe reporters was not observed in the case of Magnevist or fluorescent dye containing Lip without linkage to Tf. This may be explained by the fact that the majority of the Lip accumulated within well-perfused organs, such as the liver, spleen, bone marrow, and lung. The uptake and retention of Magnevist or fluorescent dye containing Lip were very low in tumors. This is in contrast to the uptake of Lip bound to Tf. Positive CA may be superior to the negative CA, such as an iron oxide probe. A decrease in the image intensity by negative CA will complicate interpretation of tumor necrosis and poor expression of target receptors. The advantages of using a superparamagnetic Tf-labeled iron oxide probe are the small size and long-range T_2 effect. Because of the long-range T_2 effect, it requires less compound for a greater image intensity change. Our probe

can be used for optical detection of tumors and is potentially useful for imaging the expression level of TfR and tumor cell growth. These parameters are of great value in predicting the prognosis and treatment selection. This goal can be achieved by measuring the intensity of fluorescence in optical images. However, limited penetration of fluorescence is still a problem, particularly for deep organ tumors. Clearly, use of multimodality reporter constructs can overcome many of the shortcomings of each modality alone.^{14,15}

In conclusion, we have described a novel nano-sized molecular probe with both optical and MRI reporters. *In vitro* and *in vivo* analysis confirmed the probe specificity, internalizing efficiency, and sufficiency for multimodality detection. In MRI, the probe significantly enhances the tumor contrast so that it can increase the sensitivity to detect small tumors. The tumor enhancement pattern could help evaluate the pathologic features of tumors *in vivo*, which provides more information for the clinician. Preferential accumulation of the probe NIR fluorescence makes the tumor detectable using NIR-based optical imaging. Furthermore, it provides the possibility of quantifying the specific biomarkers expressed in tumors, which will be helpful to determine the patient's prognosis and response to treatment.

Acknowledgments

We thank Dr. Elizabeth G. Snyderwine and Dr. Minshu Yu (Laboratory of Experimental Carcinogenesis, National Cancer Institute [NCI], NIH) for their scientific advice. We are grateful to Stephen M. Wincovitch and Susan H. Garfield (CCR Confocal Microscopy Core Facility, NCI, NIH) for help and consultation with confocal microscopy.

References

1. Pautler RG. Mouse MRI: concepts and applications in physiology. *Physiology* 2004;19:168–75.
2. Artemov D. Molecular magnetic resonance imaging with targeted contrast agent. *J Cell Biochem* 2003;90:518–24.
3. Massoud TF, Gambhir SS. Molecular imaging in living subjects: seeing fundamental biological processes in a new light. *Gene Dev* 2003;17:545–80.
4. Persigehl T, Heindel W, Bremer C. MR and optical approaches to molecular imaging. *Abdom Imaging* 2005;30:342–54.
5. Blasberg RG. Molecular imaging and cancer. *Mol Cancer Ther* 2003;2:335–45.
6. Funovics MA, Kapeller B, Hoeller C, et al. MR imaging of the her2/neu and 9.2.27 tumor antigens using immunospecific contrast agents. *Magn Reson Imaging* 2004;22:843–50.

7. Basilion JP. Current and future technologies for breast cancer imaging. *Breast Cancer Res* 2001;3:14–6.
8. Artemov D, Mori N, Okollie B, Bhujwala ZM. MR molecular imaging of HER-2/neu receptor in breast cancer cells using targeted iron oxide nanoparticles. *Magn Reson Med* 2003;49:403–8.
9. Mulder WJM, Strijkers GJ, Griffioen AW, et al. A liposomal system for contrast-enhanced magnetic resonance imaging of molecular targets. *Bioconjugate Chem* 2004;15:799–806.
10. Graves EE, Weissleder R, Ntziachristos V. Fluorescence molecular imaging of small animal tumor models. *Curr Mol Med* 2004;4: 419–30.
11. Ntziachristos V, Bremer C, Weissleder R. Fluorescence imaging with near-infrared light: new technological advances that enable in vivo molecular imaging. *Eur Radiol* 2003;13:195–208.
12. Hoffman RM. The multiple uses of fluorescent proteins to visualize cancer in vivo. *Nature* 2005;5:796–806.
13. Schellenberger EA, Sosnovik D, Weissleder R, Josephson L. Magneto/optical annexin V, a multimodal protein. *Bioconjugate Chem* 2004;15:1062–7.
14. Blasberg RG. In vivo molecular-genetic imaging: multi-modality nuclear and optical combinations. *Nucl Med Biol* 2003;30:879–88.
15. Veisheh O, Sun C, Gunn J, et al. Optical and MRI multifunctional nanoprobe for targeting gliomas. *Nano Lett* 2005;5:1003–8.
16. Jones DT, Trowbridge IS, Harris AL. Effects of transferrin receptor blockade on cancer cell proliferation and hypoxia-inducible factor function and their differential regulation by ascorbate. *Cancer Res* 2006;66:2749–56.
17. Hogemann-Savellano D, Bos E, Blondet C, et al. The transferrin receptor: a potential molecular imaging marker for human cancer. *Neoplasia* 2003;5:495–506.
18. Xu L, Pirollo KF, Tang WH, et al. Transferrin-liposome-mediated systemic p53 gene therapy in combination with radiation results in regression of human head and neck cancer xenographs. *Hum Gene Ther* 1999;10:2941–52.
19. Bellocq NC, Pun SH, Jensen GS, Davis ME. Transferrin-containing, cyclodextrin polymer-based particles for tumor-targeted gene delivery. *Bioconjugate Chem* 2003;14:1122–32.
20. Xu L, Frederik P, Pirollo KF, et al. Self-assembly of a virus-mimicking nanostructure system for efficient tumor-targeted gene delivery. *Hum Gene Ther* 2002;13:469–81.
21. Kursa M, Walker GF, Roessler V, et al. Novel shielded transferring-polyethylene glycol-polyethylenimine/DNA complexes for systemic tumor-targeted gene transfer. *Bioconjugate Chem* 2003;14:222–31.
22. Simoes S, Pires P, Duzgunes N, Pedrosa de Lima M. Cationic liposomes as gene transfer vectors: barriers to successful application in gene therapy. *Curr Opin Mol Theory* 1999;1:147–57.
23. Nakase M, Inui M, Okumura K, et al. p53 gene therapy of human osteosarcoma using a transferring-modified cationic liposome. *Mol Cancer Ther* 2005;4:625–31.
24. Pirollo KF, Xu L, Chang EH. Non-viral gene delivery for p53. *Curr Opin Mol Ther* 2002;2:168–75.
25. Pirollo K, Dagata J, Wang P, et al. A tumor-targeted nanodelivery system to improve early MRI detection of cancer. *Mol Imaging* 2006;5:41–52.
26. Hobbs SK, Monsky WL, Yuan F, et al. Regulation of transport pathways in tumor vessels: role of tumor type and microenvironment. *Proc Natl Acad Sci U S A* 1998;95:4607–12.
27. Umezaki S, Maruyama K, Hosoda JI, et al. Direct measurement of extravasation of poly-ethyleneglycol-coated liposomes into solid tumor tissue by in vivo fluorescence microscopy. *Int J Pharm* 1996; 144:11–7.
28. Lee SM, Kim JS. Intracellular trafficking of transferring-conjugated liposome/DNA complexes by confocal microscopy. *Arch Pharm Res* 2005;28:93–9.
29. Yin J, Lin AJ, Buckett PD, et al. Single-cell FRET imaging of transferrin receptor trafficking dynamics by sfp-catalyzed, site-specific protein labeling. *Chem Biol* 2005;12:999–1006.
30. Mankoff D. Imaging in breast cancer—breast cancer imaging revisited. *Breast Cancer Res* 2005;7:276–8.

Noninvasive Methodology for Wellness Baseline Profiling

Danny Wen-Yaw Chung¹, Yuh-Show Tsai¹; Shaou-Gang Miaou¹, Walter H. Chang¹, Yaw-Jen Chang¹,
Shia-Chung Chen¹, Y.Y. Hong¹, C.S. Chyang¹,
Quan-Shong Chang², Hon-Yen Hsu², James Hsu², Wei-Cheng Yao², Ming-Sin Hsu²;
Ming-Chung Chen³ and Shi-Chen Lee³,
Charles Hsu⁴, Lidan Miao⁴, Kenny Byrd⁴, Mohamed F. Chouikha⁴, Xin-Bin Gu⁴, Paul C. Wang⁴, and
Harold Szu^{4,5}

¹Chung Yuan Christian University, Dept. ECIS & Dept. BME, Chung-Li, Taiwan,

²Ming-Shen Hospitals at Long Tan, Chung-Li, Taiwan,

³Institute of Bio-Medical Engineering, National Taiwan University Hospital, NTU, Taipei, Taiwan

⁴School of Dentistry and Radiology Dept. of Medical School Hospital, Howard University, Wash. DC;

⁵Office of Naval Research & Q23 of NSWCDD, VA

ABSTRACT

We develop an accumulatively effective and affordable set of smart pair devices to save the exuberant expenditure for the healthcare of aging population, which will not be sustainable when all the post-war baby boomers retire (78 millions will cost 1/5~1/4 GDP in US alone). To design an accessible test-bed for distributed points of home care, we choose two exemplars of the set to demonstrate the possibility of translation of modern military and clinical know-how, because two exemplars share identically the noninvasive algorithm adapted to the Smart Sensor-pairs for the real world persistent surveillance. Currently, the standard diagnoses for malignant tumors and diabetes disorders are blood serum tests, X-ray CAT scan, and biopsy used sometime in the physical checkup by physicians as cohort-average wellness baselines. The loss of the quality of life in making second careers productive may be caused by the missing of timeliness for correct diagnoses and easier treatments, which contributes to the one quarter of human errors generating the lawsuits against physicians and hospitals, which further escalates the insurance cost and wasteful healthcare expenditure. Such a vicious cycle should be entirely eliminated by building an “individual diagnostic aids (IDA),” similar to the trend of personalized drug, developed from daily noninvasive intelligent databases of the “wellness baseline profiling (WBP)”. Since our physiology state undulates diurnally, the Nyquist anti-aliasing theory dictates a minimum twice-a-day sampling of the WBP for the IDA, which must be made affordable by means of noninvasive, unsupervised and unbiased methodology at the convenience of homes. Thus, a pair of military infrared (IR) spectral cameras has been demonstrated for the noninvasive spectrogram ratio test of the spontaneously emitted thermal radiation from a normal human body at 37°C temperature. This invisible self-emission spreads from 3 microns to 12 microns of the radiation wavelengths. This pair of cameras are used in the military satellite surveillance imaging operated at 3~5 mid IR band and 8~12 long IR band accompanied by several other UV and visible bands cameras. We can thereby measure accurately both the thermal emission bands at the mid IR and the long IR (X_1 X_2). The spectral ratio will be independent of the depth and imaging environment. Similarly, we will take six times per pair saliva samples (X_1 X_2) inside the upper jaw for three meals daily, of which the dynamics is shown as a delayed mirror image of “blood glucose level”. And for which we must design a portable lab “system on chip (SOC),” and the micro-fluidity of pair channels per chemical reactions. According to the same biochemical principle of spontaneity, we apply the identical algorithm to determine both the ratio of hidden malignant and benign heat sources (s_1 , s_2) and the blood glucose & other sources (s_1 , s_2) leaking into the saliva. This is possible because of the Gibbs isothermal spontaneous process, in which the Helmholtz free energy must be minimized for the spontaneous thermal radiation from unknown mixing of malign and benign sources or the diffusion mixing of glucose s_1^* and other sources s_2^* . We have derived a general formula relating two equilibrium values, before and after, in order to design our devices. Daily tracking the spectrogram ratio and saliva glucose levels are, nevertheless, needed for a reliable prediction of individual malignant angiogenesis and blood glucose level in real time.

Keywords: Diabetes, Blood Glucose Level, Saliva Glucose Level, Angiogenesis, Malign Tumor Detection, Point of Care, Blind Sources Separation, Free Energy, Unsupervised Learning.

1. WELLNESS BASELINE PROFILE EXAMPLARS

Why do we explore, despite of available hospitals paid by the insurance, those military high-tech instruments and clinical know-how for homecare? When we visit hospitals, we are either seriously ill or other is or we are taking annul physical check. We know we become what we eat, we need daily exercise, and both our minds and bodies related intimately to our wellness. Yet, we are less familiar with the Nyquist aliasing fact of tracking diurnal physiology change requires a minimum of twice per day sampling rate of our vital signs to help determine the complex transition from multiple healthy states to binary sickness, of which only the final consequence is familiar when it happens, but not before it does. Usually for ourselves we are often too late than early for we have nothing to help us, other than those pre-moon landing antiquity tools available at households to help maintaining a better quality of retirement life. We need developing new affordable homeowner security surveillance system, which can not only save the escalating healthcare expenditure and avoid those unnecessary litigation wastes against physicians, hospitals and health agencies [1]. To minimize human errors, we need to practice “a stitch in time saves nine” by applying advanced defense surveillance methodology against home-front infectious microorganism, where the wellness is deteriorating and the disease occurring. We need affordable and convenient household devices for protecting one of the most insidious diseases---malign tumors and diabetics, among cardiovascular, and dementia disorders attacking one-quarter of aging population of US alone. When compared to a yearly baseline physical checkup alone, this military smart sensor web can measure by noninvasive means the wellness baseline profile (WBP) for individual diagnostic aids (IDA), which promises the timeliness in early diagnosis with much less human errors.

The anatomic architecture of human brains and endocrine glands define the physiology enzymatic constraints of macroscopic variables. The central nervous system (CNS) and endocrine glands may be found in EU Neuroscience Site and Am. Acad. Otolaryngology for ENT MD. We shall refrain from complex CNS anatomy, rather call out the simpler salivary glands the parotid, submandibular, and sublingual glands depicted in Fig. 1 (lower part of endocrine thyroidal, pancreatic, kidney's and etc. are not shown). Since our report for diabetes follows the same thesis of translating military know-how of the power of pair sensors for invariant feature extraction by the same underlying unsupervised learning principle, we will further explain the details as follows:

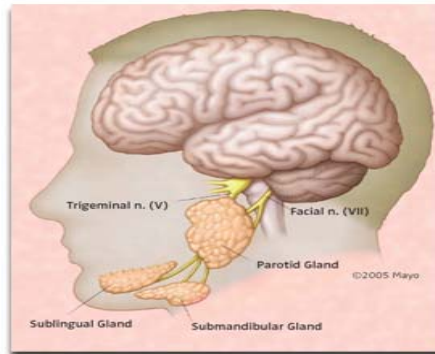


Fig. 1 Anatomy of CNS and ENT Saliva glands

To demonstrate such feasibility of the translation of military real world know-how, we focus on two exemplars for a noninvasive surveillance: early breast tumors detection and diabetic glucose level profile. The lesson learned reported in this paper may be useful for other common syndromes for aging population such as Alzheimer dementia and cardiovascular disorders. We have demonstrated early warning automatic target recognition (ATR) capability by using two infrared spectral bands satellite cameras tracking woman soldiers' breast tumors over the time that is several months ahead of the confirmation by X-ray mammograms [2].

Historically, a single infrared imaging using spectral-integrated CCD camera for temperature map was called the thermograms (as opposed to our ratio of spectrograms), which was unfortunately disapproved by

physicians. This denial for quantitative analyses is because of the procedure of measuring temperature map suffering too many variables giving different answers to an identical patient by taking two snapshots at two different times (one at the moment of disrobe, the other minutes later after hands being cooled down by ice water whereas malign tumor persist hot temperature). This new military approach should be sharply in contrast to that of single night-vision camera. The night-vision camera, of which its CCD sensory material can spectrally integrated over the full infrared spectrum, has enough SNR without the need of cumbersome liquid Nitrogen cryogenic cooling of imaging plan. On the other hand, such a CCD camera can only produce a local temperature distribution of breasts, or faces, before and after artificial cooling of the subject, known as the infrared “thermograms” plagued with both heat source depth variation and environmental uncertainty. Perhaps, this inadequacy experience was not unlike those passive SARS test by one-time and one-infrared-camera at the airport where the suspects took the Aspirin suppressing SARS fever and passed the quarantine checkpoints.

The most important of all is that our spectrogram ratio is invariant towards variable attenuations due to different breast tissues, sizes and imaging environments whose effects are cancelled naturally by the division for computing the ratio. Although both spectral components suffer individually a similar attenuation factor at arbitrary depth of malign tumors (or in the propagation through an identical turbulent atmospheric) and the same condition of imaging environment, the spectral ratio of the same hot tumor source, a tank engine, or military supply lines can cancel out the same attenuation factor, and becomes invariant to both the depth of malign tumor hot sources and the imaging environmental variation. Thus, new noninvasive IR spectral ratio over time provides credible warning signs at a much earlier stage than the invasive X-ray mammogram at the metastasis stage. It is at the Angiogenesis stage (Greek: vessel generate) promoted by the Vascular Endothelial Growth Factor (VEGF) protein generating inflammation and new capillary vessels, before the tumor extravasations and metastasis stages (behaving not unlike military buildup of supply-line before war declaration which is likewise detectable passively by multispectral satellite images).

In our patent [2] we have computed the percentage of malign versus benign tumor cells per pixel. Given only two infrared spectral data (x_1 , x_2) per pixel (x_1 at 3~5 micron wavelength and x_2 at 8~12 micron wavelength), we can predict the spontaneous thermal radiation from hot infrared sources (s_1 , s_2) (s_1 stands for the number of malign tumor cells at local inflammation elevated temperature localized at a specific depth, where s_2 for the number of normal body cells or benign tumor at the healthy temperature), without knowing individual breast tissue medium impulse response matrix [A] mixing those infrared heat sources (s_1 , s_2). The missing conditions causing an ill-posed matrix inversion are identified correctly to be the Gibb's biochemistry spontaneity principle of minimization of isothermal Helmholtz free energy. Since Gibb's principle of spontaneity will be also useful for us to estimate a saliva glucose source and the other non-glucose source in Sect.2, we explain the passive spectrograms imaging for the early screening of malign tumors. The gold standard diagnosis of well-developed breast cancers remains to be the X-ray mammograms and in situ biopsies, which has helped to discover 250 thousands women and 2 thousands men annually in US alone, and documented the trend of breast cancer risk due to modern child less syndrome [3]. According to Sweden epidemiology studies over last few decades, women with breast cancers whether taking the mammograms or not, their average life expectancy is the same about five years [4]. In other words, the discovery of breast cancers happens at the final metastasis stage too late and too dangerous in a region filled with lymph nodes for spreading. The metastasis left behind micro-calcification deposits due to the apoptosis of cells, which could not keep up the rapid growth rate. These calcium deposits became opaque to the X-ray mammogram imaging and showed a dark morphology recognizable to the oncology radiologists. There are several stages of cancers. They are the primary tumors stage; invasion blood vessel stage; blood intra-vasation stage Fig.2; extravasations transport stage; and the metastasis stage.



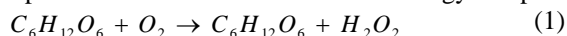
Fig. 2 Transition of military persistent surveillance to the wellness of woman soldiers for breast cancer warning at early angiogenesis stage by tracking the dual color infrared spectral ratio per pixels.

Although the diagnoses by means of two infrared spectrograms ratio over time are nonspecific, they provide noninvasive and convenient warning sign for households. This important invariant feature is derived from the signal and noise ratio (SNR) pre-conditioning allowing the blind sources separation (BSS) by the power of two cameras. While Phase II Receiver Operation Characteristics efficacy studies is going on according to FDA standard of double-blind with independent control and referee system, another hardware team works for affordable ODM/OEM of dual IR-spectral camera [5]. For affordability about \$1K, we merge two cameras into one camera. We adopt one compound lens following the main optical beam interrupted by a beam splitter which focuses the Mid IR portion of the incoming light towards a mini-cryogenic Mid IR image plan located below the main camera and is orthogonally to the main beam where the CCD night vision digital camera locates. In this report for diabetes, we translate military know-how of the power of pairs and the same underlying unsupervised learning, but a new teaming following Sony lesson of “parallel market design of sequential product line.” We choose the semiconductor ODM/OEM Taiwan and the policy-center, Washington DC, responsible for one-fifth GDP expenditure for the healthcare of 78 millions aging baby boomers.

2. SALIVA

The parotid through tubes that drain saliva, called salivary ducts, near our upper teeth, submandibular under our tongue, and the sublingual through many ducts in the floor of our mouth, and they all secrete saliva into our mouth. Besides these glands, there are many tiny glands called minor salivary glands located in our lips, inner cheek area (buccal mucosa), and extensively in other linings of our mouth and throat. Salivary glands produce the saliva used to moisten our mouth, initiate digestion, and help protect our teeth from decay. As a good health measure, it is important to drink lots of liquids daily. Dehydration is a risk factor for salivary gland disease. Obstruction to the flow of saliva most commonly occurs in the parotid and submandibular glands, usually because stones have formed. A dental x-rays may show where the calcified stones are located. The most common salivary gland infection in children is mumps (not caused by stone constriction) which involves the infectious parotid glands. In fact, many of these lymph nodes are actually located on, within, and deep in the substance of the parotid gland or near the submandibular glands. Thus, saliva is rich with IGG. Diabetes may cause enlargement of the salivary glands, especially the parotid glands. Alcoholics may have salivary gland swelling, usually on both sides. Saliva digests starch or other carbohydrate through glycerin into single monomer e.g, glucose etc easily entering intestine blood stream.

Then, the pancreatic insulin endocrine helps it enter into living cells where an oxygenated denaturalization of glucose can produce 4.3 calories of stored free energy and peroxide Eq.(1).



Equation (1) is the main chemistry reaction for the measurement of glucose by measuring the electrical charge property of the peroxide [9,10]. Optical florescence spectrum has been also used [10] for molecular tagged imaging for real time hospital kidney dialyses.

We now digress to introduce pancreas insulin and blood sugar glucose. Insulin is a long peptide chain secreted naturally by β -islets of pancreas Schwamm cell, artificially synthesized by Nobel Laureate Bruce Merrifield of Rockefeller (attached one end of peptide to a solid suspension and efficiently work on the other side chain as invented independently by a Shanghai biologist published in Chinese journal). Insulin can unlock gateways of our body's cells and help blood sugar penetrate cell membrane as energy to perform daily activities. The blood sugar is the simplest digested carbohydrate: $C_6H_{12}O_6$, as if 6 carbons C were merged with 6 waters H_2O . However, the glucose needs to store more free energy than fat and protein in 3D morphology. Unlike 6-carbon forming a flat hexagon benzene ring, the glucose has only 5 carbons, pluses 1 oxygen displacing the sixth carbon into a zigzag backbone plane in either 3 segments over the plane like a chair formation, or 2 segments like a bow-tie symmetry. All 6 carbons, including the displaced one, are further connecting to the hydrophilic hydroxide OH, which to taste sweet must be attached along the z-axis perpendicular to the backbone (otherwise along the x-y orbital plane is not sweet glucose). Evolutionally over billion years, the oxygen entering cellular metabolism provides large free energy storage, much more metabolic reactions and rich variety of trans-membrane communications for Cambrian

explosion era circa 543 MY of eukaryotic complex cellular organisms [Nature V. 455, p. 35, 2007; p.47, 2007]. Now, we return to define 3 types of diabetic disorders. In type 1 diabetes, the insulin deficiency is due to pancreatic lymph nodes, mediated by the death of pancreatic β cells, produce immunological T-cells targeting Peri-islet Schwann cell, called the “autoimmunity.” The pancreatic sensory neurons have defective capsaicin TRPV1 (Transient Receptor Potential Vanilloid-1) receptors of insulin causing pancreas islet inflammation, due to imbalance of neuron response of neuro-peptide substance p & insulin [6]. Type 2 diabetes is caused by “insulin resistance,” namely our body does not use insulin properly. As a result, glucose entry into cells is impaired as if the cells were insulin-resistive. A hybrid of “autoimmunity” and “insulin resistance” is called diabetes type 1-1/2. Recently, NICHD explored the Saliva IGG for the accurate timing for the effectively administrating the second booster shot for the vaccination of new born infant in Vietnam with their patented conjugated vaccines. Pasteur Institute of France with the inscription motto: “chances favors a prepared mind” has discovered from the saliva a new substance called Opiorphine which is about 3~6 times stronger than morphine and easily metabolized over time.

A non-invasive prototype device, monitoring the blood glucose levels, will be implemented according to the indirect measurements of pair of saliva glucose levels using the micro-fluidity-intake dual channels with a system on chip computation as a pocket lab on chips. Twenty millions’ diabetes exists in US alone, of which one out of three does not even know that they have the disease until damage is done. Diabetic symptoms are frequent urination, increase fatigue, excess thirty, irritability, extreme hunger, blurry vision, and unusual weight loss, compared to ones own past data presumably in a healthy initial state. Those seniors who are not obese and those who have weight challenge have different risk of diabetes, but increased with deteriorate physique. The excessive blood sugar, glucose, helps lipids and fatty cholesterol streaks enter the artery lining forming plagues (called atherosclerosis, due to excessive triglyceride converted from glucose by liver). The plague in veins and arteries can severely reduce blood flow, and diminish the nutrient and the oxygen supply (attached to the red blood cell via iron of hemoglobin) to the vital organs, the brain and the heart, resulting respectively in stroke and heart attack. While blood test-kits and pressure guns for insulin injection are available, the stress of intrusive measurement and the inconvenience with potential contamination are not so desirable on daily basis for both junior diabetes and aging baby boomers. In this paper, we design a noninvasive pocket saliva test kit for minutia saliva intakes, based on our exact equilibrium solution of a time-averaged model of spontaneous biochemistry diffusion of glucose substance from excessive “blood glucose level (BGL)” seeping through saliva glands mechanism. Such a dynamics profile “saliva glucose level (SGL)” is delayed and much reduced in the magnitude about few percentages. If we could measure for each individual both dynamics in a time-average sense about 30 minutes, we might deduce a correct prediction formula for the peak quantity of BGL and the time for the individual and thus reduce the unwanted frequency of real-time blood tests. This prediction aspect will report in the future studies after we finish and can apply the SOC prototype model I. We will concentrate on the development of an analytical modeling for the purpose of designing dual intake channels SOC, together with some numerical values obtained from few hospital sick patients.

However, such a hope between the correlation between “saliva and diabetics” has a mixed opinion in the last four decades, according to the archival 78 articles of NIH/National Library of Medicine. Braun et al. of Hungarian reported the first observation in 1966; Mehrotra et al. of Indian reported in 1968 of a village of diabetic seniors having serious periodontal disease. Recently in 2006, Siudikiene et al. of Lithuania studied diabetes-type 1 inferring from saliva [6,7]. Carda et al. of Espana investigated diabetes-type 2 using saliva [8]. Recent works [9] revealed large individual variation between blood and saliva glucose levels (BGL & SGL), the universal correlation between BGL and SGL has not yet been fully established [10]. We notice that most of the correlation experiments were based only on the second order statistics of selected sparse sampling, e.g. during the office hours after fasting the night before. Although the saliva kit is less accurate per se than blood tests in general; the unsupervised blind sources separation (BSS) of pair saliva sampling might produce invariant features, which over time development might relate better with arbitrary delay to those permeable blood constituents through the gland-blood barrier membrane.

3. UNSUPERVISED ALGORITHM FOR HOMEOSTASIS RESOURCE SHARING

Microscopic molecular kinetics model is currently beyond our ability to understand how exactly the unknown sources $S = (s_1, s_2) = (s_{\text{malign}}, s_{\text{benign}}) = (s_{\text{glucose}}, s_{\text{other}})$ are diffusively emissive and permeate matrix

[A?] through breast tissue and saliva glands ducts respectively. Currently, advanced in vivo studies with molecular-tagged imaging may illuminate the complete pictures of underlying signaling pathways and molecular mechanisms for physiological modeling and treatments. In this treaty, we concentrate on the equilibrium biochemistry principle to develop macroscopic model.

Following the Gibb's spontaneity principle governing biochemistry processing, we introduce a resource sharing homeostatic learning theory deriving the unsupervised learning Hebb rule and sigmoid logic for effortless sensory processing since 1999[14-16]. Accordingly, the (isothermal) Helmholtz free energy defined in thermodynamics as $H = E - T_o S$, where E is information processing synaptic energy and T_o is the local temperature of the brain at an averaged value 37°C for most healthy humans; and Shannon-Boltzmann-Clausius Entropy is $S = -s_I \log s_I - (1-s_I) \log (1-s_I)$ for two normalized component sources. Several interesting remarks are in order:

(i) Why do intelligent animals involve pair inputs and isothermal brains?

(a) Fact 1: constant temperature of their brains per species (37°C for humans; 40°C for chicken) and

(b) Fact 2: paired input sensory organs (e.g. binaural hearing, binary vision, zonal tasting, & tactile, etc) while in contrast the output sensory organ is always singular (e.g. one mouth to speak, one exit going for bathroom, etc.). An efficient fusion must happen at the points of correspondence of two sensors, based on the Gibb's principle of the aforementioned minimization of the isothermal Helmholtz free energy H . This is called the power of pairs: "agreement, the signal; disagreement, the noise" requiring no delay of outside teacher supervision. Imagine the clarity power would be if adopted for coincidence-accounted binaural hearing aids. In order to save the processor energy, H must be vanishingly small for any isothermal spontaneous processing.

(ii) About the conscience of all hot blooded animals. Nobel Laureate Francis Crick has led a frontier research for decades with the help of Dr. Cristof Koch at Neuroscience of Salt Institute who seek for the anatomical structure supporting the consciousness. In the last publication [Philos. Trans. Royal Soc. of London, 2005], he stated that the architecture must infer the functionality and vice versa. Koch and he had tentatively identified the consciousness architecture is a thin sheet of grey matter resides in parallel two way connections to and below the cortex computing feelings, seeing, hearing, language and decide what to do, known as the "Clastrum, the conductor of an orchestra binding all".

In early theory they measured an ubiquitous firing rates binding at 30Hz as the wakening of consciousness. Our free energy theory might estimate a bound on the size of neurons involved in the Clastrum. In other words, such a spontaneous firing rate must be satisfied a minimum isothermal free energy. The firing rate involves the phase transition from the un-consciousness randomness to the consciousness ground state. Gibbs theory of the biochemical spontaneity support the Crick-Koch ubiquitous firing rates, for which the minimum Helmholtz free energy associated at the 37°C Celsius temperature, should effortlessly support all neurons. Owing to the linearity of the Einstein-Boltzmann energy formula the uncertainty of our brain size can be estimated

$$E = Nhf = K_B T_o,$$

ranging between 20 billions and 10 billions neurons corresponding to the range between 30Hz and 60 Hz firing rates respectively for the ground state of mindlessness for which it must be less than the consciousness decision at a synaptic junction as measured experimentally by Nobel Laureates Hodgkin and Huxley about 100Hz firing rates. The computation follows from a physics units table issued by NIST as follows:

$$\begin{aligned}
E &= N hf = N \times 6.67 \times 10^{-34} \text{ Joule} \cdot \text{sec} \times 30 \text{ sec}^{-1} = N \times 200.1 \times 10^{-34} \text{ Joule} \\
&= K_B T_o = K_B (273 + 37) = 310 \times 1.38 \times 10^{-23} \text{ J} = 427.8 \times 10^{-23} \text{ Joule} \\
\text{Thus, the number of neurons of a human brain is } N &\cong 2 \times 10^{11} \text{ about 2 times 10 billions} \\
\text{The body thermal energy} &= \frac{310}{300} \left(\frac{1}{40} \text{ eV} \right) = 0.025825 \text{ eV} = 2.6 \% \text{ eV} \\
\text{which emits a Planck spectrum peaked at the long IR at } \lambda &\cong 8 \sim 12 \text{ micron} \\
\text{where the Planck } h &= 6.67 \times 10^{-34} \text{ J} \cdot \text{sec} = 6.67 \times 10^{-34} \text{ J} \cdot \text{sec} \frac{1 \text{ eV}}{1.6 \times 10^{-19} \text{ J}} = 4.17 \times 10^{-15} \text{ eV} \cdot \text{sec} \\
\text{Boltzmann } K_B &= 1.38 \times 10^{-23} \text{ J} \cdot \text{K}^{-1} = 1.38 \times 10^{-23} \text{ J} \cdot \text{K}^{-1} \frac{1 \text{ eV}}{1.6 \times 10^{-19} \text{ J}} = 0.86 \times 10^{-4} \text{ eV} \cdot \text{K}^{-1} \leq 0.01 \% \text{ eV} \cdot \text{K}^{-1}
\end{aligned}$$

In summary, if we take seriously Crick and Koch model of ubiquitous binding of firing rates for the wakening of consciousness, we can estimate our brain beginning at the binding of 30Hz firing rates which might effortlessly support up to all 20 billions' neurons per an isothermal brains kept at 37°C.

(iii) We assert that the sharing of (neural transmitting) resources at isothermal equilibrium value may be responsible for Gibb's phenomena and lateral inhibition at ganglion neurons level (for computational proof, see Frank McFadden & Szu [17]). The Gibb's overshooting & undershooting phenomena could be understood as resource sharing at the isothermal equilibrium. In other words, a limited constant resource of neuro-transmitting must be shared by neighborhood neurons. For example, a ideal step-function light illumination is shown in Figure 3 a), in which (beneath layers of 150 millions of rods & 6.2 millions of cons) the sensory bipolar and ganglion neurons on the bright side at a light-dark edge boundary can utilize locally shared resources that are underutilized by the neurons on the dark side; therefore, they are relatively overexcited compared with other neurons on the bright side. This over-utilization of un-used resource by dark side neurons, in turn, leads to depletion of resources in the isothermal equilibrium available to the neurons on the dark side near the boundary. A similar phenomenon occurs with a rectangular light illumination in Fig 3 b) with the phenomena of lateral inhibition (as seen in the Mexican hat shaped response curve at the ganglion level) –over-utilization of local resources by neurons closer to the peak depletes resources that would otherwise be available to nearby neurons. Fig. 3c shows the limited resource due to the isothermal free energy minimization.

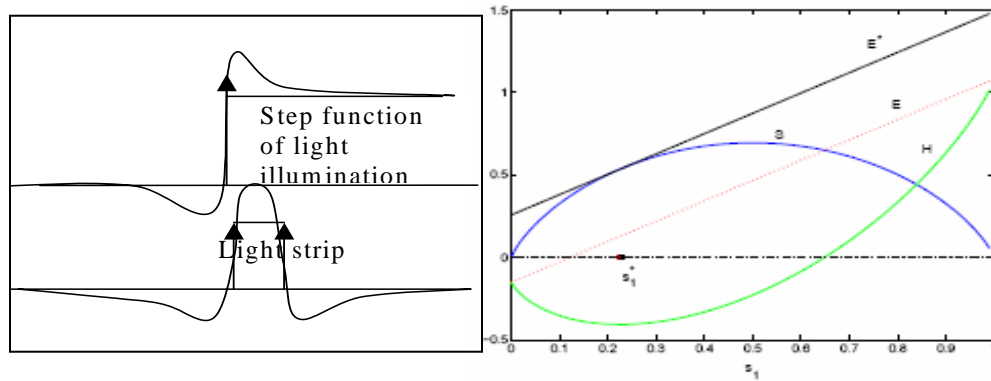


Figure 3. Over-utilization of shared resources among neurons of those light-stimulated receptors in the neighborhood of non-stimulated receptors responsible for the a) Gibb's overshooting & undershooting; in case of a lighted stripe we obtain by the symmetry of two opposite step functions b) Lateral inhibition in the Mexican hat shape, and c) Gibbs spontaneity principle for effortless fusion of early vision mediated by local sharing of neuro-transmission resources: namely the equilibrium predicted by Szu³⁶ occurs at s_1^* , where minimum isothermal free energy H is minimized. [17]

A difficulty of this explanation in terms of equilibrium model is associated with the long replenish time needed neuro-transmitting vesicle substance associated slow thermal diffusion process. However, this phenomenon is overcome by eyeballs jittering with different focal points, called saccades at hundred Hertz frequency, in order to rapidly utilize those under-used neighborhood receptors and firing neurons, so long that internally the brain keeps track of eye motion with respect to the inertial frame (as the neural circuitry to accomplish this detail balance reported in Nature 2007). As a result, we stabilize the jittering and mosaic images (Hsu et al. on UAV videos, loc. Cit.).

(iv) Szu assumed further that E is analytic in the input sensory pair vector X and the output feature vector S , such that a piecewise linear model is $X \cong [A]S$ where matrix $[A]$ is an unknown impulse response matrix. The information fusion energy can be analytically expanded near the unexcited equilibrium state E_o as Taylor series $E = E_o + \text{linear} + \text{higher order terms}$. In fact, the Hebbian learning rule for unsupervised learning of data X_j drops out from the analyticity of information fusion energy

$$E = E_o + \mu ([W]X - S) + \text{second order} \quad (2a)$$

$$\frac{\partial W_{ij}}{\partial t} = -\frac{\partial H}{\partial W_{ij}} \Rightarrow \Delta W_{ij} \approx \mu_i X_j \quad \text{Unsupervised Hebb learning rule} \quad (2b)$$

The sigmoid logic follows from rigorously from the minimization of free energy [15,16] yields the components of feature vector S .

$$\frac{\partial H}{\partial s_i} = 0 \Rightarrow \sigma(\mu_i) = s_i \quad \text{McCullough \& Pitts neuronal sigmoid logic rule} \quad (2c)$$

This basic theorem has established biological observations by Hebb, for synaptic efficacy Eq.(2a), McCullough and Pitts neuron threshold logic Eq.(2b) from the Gibbs principle of biochemistry—spontaneity according to which the isothermal free energy Eq(4a) must be at the minimum. An exact solution for simple two component case is recently derived by Szu, Miao and Qi [11] as $s^*_i = 1 - \exp(-E_o/K_B T_o)$.

(v) We remark on the biomedical relevance of the biological natural intelligence (NI) model as follows: Szu conjectured (in his space-variant breast tumor research by means of a single-pixel blind source separation (BSS) [1,11,15,16] that the Lagrange multiplier vector μ must be measured in the units of Amperes (of which a single ion contributing to dendrite ion current has been measured in pico-Amperes first by Nobel Laureates Neher and Zsigmond) behaving like a house-keeping glial cells. This is because of its physics unit nature of Lagrange multiplier with the synaptic weight $[W]$ in Volts (of which a millivoltage was measured first by Nobel Laureates Hodgkin and Huxley). Thus, we can obtain the internal energy E at homeostasis temperature T_o .

4. APPLICATION TO SOLVE ILL-POSED INVERSE SOURCE PROBLEM

We follow the minimum thermodynamic free energy methodology introduced first by Gibbs and recently for passive breast two color infrared spectrum imaging by Szu [1,11,16,17] for earliest tumor detection at a single pixel in question. Szu took two (3~5 μ , & 8~12 μ) infrared (IR) spectrum measurements $X = (x_{\text{long IR}}, x_{\text{mid IR}})$ per pixel [1]. Likewise, in saliva case, sources are glucose and other none-glucose at one sample point after meal together few neighborhood distant time points pre-meal as individual baseline. Given single-time-point two components' vector measurements of the saliva quantity for left and right upper jaws (taken after brush cleaning etc. standardization only for establish correlation with blood test, not needed for household practice):

$$X = (x_{\text{left}}, x_{\text{right}})^T \quad (3)$$

Where the superscript T denotes the matrix transpose without knowing how the diffusively mixing of the sipping of excessive blood glucose level with other liquids sources $S = (s_1, s_2)^T$ as represented by the mixing matrix $[A]$. We wish to invert the 2x2 matrix $X = [A?] S$ in case of an unknown mixing matrix $[A]$. This is called Blind Sources Separation (BSS). We develop a unique single-time-point BSS formula for senior saliva test kit. All other direct measurements, based on glucose chemical reaction Eq.(1), must be bounded by two equilibrium values pre-meal and after-meal to be given in the following:

The first *principle of biochemistry* is the "*spontaneity*" principle, according to which the thermodynamic isothermal free energy of cellular reaction process---namely the glucose leakage through blood-gland membrane into saliva for isothermal diffusion at mouth temperature $T_o = 37^\circ\text{C}$. According to the biochemical minimum free energy principle of the spontaneity, the isothermal free energy Helmholtz is reduced to zero for an equilibrium spontaneous diffusion of the glucose through the saliva glands at the fixed point s^*_i where all slopes vanish.

H(isothermal free energy) = (diffusion energy)E - (mouth temperature)T_o (Shannon entropy)S

$$H \equiv E - T_o S; \quad (4a,b,c)$$

$$H = 0;$$

$$\frac{dH}{ds_1} = 0$$

We define a time-integrated average results of saliva vector \mathbf{X} , mixing impulses response matrix $[\mathbf{A}]$, and glucose & other sources vector \mathbf{S} in terms of slow macroscopic time scales minutes t , while the fast time scale of dynamics is denoted by the time-integrated microscopic variable τ .

$$\mathbf{X}(t) = \frac{1}{t} \int_{\tau_o}^{\tau_o+t} d\tau \mathbf{X}(\tau) \quad (4d)$$

After the time average, we assume a linear model valid usually in the averaged limit of weak signals. Then, a single macroscopic time point data model is:

$$\mathbf{X}(t) = a_o [\mathbf{A}(t)] \mathbf{S}_o(t) \quad (4e)$$

Equation (3) has introduced two independent measurements of saliva quantity vector \mathbf{X} , and we need to invert the unknown saliva-gland-blood-glucose mixing matrix to determine three unknowns (two unit demixing vectors of matrix $[\mathbf{A}]$ and one percentage sources \mathbf{S}), other than a damping scaling factor a_o to be determined by experimental measurement of blood glucose level. Such an ill-posed inverse problem is common in physics inverse problem, which is usually consistently determined by applying the physics conservation and symmetry laws. In our case, we apply the biochemistry spontaneity reaction Gibbs principle Eq(4a-e) of minimum isothermal free energy of Helmholtz, Eqs(4a,b,c). First, we demonstrate that the isothermal free energy for an equilibrium spontaneous diffusion of the glucose through the saliva glands is indeed a linear function of source s_1 and the baseline energy interception E_o is associated with the so-called fasting saliva level. The diffusion energy E must be macroscopically determined [4] within measurement accuracy as an analytic, or differentiable, function of input and output data

$$E = E_o + \sum_{i=1,2} \frac{\partial E}{\partial s_i^{(o)}} (s_i - s_i^{(o)}) = E_o + \sum_{i=1,2} \mu_i \left(\sum_{j=1,2} [W_{ij}] X_j - S_i \right) \quad (5)$$

where μ_i is called Lagrange vector parameter to be consistently determined by unsupervised learning of Artificial Neural Network (ANN)[1,4]. While the entropy is a concave function as illustrated in Fig. 1, it peaks at 50-50% minimum information. The informative diffusion energy E is linear. Free energy diagram in it the simple complex curve is the entropy, and internal energy is a linear line their intersection defines the Helmholtz isothermal free energy

$$E = E_o + [\mu_1 \ \mu_2] \begin{bmatrix} (W_1^T, X) - s_1 \\ (W_2^T, X) - s_2 \end{bmatrix} = E_o + \mu_1 (W_1^T, X) + \mu_2 (W_2^T, X) - \mu_2 + (\mu_2 - \mu_1) s_1 \quad (6)$$

Secondly, we derive the linear energy expression, according to the biochemical principle of spontaneity, i.e. the minimum Helmholtz free energy Eq(4a) summarized in the following theorem.

Theorem 1 Minimum Helmholtz free Energy determines a linear & stationary function of saliva glucose level of saliva measurements: *Given isothermal equilibrium system at the minimum Helmholtz free energy defined by Eqs.(4,5), the departure from an individual baseline level satisfies a canonical ensemble average behavior, in terms of analytic input & output data \mathbf{X} and \mathbf{S} . Then, the departure of the baseline according to minimum thermodynamics free energy one obtains*

$$s_{\text{glucose}}(t_+) = 1 - \exp(-E_o^*(t_-)/K_B T_o) \quad (7)$$

Proof:

In order to determine the correct zero-order formulation for the baseline E_o , one need to derive the relationship between the true solution E_o^* (indicated by the superscript *) and the true unknown source s^*_1 . Shannon using the unit-sum-rule entropy formulae:

$$S = -s_1 \log s_1 - (1 - s_1) \log (1 - s_1) \quad (8)$$

The first order slope of energy tangent line at each point is obtained by calculating the derivative of the entropy S with respect to s_1

$$\frac{dS}{ds_1} = -\log s_1 - \frac{s_1}{s_1} + \frac{1-s_1}{1-s_1} + \log(1-s_1) = \log(1-s_1) - \log s_1 \quad (9)$$

Since at equilibrium $H=E-T_oS=0$, then $E=T_oS$, and the slope of the energy line equals to the slope of the entropy line. If we know the intercept E_o^* from the immediately previous baseline measurement, the energy line can be uniquely determined

$$E/K_B = \text{slope } s_1 + \text{intercept} = T_o \frac{dS}{ds_1} s_1 + E_o^* = T_o \{\log(1-s_1) - \log s_1\} s_1 + E_o^* / K_B \quad (10)$$

Then, substituting the aforementioned entropy formula S Eq(8) and equaling it to the derived energy E formulae Eq(10) (because Eq(2a) $H=0$ implying $E=T_oS$), we have obtained

$$S = -s_1 \log s_1 - (1-s_1) \log(1-s_1) = \{\log(1-s_1) - \log s_1\} s_1 + E_o^* / K_B T_o = E / K_B T_o \quad (11)$$

which is simplified as follows

$$E_o^* / K_B T_o = -\log(1-s_1^*), \text{ or,} \quad (12)$$

$$s_1^* = 1 - \exp\left(-\frac{E_o^*}{K_B T_o}\right) \quad (13) \quad \text{Q.E.D.}$$

Note that there is a one-to-one mapping between the informative diffusion baseline energy at the immediately previous time point t , say after the fasting saliva test with blood test. We determine the unknown glucose source s_1^* at time t_+ . Moreover, the mapping is exponentially nonlinear as typical solution of the statistical-mechanical canonical ensemble under local mouth temperature T_o . If we can get the true information energy from data, the abundance fraction can be directly according to Canonical ensemble calculated without a learning process. Let $X = (X_1, X_2, X_3, \dots, X_n)$ denote the data within a time neighborhood, where each column vector represents a data point and n is the size of neighborhood. The center pixel is represented by X_c . The informative diffusion energy E_o^* is calculated by the summation of the angles between the center pixel and its neighbors expressed as

$$E_o^* = \sum_{i=1}^n \arccos\left(\frac{X_i^T X_c}{\|X_c\| \|X_i\|}\right) \quad (14)$$

After calculating the baseline E_o^* , the source solution can be tabulated through aforementioned equilibrium solution.

4. HOSPITAL TRAINING DATA GATHERING

The Phase II clinical investigation of noninvasive dual color IR imaging tracking early breast cancer detection has been going on at both Vatican of Rome, and Taiwan National University Hospital [5,11]. We will have results to share in the near future. Meanwhile, we concentrate on the Phase I study of saliva glucose level experiments. The blood droplet data are likewise collected with left and right fingertips capillary blood draw. Different informative diffusion energy is estimated to lead by the Theorem 1 the desired glucose content. We augment our Institute Review Board & Patient Consent Form under Ming-Shen Hospital IRB & PCF led by Physician of Endocrinology and Metabolism, Dr. Chang, who understood a pair of independent saliva measurements, and concurrently another pair of blood droplet measurements. Extraction of both glucose levels shall be processed according to MS hospital protocol in conformity with the experiments of Tokyo Agriculture & Technology University.

We integrate personnel saliva over time through three pairs of micro-fluidity channels front ends for measuring pH, glucose and IGG, respectively, and a smart System on Chip (SOC) back-end. The intelligent part of SOC will be embedded with unsupervised learning Automatic Target Recognition (ATR) algorithm in handling unpredictable environmental variability for hourly noninvasive measurements and unbiased feature extraction of useful personnel baseline profile. Then, a higher order statistics, or ICA,

could extract his feature vectors to compare with temporal field tests for better assurance of authentication. Such an interface philosophy tracks hundreds points temporal heavier to reveal the stable higher order feature statistics (HOS) for better predict the tide of blood glucose level, so that an appropriate quantity of insulin may be administrated at proper lead time for maximum control of physiology. Toward a more timely response of continuously deteriorating aging baby boomers, a yearly baseline check-up is not sufficient and proves often the missing of the timeliness of critical treatment period. Thus, preferably daily checkups at the convenience of home may produce continuous profile of health dynamics in a so-called “baseline profile” trend, which may help medical doctors (MD) conduct hospital check-up with less errors in critical diagnosis judgment call. Therefore, we suggest that an idea situation for early diagnosis should include the first line defense at households (beyond traditional hospitals, insurance agencies, social service and governing body).

1. Two groups of volunteers, one cohort with diabetes and another cohort without it (but may need to stay hospital for different reasons).
2. Carry out their routine daily life at the hospital, so that nurse can take their hourly droplet-blood for lab tests together with lab saliva hourly tests. Every sample should be pairs (e.g. left & right side of fingers, left & right deep inside of mouth).
3. We need enough sample size to measure the Glucose, & the others, e.g. amylase, IGG, etc.
4. One-day 24 hours including fast baseline at early morning wake up before and after a breakfast.
5. Although a commercial saliva test could be used for the soaking sponge at inner gum area, in hospital setup, we can design our own way so long as it is consistent.

The device frequency is to be determined by doctor in the future, but in this training data for our to-be-design device we would like to have over sampling--- for example hourly two blood-droplets (left & right), and half-hour two saliva samples at exact time marked.

Without yet using the test kit, we intend to have your Hospital at Long Tan co-worked on a test bed training data gathering for the necessary benchmark of our pocket test kit.

5. SYSTEM ON CHIP & MICROFLUIDITY

The use of saliva for disease diagnostics and normal health surveillance will bridge the oral health research into systemic diseases through the biofluid that filters and processes itself from the vasculature that nourishes the salivary glands (Fig.1). Due to the recently developed technologies, the barriers to widespread implementation of salivary diagnostics have been largely overcome. Techniques are emerging from a combination of miniaturization technologies and discoveries in many different fields including biology, chemistry, physics, and engineering that are leading to high throughput (the ability to process and analyze a large number of samples in the real time), automated, portable, low cost, compact, more efficient, and rapid biochemical analyses. Miniaturized diagnostic technologies will be able to yield patient information reflecting health and disease status with minute amounts of body fluids. The advent of digital microfluidic MEMS/NEMS (Micro/Nano Electro-Mechanical Systems) technology offers such a detection system due to the advantages in portability, reduction of the volumes of the sample and reagents, faster analysis times, increased automation, low power consumption, compatibility with mass manufacturing, and high throughput. Fig.4.a shows a demonstration of the electrowetting MEMS integrated with optical detection. MEMS/NEMS are integrating systems consisting of mechanical elements, sensors, actuators, and electronics on a common silicon substrate (a substance upon which an enzyme acts) developed through microfabrication technology. These systems use a small sample and a reagent volume (a substance used to produce a chemical reaction, so as to detect, measure, or produce other substances), coupled with integrated detection methods to perform analyses. While the economic outlook seems grim for many sectors, Nanoelectronic technology is thriving. Built with nanotubes and various self-assembling molecular structures, scientists can anticipate a switch from lithographed silicon chips to nanoelectronics. The switch

is attributed to the physical limitations of silicon-based circuits. These constraints will soon be met, so scientists have been searching for other options to conventional silicon electronics. Not without its share of problems, nanotechnology will still profoundly impact the electronics sector.

A new technology named System on a Chip (SoC) will be able to perform multiple operations in parallel in nonlaboratory settings such as the field, factory, hospital clinic, or home. Such technologies will allow the simultaneous assessment of multiple conditions of health and disease and provide clinicians with prevention and therapeutic strategies to meet patient needs. System on Chip (SoC or SOC) is an idea of integrating all components of a computer or other electronic system into a single integrated circuit (chip). It may contain digital, analog, mixed-signal, and often radio-frequency functions – all on one chip. A typical application is in the area of embedded systems. Our SoC design Fig. 4b) provides a compact, cost-effective, low-power, portable, solution, which consists of one microcontroller or DSP; memory blocks including a selection of ROM, RAM, EEPROM and Flash; timing sources including oscillators and phase-locked loops; peripherals including counter-timers; real-time timers and power-on reset generators; external interfaces including industry standards such as USB, FireWire, Ethernet, USART, SPI; analog interfaces including ADCs and DACs; voltage regulators and power management circuits. The bio-sensor IC implemented in another device is connected and digitized through the ADC of our SoC solution, and the detection and diagnosis program can be downloaded via the USB device into the local memory device. This configuration and infrastructure provide the most effective solution. The SoC structure with MEMS/NEMS technology is depicted as follows Fig. 4c):

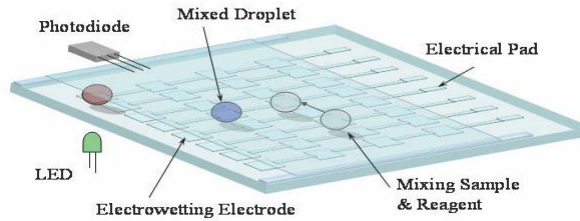


Fig.4.a) The schematic of the electrowetting MEMS integrated with optical detection

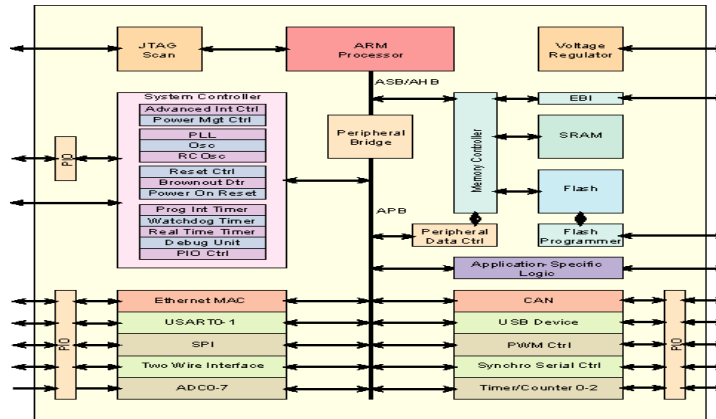


Fig.4.b) Functional Block Diagram of the SoC System.

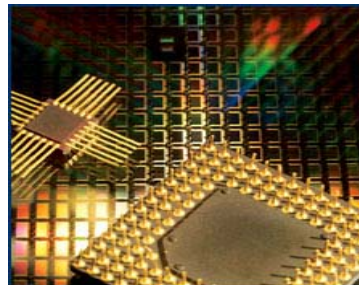


Fig.4.c) An SOC Fabrication Example

Once we have made a prototype model I, we will conduct large scale phase I & IIa studies in order to prove it do no harm, since the controversy remains about the utility of measuring saliva glucose levels. Tokyo team concluded significant differences were observed in individuals between the time-course changes of SGL and BGL. Furthermore, they observed the shape of the flow cell was an important factor in measurement accuracy. The shape of the flow cell (made of acrylic resin) in the saliva analyzing system was designed so that low-level glucose concentrations, in the order of 0.1 mg/dl, could be measured. Since the volume of saliva sample was limited to 200:1, the flow cell volume was set as 147:1, nearly two thirds of the sample volume. The shape of inflow port was designed so that the sample solution could be poured vertically onto the measuring plane of the enzyme sensor. The sensor current was first measured using 200:1 of the sample solution, with flow rate in the range of 0.3 to 0.5 ml/min, the same conditions as used for the saliva sample. Then, the OGIT was carried out on a subject. The time-course changes of BGL and SGL were simultaneously measured with the blood glucose auto-analyzer and the saliva analyzing system, respectively.

- (i) In hardware design, we take geriatrics into account the saliva quantity requiring the micro-fluidity channels, which match well with the micron electrical-mechanical system (MEMS) together with a smart System on Chip (SOC).
- (ii) In software design, we follow the principle of binaural hearing based on the “power of two measurements per time-sampling” useful for signal pre-conditioning: “coincidence, the signal; otherwise, noise”. We can further apply channel equalization with sensible normalization.
- (iii) Our methodology adopt for each individual the unsupervised learning methodology based on single-time multiple-point Blind Sources Separation beyond the second order of statistics.
- (iv) In logistics operation, we accept no universality correlation between blood & saliva, but treat personnel variation individually, and conduct a persistent surveillance individual blood and saliva data gathering for individual “baseline profiles.”
- (v) To commence the design, we took a hospital-lab data acquisition system to gather a few healthy & diabetic adult volunteers with complete BGL and SGL daily dynamics.
- (vi) To benchmark the performance, we conduct large-scale experiments at the Senior Wellness Centers (operated in association with Ming-Shen Hospitals, Howard University Hospital and Senior Wellness Centers of DC) in order to assure the utility in preserving quality of life.

6. TEST & EVALUATION METHODOLOGY

Sweden scientists Annika Borg Andersson, Döwen Birkhed, et. al. (birkhed@odontologi.gu.se, Eur J Oral Sci 1998; 106: 931–937) had found significant correlation after 2 hours after intake for tenth diabetes patients of type 2 & 1, divided into insulin treatment or not, compared with healthy control groups. All the teeth which were sampled were located in upper jaw. Cotton rolls were placed in the *vestibulum* region 13–23 and easy air blow was performed to dry the teeth before sampling. The extract was frozen at –20°C until it was analyzed for glucose. An *enzymatic method* was used (Cat. No 139041, Boehringer Mannheim, Germany) (cf. Secretion of glucose in human parotid. Borg et al., Scand J Dent Res 1988; 96: 551–556.). In Study A, samples Study B. were analyzed using a *hexokinase method* (A colorimetric serum glucose determination using hexokinase and glucose-6-phosphate dehydrogenase. cf. Carroll et al., Biochem Med 1970; 4: 171–180.) and in Study B using the *Exatech system* (Medisense Sverige, Sollentuna, Sweden). Glycosylated hemoglobin (HbA1c) was determined using a *liquid chromatographic assay* (Measurement of hemoglobin A1c by new liquid chromatographic assay: methodology, clinical utility and relation to glucose tolerance evaluated. Jeppsson et al. Clin Chem 1986; 32: 1867–1872).

The concentration of glucose in parotid saliva was measured after glucose/food intake in two separate studies (A and B). In Study A, 10 subjects with impaired glucose tolerance (IGT), 10 subjects with newly diagnosed Type 2 diabetes and 12 healthy controls were included. Study B comprised 15 subjects with Type 1 or Type 2 diabetes on insulin treatment, nine subjects with Type 2 diabetes on treatment with oral antidiabetic drugs and 12 healthy controls. After a 10-h overnight fast, the participants in Study A were given a 75 g oral glucose load, while those in Study B received a standardized breakfast. Citric acid-stimulated parotid saliva was collected up to two hours after the intake. Capillary blood and gingival exudate samples were also taken. On the basis of AUC values (area under the curve over baseline), the glucose concentration in parotid saliva increased significantly in individuals with IGT and Type 2 diabetes

compared with controls in Study A and in diabetic patients on treatment with insulin and oral antidiabetic drugs compared with controls in Study B. No effect by the glucose/food intake on the glucose concentration in gingival exudate could be demonstrated in any of the studies. The correlation coefficient between the AUC values of glucose in saliva and blood, when all three groups were combined, was 0.38 in Study A and 0.52 in Study B. It is concluded that the concentration of glucose in parotid saliva is elevated at least 2 h after glucose/food intake in individuals with both IGT and manifest diabetes mellitus.

Unfortunately, we also mention that Hashemipour et al. (Iran. J.Endocrinol Metab 2001, V.2 ,No.4) found an insignificant relationship between blood and saliva glucose levels in 10 healthy men. This was a cross sectional study. 130 blood and 130 saliva samples were obtained from 10 healthy men 13 times in 5 days. Each day samples were taken in 3 times, fasting, postprandial and evening. Samples were analyzed with glucose oxidase method. Value of blood glucose level ranged from 58mg/dl to 118 mg/dl. Mean of fasting blood glucose level was 84.9 ± 3.13 mg/dl. Value of saliva glucose level ranged from 0.322mg/dl to 4.941 mg/dl. Mean of saliva glucose level was 1.22 ± 0.81 mg/dl. Correlation coefficient between BGC and SGL from the 5 days of measurement was 0.23. Correlation coefficient for each day was 0.38 (first day), 0.21 (second day), 0.01 (third day) 0.37 (fourth day). Correlation coefficient for each person was 0.31 (case A), 0.07 (case B), 0.07 (case C), 0.07 (case D), 0.45 (case E), 0.10 (case F), -0.05 (case E), 0.32 (case H), 0.87 (case I), 0.87 (case J). Unfortunately, considering the values of correlation coefficients and the limited range of SGL, we cannot use saliva for detecting BGL.

Experiments led by Masaki Yamaguchi et al. Fig. 5 of Tokyo Agriculture & technology University in 1998 [9] took six young adults of ages 24 ± 4.6 with fast BGL at 93.1 ± 7.9 mg/dl to produce second order statistics as follows. Alternatively to photometric methods, biological screening using body fluids that are obtained non-invasively, such as urine, sweat, lacrima, etc., have long been considered. K. S. Arai et al. of Japan 1991 [11] have attempted to establish a non-invasive saliva enzyme method for measurement of BGL. Their study consisted of administration of the 75 g oral glucose tolerance test (OGTT) to determine the time-course changes in BGL and SGL. In addition, a new system for saliva analysis using an enzyme sensor was developed. The measurement transducer used was an enzyme Amperometric glucose sensor (7820L, DKK Co., Tokyo), with electrodes of silver (anode) and gold (cathode), and a potassium chloride electrolyte solution. The voltage applied across the electrodes was 0.7 volts. The electrodes were covered with a Teflon membrane, over which an immobilized enzyme membrane was placed. As a test solution, a phosphate-buffer (pH 7.3) with temperature held at 37°C was passed through the flow cell by a rotary pump (U4-XV, ALITEA, Sweden). The enzyme sensor generated a current that was proportional to the concentration of dissolved oxygen in the buffer. Using a micro-syringe, a sample solution was then injected, and the following reaction took place at the enzyme sensor.

The concentration of dissolved oxygen to reach the sensor is reduced as the above reaction progresses, resulting in a decrease in the output current from the sensor. When the amount of oxygen consumed on the enzyme membrane equilibrates with the amount released from the sensor, a constant current is generated. The magnitude of this current is proportional to the glucose concentration of the sample solution. This current was detected by an ion meter (IOL-50, DKK Co., Tokyo). SGL was determined by the enzymatic Glucose CII-Testwako, GOD-POD method (Wako Pure Chemical Industries, Ltd., Tokyo). Three ml of the enzymatic reagent was added to 200 μ l of saliva and incubated at 37°C for 5 mins after mixing. The optical density (OD) at 505 nm was measured with a spectrophotometer (U-2000A, Hitachi Ltd., Tokyo).

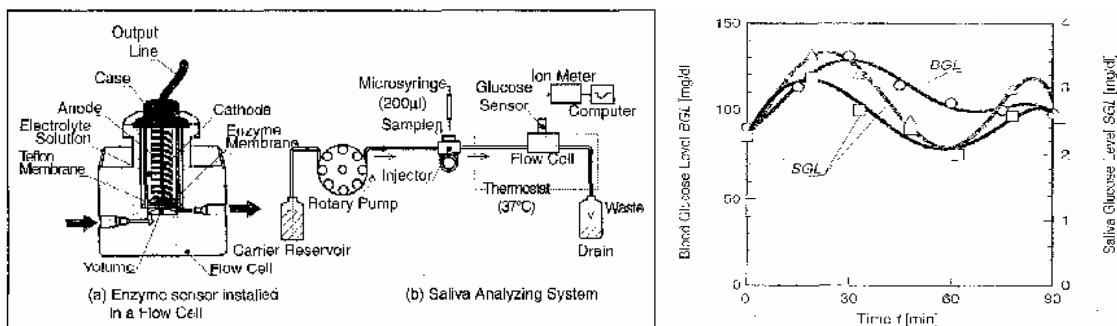


Fig. 5 Cross-section of enzyme sensor installed in a flow cell (a), and schematic diagram of a flow-injection-type saliva analyzing system (b). (c) Results of oral glucose tolerance test (OGTT) in normal subjects using the saliva analyzing system. (O: BGL, U: SGL measured by saliva analyzing system, Δ : SGL Measured by spectrophotometer (Courtesy of [9])

7. CONCLUSION

We have assumed that the saliva glands in the mouth jaw produce saliva samples (X_1 X_2) through a linearly, instantaneous, and time-independent mixing of pre-gland glucose s_1^* with other liquid s_2^* during the slow time scale of minute sampling. In this paper, we have proved a macroscopic permeable equilibrium theorem to determine the inverse sources by a single-time Blind Sources Separation (BSS). In reality, this might be only the zero-th order equilibrium approximation of a general time-dependent nonlinear convolution-mixing problem. Our equilibrium solution could be considered as a useful time average over minute's saliva sampling. It could serve as the first term for perturbation correction terms, e.g. a time-dependent linear convolution equation solved by Fourier transforms methodology. In other words, we have theoretically derived a local equilibrium glucose s_1^* content, whose time integration average over minutes shall equal to the experimental glucose quantity present in the saliva. However, we argue that the equilibrium average saliva glucose level should be sufficient for monitoring a relatively slow-time variation of blood glucose level over hours. Hopefully, with a slow variation function of time after a meal, our equilibrium model of saliva test kit can serve as a useful predictor for each individual his or her blood glucose level when & how much, after the saliva glucose level is benchmarked with his or her own equilibrium dynamics of blood glucose levels. Then, appropriate amount of insulin could be administrated to help glucose entering cells for needed energy conversion metabolism without damaging the delicate balance of blood glucose and insulin levels in the long run. We can help achieve better quality of life for aging population worldwide.

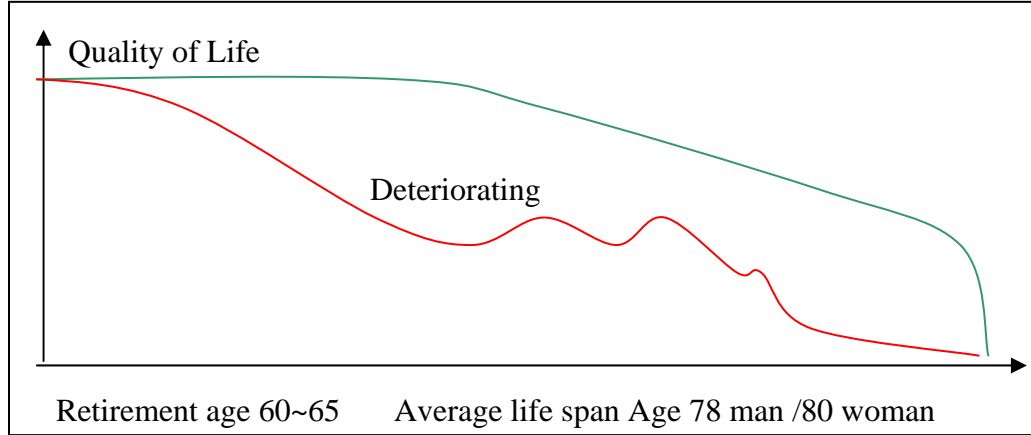


Fig. 6. The gain over an individual Quality of Life insures a productive second & third career in value-added production as opposed to a normal red deficit burden to the society.

The root cause is identified in this and other related paper that is waiting for nothing can be done in the current healthcare payment policy until missing the timeliness and early diagnosis getting seriously sick at hospital retreat. Affordable point of care smart sensors system, which implements two new concepts of Wellness Baseline Profile (WBP) for physician Individual Diagnostic Aids (IDA), must comprise biological power of pair concept translated from military real world experience on the persistent surveillance, together with military know-how of authenticated privacy communication Next Gen Network. Saliva test kit is merely one of four type's surveillance tools for WBP and IDA. The others and this one will be further developed and tested by concerned citizen and numerous collaborators worldwide.

In the near future, we will describe experimental findings and SOC results. We seek worldwide collaboration to predict blood glucose level as a function of time near hours after meal by measuring a time point of saliva glucose level. This will be a challenging application. Our initial approach is applying Neural Control Methodology to construct both a plant model and a feedback control loop, based on lot of past

history data to extract the invariant feature by means of the stationary Kurtosis analysis. Artificial Neural Network model similar to Narandra of Yale University in Trans IEEE NN V.1 might be useful.

ACKNOWLEDGEMENT:

The project described was supported by Ming-Shen Hospitals for Ubiquitous Health Care Project, partially by the Excellency Grant of Chung Yun Christian University, and partially by the grants to Dr. Chung and Dr. Tsai from National Science Council. Dr. Wang of the Radiology Department of Howard University Hospital wishes to thank NIH/NCI/NCRR Grant 2G12RR00304816A1, USAMRA Grant W81XWH-05-1-0291, and NIH Grant 2U54 CA091431-06A1. Dr. Gu of the School of Dentistry of Howard University wishes to acknowledge a partial support from NIH grant: NIH/NCI P20CA118770-01. Institute of Biomedical Engineering of National Taiwan University wishes to acknowledge the Excellence Grant of NTU, and the Grant by Taiwan National Science Council. Ming-Shen Hospital wishes to acknowledge the U-Care partial supported by Taiwan Ministry of Economic Yuan.

REFERENCES:

- [1]. General Account Office (GAO) Report 2002 on 78 Million aging baby boomers costs ranging from 1/5 GDP toward ¼ GDP in decades; Federal Reserve Chair Mr. Alan Greenspan thanked China 2006 Sept. for low cost quality product to keep US inflation in check, his successor Mr. Ben Benanke warned 2006 Oct. the financial un-sustainability of social entitlement due to the retirement of aging baby boomers.
- [2] Szu, Harold, ONR Press Release "From Tanks to Tumors," 2002; Szu et al., Publication of US Patent Trade Office **2004/0181375**.
- [3] Seow, S.W. Duffy, M. A. McGeem, J. Lee, and H. P. Lee, "Breast Cancer in Singapore trends in incidence 1968-1992," *Int'l J. of Epidemiology*, V. **25**, pp. **40-45**, **1996**;
- [4] Kelsey J. L. and Gammon, M. D. "the epidemiology of breast cancer," *Cancer J. for clinicians*, V. **41**, pp. **146-165**, **1991**;
- [5] While Prof. Basti of Lateran Pontific University is leading a team using passive infrared imaging at Lateran Hospital near Vatican of Rome for Phase Ib studies under EU/Italy funding, Prof. Ming-Chung Chen is leading a team of Biomedical Institute and Hospital of National Taiwan University under NTU Excellence Grant for Phase II efficacy studies. President Shi-Chen Lee of NTU leads a third team to design single co-axial lens camera for double infrared spectral band under National Science Council grant.
- [6] Bour-Jordan H., Bluestone J. A., "Sensory neurons link the nervous system and autoimmune diabetes," *Cell* **127**, pp. **1097-1099**, Dec 15 2006; R. Razavi, Y. Chan, F.N. Afifyan, X. J. Liu, X. Wan, J. Yantha, H. Tsui, L. Tang, S. Tsai, P. Santamaria, J.P. Driver, D. Serreze, M. W. Salter, and H.-M. Dosch, "TRPV1⁺ Sensory neurons control b cell stree and islet inflammation in autoimmune diabetes," *Cell* **127**, pp. **1123-1137**, Dec 15 2006.
- [7] Siudikiene Jolanta, Machiulskiene Vita, Nyvad Bente Tenovuo, Jorma, Nedzeiskienu Irena, "Dental caries and salivary status in children with type 1 diabetes mellitus, related to the metabolic control of the disease, *Eur. J. Oral Sci.* V. **114**, pp. **8-14**, **2006**.
- [8] Carda Carmen, Mosquera-Lloreda Nezly, Salom Lucas, Gomez de Ferraris Maria Elsa, Peydro Amando, "Strutural and functional salivary disorders in type 2 diabetic patients, *Med. Oral ptol Oral Bucal* V. **11**, pp. **E309-314**, **2006**.
- [9] Masaki Yamaguchi, Masayuki Mitsumori, and Yoshio Kano, "Noninvasive Measuring Blood Glucose Using Saliva," *IEEE Trans on Biomedical Eng.* V. **45**, pp. **59-63**, May/June 1998.
- [10] Kayashima S, Arai T, Kikuchi M, Sato N, and Nagata N, et al.: New noninvasive transcutaneous approach to blood glucose monitoring: Successful glucose monitoring on human 75g OGTT with novel sampling chamber, *IEEE Trans on Biomed. Eng.* V. **38**, pp. **752-757**, **1991**.
- [11] Szu, Harold. Miao, Lidan, Qi, Hairong, "Thermodynamic Free-energy Minimization for Unsupervised Fusion of Dual-color Infrared Breast Images," *Proc. SPIE* V. **6247**, "ICA Wavelets etc. (editor Szu)" pp. (Orlando, FL 2005)
- [12] Chung, Wen-Yaw, Yang, Chung-Huang, Wang, Yaw-Feng, Chan, Yi-Je, Torbicz W., Pijanowski Dorota G., "A signal processing ASIC for ISFET-based chemical sensors," *Microelectronics Journal* V. **35** (2004) pp. **667-675**

- [13] Chang Y.J., Chang Y.P., and Cheng K.Y. (2005), "Operation Principle And Simulation of Loop-Type Microfluidic Biochips", Proceedings of ICAM 2005 .
- [14] Szu Harold & Mehmood Amir, "RFID/SC Hybrid Solutions for Authentication, Privacy & Security Applications," Proc. SPIE V. **6247** "ICA Wavelets etc. (edited Szu)", pp. (Orlando FL, 2005)
- [15] Szu H., "Unsupervised learning Artificial Neural Networks," IN: "*Computational Intelligence, the experts speak*," (ed. Fogel & Robinson) Wiley Interscience and IEEE Press, **2003, Ch. 16, pp.219-245**.
- [16] Szu H., "Thermodynamics Energy for both supervised and unsupervised learning neural nets at a constant temperature," *Int'l J. Neural Sys.* **9, 175-186, June 1999**.
- [17] McFadden F., Szu, H. "Implicit differential analysis for cortical models," loc. cit. SPIE Proceeding V. **6576 (2007)**

Neuropathological quantification of dtg APP/PS1: neuroimaging, stereology, and biochemistry

Kebreten F. Manaye · Paul C. Wang ·
Jahn N. O'Neil · Sophia Y. Huang · Tao Xu ·
De-Liang Lei · Yousef Tizabi ·
Mary Ann Ottinger · Donald K. Ingram ·
Peter R. Mouton

Received: 12 January 2007 / Accepted: 25 May 2007 / Published online: 3 August 2007
© American Aging Association 2007

Abstract Murine models that mimic the neuropathology of Alzheimer's disease (AD) have the potential to

provide insight into the pathogenesis of the disease and lead to new strategies for the therapeutic management of afflicted patients. We used magnetic resonance imaging (MRI), design-based stereology, and high performance liquid chromatography (HPLC) to assess the age-related neuropathology in double transgenic mice that over-express two AD-related proteins—amyloid precursor protein (APP) and presenilin 1 (PS1)—and age- and gender-matched wild-type (WT) controls. In mice ranging in age from 4–28 months, total volumes of the hippocampal formation (V_{HF}) and whole brain (V_{brain}) were quantified by the Cavalieri-point counting method on a systematic-random sample of coronal T2-weighted MRI images; the same stereological methods were used to quantify V_{HF} and V_{brain} after perfusion and histological processing. To assess changes in AD-type beta-amyloid ($A\beta$) plaques, sections from the hippocampal formation and amygdaloid complex of mice aged 5, 12, and 15 months were stained by Congo Red histochemistry. In aged mice with large numbers of amyloid plaques, systematic-random samples of sections were stained by GFAP immunocytochemistry to assess gender and genotype effects on total numbers of astrocytes. In addition, levels of norepinephrine (NE), dopamine (DA), serotonin (5-HT) and 5-HT metabolites were assayed by HPLC in fresh-frozen samples from neocortex, striatum, hippocampus, and brainstem. We confirmed age-related increases in amyloid plaques, beginning with a few plaques at 5 months of age and increasing densities by

K. F. Manaye (✉) · J. N. O'Neil · T. Xu · D.-L. Lei
Department of Physiology and Biophysics,
Howard University College of Medicine,
520 W. Street, NW, Suite 2305,
Adams Bldg., Washington, DC 20059, USA
e-mail: kmanaye@howard.edu

P. C. Wang · S. Y. Huang
Department of Radiology, Howard University
College of Medicine, Washington, DC, USA

Y. Tizabi
Department of Pharmacology, Howard University
College of Medicine, Washington, DC, USA

M. A. Ottinger
University of Maryland, College Park, MD, USA

M. A. Ottinger · D. K. Ingram
Laboratory of Experimental Gerontology,
National Institute on Aging, NIH, Baltimore, MD, USA

D. K. Ingram
Nutritional Neuroscience and Aging Laboratory,
Louisiana State University, Baton Rouge, LA, USA

P. R. Mouton
Stereology Resource Center, Chester, MD, USA

J. N. O'Neil
School of Medicine, Johns Hopkins University,
Baltimore, MD, USA

12 and 15 months. At 15 months of age, there were robust genotype effects, but no gender effects, on GFAP-immunopositive astrocytes in the amygdaloid complex and hippocampus. There were no effects on monoamine levels in all brain regions examined, and no volume changes in hippocampal formation or whole brain as quantified on either neuroimages or tissue sections. Strong correlations were present between volume estimates from MRI images and histological sections, with about 85% reduction in mean V_{HF} or mean V_{brain} between MRI and processed histological sections. In summary, these findings show that the double transgenic expression of AD-type mutations is associated with age-related increases in amyloid plaques and astrocytosis; however, this model does not recapitulate the cortical atrophy or neurochemical changes that are characteristic of AD.

Keywords MRI · Alzheimer's disease · Hippocampal formation · Amygdala · Unbiased stereology

Introduction

About a century ago Alois Alzheimer described neurofibrillary tangles and neuritic plaques in cortical brain regions of a 51-year-old woman with progressive dementia (Alzheimer 1907). Although neuritic plaques and their amyloid components continue to play a critical role in the diagnosis of Alzheimer's disease (AD), semi-quantitative studies in groups of normal-aged and AD patients have reported that these so-called neuropathological markers of AD also occur to varying degrees in cortical tissue during normal aging, and that their accumulation does not directly correlate with the progression of dementia (Mirra et al. 1993; McKeel et al. 2004; Tiraboschi et al. 2004). Stereological and neurochemical studies of brain tissue from patients with AD have confirmed widespread astrocytosis and microgliosis in cortical brain regions and significant reductions in neurotransmitter-specific subcortical nuclei, including the locus coeruleus (LC) and dorsal raphe (DR), and diminished concentrations in their cortical projections of corresponding monoamine neurotransmitters, norepinephrine (NE) and 5-hydroxytryptamine (5-HT); in contrast, these parameters remain relatively stable in brains of persons that undergo normal (non-demented) brain aging (Aletrino et al.

1992; Mouton et al. 1994; Storga et al. 1996; Zarow et al. 2003; Tuppo and Arias 2005). The strongest correlations with dementia severity have been reported in the loss of cortical volume (atrophy), observed by either ante-mortem or post-mortem analyses, and the reduction in cortical synapses (de la Monte 1989; DeKosky and Scheff 1990; Terry et al. 1991; Convit et al. 1993; Jobst et al. 1994; Stout et al. 1996; Mouton et al. 1998; Zarow et al. 2003; de Leon et al. 2004). Thus, the evidence to date indicates that, while the diagnosis of AD depends heavily on the presence of amyloid plaques in neocortical brain regions, the progression of AD dementia appears to correlate more closely with degeneration of subcortical neurotransmitter systems that project to cortex, cortical synapse loss, and reduction of cortical volumes.

The transgenic murine expression of amyloid precursor protein (APP) and presenilin 1 (PS1) human mutation cloned from patients with familial AD results in the deposition of mutant beta-amyloid ($A\beta$) protein and the formation of amyloid plaques that appear indistinguishable from those in AD (Sze et al. 1997; McGowan et al. 2003). However, no studies have reported on the question of double transgenic (dtg) mice that undergo the progressive cortical atrophy and biochemical degeneration that are characteristic of AD. To address this question we quantified AD-type neuropathology in dtg APP/PS1 mice across the adult mouse lifespan using stereological analyses of ante-mortem neuroimages and post-mortem histological tissue, and neurochemical measurement of NE, dopamine (DA), 5-HT and metabolites by high performance liquid chromatography (HPLC). The results indicate that this line of dtg APP/PS1 mice show some of the neuropathological characteristics associated with AD (amyloid plaque deposition and astrocytosis), but not others (cortical atrophy and reductions in cortical monoamines).

Materials and methods

Mice for these studies were dtg APP/PS1 [Tg (APP^{swe}, PSEN1^{dE9}) 85Dbo, stock #005864] from the Jackson Laboratory (Bar Harbor, Maine, USA) and age- and gender-matched, non-tg, littermate controls (wild-type, WT). At the start of the study all mice weighed between 25 and 28 g and were randomized into dtg APP/PS1 and non-tg groups for

MRI and HPLC ($n=13/\text{group}$) or histology ($n=10/\text{group}$). The age of the 13 mice in the MRI studies spanned the adult lifespan of the mice (4–28 months), with dtg and WT mice matched for age and gender.

MRI Mice were anesthetized with 1.5–2.0 vol% isoflurane mixed with oxygen at a 200 cm³/min flow rate administered through a nasal cone mask. Mice were placed in the supine position at the center of a Varian 4.7 Tesla NMR machine with 33 cm horizontal magnet bore. A 25-mm long birdcage RF (radio frequency) coil with 20 mm inner diameter was placed around the head of the mouse and used as an RF transmitter and receiver.

High resolution spin echo MRI Spin-echo T2-weighted MRI was used to capture images through the entire brain and hippocampus at scan times of 1.5 h using a 4.7 Tesla NMR machine with the following parameters: repetition time (TR) 2.5 s; echo time (TE) 40 ms; field-of-view 14 mm × 14 mm; and, matrix size 256 × 256 pixels. The resulting images had a spatial resolution of 55 μm and a slice thickness of 1 mm. Two sets of 15 images were taken interleavedly through each brain. The total brain volume and hippocampal formation were measured randomly by two investigators hand-drawing the outlines of the regions of interest and then analyzed using the Cavalieri method (Fig. 1). The two investigators were blind to the grouping of the animals. The results were collapsed across age and gender and analyzed for possible transgene effects on V_{HF} and V_{brain} .

Histology Mice were deeply anesthetized via CO₂ inhalation, and then transcardially perfused with phosphate-buffered saline (PBS), 4% paraformaldehyde in 0.1 M PBS (pH 7.4) and postfixed in the 4% paraformaldehyde fixative overnight. The brains were transferred to a 30% sucrose phosphate buffer solution until they sank, then frozen in CO₂/isopentane and stored at −80°C until sectioning. Each brain was serially sectioned in the coronal plane on a sliding freezing microtome. Sections were cut at an instrument setting of 50 μm and sampled in a systematic-random manner, i.e., with random start in the first five sections, then systematic for every fifth section. For estimation of the volume of hippocampal formation (V_{HF}), which included neuronal and molecular layers of DG and CA1–4 regions, sampling was carried out through the entire hippocampus. A similar approach was applied to sampling every tenth section of the total sections through a complete hemisphere for estimation of total brain volume (V_{brain}). Sampled sections were stained using routine cresyl violet (CV) for Nissl substance and cover-slipped for microscopic visualization (Fig. 2). For neurochemistry studies of monoamine concentrations, a separate cohort of mice was sacrificed by cervical dislocation, the brain quickly removed and frozen on powdered dry ice, and stored at −80°C until analysis.

Stereology Using computer-assisted stereology, volumes for MRI slices and tissue sections were estimated using the Cavalieri principle with point counting (Gundersen and Østerby 1981; Gundersen

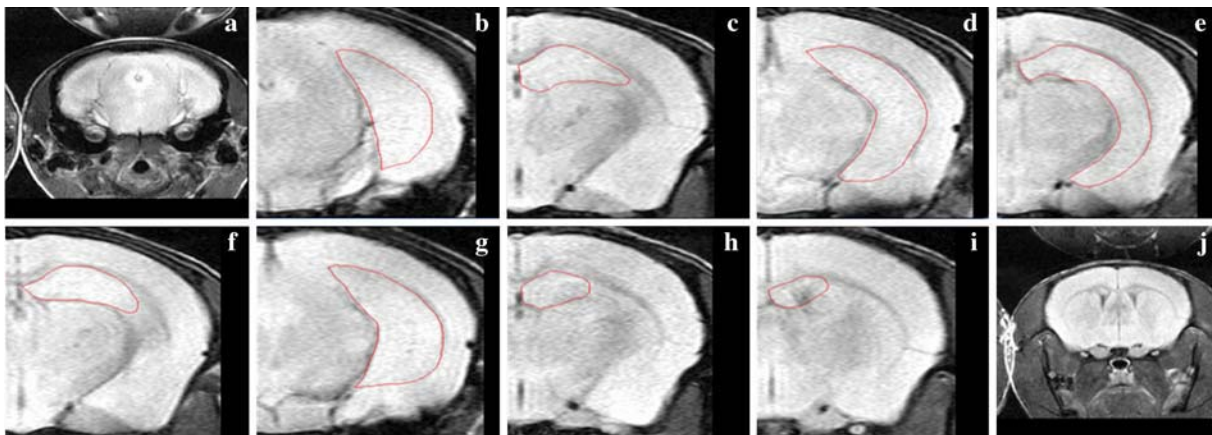
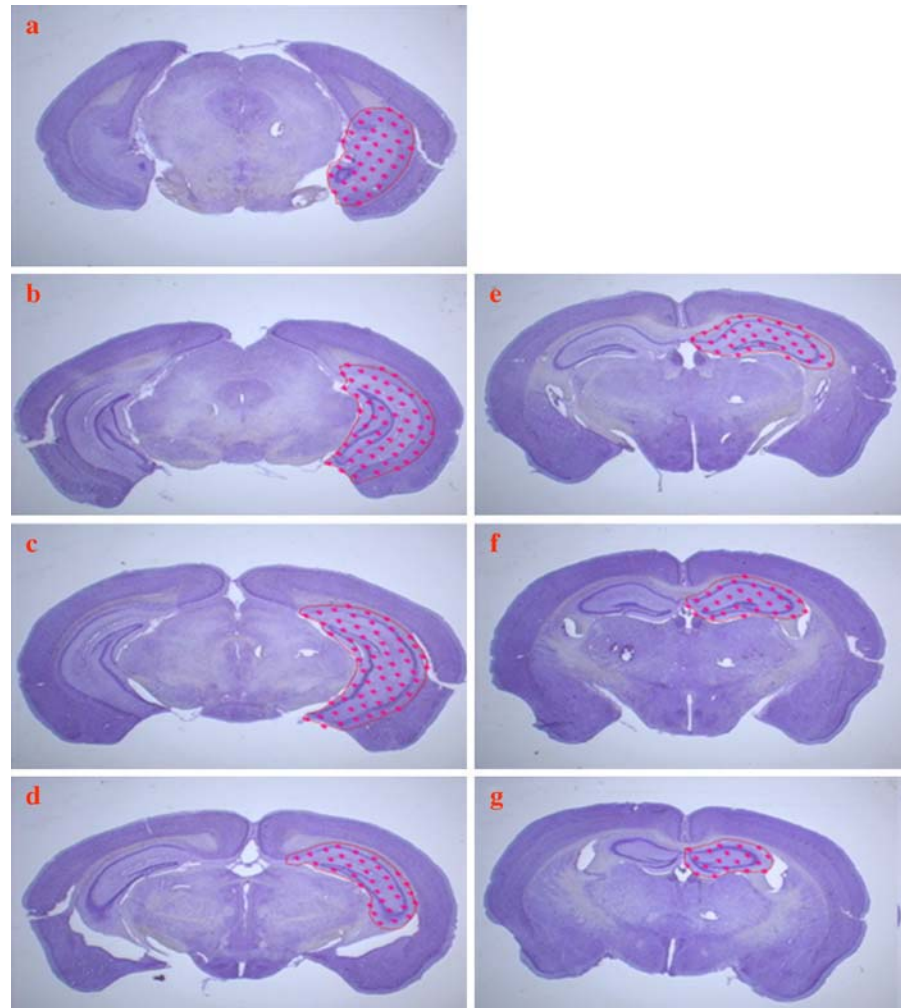


Fig. 1 a–j Representative T2-weighted MRI of serial sections through the entire mouse hippocampus (outlined), with an interslice distance of 1 mm. Note that the first and the last image (shown at lower magnification) do not contain hippocampus

Fig. 2 a–g Low power photomicrographs of serial sections through the entire mouse hippocampus; sections were cut at an instrument setting of 50 μm and stained with CV



and Jensen 1987; Long et al. 1998; Gundersen et al. 1999; Roberts et al. 2000; O'Neil et al. *in press*), as we have detailed previously for brain and hippocampus volumes in human, non-human primate, and rodent brains (de la Monte 1989; Subbiah et al. 1996; Mouton et al. 1997; Mouton 2002; for review Cavalieri 1635 with reprint 1966). The relevant equation for volume estimation: $V_{\text{ref}} = \sum \text{Area}_{\text{slices}} \cdot \text{Mean } t$

where,

V_{ref} Reference volume (hippocampal formation or whole brain, in mm^3)
 $\sum \text{Area}_{\text{slices}}$ area on slice or section, in mm^2

Mean t mean post-processing section or slice thickness, mm

In order to capture the majority of variability within- and between-mice for each group, data were collected at a high level of stringency, i.e., the coefficient of error (CE) was less than one-half of the biological variability (Gundersen and Østerby 1981; Long et al. 1998; Gundersen et al. 1999). The results were calculated as mean \pm (SEM) for each group and for each modality (MRI or histology); inter-rater variation between the volumetric measurements was less than 2%. Quantification of total numbers of GFAP-positive astrocytes used the optical disector method, as

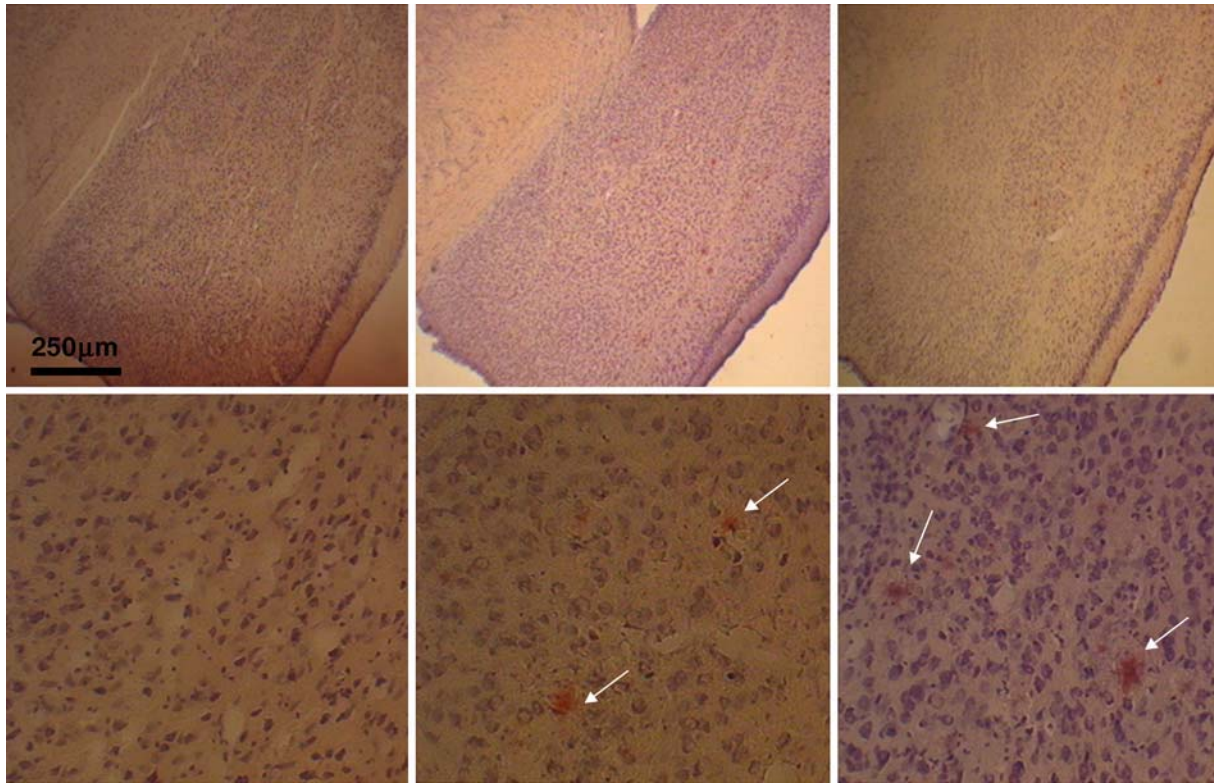


Fig. 3 Congo Red stained sections through the amygdaloid complex of female dtg APP/PS1 mouse brain at increasing ages (from left to right, 5, 12, 16 months of age). Pink staining amyloid-containing plaques present at 12 months, and increase in areal density at 15 months (*white arrows* show amyloid plaques). Magnification bar=250 μ m

detailed previously (West 1993; Subbiah et al. 1996; Mouton et al. 1997, 2002; Jankowsky et al. 2003; for review Cavalieri 1635 with reprint 1966).

Monoamine Analyses Due to the stress of MRI procedures, a separate cohort of age-matched mice was sacrificed for analysis of catecholamines and indolamines by HPLC using electrochemical detection (Bioanalytical Systems, West Lafayette, Indiana, USA). Brains were stored frozen (-80°C) then micro-dissected regions immediately placed into 0.1M HCl for homogenization. Regions analyzed in this study included the hippocampus, striatum, and cortex. Following homogenization, each sample was centrifuged and filtered (0.2u ACRO, Gelman Sciences, Ann Arbor, Michigan, USA). Samples were assayed individually and kept covered on ice to slow degradation. Monoamines analyzed included NE, DA, 5-HT, and 5-hydroxy-indole-amino acid (5-HIAA). Sample

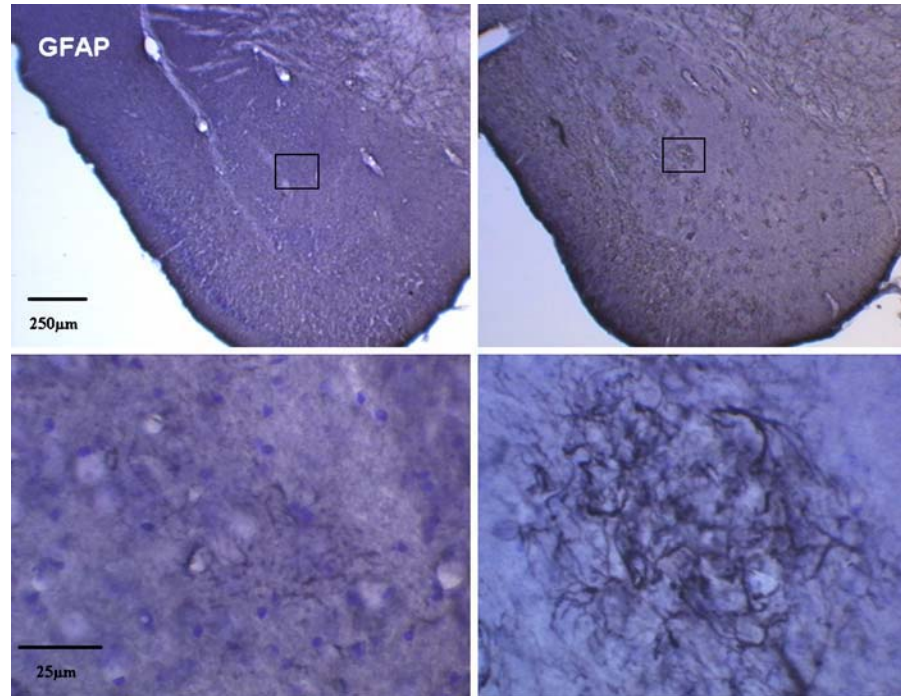
concentrations were calculated against standards that were measured on two channels on the electrochemical detector, which were set at two sensitivities to allow measurement over a greater range of sample concentrations. The software utilized the area under the curve for each standard and unknown for calculations of concentrations. Intra-assay variability was 3–5% and sensitivity was 25–50 pg/sample, with average recovery ranges from 80–90%.

Statistical analysis The groups were analyzed for statistical difference using independent two tailed t-tests; the level for significance was set at $p < 0.05$.

Results

Using the Cavalieri-point counting method, V_{HF} and V_{brain} were quantified on systematic-random samples

Fig. 4 GFAP-immunostained sections counterstained with CV through amygdaloid complex of 15-month-old female wild-type control (*left*) and dtg APP/PS1 mice (*right*). Note the presence of activated astrocytes in a reticular network around the amyloid deposit at lower right. Magnification bar=25 μ m



of MRI images and histology sections from dtg APP/PS1 and WT controls (Figs. 1 and 2). No genotype-based differences were observed in either hippocampus or whole brain volumes from MRI images of dtg APP/PS1 mice [$V_{HF}=30.4$ (0.12) mm^3 , $V_{\text{brain}}=451.5$ (4.31) mm^3 , parenthesis represent (SEM)] compared to that for WT controls [$V_{HF}=30.7$ (0.66) mm^3 , $V_{\text{brain}}=449.6$ (0.54) mm^3]. Similarly, the analyses on histological sections revealed no genotype effects on V_{HF} and V_{brain} , with average volumes in the dtg APP/PS1 mice [V_{HF} 4.6 (0.12) mm^3 , $V_{\text{brain}}=61.5$ (1.12) mm^3] comparable to that for the WT controls [$V_{HF}=4.8$ (0.13) mm^3 , $V_{\text{brain}}=60.2$ (2.05) mm^3]. Comparison of the ratio of hippocampus to whole brain volumes [(mean V_{HF} / mean V_{brain}) $\cdot 100$] showed no differences for volume estimates on MRI images (dtg APP/PS1=6.73% vs. WT=6.83%) or histological sections (dtg APP/PS1=7.48% vs. WT=7.97%). The effects of agonal and tissue processing reduced the average volumes in histological sections by about 84–87% of the same volumes in MRI images.

Congo Red staining of sections showed amyloid deposits in the amygdaloid complex and hippocampus (Figs. 3 and 4), with few deposits at 5 months of age, large numbers by 12 months, and marked increases in densities by 16 months of age. Stereological analysis

of total astrocyte numbers in the amygdaloid complex and hippocampus starting at age 15 months revealed significant genotype effects for both males and females (Figs. 5 and 6) compared to age-matched wild-type controls. In the amygdaloid complex this effect was particularly strong, as shown in Fig. 7, with the total number of astrocytes in both male and female dtg APP/PS1 mice more than twice that in the same

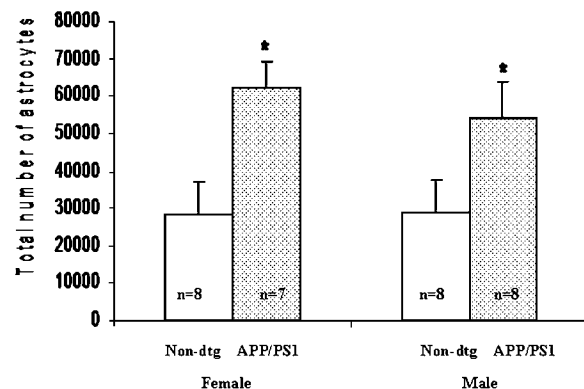


Fig. 5 Stereological counts of mean total numbers of GFAP-immunopositive astrocytes in amygdaloid complex of wild-type and dtg APP/PS1 mice aged 15–23 months ($n=7$ –8/group). Asterisk indicates significant genotype effect ($p<0.001$); there was no significant effect of gender

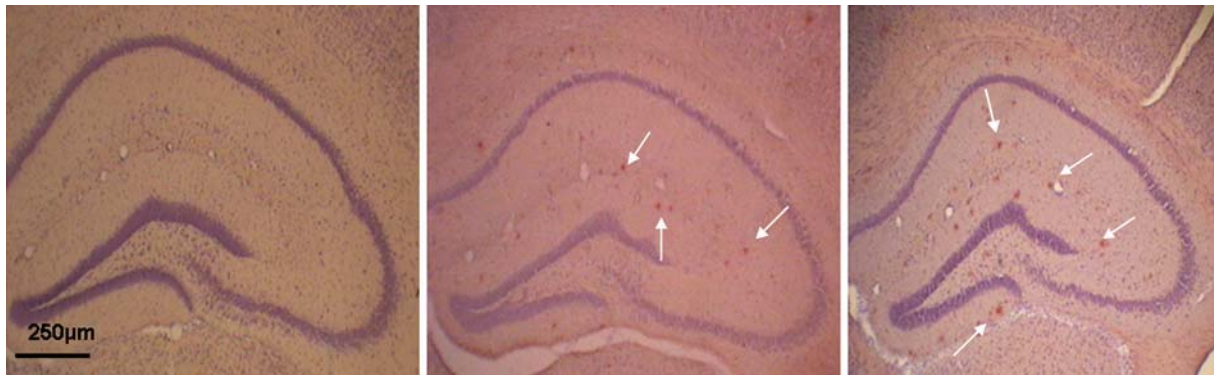


Fig. 6 Congo Red stained sections through hippocampal formation of female dtg APP/PS1 mouse brain at increasing ages. Pink staining amyloid-containing plaques present at 12 months, and increase in areal density at 16 months. Magnification bar=250 μ m; arrows point to amyloid plaques

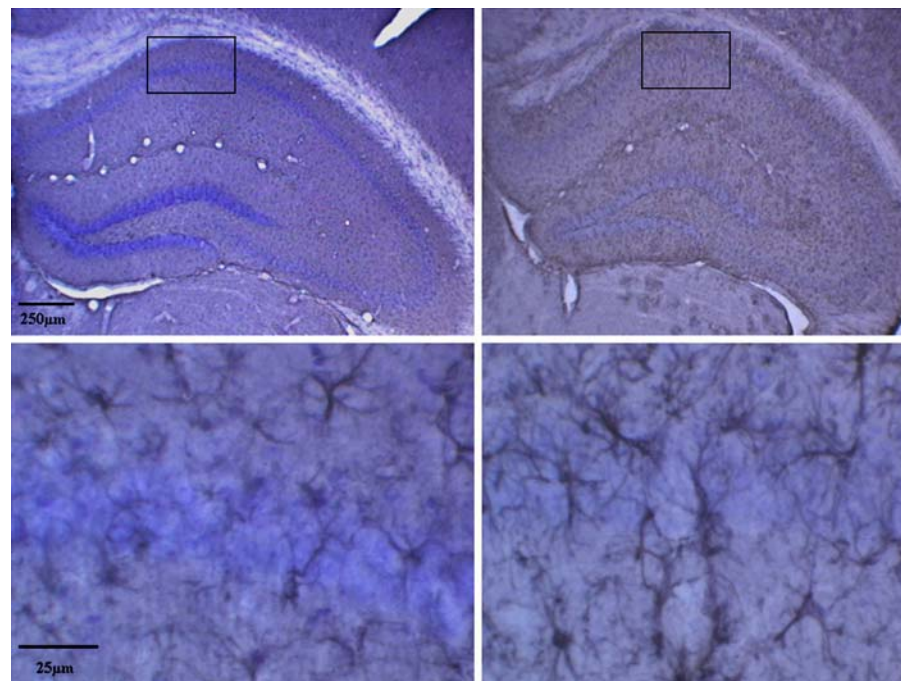
regions of age- and gender-matched wild-type controls (Fig. 5). The number of astrocytes increased significantly in hippocampal formation of dtg APP/PS1 compared to age- and gender-matched wild-type controls (Figs. 6 and 8), though this increase was less robust than in the amygdaloid complex.

The results of neurochemistry studies in hippocampus, striatum, or cortex did not reveal any significant differences in monoamine concentrations in brains of dtg APP/PS1 mice compared with values from the same brain regions in age- and gender-matched WT controls.

Discussion

An important criterion for assessing neurodegenerative progression, as seen in AD, is to quantify the neuropathological changes that exist in murine models that overexpress AD-type mutations in relation to those that occur in AD. The present study used neuroimaging, design-based stereology, and HPLC to begin to understand the genotype and gender effects of APP and PS1 co-expression in dtg mice, a strain that forms AD-type amyloid plaques at a much earlier age than single tg APP mice (Jankowsky et al. 2003;

Fig. 7 GFAP-immunostained sections counterstained with CV through hippocampal formation of 15-month-old female wild-eyed control (*left*) and dtg APP/PS1 mice (*right*; at magnification bar=250 μ m). Note the presence of activated astrocytes in the layer of CA1 pyramidal neurons at lower right (magnification bar=25 μ m). Localization of high magnification image in lower panel indicated by small box in upper panel



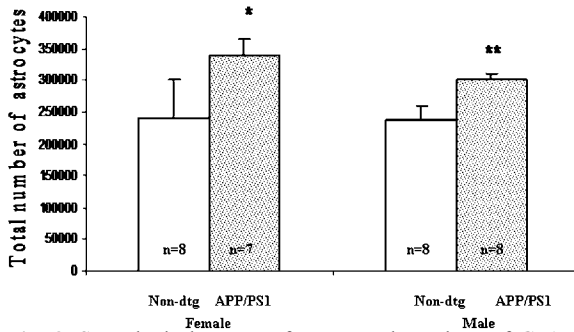


Fig. 8 Stereological counts of mean total numbers of GFAP-immunopositive astrocytes in hippocampal formation of wild-type and dtg APP/PS1 mice aged 15–23 months ($n=7-8$ /group). Asterisks indicate significant genotype effect (* $p<0.01$, ** $p<0.001$); there was no significant effect of gender

McGowan et al. 2003). The findings reported in this study appear to show that dtg APP/PS1 mice manifest certain forms of AD-type neuropathology and fail to manifest others.

The dtg APP/PS1 mice in the present study hyperaccumulate 42 amino acid A β residues and A β , leading to the earlier appearance of amyloid plaque formation compared to that in single tg APP mice (Jankowsky et al. 2003; McGowan et al. 2003). Sections from age-matched dtg APP/PS1 mice and WT controls were histochemically stained by Congo Red to assess age-related changes in AD-type beta-amyloid (A β) plaques. This study confirmed age-related increases in A β plaques beginning at 5 months of age and increasing progressively by 12 and 15 months, in agreement with a previous study in a different cohort of the same line of dtgAPPswe/PS1dE9 (Ohno et al. 2006).

Total numbers of GFAP-immunopositive-astrocytes in hippocampal formation and amygdala were quantified by the optical fractionator method. These stereological studies from age 15–23 months confirmed robust astrogliosis in both cortical regions examined, particularly the amygdaloid complex, with no gender effects. With regard to other morphological changes in this strain of dtg APP/PS1 mice, we have previously found evidence of reduced capillary branching at 7 months of age (Lee et al. 2005). We have also reported a significant degeneration in noradrenergic neurons in the LC in dtg APP/PS1 mice at 15 months of age (O’Neil et al. *in press*). Another study in the same line of dtg APP/PS1 mice (Savenenko et al. 2005), which found no differences in cognitive performance at 6- or 18-months of age, have reported mild

decreases in acetylcholinesterase histochemical staining and somatostatin levels in cortex at 18 months of age. Szapacs et al. (2004) reported reduced 5-HT levels in hippocampus at 18 months of age and reduced NE levels at 12- and 18-months of age. In 5-month-old dtg APP/PS1 in this line using a different PS1 mutation (PS1M146V), no differences were found in paired-pulse facilitation (PPF) or post-tetanic potentiation (PTP), two markers of presynaptic component of neurotransmitter release (Szapacs et al. 2004). Thus, neuropathological changes appear to occur in dtg APP/PS1 mice primarily in older age groups.

We found no genotype or gender effects on total volumes of the hippocampal formation (V_{HF}) and whole brain (V_{brain}) quantified either by the stereological method on T1-weighted MRI images or tissue sections after perfusion and histological processing. Since the aim of this study was to quantify total volumes for defined reference spaces, it was not necessary to co-register matched areas on the same coronal level between the MRI images and histological tissues. There were robust quantitative correlations with agonal and tissue-processing changes accounting for ~85% of the differences in cortical and brain volumes in vivo when comparing volume measurements using MRI with the same parameters on cover-slipped histological sections. These robust reductions in mean volumes occurred in both dtg APP/PS1 and wild-type. Brain volumes were quantified at an intermediate step in tissue processing, i.e., after sections were cut, but prior to further tissue processing, which allows the total tissue shrinkage to be partitioned into two components: ~15% shrinkage from agonal effects and the initial steps of tissue processing (fixation and sectioning), and ~70% volume loss during the final steps of tissue processing for microscopic visualization (i.e., dehydration, cresyl violet histochemistry, and coverslipping). The close correspondence in the ratios of hippocampal to whole brain volumes on MRI images and histological sections, along with inter-rater variation of the volumetric measurement of less than 2%, confirms the reliability of the technique for quantification of volumes. Finally, these comparable ratios indicate that the methods for immobilization and monitoring of cardiac and respiratory function did not blur the MRI images enough to confound the quantification process.

Another important goal of this research is to investigate the potential of ante-mortem neuroimaging

of A β -containing plaques in cortical brain regions to assist in the early clinical diagnosis of AD (Convit et al. 1993; Benveniste et al. 1999; Dedeoglu et al. 2004). Previous studies using T1 ρ ("T-1-rho")-weighted MRI have been moderately successful in demonstrating A β -containing plaques in vivo based on local variations in protein content (Poduslo et al. 2002). Enhanced visualization of amyloid plaques in dtg APP/PS1 mice has been demonstrated by pre-injecting A β peptides magnetically labeled with gadolinium or iron oxide nanocrystals (Borthakur et al. 2003). A recent MRI study of dtg APP/PS1 mice reported differences with respect to non-tg controls in the transverse relaxation time *T*₂, in several regions of cortical grey matter (hippocampus, cingulate, and retrosplenial cortex), which may reflect impaired cell physiology in these regions (Wadghiri et al. 2003). The absence of differences in T1-weighted or proton density weighted MRI images suggests that heavily T2-weighted images may be more sensitive to amyloid accumulation in the dtg APP/PS1 mice (Helfern et al. 2004).

In summary, this line of dtg APP/PS1 mice show several morphological changes associated with AD, including age-related increases in amyloid plaques, astrogliosis, and LC degeneration, and fail to recapitulate the loss of cortical volume and reductions in cortical monoamine concentrations that characterize AD. Among the possible explanations for this observation is the likelihood that compensatory sprouting of surviving LC neurons occurs in those mice to ensure neurochemical innervation to all main areas; in AD, similar compensation may occur until the final stage of the disease prior to death. Our studies will continue to develop the optimal MRI parameters to visualize ligands that effectively cross the blood brain barrier and bind to microscopic targets associated with AD neuropathology. Further cross-sectional and time-course studies are needed to help build a stronger view of the neuropathological profile in the brains of these mice with respect to the neuropathology associated with AD.

Acknowledgements The authors would like to recognize the Public Health Service for funding support for these studies (SNRP2U54NS039407-06, NIH grant MH076541-02A1, RCMI/NCRR/NIH G12RR03048, US Army USAMRMC W81XWH-05-1-0291, NIH MHIRT 9T 37-MD001582-08) and the technical support of Armand Oei and Huaifu Song in the laboratory of Biomedical NMR at the Howard University School of Medicine. The authors also appreciate the support of

Nikki Thompson for the monoamine assays through the Maryland Agriculture Experiment Station of the University of Maryland.

References

- Aletrino MA, Vogels OJ, Van Domburg PH, Ten Donkelaar HJ (1992) Cell loss in the nucleus raphe dorsalis in Alzheimer's disease. *Neurobiol Aging* 13(4):461–468
- Alzheimer A (1907) Ueber eine eigenartige Erkrankung der Hirnrinde. *Allgemeine Zeitschrift für Psychiatrie* 64:146–148
- Benveniste H, Einstein G, Kim KR, Hulette C, Johnson GA (1999) Detection of neuritic plaques in Alzheimer's disease by magnetic resonance microscopy. *Proc Natl Acad Sci USA* 96(24):14079–14084
- Borthakur A, Urya K, Chively SB, Poptani H, Corbo M, Charagundla SR, Trojanoqski JQ, Lee VM, Reddy R (2003) In Vivo T₁ weighted MRI of amyloid transgenic mouse model of Alzheimer's disease. *Proc Intl Soc Mag Reson Med* 11:2039
- Cavalieri B (1635) *Geometria indivisibilibus continuorum*. Bononi: Typis Clementis Ferronij. Reprint from (1966) *Geometria degli indivisibili*. Torino: Unione Tipografico-Editrice Torinese
- Convit A, de Leon MJ, Golomb J, George AE, Tarshish CY, Bobinski M, Tsui W, De Santi S, Wegiel J, Wisniewski H (1993) Hippocampal atrophy in early Alzheimer's disease: anatomic specificity and validation. *Psychiatr Q* 64:371–387
- Dedeoglu A, Choi JK, Cormier K, Kowall NW, Jenkins BG (2004) Magnetic resonance spectroscopic analysis of Alzheimer's disease mouse brain that express mutant APP shows altered neurochemical profile. *Brain Res* 1012(1–2):60–65
- DeKosky ST, Scheff SW (1990) Synapse loss in frontal cortex biopsies in Alzheimer's disease: correlation with cognitive severity. *Ann Neurol* 27:457–464
- de la Monte SM (1989) Quantitation of cerebral atrophy in preclinical and end-stage Alzheimer's disease. *Ann Neurol* 25:450–459
- de Leon MJ, DeSanti S, Zinkowski R, Mehta PD, Pratico D, Segal S, Clark C, Kerkman D, DeBernardis J, Li J, Lair L, Reisberg B, Tsui W, Rusinek H (2004) MRI and CSF studies in the early diagnosis of Alzheimer's disease. *J Intern Med* 256:205–223
- Gundersen HJ, Jensen EB (1987) The efficiency of systematic sampling in stereology and its prediction. *J Microsc* 147(Pt 3):229–263
- Gundersen HJG, Jensen EV, Kieu K, Nielsen J (1999) The efficiency of systematic sampling in stereology - revisited. *J Microsc* 193:199–211
- Gundersen HJG, Østerby R (1981) Optimizing sampling efficiency of stereological studies in biology: or "Do more less well." *J Microsc* 121:65–73
- Helfern JA, Lee S-P, Falangol MF, Dyakin VV, Bogart A, Ardekani B, Duff K, Branc C, Wisniewski T, de Leon MJ, Wolf O, O'Shea J, Nixon RA (2004) MRI assessment of neuropathology in a transgenic mouse model of Alzheimer's disease. *Magn Reson Med* 51:794–798

- Jankowsky J, Fadale DJ, Andersen JK, Xu G, Gonzales V, Jenkins NA, Copeland NG, Lee MK, Younkin LH, Wagner SL, Younkin SG, Borchelt DR (2003) Mutant presenilins specifically elevate the levels of the 42 residue beta-amyloid peptide in vivo: evidence for augmentation of a 42-specific gamma secretase. *Hum Mol Genet* 13(2):159–170
- Jobst KA, Smith AD, Szatmari M, Esiri MM, Jaskowski A, Hindley N, McDonald B, Molyneux AJ (1994) Rapidly progressing atrophy of medial temporal lobe in Alzheimer's disease. *Lancet* 343:829–830
- Lee GD, Aruna JH, Barrett JM, Lei D-L, Ingram DK, Mouton PR (2005) Stereological analysis of microvascular parameters in a double transgenic model of Alzheimer's disease. *Brain Res Bull* 65:317–322
- Long JM, Kalehua AN, Muth NJ, Calhoun ME, Jucker M, Hengemihle JM, Ingram DK, Mouton PR (1998) Stereological analysis of astrocyte and microglia in aging mouse hippocampus. *Neurobiol Aging* 19:497–503
- McGowan E, Pickford F, Dickson DW (2003) Alzheimer animal models: models of A β deposition in transgenic mice. In: Dickson DW (ed) *Neurodegeneration: the molecular pathology of dementia and movement disorders*. ISN Neuropath Press, Basel, pp 74–79
- McKeel DW, Price JL, Miller JP, Grant EA, Xiong C, Berg L, Morris JC (2004) Neuropathologic criteria for diagnosing Alzheimer disease in persons with pure dementia of Alzheimer type. *J Neuropathol Exp Neurol* 63(10):1028–1037
- Mirra S, Hart MH, Terry RD (1993) Making the diagnosis of Alzheimer's disease. A primer for practicing pathologists. *Arch Pathol Lab Med* 117:132–144
- Mouton PR (2002) Principles and practices of unbiased stereology: an introduction for bioscientists. Johns Hopkins University Press, Baltimore
- Mouton PR, Long JM, Lei DL, Howard V, Jucker M, Calhoun ME, Ingram DK (2002) Age and gender effects on microglia and astrocyte numbers in brains of mice. *Brain Res* 956(1):30–35
- Mouton PR, Martin LJ, Calhoun ME, Dal Forno G, Price DL (1998) Cognitive decline strongly correlates with cortical atrophy in Alzheimer's dementia. *Neurobiol Aging* 19: 371–377
- Mouton PR, Pakkenberg B, Gundersen HJG, Price DL (1994) Absolute number and size of pigmented locus coeruleus neurons in the brains of young and aged individuals. *J Chem Neuroanat* 7:185–190
- Mouton PR, Price DL, Walker LC (1997) Empirical assessment of synapse numbers in primate neocortex. *J Neurosci Methods* 75:119–126
- Ohno M, Chang L, Tseng W, Oakley H, Citron M, Klein WL, Vassar R, Disterhoft JF (2006) Temporal memory deficits in Alzheimer's mouse models: rescue by genetic deletion of BACE1. *Eur J Neurosci* 23(1):251–260
- O'Neil JN, et al. Catecholaminergic neuronal loss in locus coeruleus of aged female dtg APP/PS1 mice. *J Chem Neuroanat* (in press)
- Poduslo JF, Wengenack TM, Curran GL, Wisniewski T, Sigurdsson EM, Macura SI, Borowski BJ, Jack CR Jr (2002) Molecular targeting of Alzheimer's amyloid plaques for contrast-enhanced magnetic resonance imaging. *Neurobiol Dis* 11(2):315–329
- Roberts N, Puddephat MJ, McNulty V (2000) The benefit of stereology for quantitative radiology. *Br J Radiol* 73 (871):679–697
- Savenko A, Xu GM, Melnikova T, Morton J, Gonzales V, Wong M, Price DL, Tang F, Markowska AL, Borchelt DR (2005) Episodic-like memory deficits in the APPsw/PS1dE9 mouse model of Alzheimer's disease: relationship to β -amyloid deposition and neurotransmitter abnormalities. *Neurobiol Dis* 18(3):602–617
- Storga D, Vrecco K, Birkmayer JG, Reibnegger G, Cavalieri B (1996) Monoaminergic neurotransmitters, their precursors and metabolites in brains of Alzheimer patients. *Neurosci Lett* 203(1):29–32
- Stout JC, Jernigan TL, Archibald SL, Salmon DP (1996) Association of dementia severity with cortical gray matter and abnormal white matter volumes in dementia of the Alzheimer type. *Arch Neurol* 53:742–749
- Subbiah P, Mouton PR, Fedor H, McArthur JC, Glass JD (1996) Stereological analysis of cerebral atrophy in human immunodeficiency virus-associated dementia. *Exp Neurol* 55(10):1032–1037
- Szapacs ME, Numis AL, Andrews AM (2004) Late onset loss of hippocampal 5-HT and NE is accompanied by increases in BDNF protein expression in mice co-expressing mutant APP and PS1. *Neurobiol Dis* 16(3):572–580
- Sze CI, Troncoso JC, Kawas C, Mouton PR, Price DL, Martin LJ (1997) Loss of the presynaptic vesicle protein synaptophysin in hippocampus correlates with cognitive decline in Alzheimer disease. *J Neuropathol Exp Neurol* 56(8):933–944
- Terry RD, Masliah E, Salmon DP, Butters N, DeTeresa R, Hill R, Hansen LA, Katzman R (1991) Physical basis of cognitive alterations in Alzheimer's disease: synapse loss is the major correlate of cognitive impairment. *Ann Neurol* 30:572–580
- Tiraboschi P, Hansen LA, Thal LJ, Corey-Bloom J (2004) The importance of neuritic plaques and tangles to the development and evolution of AD. *Neurology* 64:1984–1989
- Tuppo EE, Arias HR (2005) The role of inflammation in Alzheimer's disease. *Int J Biochem Cell Biol* 37(2):289–305
- Wadghiri YZ, Sigurdsson EM, Sadowski M, Elliott JI, Li Y, Scholtzova H, Tang Cy, Aguinaldo G, Pappolla M, Duff K, Wisniewski T, Turnbull DH (2003) Detection of Alzheimer's amyloid in transgenic mice using magnetic resonance microimaging. *Magn Reson Med* 50(2): 293–302
- West MJ (1993) Regionally specific loss of neurons in the aging human hippocampus. *Neurobiol Aging* 14(4):287–293
- Zarow C, Lyness SA, Mortimer JA, Chui HC (2003) Neuronal loss is greater in the locus coeruleus than nucleus basalis and substantia nigra in Alzheimer and Parkinson diseases. *Arch Neurol* 60(3):337–341

A Mammography Database and View System for African-American Patients

Shani Ross,^{1,2} O'tega Ejofodomi,² Ahmed Jendoubi,² Lisa Kinnard,³ Mohamed Chouika,² Ben Lo,³
Paul Wang,⁴ and Jianchao Zeng²

We have digitized mammography films of African-American patients treated in the Howard University Hospital Radiology Department and have developed a database using these images. Two hundred and sixty cases totaling more than 5,000 images have been scanned with a high resolution Kodak LS85 laser scanner. The database system and web-based search engine were developed using MySQL and PHP. The database has been evaluated by medical professionals, and the experimental results obtained so far are promising with high image quality and fast access time. We have also developed an image viewing system, D-Viewer, to display these digitized mammograms. This viewer is coded in Microsoft Visual C# and is intended to help medical professionals view and retrieve large data sets in near real time. Finally, we are currently developing an image content-based retrieval function for the database system to provide improved search capability for the medical professionals.

KEY WORDS: African-American women, breast cancer, database, mammography, mammogram, digitization, image viewer, Howard University

INTRODUCTION

The American Cancer Society estimates that in the United States alone, approximately 40,000 women die each year from breast cancer and that over 200,000 new breast cancer cases are diagnosed each year.^{1,2} Typically, there are four main types of breast cancer: ductal carcinoma in situ (DCIS) where the cancer is confined within the ducts of the breast, lobular carcinoma in situ (LCIS) where the cancer is confined within the lobules or glands of the breast, invasive ductal carcinoma (IDC), and invasive lobular carcinoma (ILC).^{1,3} IDC and ILC refer to the type of breast cancer where the tumor has spread from the ducts

or lobules it originated from, respectively, into the surrounding tissue of the breast. Other less common breast cancers include medullary carcinoma, mucinous carcinoma, Paget's disease of the nipple, Phyllodes Tumor, and tubular carcinoma.³

Breast cancer is grouped into stages which indicate the invasiveness of the disease. There are four stages—I, II, III, IV—defined by the American Joint Committee on Cancer^{1,3} based on a combination of tumor size, lymph node involvement, and presence or absence of distant metastasis. There is also a more general classification: early/local stage where tumor is confined to the breast, late/regional stage where cancer has spread to the surrounding tissue or nearby lymph nodes, and advanced/distant stage where cancer has spread to other organs beside the breast.^{1,4}

There has been a decline in breast cancer mortality rates of about 2.3% over the last decade^{1,2} due to improved screening techniques leading to earlier detection, increased awareness,

¹From the Biomedical Engineering, University of Michigan, Ann Arbor, MI, USA.

²From the Electrical and Computer Engineering, Howard University, Washington, DC, USA.

³From the Radiology, Georgetown University, Washington, DC, USA.

⁴From the Radiology, Howard University Hospital, Washington, DC, USA.

Correspondence to: Mohamed Chouika, 2300 Sixth St., NW, Rm 1022, Washington DC 20059; tel: 202-806-4816; fax: 202-332-3152; e-mail: mchouika@howard.edu

Copyright © 2007 by Society for Imaging Informatics in Medicine

Online publication 29 March 2007

doi: 10.1007/s10278-007-9019-6

and improved treatments. Improved screening techniques include regular self breast examination, breast physical examination by a doctor, and regular mammogram examinations. In a mammogram, a radiologist looks for any unusual signs. These include asymmetry between the two breasts, any irregular areas of increased density, or any areas of skin thickening all of which can indicate whether there is a mass, or lump, in the breast tissue.^{1,3} As this mass can either be cancerous or benign, further tests such as a biopsy of the suspicious area are done to differentiate between the two. In addition, doctors look for calcifications which are tiny calcium deposits that indicate changes within the breast possibly pointing to cancer. Microcalcifications especially are usually associated with cancer.

Despite improved screening techniques, this decline has been much smaller in African-American women compared to Caucasian-American women even with increased participation by African-Americans in routine mammography screening since 1980.⁵ Furthermore, statistics have shown that although Caucasian-American women have an overall higher incident rate of breast cancer than African-American women, African-American women have a slightly higher incident rate of breast cancer before the age of 35 and are more likely to die of breast cancer at any age.^{1,6} Also, in comparison to Caucasian women, African-American women are less likely to be diagnosed with tumors of diameter less than or equal to 2.0 cm and in the early stage of breast cancer, but more likely to be diagnosed with tumors of diameters greater than 2.0 cm and in later and advanced stages of the cancer.^{1,6,7} Some of this disparity could be explained by an overall lower socioeconomic status, unequal access to medical care, and additional illnesses,⁸⁻¹⁰ which results in a much smaller percentage of African-American women getting early and regular mammograms compared to Caucasian women. Hence, they are usually not diagnosed with cancer until at a much later date when the cancer is at an advanced stage, which increases their mortality risk.

Some studies have also reported differences in breast cancer histology in African-American women and Caucasian women, although they noted that these results are not conclusive. Some of these studies found that African-American women had a greater chance of developing ductal tumors, whereas Caucasian women had a greater

chance of developing more lobular tumors.^{11,12} This could be significant in the difference in outlook for the two racial groups, as lobular carcinoma is usually less aggressive. Other studies reported that African-American women had a greater frequency of medullary carcinoma than Caucasian women.^{5,7} Medullary carcinoma is similar to ductal carcinoma but has a clearer distinction between the cancerous and normal cells.

Perhaps the most statistically significant differences seen between the two racial groups are the steroid receptor status of the tumor and the tumor proliferation rates. These differences are evident even when comparisons were adjusted for age, stage, treatment and screening opportunities, and risk factors. Typically African-American women had more estrogen- and progesterone-receptor negative tumors. Such tumors are generally unaffected by changing levels of these hormones and are thus less responsive to antihormonal treatments. African-American women also tended to have more poorly defined tumors, increased cell growth, and marked tumor necrosis. All these factors contribute to more aggressive tumors for African-American women.^{5,7,11,12}

The epidemiological and tumor biology differences seen in African-American women compared to Caucasian women, leading to higher mortality rates, stress the particular importance in trying to fully understand why these disparities arise. One possible step towards addressing these issues is to have a larger number of African-American breast cancer cases available for study. Currently, there are no breast cancer databases primarily developed for African-American patients, although general breast cancer database systems do exist.^{13,14} Hence, the main objective of this research is to develop the first major African-American Breast Cancer Mammography database for the use of training radiologists and other personnel involved in the detection and treatment of breast cancer. This could thus help in further understanding the nature of the breast cancer in African-American women. Part of this study also includes developing a view system that will allow radiologists to retrieve and view the digital imaging and communications (DICOM)-formatted images in the database in near real time.

This research is divided into three main parts. The first part is the collection of actual data for the

database, which includes the obtaining, scanning, and organization of the mammography films. The second part is the development of the database and web-search engine using database management software and webpage development programming languages. The third part is the development of the viewing software.

METHODS

This study is in collaboration between the Howard University Electrical and Computer Engineering Department, the Howard University Hospital Radiology Department, and the Georgetown University Radiology Department. The database and viewing software development are being done through the Howard University Electrical Engineering Department with the films being supplied by the Howard University Hospital Radiology Department. Consulting support is provided by the Georgetown University Radiology Department. Before conducting the study, approval was obtained from the Institutional Review Board. The primary investigators, who worked directly with the films, took the Human Participants Protection Education for Research Teams online certification course¹⁵ to meet the National Institute of Health (NIH) requirements on patient privacy issues. The investigators also attended seminars required by Howard University Hospital on the Health Insurance Portability and Accountability Act (HIPAA) of 1996.

Digitization of the Mammography Films

Film Collection

Currently, mammography films from 260 patients from the Howard University Radiology Department have been digitized and entered into the database. All of these patients were diagnosed with breast cancer between 1994 and 2004 and were between the ages of 24 and 88. The patients' histology includes masses of different sizes with and without poorly defined borders, microcalcifications, clusters of calcifications, adenopathy, heterogeneous density, and solid nodules. Furthermore, the majority of these patients had undergone more than one mammography examination. For

these patients, the earlier exams typically were regular screening mammograms, which showed normal and benign images. Normal images were mammograms in which nothing suspicious was seen, and benign images were mammograms in which something suspicious was seen initially but with further examination found to be nonmalignant. The cancer appeared and was diagnosed in the later exam dates. Thus, we were able to obtain a wide variety of films showing normal, benign, and cancerous images. Table 1 gives an overview of the patient characteristics of the database.

Each examination date, on average, contained four films corresponding to the four typical views taken of the breasts during a mammogram. These views are: left mediolateral oblique view (LMLO), right mediolateral oblique view (RMLO), left craniocaudal view (LCC), and right craniocaudal view (RCC) (Fig. 1). The films generally came in two sizes: 8×10 and 10×12 in.

Majority of these mammograms had been done at Howard University Hospital using the MGX 2000 mammography machine from Instrumentarium Corporation, Imaging Division, Tuusula, Finland. The machine parameters include: a film focus distance of 26 in., AGFA Mamoray HDR-C high dynamic range film $24 \text{ cm} \times 32 \text{ cm}$, exposure of 75–130 mAs (depending on patient), tube voltage of 27–30 KeV, and a filter of 0.025 mm molybdenum, or 0.025 mm rhodium, or 0.5 mm aluminum. Some of the older mammograms had been done at the patient's previous hospital and the technical parameters of the machine used are unknown.

Scanning and Technical Procedure

The scanner used is the Kodak LS85 Laser Digitizer, specifically designed for high resolution teleradiology. Films can be converted into high resolution digital images of up to 5,120 pixels by 6,140 lines with 12 bits per pixel. Each pixel is assigned an optical digital value equal to $1,000 \times$ optical density and has a spot size of $50 \mu\text{m}$. The digitizer has a scan rate of approximately 75 lines per second. It was purchased along with accompanying support software from RADinfo Systems, Dulles, Virginia. This accompanying software supports the digitization and burning of the images and includes: the Inter2000 Film Digitizer™

Table 1. Representative Sample of the Patient Characteristics of the Database

Patient	Age	Year Cancer Diagnosed	Histology	Digitization Date
MK833AI543	24	1999	Spiculated mass and speculated density in R. breast	6/10/2004
WM980RI062	26	2001	Abnormal, dilated ducts and microcalcifications	6/14/2004
BR815AA561	32	1999	Cluster of calcifications	1/22/2004
TN989IA352	39	2001	Malignant calcifications in L. breast, extensive ductal carcinoma in situ	6/2/2004
HS963AH074	45	1999	Large medial calcifications in L. breast	4/6/2004
BM869OI885	46	1998	Microcalcifications in L. Breast	6/19/2004
ME729OM197	55	2001	Malignant calcifications and solid mass	5/19/2004
AJ337DU655	56	1997	Solid mass with poorly defined borders in L. breast	7/7/2004, 7/8/2004
BJ567RA821	58	2001	Cluster of calcifications in L. Breast	1/30/2004
GI759HZ353	59	1998	Microcalcifications and lateral calcifications in L. breast	6/21/2004
DM795AA866	62	1999	Spiculated mass in R breast	3/25/2004
BM169AE858	62	1996	Density with obscured borders in L. breast	6/20/2004
MA935CN074	63	1999	Metastative adenopathy in L axillary	6/10/2004
BD759AO805	65	2000	Breasts heterogeneously dense, highly suspicious mass with speculated borders and associated microcalcifications	2/24/2004, 3/1/2004
SS913TY027	66	2000	R. breast ductal carcinoma in situ	6/1/2004
DM710AA630	70	1998	Large mass and microcalcifications in R. breast	6/22/2004
GN216OO404	70	1997	Macro and micro calcifications in R breast	6/22/2004
KC717EL219	71	2000	R. breast carcinoma—irregular nodal density; Previous L. breast carcinoma (now irradiated)—spiculated mass with microcalcifications at the peripheral	5/28/2004
CG362AE888	71	1998	Large pulp mass solid with lobulated borders, small satellite lesions and large abnormal axillary node in L. breast	6/21/2004
BL316YO065	72	1999	Cluster of calcifications	1/23/2004
DS833AA858	73	1997	Mass and poorly defined post border in R. breast	6/21/2004
BM065RA569	74	1996	Malignant appearing calcifications in R. breast	6/19/2004
FD103LE602	76	1998	Irregular asymmetric density with associated microcalcifications in L breast	7/15/2004
JF393AR669	77	2001	Two spiculated masses, poorly defined	5/28/2004
MD782IE169	82	1998	Spiculated mass in L breast	6/24/2004
HK862AA996	83	2000	Solid and irregular polyp mass	5/17/2004

(I2000FD), RSVS Viewer TM, and CD Power-PACS TM.

The I2000FDTM is the interface for the film digitizer. This is where patient information is

entered, the digitizer is accessed for scanning, and where any necessary changes can be made to the film before the digital image is saved. Before scanning, patient information required by

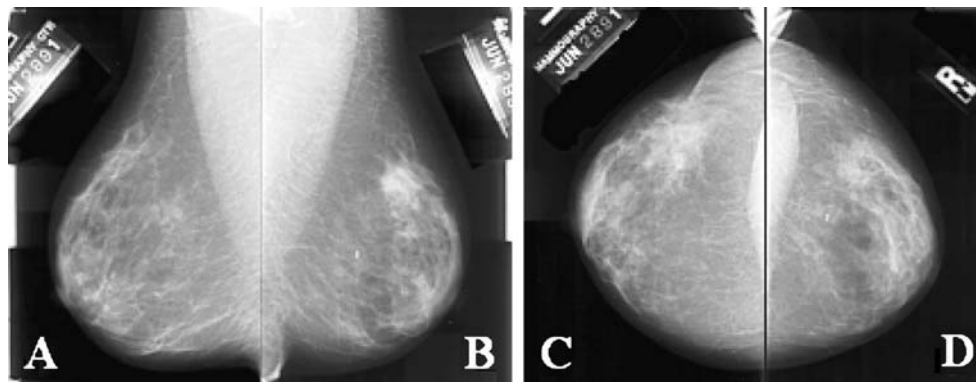


Fig 1. A typical mammography view: a LMLO, b RMLO, c LCC, and d RCC.¹³

I2000FD™ is entered. This information includes: the patient name written in a code to preserve patient's privacy rights, birth date, exam date, the ascension number used to keep track of each series, and the time and date of digitization of each film. This information is the essential information required by the program to stamp and classify each resulting digitized image. Next, the user specifies the resolution, bit depth, window level settings, and size of the film to be scanned. In this study, films are digitized at a resolution of 512 pixels/in. and a bit depth of 12, both of which are maximum values of the scanner, to give the highest image quality. The scan size chosen is either 8×10 or 10×12 in., depending on the size of the film to be scanned. Once the settings have been entered, the film is loaded into the Kodak scanner and digitized. Furthermore, the software allows us to cover the patient's name and other identifying information so that this is not seen in the digitized image in the software. The images are then saved and copies of them are transferred to the viewing software (RSVS™) and burning software (CD PowerPACS™). The sizes of these saved images are generally 40 MB for the 8×10 films and 60 MB for the 10×12 films. The RSVS™ is a viewing software for DICOM-formatted images, which allow us to further view and verify the digitized images. The CD PowerPACS™ software allows us to save and transfer the images to CD-R storage media. This program also saves a copy of the RSVS viewer on each CD.

Development of the Database

The Howard University Mammography Database¹⁶ was developed using PHP and MySQL. MySQL is a simple relational database management system that allows users to add, access, and process data stored in a database.¹⁷ The database contains relevant information such as encrypted patient name, patient ID, date of birth, type of scanner used, number of series in a case, exam date, total image count in a case, malignancy, and available image views (RMLO, LCC, etc.). New information can also be added when necessary. Our database is linked to a web-based search engine powered by PHP-recursive acronym for "PHP: Hypertext Preprocessor,"¹⁸ which is a general-purpose open source scripting language that can be embedded in hypertext markup

language (HTML) for web-page development and which can run directly on the server, unlike other languages such as java script. Queries on the database are carried out using PHP. In addition, digitized images and patient information are stored in the database using PHP. Information in the database is first entered into Microsoft EXCEL, and then from there, is imported into the MySQL tables via PHP. This process makes entering new information into the database less tedious than directly entering it into MySQL from the Microsoft Windows command line. Furthermore, a login web page for the web-based search engine is also developed using PHP to limit use of this system to authorized users only. After being logged on to the system, a user can then specify search criteria via the web page. The query is then searched through the MySQL database, and the search results are displayed on the web page. The results are displayed as a list of case names with links to the actual images.

Development of the D-Viewer

The D-viewer is a viewing system developed for visualizing the digitized mammograms. By using this system, radiologists would not only be able to perform various image manipulations, such as circling the area of the cancer and making notes on the image, but could also save these markings as needed. The view system uses graphical user interface (GUI) for easy use and is to be DICOM compliant. The D-viewer system is developed with Microsoft Visual C#, an object-oriented programming language from Microsoft that is easy for manipulating graphics and creating window forms. Currently, the system accepts the following image formats: Windows bitmap (bmp), joint photographic experts group (jpg), tagged image file format (tif/tiff), graphics interchange format (gif), and portable network graphics (png).

RESULTS

Mammography films from 260 patients, each having approximately 20 to 40 images, have been digitized using the Kodak LS85 Laser Scanner. This has resulted in over 5,000 digitized images that have been stored into our database. Many patients had typically 20 to 40 images because they did several

regular screening mammograms before the mammography exam in which the cancer was diagnosed. Hence, on average for each patient, one could be looking at 4–10 different exam dates each of which would contain the four films representing the four typical views (LMLO, RMLO, LCC, RCC). Sometimes, for a particular examination, extra images were taken, depending on if the radiologist was interested in a particular region. All these patients are African-American women from Howard University Hospital who have been diagnosed with cancer between the years 1994 and 2004. In addition, we can compare normal images and images of benign and malignant lesions of the same patient. The image quality is excellent, as the films were digitized at the highest resolution possible by the Digitizer, which was at 512 pixels per inch at a bit depth of 12. Furthermore, there were no observable distortions or artifacts due to the digitization process, although there is some concern that some noise may have been picked up due to possible dirt spots on the films. These images were also approved by the radiologist consultant associated with this study. The digitized image size is either 40 or 60 MB, depending on the size of the mammogram film (8 × 10 or 10 × 12 in., respectively).

A database and a web-based search engine have been developed using MySQL and PHP. Patient information and the corresponding images can be retrieved when queries are made by selecting various criteria. A user is first required to login to access the database (Fig. 2). User accounts will be set up for general users just wanting to learn more about breast cancer and to peruse the database and for users requesting more functionality from the database, such as being able to download the images.

After a user logs in, he or she is directed to the web-search page where he or she can select his or her search criteria (Fig. 3). Currently, the search criteria available include whether the image is normal, benign, or cancer, the year the patient was born, the year the exam was done, total number of examinations for a patient, total number of images for a patient, and the mammography view. For example, a user may want to see all the cancer images of patients who were diagnosed with cancer during 1999–2000 and were born during 1961–1970. There is also a reset button on this page that clears all the search fields. After the search criteria has been selected and submitted, the database returns a list of all patient cases corresponding to that search. The list of cases contains the code name associated with that patient, each series and corresponding exam date of that series, the digitization date for each series, the total number of images in each series, and all available image views done. Figure 4 shows a sample results page of a search.

Finally, Figure 5 shows a snapshot of the D-viewer system with the LCC and RCC views of one of our digitized mammograms. The system can accept bitmap, tiff, jpg, gif, and png image formats. The D-viewer is currently under development.

DISCUSSION

Our research attempts to provide the first major breast cancer database for African-American women. This would allow radiologists and other applicable parties to study various types of African-American women breast cancer cases. Howard University Hospital was chosen not only



Fig 2. Login page of the web-based search engine linked to the breast cancer database.

Volume Type: ☐ Normal ☒ Benign ☒ Cancer ☐ Any

case name:

Density: ☐ 1 ☐ 2 ☐ 3 ☐ 4 ☒ Any

Scanner: ☐ DBA ☐ Lumisys ☐ Howtek ☐ LSS5 ☒ Any

Pathology: ☐ Malignant ☐ Benign ☐ Benign_Without_Callback ☒ Any

Assessment: ☐ 1 ☐ 2 ☐ 3 ☐ 4 ☐ 5 ☒ Any

Subtlety: ☐ 1 ☐ 2 ☐ 3 ☐ 4 ☐ 5 ☒ Any

Lesion Type: ☒ Mass ☐ Calcification

Mass Options		Calcification Options	
Shape (<input type="radio"/> and <input checked="" type="radio"/> or)	Margin (<input type="radio"/> and <input checked="" type="radio"/> or)	Type (<input checked="" type="radio"/> and <input type="radio"/> or)	Distribution (<input checked="" type="radio"/> and <input type="radio"/> or)
<input type="checkbox"/> Round	<input type="checkbox"/> Circumscribed	<input type="checkbox"/> Punctate	<input type="checkbox"/> Clustered
<input type="checkbox"/> Oval	<input type="checkbox"/> Microlobulated	<input type="checkbox"/> Amorphous	<input type="checkbox"/> Linear
<input type="checkbox"/> Lobulated	<input type="checkbox"/> Obscured	<input type="checkbox"/> Pleomorphic	<input type="checkbox"/> Segmental
<input type="checkbox"/> Irregular	<input type="checkbox"/> Ill_Defined	<input type="checkbox"/> Round_And_Regular	<input type="checkbox"/> Regional
<input type="checkbox"/> Architectural_Distortion	<input type="checkbox"/> Spiculated	<input type="checkbox"/> Lucent_Center	<input type="checkbox"/> Diffusely_Scattered
<input type="checkbox"/> Tubular	<input checked="" type="checkbox"/> Any	<input type="checkbox"/> Fine_Linear_Branching	<input checked="" type="checkbox"/> Any
<input type="checkbox"/> Lymph Node		<input type="checkbox"/> Skin_Calcification	
<input type="checkbox"/> Asymmetric_Breast_Tissue		<input type="checkbox"/> Vascular	
<input type="checkbox"/> Focal_Asymmetric_Density		<input type="checkbox"/> Coarse	
<input checked="" type="checkbox"/> Any		<input type="checkbox"/> Large_Rodlike	
		<input type="checkbox"/> Round	
		<input type="checkbox"/> Egg_Shell	
		<input type="checkbox"/> Milk_of_Calcification	

Fig 3. Web-based search page.

for its accessibility, but more importantly, because it services a large African-American community in the Washington DC, Maryland, and Virginia area, thus, providing a large number of African-American women mammography cases. This

research is also significant in an effort to close the gap of diversity in breast cancer mortality.

However, this research is not just about digitizing a large number of mammograms. The database is also being developed as an online

Welcome to the hucb online

Authenticated

Volume_No	Volume_type	case_name
benign_07	benign	case1292
benign_04	benign	case0280
benign_06	benign	case3226
benign_13	benign	case3460
benign_01	benign	case3091
cancer_02	cancer	case0022
cancer_02	cancer	case0024
cancer_01	cancer	case3024
cancer_05	cancer	case0022
cancer_07	cancer	case1233

Your search Criteria was:

Volume type	benign cancer
Density	any
Scanner	any
Pathology	any
Assessment	any
Subtlety	any
Mass Shape	any
Mass Margin	any

Fig 4. Results page of search.

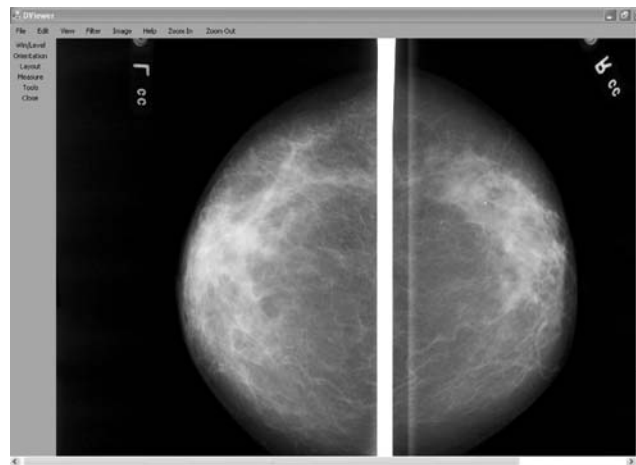


Fig 5. D-viewer user interface.

interactive teaching/training tool geared towards both the radiology students and others interested in learning more about breast cancer. For example, the site would contain general information on breast cancer and more detailed information. Medical students could be asked to perform tasks such as determining, from the image alone, the search criteria required to produce that particular image. This would require the students to be able to accurately identify specific characteristics of that image. Radiologists could also use this database to help their diagnosis process of difficult new cases by searching for similar cases or images.

Our database differs from current major databases such as the one developed by the University of South Florida¹⁴ in that our patient data set consists of African-American women only. Furthermore, we intend our database to be an interactive training tool where the users can look at images and guess the search criteria that they would have had to put in to obtain that image. We also plan to extend the functionality of the database by making it an image-based retrieval system in which features in the image can be used to define the search criteria.

CONCLUSIONS

We have digitized more than 5,000 mammography images of 260 African-American women patients and developed a database and viewing

system for these images. All patients in this study have already been diagnosed with breast cancer. The digitized images include normal, benign, and malignant mammograms, which were taken between the years 1994 and 2004. The normal and benign mammograms of a patient were from routine screenings done before breast cancer was diagnosed. All the mammography images are searchable in the database system via a web-based search engine. They can be viewed in the viewing system and easily manipulated during the viewing process.

Further research will be performed to improve the database and the viewing system. First of all, we will seek input from radiologists when they test our database and viewing system. They will be asked to identify key information from the images such as the presence or absence of malignant cancer, location of cancer, type of cancer (mass or calcification), assessment, subtlety, and density of the breast. Locations of the cancers, if present, on the digitized mammograms, will be marked and saved. The database will also be updated with these added data.

New mammograms will also be collected and digitized to increase the size of our database. The D-viewer system will be further enhanced to improve its functionalities based upon input from the radiologists after testing the system. We will also develop an interactive web-based learning/training/testing system, which can provide detailed information on breast cancer, training sessions for breast cancer diagnosis, and test platforms. To

improve the quality and versatility of our database, we plan to develop an image-based retrieval database, whereby, we can use images instead of words to determine our search criteria. For example, if we circle a region of interest on an image such as a mass, we could query the database to return all images and corresponding information that have a similar region of interest.

This database will be made accessible to radiologists and students via announcements on the Howard Medical School website and on the Howard University Electrical and Computer Engineering Department website. No fees will be charged for basic database access, but fees will be charged for any advanced functions such as image processing or content-based retrieval operations.

ACKNOWLEDGEMENTS

We would like to thank the radiologists and other medical professionals in the Department of Radiology at Howard University Hospital who made significant contributions to this research. This research was supported by the US Army MPMC Breast Cancer Research Partnership Program (No. DAMD17-01-1-0267). Paul Wang was also supported by the following grants: NIH NCCR No. 2G12RR003048, NIH No. 5U54CA091431, US Army MPMC No. W81XWH-05-1-0291 and No. DAMA17-00-1-0291.

REFERENCES

1. American Cancer Society: Breast Cancer Facts and Figures 2005–2006. Atlanta, GA: American Cancer Society, Inc., 2005
2. American Cancer Society: Cancer Facts and Figures 2006. Atlanta, GA: American Cancer Society, Inc., 2006
3. Abeloff MD, Wolff AC, Wood WC, McCormick B, Weber BL: Cancer of the Breast. In: Clinical Oncology, Philadelphia, PA: Elsevier, 2004
4. Young Jr, JL, Roffers SD, Ries LAG, Fritz AG, Hurlbut A, Eds.: SEER Summary Staging Manual—2001: Codes and Coding Instructions, Bethesda, MD: National Cancer Institute, 2001
5. Rovak-Schaler R, Rose DP: Mammography screening and breast cancer biology in African American women—a review. *Cancer Detect Prev* 26:180–191, 2002
6. SEER Cancer Statistics Review, 1975–2002, National Cancer Institute. Available at http://seer.cancer.gov/csr/1975_2002/. Accessed 31 May 2006
7. Elledge RM, Clark GM, Chamness GC, Osborne CK: Tumor biologic factors and breast cancer prognosis among white, hispanic, and black women in the United States. *J Natl Cancer Inst* 86:705–712, 1994
8. Bach PB, Schrag D, Brawley OW, Galaznik A, Yakren S, Begg C: Survival of blacks and whites after a cancer diagnosis. *JAMA* 287:2106–2113, 2002
9. Joslyn SA: Racial differences in treatment and survival from early stage breast carcinoma. *Cancer* 95:1759–1766, 2002
10. Shavers VI, Brown ML: Racial and ethnic disparities in the receipt of cancer treatment. *J Natl Cancer Inst* 95:334–357, 2002
11. Chlebowski RT, Chen Z, Anderson GL, Rohan T, Aragaki A, Lane D, Dolan N, Paskett E, McTiernan A, Hubbell FA, Adams-Campbell LL, Prentice R: Ethnicity and breast cancer factors influencing difference in incidence and outcome. *J Natl Cancer Inst* 97:439–448, 2005
12. Porter PL, Lund MJ, Lin MG, Yuan X, Liff JM, Flag EW, Coates RJ, Eley JW: Racial differences in the expression of cell cycle-regulatory proteins in breast carcinoma: study of young African American and white women in Atlanta, Georgia. *Cancer* 100:2533–2542
13. Digital Database for Screening Mammography. Available at http://figment.csee.usf.edu/Mammography/DDSMD/thumbnails/normals/normal_01/case0130/A-0130-1.html. Accessed 31 May 2006
14. University of South Florida Digital Mammography Home Page. Available at <http://figment.csee.usf.edu/Mammography/Database.html>. Accessed 31 May 2006
15. Human Participant Protections Education for Research Teams, National Cancer Institute. Available at <http://cme.cancer.gov/clinicaltrials/learning/humanparticipant-protections.asp>. Accessed 31 May 2006
16. Ross S, Ejofodomi O, Jendoubi A, Chouikha M, Lo B, Wang P, Zeng J: A mammography database and view system for the African American patients. In: Emerging Technologies and Applications for Imagery Pattern Recognition, Los Alamitos, CA: IEEE Computer Society, 2005
17. MySQL Reference Manual. Available at <http://dev.mysql.com/doc/refman/5.0/en/>. Accessed 31 May 2006
18. PHP: PHP Manual - Manual. Available at <http://www.phpbuilder.com/manual/>. Accessed 31 May 2006

Alexa Fluor 680-labeled transferrin-cationic (NBD-labeled DOPE-DOTAP) liposome-encapsulated gadopentetate dimeglumine complex

Tf^{NIR}-Lip^{NBD}-CA complex

Kenneth T. Cheng, Paul C. Wang, and Liang Shan

National Center for Biotechnology Information, NLM, NIH, Bethesda, MD
E-mail: Chengke@mail.nih.gov

Department of Radiology, Howard University, Washington, DC, Corresponding Author
E-mail: pwang@howard.edu

Department of Radiology, Howard University, Washington, DC
E-mail: lshan@howard.edu

Created: October 18, 2007
Updated: December 17, 2007

Chemical name: Alexa Fluor 680-labeled
transferrin- cationic (NBD-
labeled DOPE-DOTAP)
liposome-encapsulated
gadopentetate dimeglumine
complex

Abbreviated name: Tf^{NIR}-Lip^{NBD}-CA complex

Synonym: Alexa Fluor 680-Tf-Lip-CA

Backbone: Liposome

Target: Transferrin receptor (TfR)

Mechanism:

Method of detection: Optical (Near-infrared (NIR)
fluorescent) imaging,
magnetic resonance imaging
(MRI)

Source of signal/ contrast: Alexa Fluor 680, gadolinium

Activation: No

Studies: ✓ *In vitro*
✓ Rodents

Click on protein [<http://www.ncbi.nlm.nih.gov/entrez/viewer.fcgi?db=protein&id=4507457>], nucleotide (RefSeq), [<http://www.ncbi.nlm.nih.gov/entrez/viewer.fcgi?db=nucleotide&id=123999041>] and gene [http://www.ncbi.nlm.nih.gov/sites/entrez?Db=gene&Cmd=ShowDetailView&TermToSearch=7037&ordinalpos=1&itool=EntrezSystem2.PEntrez.Gene.Gene_ResultsPanel.Gene_RVDocSum] for more information about transferrin receptors.

Background

[PubMed [

Alexa Fluor 680-labeled transferrin-cationic (NBD-labeled DOPE-DOTAP) liposome-encapsulated gadopentetate dimeglumine complex (Tf^{NIR}-Lip^{NBD}-CA complex) is a dual (multimodality) molecular imaging probe with fluorescent and magnetic properties that can be used for imaging tumors with overexpressed transferrin (Tf) receptors (1). Alexa Fluor 680 is a near-infrared (NIR) fluorescence dye with an absorption maximum of 679 nm, an emission maximum of 720 nm, and an extinction coefficient of 180,000 cm⁻¹M⁻¹ (2). Gadopentetate dimeglumine (Gd-DTPA) is a water-soluble paramagnetic contrast agent approved by the United States Food and Drug Administration for contrast enhancement in magnetic resonance imaging (MRI) (3).

Tf is part of a family of proteins that includes serum Tf, ovotransferrin, and lactoferrin (4). Serum Tf is a monomeric glycoprotein (molecular mass, 80 kDa) that binds Fe³⁺ for delivery to vertebrate cells through receptor-mediated endocytosis (1). The Tf receptor (TfR) mediates the internalization of iron-loaded Tf into cells (4, 5). The TfR (CD71) is a type II transmembrane glycoprotein and is found primarily as a homodimer (molecular mass, 180 kDa). It also contains other growth regulatory properties in certain normal and malignant cells. The elevated levels of TfR in some malignancies (e.g., 74% breast carcinomas, 76% lung adenocarcinomas, and 93% lung squamous cell carcinomas) and the extracellular accessibility of this molecule make TfR a potential molecular target for cancer imaging or therapy.

Liposomes (Lips) are small nontoxic vesicles composed of lipid bilayers enclosing aqueous volume, and they are versatile carriers of both therapeutic drugs and imaging agents (5-7). Although Lips are naturally taken up by the reticuloendothelial system, the size, charge, and surface of Lips can be modified for targeting purposes. Because of the intrinsically low sensitivity of MRI and the low penetration of light, optical and MRI multifunctional probes have been developed as one of the possible approaches to enhance the clinical and research applications of both imaging modalities (1, 8, 9). Shan et al. (1) reported the preparation of a dual probe with fluorescent and magnetic properties based on Lips targeting to TfR-overexpressed tumors. In this Tf^{NIR}-Lip^{NBD}-CA complex, Alexa Fluor 680-labeled Tf was linked on the surface of cationic Lips with Gd-DTPA encapsulated inside the vesicles.

Synthesis

[PubMed [

The Tf^{NIR}-Lip^{NBD}-CA complex was synthesized with the Alexa Fluor 680 conjugate of human Tf (Tf^{NIR}), cationic Lips (Lip^{NBD}) and commercially available Gd-DTPA (CA) (1). The cationic Lip^{NIB} used the green fluorescent formula of 1,2-dioleoyl-3-trimethylammonium-propane (DOTAP): 1,2-dioleoyl-sn-glycero-3-phosphoethanolamine (DOPE) in a ratio of 1:1 (w/w) plus 0.1% DOPE-*N*-(7-nitro-2-1,3-benzoxadiazole-4-yl) (NBD-DOPE). Briefly, the lipids were mixed in chloroform and then dried under a nitrogen stream. The Lip^{NBD}-CA was formed by reconstituting the dried lipid

mixture with 50 μ l water containing 12 μ l of Gd-DTPA (commercial formulation of 469.01 μ g/ μ l). The Lip^{NBD}-CA was homogenized and incubated for 10 min. The Lip volume was adjusted to 175 μ l with water and then sequentially downsized by sonication (80–90 W, 10 min) and filtration with decreasing pore diameter from 0.2 to 0.1 μ m. Finally, Tf^{NIR} (5 mg/ml) was added and incubated for at least 10 min. Unencapsulated CA and free Tf^{NIR} were removed by gel filtration chromatography. The final Lip:Tf:Gd-DTPA ratio was 10:12.50:0.56 (nmol: μ g:mg).

In Vitro Studies: Testing in Cells and Tissues

[PubMed [[http://www.ncbi.nlm.nih.gov/sites/entrez?Db=pubmed&Cmd=DetailsSearch&Term=\(\(liposome\)+AND+\(Fluorescent\)\)+AND+\(Magnetic\)\)+AND+in+vitro](http://www.ncbi.nlm.nih.gov/sites/entrez?Db=pubmed&Cmd=DetailsSearch&Term=((liposome)+AND+(Fluorescent))+AND+(Magnetic))+AND+in+vitro)]]

Shan et al. (1) conducted cellular uptake tests of Tf-Lip^{NBD}-NIR dye with TfR-overexpressed MDA-MB-231-luc human breast cancer cells. In this study, Tf was not labeled with Alexa Fluor 680. Instead, Alexa Fluor 680 (red dye) was encapsulated by Lip^{NBD} (green fluorescent) so that the encapsulated reagent (the red dye in place of CA) and the Lip could be observed by confocal microscopy. After incubation with the cells, both the green Lip^{NBD} and the encapsulated red dye were observed in the cell cytoplasm as early as 5 min. The fluorescent intensity (FI) within the cytoplasm increased gradually and reached a maximum at ~1 h. The Lip^{NBD} and red dye then accumulated again to form multiple endosomes at the peripheral area of the cytoplasm. The authors suggested that this might represent the release or degradation of the probe through the action of lysosomal enzymes. In comparison, when the red dye alone was incubated with the cells, no cellular uptake was observed. The efficiency of the uptake was quantified on cell pellets after 1 h of incubation. The red dye FI values ($\text{p/s/cm}^2/\text{steradian (sr)} \times 10^9$; $n = 3$) were 6.88 ± 0.59 , 4.99 ± 0.51 , and 0.23 ± 0.006 for Tf-Lip^{NBD} dye, Lip^{NBD} -dye, and dye alone, respectively. The green dye FI values ($\text{p/s/cm}^2/\text{sr} \times 10^7$; $n = 3$) were 2.03 ± 0.14 , 1.64 ± 0.09 , and 1.10 ± 0.13 for Tf-Lip^{NBD}-dye, Lip^{NBD}-dye, and dye alone, respectively. In the blocking study in which the cells were pretreated with unlabeled Tf (three-fold higher amount) before incubation with Tf-Lip^{NBD} dye, the red dye FI value decreased from 3.42×10^9 p/s/cm²/sr to 2.45×10^9 p/s/cm²/sr with a 65.6% blockage of dye uptake. The green dye FI value for Lip^{NBD} dye decreased from 3.45×10^7 p/s/cm²/sr to 2.57×10^7 p/s/cm²/sr with a 71.0% blockage of Lip^{NBD} uptake.

In another study, where Tf^{NIR}-Lip^{NBD}-CA was incubated with the cells, optical imaging and confocal microscopy confirmed that both Tf^{NIR} and Lip^{NBD} were colocalized within cell cytoplasm after 5 min of incubation (1). To measure the presence of CA within the cells, MRI (400-MHz NMR spectrometer) was also performed on cell pellets obtained from cells incubated with Tf^{NIR}-Lip^{NBD}-CA. The T₁ relaxation times ($n = 3$) were 408.1 ± 13.8 ms, 374 ± 17.3 ms, and 366 ± 17.1 ms for cells incubated with CA, Lip^{NBD}-CA, and Tf^{NIR}-Lip^{NBD}-CA, respectively.

Animal Studies

Rodents

[PubMed [http://www.ncbi.nlm.nih.gov/sites/entrez?Db=pubmed&Cmd=DetailsSearch&Term=((liposome)+AND+(Fluorescent)+AND+(Magnetic))+AND+mice]]

Shan et al. (1) evaluated the tumor signal enhancement in nude mice ($n = 10$) bearing the subcutaneous MDA-MB-231-luc human breast cancer (0.4–1.2 cm diameter). Each mouse received 200 μ l of Tf^{NIR}-Lip^{NBD}-CA (containing 12 μ l Gd-DTPA) by i.v. injection. MRI imaging using a 400-MHz NMR spectrometer and a T₁-weighted spin-echo sequence (repetition time = 800 ms, echo time = 11.4 ms) showed significant tumor contrast enhancement as early as 10 min and reached a maximum at 90–120 min. The enhancement appeared to be more heterogeneous in larger tumors but more uniform in smaller tumors. Pathology results showed that the highly enhanced regions represented the more actively proliferating tumor cells. The weakly enhanced areas contained dying cells and the necrotized regions. Giving the CA alone enhanced the tumor contrast only slightly. The CA enhancement started from the peripheral area to the center and reached the maximum in 30–60 min. CA containing Lip without linkage to Tf showed an even weaker signal enhancement. No blocking study was performed.

Optical imaging of Tf^{NIR}-Lip^{NBD}-CA based on Tf^{NIR} showed clear tumor signal as early as 10 min and reached a maximum at 90–120 min (1). The FI was related to the tumor sizes and showed detectable FI in larger tumors (>0.8 cm diameter) after 2 days. The FI of Lip^{NBD} was too weak to be detected. The probe was rapidly distributed throughout the body. It was taken up by well-perfused organs and then rapidly washed out. The probe activity remained in the tumor and was not washed out. The tumor/contralateral muscle ratios varied from 1.3 to 3.4 within 10 min to 48 h. This ratio appeared to be dependent on tumor sizes. Small tumors (<3 mm diameter) showed less FI than the bigger tumors. In comparison, administration of the red dye containing Lip without linkage to Tf showed no tumor signal enhancement.

Other Non-Primate Mammals

[PubMed [http://www.ncbi.nlm.nih.gov/sites/entrez?Db=pubmed&Cmd=DetailsSearch&Term=((liposome)+AND+(Fluorescent)+AND+(Magnetic))+AND+(dog+OR+rabbit+OR+pig+OR+sheep)]]

No publication is currently available.

Non-Human Primates

[PubMed [http://www.ncbi.nlm.nih.gov/sites/entrez?Db=pubmed&Cmd=DetailsSearch&Term=((liposome)+AND+(Fluorescent)+AND+(Magnetic))+AND+(primate+NOT+human)]]

No publication is currently available.

Human Studies

[PubMed [[http://www.ncbi.nlm.nih.gov/sites/entrez?Db=pubmed&Cmd=DetailsSearch&Term=\(\(liposome\)+AND+\(Fluorescent\)+AND+\(Magnetic\)\)+AND+human](http://www.ncbi.nlm.nih.gov/sites/entrez?Db=pubmed&Cmd=DetailsSearch&Term=((liposome)+AND+(Fluorescent)+AND+(Magnetic))+AND+human)]]

No publication is currently available.

NIH Support

NCRR 2G12RR003048, NIH 5U54CA091431.

References

1. Shan L., Wang S., Sridhar R., Bhujwalla Z.M., Wang P.C.. *Dual probe with fluorescent and magnetic properties for imaging solid tumor xenografts*. Mol Imaging **6**(2):85–95; 2007. (PubMed)
2. Berlier J.E., Rothe A., Buller G., Bradford J., Gray D.R., Filanoski B.J., Telford W.G., Yue S., Liu J., Cheung C.Y., et al. *Quantitative comparison of long-wavelength Alexa Fluor dyes to Cy dyes: fluorescence of the dyes and their bioconjugates*. J Histochem Cytochem **51**(12):1699–1712; 2003. (PubMed)
3. Runge V.M.. *Safety of approved MR contrast media for intravenous injection*. J Magn Reson Imaging **12**(2):205–213; 2000. (PubMed)
4. Daniels T.R., Delgado T., Rodriguez J.A., Helguera G., Penichet M.L.. *The transferrin receptor part I: Biology and targeting with cytotoxic antibodies for the treatment of cancer*. Clin Immunol **121**(2):144–158; 2006. (PubMed)
5. Daniels T.R., Delgado T., Helguera G., Penichet M.L.. *The transferrin receptor part II: targeted delivery of therapeutic agents into cancer cells*. Clin Immunol **121**(2):159–176; 2006. (PubMed)
6. Cheng K.T., Seltzer S.E., Adams D.F., Blau M.. *The production and evaluation of contrast-carrying liposomes made with an automatic high-pressure system*. Invest Radiol **22**(1):47–55; 1987. (PubMed)
7. Hatakeyama H., Akita H., Maruyama K., Suhara T., Harashima H.. *Factors governing the in vivo tissue uptake of transferrin-coupled polyethylene glycol liposomes in vivo*. Int J Pharm **281**(1-2):25–33; 2004. (PubMed)
8. Veisheh O., Sun C., Gunn J., Kohler N., Gabikian P., Lee D., Bhattarai N., Ellenbogen R., Sze R., Hallahan A., et al. *Optical and MRI multifunctional nanoprobe for targeting gliomas*. Nano Lett **5**(6):1003–1008; 2005. (PubMed)
9. Kircher M.F., Mahmood U., King R.S., Weissleder R., Josephson L.. *A multimodal nanoparticle for preoperative magnetic resonance imaging and intraoperative optical brain tumor delineation*. Cancer Res **63**(23):8122–8125; 2003. (PubMed)

Regulation of Inflammation- and Angiogenesis-related Gene Expression in Breast Cancer Cells and Co-cultured Macrophages

GISELLE T. BURNETT¹, DENISE C. WEATHERSBY^{1,2}, TIFFANY E. TAYLOR¹ and THEODORE A. BREMNER^{1,3}

¹Department of Biology, Howard University, 415 College St, NW, Washington DC 20059;

²University of Texas, Graduate School of Biomedical Sciences at Houston, 6767 Bertner, Houston, TX 77030;

³Howard University Cancer Center, 2041 Georgia Avenue, NW, Washington, DC 20060, U.S.A.

Abstract. *Background:* Tumor-associated macrophages (TAMs) secrete key modifiers of tumor progression and their modification has been proposed as a therapeutic strategy. Phenotypic changes that may render TAMs selectively vulnerable to anti-cancer agents were examined. *Materials and Methods:* Gene arrays, reverse transcription-polymerase chain reaction and Western blotting were used to study inflammation- and angiogenesis-related gene expression in co-cultured breast cancer cells and macrophages and to determine how their interactions were affected by tamoxifen and aspirin. *Results:* MCF-7 (mammary adenocarcinoma) cells down-regulated macrophage migration inhibitory factor (MIF), but tamoxifen-pretreated MCF-7 cells up-regulated MIF in co-cultured macrophages. Two molecular variants of MIF were observed in the co-cultured MCF-7 cells. Aspirin induced IL-10 expression in the macrophages, MCF-7 and tamoxifen-pretreated MCF-7 cells. Aspirin-pretreated macrophages potently induced IL-10 expression in the MCF-7 cells. *Conclusion:* Because MIF is a determinant of the M1 macrophage activation state, the MCF-7-induced ablation of MIF in TAMs is suggestive of partial M2 polarization. Tamoxifen modulates MCF-7 regulation of TAM gene expression and aspirin alters macrophage regulation of MCF-7 gene expression.

The microenvironment of epithelial tumors plays a decisive role in tumor progression (1, 2). Tumor-associated macrophages (TAMs) can initiate both angiogenesis and invasion (3-5). Two alternate activation states of macrophages

are generally recognized, M1, characterized by the production of pro-inflammatory cytokines, reactive oxygen species and nitric oxide and M2, characterized by the production of anti-inflammatory cytokines, synthesis of prostaglandin E₂ and the ability to stimulate angiogenesis (6). The specific nature of the macrophage contribution to disease may depend on its polarization status. Inflammatory macrophages can alter prostate cancer cell responsiveness to selective androgen receptor modulators (SARMs) (7), whereas, M2 macrophages may play a role in reversing insulin resistance (8). Furthermore, stromal cells and epithelial cells may respond differentially to the same pharmacological agents, as has been demonstrated for hedgehog signaling in breast cancer (9).

Macrophage migration inhibitory factor (MIF), a pro-inflammatory cytokine and key modulator of immune responses, is constitutively expressed by macrophages, potentiates their inflammatory activity and sustains survival by inhibiting activation-induced, p53-mediated apoptosis (10-14). MIF is also secreted by cancer cells and has been implicated in several stages of tumor progression (14-16). MIF knockdown in murine ovarian cancer cell implants was associated with decreased expression of *TNF- α* , *IL-6* and *IL-10* and reduced macrophage recruitment (17). MIF prevents apoptosis of neutrophils by inhibiting the intrinsic pathway (18) and promotes the survival of primary and immortalized fibroblasts and various breast cancer cell lines, by activating the phosphoinositide 3-kinase (PI3K)-Akt pathway (19, 20). MIF may also promote monocyte recruitment and metastasis because it is a non-cognate ligand for the chemokine receptors CXCR2 and CXCR4 (21, for a review of CXCR4 see 22). MIF signals through the CD (cluster of differentiation) 74-CD44 membrane receptor complex to activate extracellular signal-regulated kinase (ERK) 1/2 and the PI3K-Akt pathway to promote proliferation and survival (23, 24). Upon binding of MIF, the CD74 intracellular domain (ICD) translocates to the nucleus and induces activation of nuclear factor-kappa B (NF- κ B) (25). MIF potentiates lipopolysaccharide (LPS)

Correspondence to: Theodore A. Bremner, Ph.D., Department of Biology, Howard University, 415 College Street, NW, Washington, DC 20059, U.S.A. Tel: +202 806 6957, Fax: +202 806 4564, e-mail: tbremner@howard.edu

Key Words: Angiogenesis, inflammation, MIF, IL-10, tamoxifen, aspirin.

signaling by up-regulating Toll-like receptor (TLR) 4. MIF-deficient macrophages are hyporesponsive to LPS, as shown by a reduction in NF- κ B activity and TNF- α production (26). MIF has been proposed to function both as a systemically acting, 'endocrine' cytokine and as part of a locally acting feedback loop limiting the anti-inflammatory actions of glucocorticoids (27, 28).

Because anti-cancer therapies that include targeting of stromal cells are likely to be more effective, inflammation- and angiogenesis-related gene expression in co-cultured breast cancer cells and macrophages, which may render macrophages selectively vulnerable to pharmacological agents, was examined. MIF interferes with p53 activity (13, 14), and p53 and phosphatase and tensin homologue deleted on chromosome 10 (PTEN) function collaboratively in a tumor-suppressive network (29). Therefore, the expression of p53 and PTEN in recombinant human MIF (rhMIF)-treated breast cancer cells and macrophages was also examined. Additionally, the effects of tamoxifen and nonsteroidal anti-inflammatory drugs (NSAIDs) on the regulation of gene expression in macrophages and breast cancer cells were also investigated. Tamoxifen is widely used for the prevention and treatment of breast cancer and NSAIDs are thought to be effective in cancer prevention (30).

Materials and Methods

Materials. Phorbol-12 myristate 13-acetate (PMA) was obtained from Alexis® Biochemicals (San Diego, CA, USA). LPS (*E. coli* 055: B5), tamoxifen citrate and aspirin were obtained from Sigma Chemical Company (St. Louis, MO, USA). Recombinant human MIF (rhMIF, 289-MF) was obtained from R&D Systems (Minneapolis, MN, USA). RPMI Medium 1640, Minimum Essential Medium (MEM), FBS, penicillin, streptomycin, L-glutamine and all the primers for PCR were obtained from Invitrogen Corporation (Carlsbad, CA, USA). The rabbit anti-human MIF polyclonal antibody (sc-20121) was obtained from Santa Cruz Biotechnology (Santa Cruz, CA, USA).

Cell culture. THP-1 (human monocytic leukemia) cells, MCF-10A (pseudonormal mammary epithelial) cells, MCF-7 (mammary adenocarcinoma) cells and MDA-MB-231 (mammary adenocarcinoma) cells were obtained from American Type Culture Collection (ATCC) (Manassas, VA, USA). The THP-1 cells were differentiated to macrophages with PMA (100 nM) for 3 days, then activated with LPS (20 ng/ml) for 5 h.

The THP-1 cells were cultured in RPMI Medium 1640 supplemented with 7.5% FBS, 100 units/ml penicillin, 100 μ g/ml streptomycin and 50 μ M β -mercaptoethanol (β -EtSH). The MCF-10A, MCF-7 and MDA-MB-231 cells were propagated in MEM supplemented with 8% FBS, 100 units/ml penicillin, 100 μ g/ml streptomycin and 292 μ g/ml L-glutamine. All the cells were grown at 37°C in a humidified atmosphere of 95% air:5% CO₂.

For the co-culture experiments, 1 \times 10⁶ THP-1 cells per well were seeded in the inserts (3- μ m pore size) of 6-well Transwell™ chambers (Corning Incorporated, Corning NY, USA), differentiated one day later with PMA and activated with LPS. The MCF-7 cells

at 5 \times 10⁵ per well were seeded in a separate chamber, two days after the THP-1 cells were seeded. The medium of both the breast cancer cells and the activated macrophages was changed, the inserts with the activated macrophages were placed above the breast cancer cells and the chambers were incubated for 3 days. Where indicated, the cells were treated with tamoxifen (10 μ M) for 24 h, aspirin (1 mM) for 24 h, and rhMIF (10 ng/ml) for 6 h prior to RNA isolation. Where pre-treatment is indicated, cells were exposed to the first agent for a specified time period and then to the second.

Cell lysis and Western blotting. The cells were washed with phosphate-buffered saline (PBS) and lysed with buffer (10 mM hydroxyethyl piperazine-ethanesulfonic (HEPES) pH 7.5, 1% sodium dodecyl sulfate (SDS), and 1 mM sodium orthovanadate) at 100°C. The lysate was heated for 4 min at 95°C, then passed through a 26-gauge needle. The protein concentration was determined by the BIO-RAD detergent-compatible protein microassay (Sigma Chemical Company, St. Louis, MO, USA). Fifty μ g of lysate protein was heated at 95°C for 5 min in Laemmli sample buffer containing 4% SDS, 20% glycerol, 10% 2-mercaptoethanol, 0.004% bromophenol blue and 0.125 M Tris HCl pH 6.8 (Sigma Chemical Company, St. Louis, MO, USA). The samples were subjected to SDS-polyacrylamide gel electrophoresis on 4-20% Precise™ protein gels (Pierce, Rockford, IL, USA), and the separated proteins were transferred onto a nitrocellulose membrane. The membrane was blocked with Tris-buffered saline containing 0.1% Tween-20 (TBST) and 5% non-fat dry milk for 1 h at room temperature (RT) and then incubated with primary antibody diluted in TBST containing 0.5% non-fat dry milk for 1 h at RT. The membrane was incubated with horseradish peroxidase-conjugated goat anti-rabbit antibody (sc-2004, Santa Cruz Biotechnology) at RT for 1 h. The proteins were visualized using the enhanced chemiluminescence (ECL) Plus Western Blotting Detection System (Amersham Biosciences UK Limited, Buckinghamshire, England), as recommended in the manufacturer's instructions.

RNA extraction and cDNA synthesis. The cells were washed with PBS and RNA was extracted using Trizol reagent (Invitrogen Corporation), or the Versagene™ RNA Purification kit (Gentra Systems, Minneapolis, MN, USA), in accordance with the manufacturer's protocol. The cDNA was synthesized using the Advantage™ RT-for-PCR kit (Clontech Laboratories, Mountain View, CA, USA), according to the manufacturer's instructions.

Pathway-focused gene arrays. For the pathway-focused gene arrays (SuperArray Bioscience Corp., Frederick, MD, USA), 5 μ g total RNA from monocytes, unactivated macrophages, co-cultured unactivated macrophages, MCF-7 cells and co-cultured MCF-7 cells was reverse transcribed into biotin-labeled cDNA. The labeled cDNA was hybridized to pathway-focused microarrays for human pro-inflammatory cytokine and receptor genes (HS-015.2), or for angiogenesis-related genes (HS-009), each containing 96 test genes and four positive control (housekeeping) genes. The membranes were incubated with alkaline phosphatase (AP)-streptavidin, visualized by chemiluminescence and exposed to x-ray film.

Semiquantitative reverse transcription-polymerase chain reaction (RT-PCR). A 3- μ l aliquot of the cDNA was used for PCR amplification together with the primer pairs (10 μ M each), 10 \times

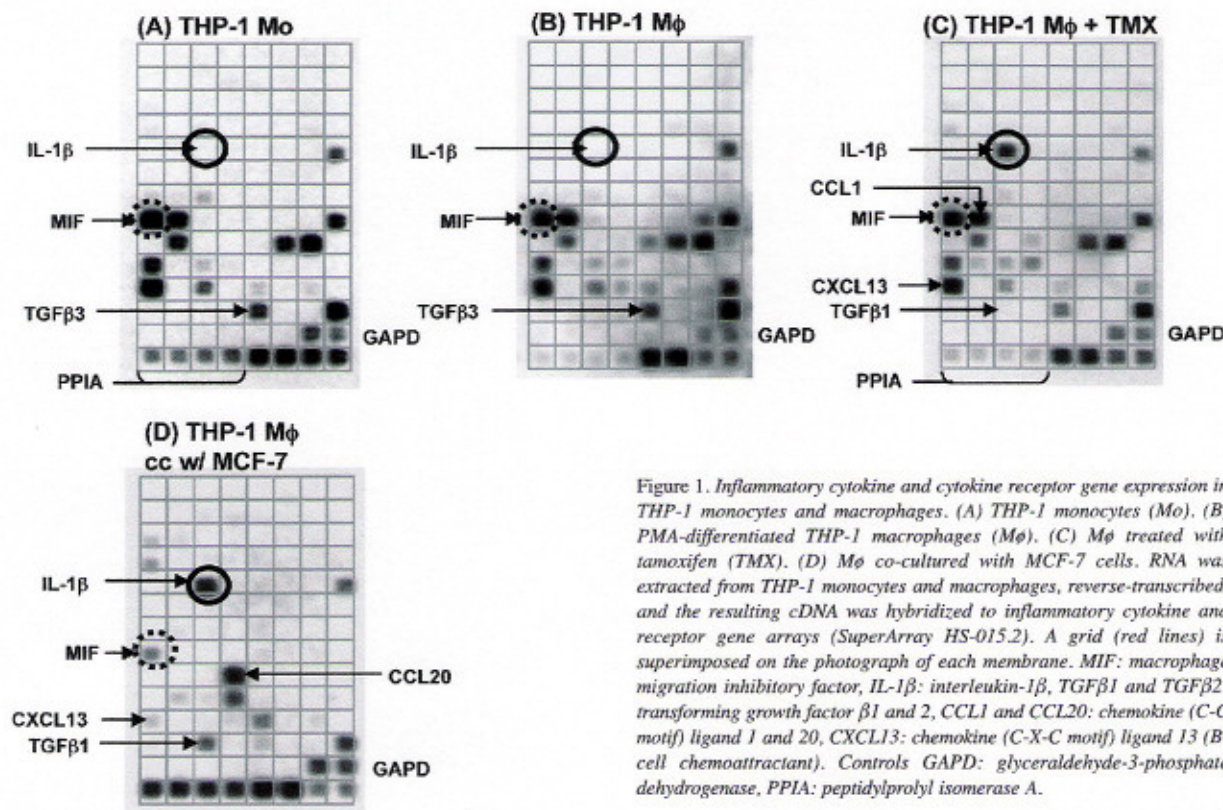


Figure 1. Inflammatory cytokine and cytokine receptor gene expression in THP-1 monocytes and macrophages. (A) THP-1 monocytes (Mo). (B) PMA-differentiated THP-1 macrophages (Mφ). (C) Mφ treated with tamoxifen (TMX). (D) Mφ co-cultured with MCF-7 cells. RNA was extracted from THP-1 monocytes and macrophages, reverse-transcribed, and the resulting cDNA was hybridized to inflammatory cytokine and receptor gene arrays (SuperArray HS-015.2). A grid (red lines) is superimposed on the photograph of each membrane. MIF: macrophage migration inhibitory factor, IL-1β: interleukin-1β, TGFβ1 and TGFβ2: transforming growth factor β1 and 2, CCL1 and CCL20: chemokine (C-C motif) ligand 1 and 20, CXCL13: chemokine (C-X-C motif) ligand 13 (B-cell chemoattractant). Controls GAPD: glyceraldehyde-3-phosphate dehydrogenase, PPIA: peptidylprolyl isomerase A.

PCR buffer, deoxynucleoside triphosphates (dNTPs) (100 μM each), MgCl₂ and AmpliTaq Gold DNA polymerase (1.25 Units/reaction volume) (Applied Biosystems, Foster City, CA, USA), in a final volume of 25 μl. The following primers were used for PCR: *MIF*, 5'-CTCTCCGAGCTC-ACCCAGCAG-3' (forward) and 5'-CGCGT TCATGTCGTAATA-GTT-3' (reverse); *p53*, 5'-CAGCCAAGTCTG TGAATTGCA-CGTAC-3' (forward) and 5'-CTATGTCGAAAAGT GTTT-CTGTCATC-3' (reverse); *PTEN*, 5'-CTTCTCTTTTTTCT GTCC-3' (forward) and 5'-AAG-GATGAGAATTTCAAGCA-3' (reverse). The PCR conditions included: for *MIF*, 35 cycles of 94°C, 1 min, 60°C, 1 min, 72°C, 1 min and 72°C, 10 min; for *p53*, 95°C, 15 min and 50 cycles of 94°C, 15 sec, 55°C, 15 sec, 72°C, 15 sec; for *PTEN*, 95°C, 2 min and 35 cycles of 94°C, 30 sec, 57°C, 30 sec, 72°C, 30 sec, and 72°C, 10 min. The expected amplicon sizes were 255 bp, 293 bp and 191 bp for *MIF*, *p53*, and *PTEN*, respectively. The PCR products were separated on 1.2% agarose gels.

Results

Inflammatory cytokine and cytokine receptor gene expression. MIF RNA was slightly down-regulated in the macrophages (Figure 1A, 1B), but dramatically down-regulated in the macrophages co-cultured with the MCF-7 cells (Figure 1D). While *IL-1β* was not expressed in the THP-1 monocytes or macrophages, it was highly induced in

the macrophages co-cultured with the MCF-7 cells (Figure 1A, 1B and 1D). Surprisingly, tamoxifen potently induced *IL-1β* expression in the macrophages (Figure 1B and 1C).

Angiogenesis-related gene expression. The macrophages (Figure 2A), tamoxifen-treated macrophages (Figure 2B) and co-cultured macrophages (Figure 2D) did not express *IL-10*. Aspirin potently induced *IL-10* expression in the macrophages (Figure 2C), but not in the co-cultured macrophages (Figure 2F). However, aspirin pre-treated macrophages induced *IL-10* in both untreated and tamoxifen-pretreated MCF-7 cells (data not shown).

RT-PCR for MIF. RT-PCR was used to confirm the changes in *MIF* expression observed in the gene arrays. All the cells studied expressed *MIF* RNA. *MIF* RNA was up-regulated in the MCF-7 cells co-cultured with activated macrophages. The RT-PCR confirmed the observation that the *MIF* levels were down-regulated in the macrophages co-cultured with the MCF-7 cells (Figure 3A).

Variants of MIF protein in co-cultured MCF-7 cells. Western blot analysis showed two forms of MIF, a larger, macrophage-type and a smaller, MCF-7-type. Although the

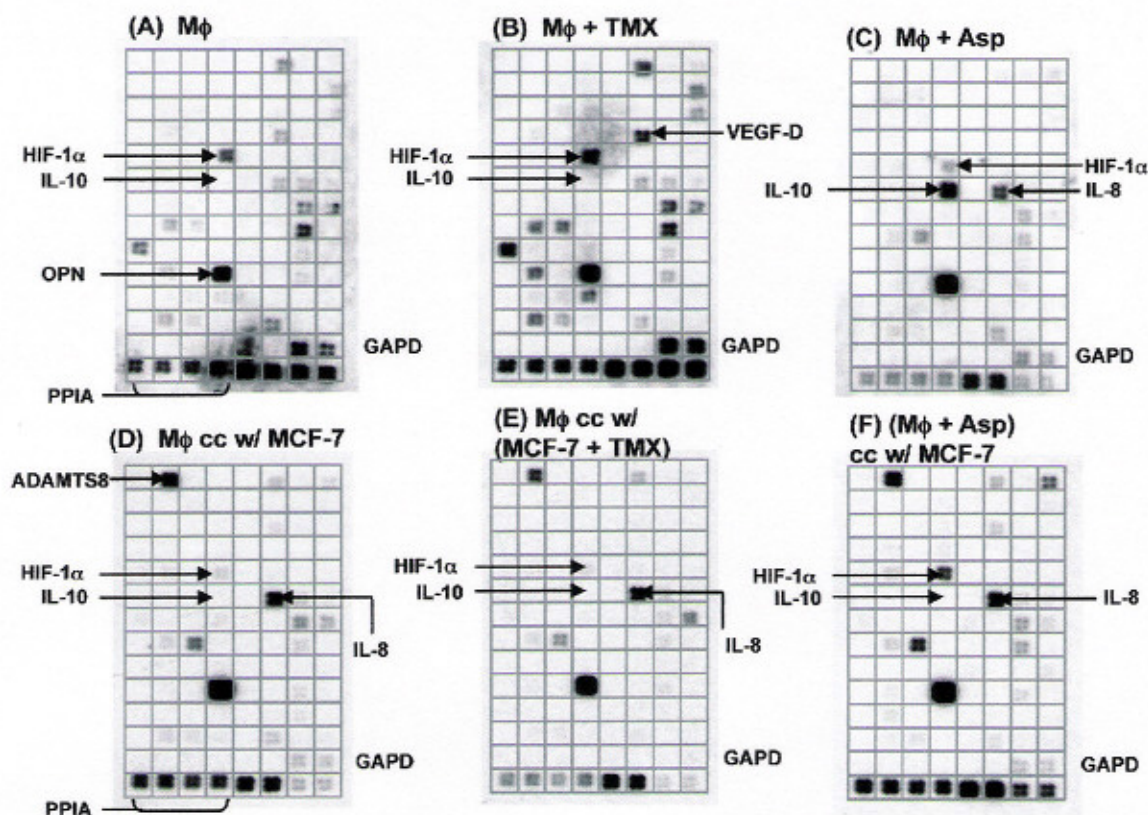


Figure 2. Angiogenesis-related gene expression in THP-1 macrophages. (A) PMA-differentiated THP-1 macrophages ($M\phi$). (B) $M\phi$ treated with tamoxifen (TMX). (C) $M\phi$ treated with aspirin (Asp). (D) $M\phi$ co-cultured with MCF-7 cells. (E) $M\phi$ co-cultured with tamoxifen-pretreated MCF-7 cells. (F) Aspirin-pretreated $M\phi$ co-cultured with MCF-7 cells. RNA was extracted from THP-1 macrophages and used for gene arrays (SuperArray HS-009). HIF-1 α : hypoxia-inducible factor 1, α subunit (basic helix-loop-helix transcription factor), IL-8 and IL-10: interleukin 8 and 10, VEGF-D: vascular endothelial growth factor D, OPN: osteopontin, ADAMTS8: a disintegrin-like and metalloprotease (reprolysin type) with thrombospondin type 1 motif, 8. Controls GAPD: glyceraldehyde-3-phosphate dehydrogenase, PPIA: peptidylprolyl isomerase A.

MIF RNA levels were increased in the activated macrophages (Figure 3A), the MIF protein was decreased (Figure 3B). The MIF protein levels were higher in the co-cultured, activated macrophages than in the activated macrophages, although the MIF RNA levels were lower. Both the MIF RNA and protein levels were increased in the co-cultured MCF-7 cells, which contained both MIF variants.

Effect of recombinant human MIF on p53 and PTEN. The rhMIF down-regulated p53 in all of the cells (Figure 4A). p53 was detectable in THP-1 cells, and in unactivated and activated macrophages. The activated macrophages increased PTEN RNA in the MCF-7 cells (Figure 4B). Of the three breast cell lines studied, MCF-10A had the highest level of PTEN RNA, which was consistent with its non-transformed status (Figure 4B). rhMIF down-regulated PTEN in all of the cells (data not shown).

Discussion

The MIF gene was dramatically down-regulated in co-cultured macrophages, but, consistent with previous reports (31), up-regulated in co-cultured MCF-7 cells. Given the role of MIF in macrophage activation, the present results suggest that MCF-7 down-regulation of macrophage MIF is protective for cancer cells, while MIF up-regulation in cancer cells is adaptive for the tumor. The silencing of MIF expression observed in this study may represent a phenotypic difference that can be exploited for inhibiting TAM function.

Two variants of the MIF in co-cultured MCF-7 cells were identified, which may be the result of covalent modifications of MIF, or uptake of the macrophage form by the MCF-7 cells. It has been suggested that the genetic stability of stromal cells makes them less likely to develop drug resistance and, therefore, good targets for inhibitors of macrophage functions that contribute to tumor progression

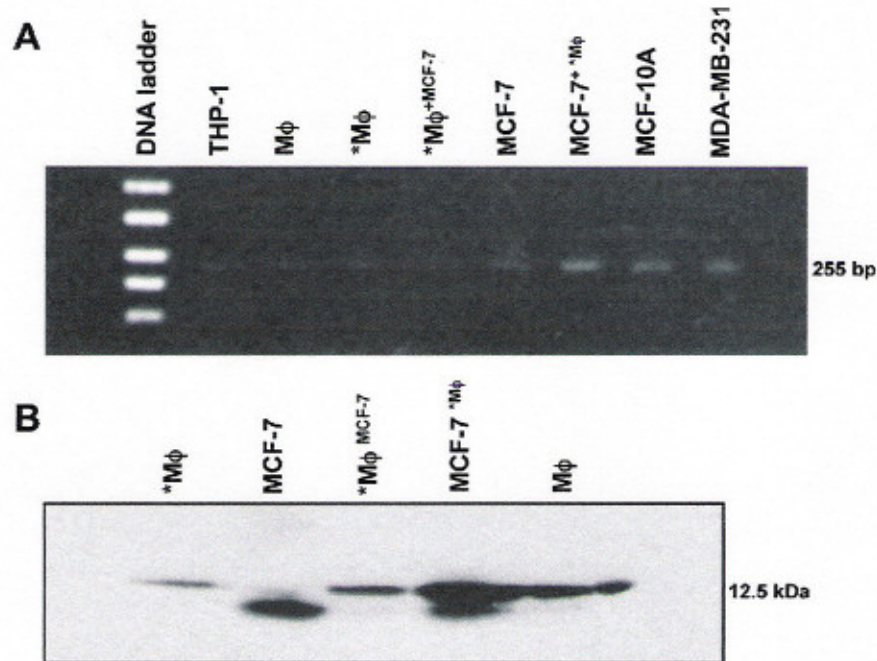


Figure 3. Analysis of MIF RNA and protein in breast cancer cells and macrophages. (A) RT-PCR of MIF mRNA (255 bp) in breast cancer cells and macrophages. In activated macrophages (*Mφ) co-cultured with MCF-7 cells (*Mφ+MCF-7), MIF RNA expression was down-regulated when compared with activated macrophages (*Mφ). (B) Western blot of MIF in THP-1 macrophages and MCF-7 cells. *Mφ, LPS-activated macrophages; *Mφ+MCF-7, activated macrophages (source of protein) co-cultured with MCF-7 cells; MCF-7*Mφ, MCF-7 cells (source of protein) co-cultured with activated macrophages and unactivated macrophages (Mφ) were probed for MIF protein. A 50-μg aliquot of lysate protein was resolved in 4-20% SDS-PAGE gradient gels, electroblotted onto nitrocellulose membrane and probed with rabbit polyclonal anti-human MIF IgG.

(4). The detection of *p53* in the THP-1 cells and the macrophages, in the present study, was unexpected because previous reports suggested that THP-1 cells were *p53*-negative (32). Nonetheless, if cancer cells secrete MIF, which is known to inhibit *p53* function, mutations may accumulate in TAMs without *p53* loss. A frequent association of *MIF* expression with the presence of *p53* in tumors (33) suggests that there is no selective pressure for *p53* loss in stromal cells when cancer-cell MIF is present. Extracellular and intracellular forms of MIF may function in distinct molecular pathways. The rhMIF down-regulation of *p53* and *PTEN* in the breast cancer cells and macrophages suggested a mechanism by which MIF may promote survival of both transformed and nontransformed cells.

IL-10 has been shown to inhibit MIF synthesis in T cells (34). The definitive signal that down-regulated *MIF* in co-cultured macrophages in the present study was not likely to be IL-10, because *IL-10* was not expressed in the MCF-7 cells or the activated macrophages in co-culture. Only the aspirin-treated MCF-7 cells and macrophages cultured separately expressed *IL-10*, and aspirin increased the level of IL-10 mRNA in the MCF-7 cells and macrophages. Thus *IL-10* up-regulation may be a part of the mechanism by which

aspirin exerts its anti-inflammatory effects. Additionally, the present results show that aspirin could imprint the macrophages to induce *IL-10* expression in the MCF-7 cells and suggest that NSAIDs may modulate the ability of macrophages to regulate gene expression in cancer cells.

In contrast to *MIF*, co-culture up-regulated *IL-1β* and *IL-8* expression (data not shown) in the macrophages. *IL-1β* was also up-regulated by tamoxifen in the macrophages. The reciprocal relationship between *IL-8* and *MIF* may be of physiological importance to tumor cells by allowing them to sustain a partial inflammatory microenvironment while maintaining the benefits of angiogenesis. The interactions that occurred between breast cancer cells and macrophages did not result in a complete differentiation to the M2 phenotype, but engaged selective components of each activated state (M1 and M2).

The mechanisms that underlie aggressive behavior in breast tumors are not intrinsic to cancer cells and include their ability to control the phenotypes of TAMs. Discrete stages of tumor progression are the product of evolving interactions between components of the tumor microenvironment. Consequently, the design of chemotherapeutic agents to target both epithelial and

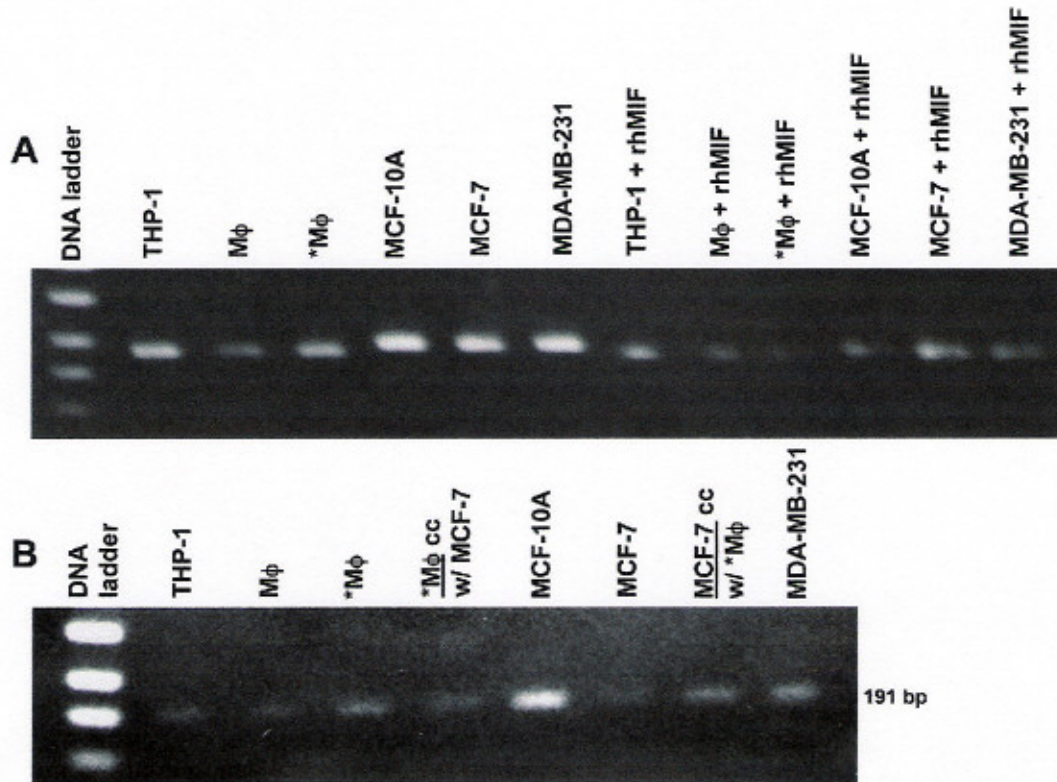


Figure 4. *p53* and *PTEN* expression in breast cancer cells and macrophages. (A) *p53* expression in untreated and rhMIF-treated cells. Total RNA was extracted and RT-PCR for *p53* was performed, as described. Mφ, macrophage; *Mφ, LPS-activated macrophages; MCF-10A, MCF-7, and MDA-MB-231 breast cell lines. Amplimer size 293 bp. (B) *PTEN* expression in THP-1 (monocytes); THP-1 macrophages (Mφ); activated macrophages (*Mφ); MCF-10A, MCF-7, and MDA-MB-231 breast cell lines. Cells were cultured alone, or in co-culture (cc), as indicated. A 1-μg aliquot of total RNA from each culture was reverse transcribed in a total reaction volume of 20 μl, and 3 μl of each RT mixture was used for PCR. In co-cultures, the cell line underlined was the source of RNA.

stromal cells should take into consideration these evolving complexities. If altered gene expression in the tumor microenvironment can enhance the tumor-promoting activities of macrophages, it is conceivable that it may also confer contextual vulnerabilities that can be exploited for pharmacological targeting. Given the importance of macrophages in the immune response, a systemic inhibition of macrophage functions would be counterproductive. It is important that anti-macrophage therapies designed to inhibit tumor progression are specific for TAMs. In this regard, a search for inhibitors of MIF-related survival signaling would be desirable.

Acknowledgements

The study was sponsored by the U.S. Army Medical Research and Acquisition Activity, 820 Chandler Street, Fort Detrick MD 21702-5014, Award NO: DAMD17-02-1-0408 to T. Bremner (PI). The content of this report does not necessarily reflect the position or the policy of the government and no official endorsement should be inferred.

References

- Guiducci C, Vicari AP, Sangaletti S, Trinchieri G and Colombo MP: Redirecting *in vivo* elicited tumor infiltrating macrophages and dendritic cells towards tumor rejection. *Cancer Res* 65: 3437-3446, 2005.
- Gupta PB, Proia D, Cingoz O, Weremowicz J, Naber SP, Weinberg RA *et al*: Systemic stromal effects of estrogen promote the growth of estrogen receptor-negative cancers. *Cancer Res* 67: 2062-2071, 2007.
- Condeelis J and Pollard JW: Macrophages: obligate partners for tumor cell migration, invasion, and metastasis. *Cell* 124: 263-267, 2006.
- Cheng J, Huo D-H, Kuang D-M, Yang J, Zheng L and Zhuang S-M: Human macrophages promote the motility and invasiveness of osteopontin-knockdown tumor cells. *Cancer Res* 67: 5141-5147, 2007.
- Lin EY and Pollard JW: Tumor-associated macrophages press the angiogenic switch in breast cancer. *Cancer Res* 67: 5064-5066, 2007.
- Rauh MJ, Sly LM, Kalesnikoff J, Hughes MR, Cao LP, Lam V *et al*: The role of SHIP1 in macrophage programming and activation. *Biochem Soc Trans* 32: 785-788, 2004.

- 7 Zhu P, Back SH, Bourk EM, Ohgi KA, Garcia-Bassets I, Sanjo H *et al*: Macrophage/cancer cell interactions mediate hormone resistance by a nuclear receptor derepression pathway. *Cell* 124: 615-629, 2006.
- 8 Odegaard JI, Ricardo-Gonzalez RR, Goforth MH, Morel CR, Subramanian V, Mukundan L *et al*: Macrophage-specific PPAR γ controls alternative activation and improves insulin resistance. *Nature* 447: 1116-1120, 2007.
- 9 Mukherjee S, Frolova N, Sadlonova A, Novak Z, Steg A, Page GP *et al*: Hedgehog signaling and response to cyclopamine differ in epithelial and stromal cells in benign breast and breast cancer. *Cancer Biol Ther* 5: 674-683, 2006.
- 10 Arcuri F, Cintonio M, Vatti R, Carducci A, Liberatori S and Paulesu L: Expression of macrophage migration inhibitory factor transcript and protein by first-trimester human trophoblasts. *Biol Reprod* 60: 1299-1303, 1999.
- 11 Bacher M, Meinhardt A, Lan HY, Mu W, Metz CN, Chesney JA *et al*: Migration inhibitory factor expression in experimentally induced endotoxemia. *Am J Pathol* 150: 235-246, 1997.
- 12 Calandra T and Roger T: Macrophage migration inhibitory factor: a regulator of innate immunity. *Nat Rev Immunol* 3: 791-800, 2003.
- 13 Hudson JD, Shoaibi MA, Maestro R, Carnero A, Hannon GJ and Beach DH: A proinflammatory cytokine inhibits p53 tumor suppressor activity. *J Exp Med* 190: 1375-1382, 1999.
- 14 Mitchell RA, Liao H, Chesney J, Fingerle-Rowson G, Baugh J, David J *et al*: Macrophage migration inhibitory factor (MIF) sustains macrophage proinflammatory function by inhibiting p53: Regulatory role in the innate immune response. *Proc Natl Acad Sci USA* 99: 345-350, 2002.
- 15 Agarwal R, Whang DH, Alvero AB, Visintin I, Lai Y and Segal EA: Macrophage migration inhibitory factor expression in ovarian cancer. *Am J Obstet Gynecol* 196: 348.e1-5, 2007.
- 16 Wilson JM, Coletta PL, Cuthbert RJ, Scott N, MacLennan K, Hawcroft G *et al*: Macrophage migration inhibitory factor promotes intestinal tumorigenesis. *Gastroenterology* 129: 1485-1503, 2005.
- 17 Hagemann T, Robinson SC, Thompson RG, Charles K, Kulbe H and Balkwill FR: Ovarian cancer cell-derived migration inhibitory factor enhances tumor growth, progression, and angiogenesis. *Mol Cancer Ther* 6: 1993-2002, 2007.
- 18 Baumann R, Casaulta C, Simon D, Conus S, Yousefi S and Simon H-U: Macrophage migration inhibitory factor delays apoptosis in neutrophils by inhibiting the mitochondria-dependent death pathway. *FASEB J* 17: 2221-2230, 2003.
- 19 Lue H, Thiele M, Franz J, Dahl E, Speckgens S, Leng L *et al*: Macrophage migration inhibitory factor (MIF) promotes cell survival by activation of the Akt pathway and role for CSN5/JAB1 in the control of autocrine MIF activity. *Oncogene* 26: 5046-5059, 2007.
- 20 Nguyen MT, Lue H, Kleemann R, Thiele M, Tolle G, Finkelmeier D *et al*: The cytokine macrophage migration inhibitory factor reduces pro-oxidative stress-induced apoptosis. *J Immunol* 170: 3337-3347, 2003.
- 21 Bernhagen J, Krohn R, Lue H, Gregory JL, Zernecke A, Koenen RR *et al*: MIF is a noncognate ligand of CXC chemokine receptors in inflammatory and atherogenic cell recruitment. *Nat Med* 13: 587-596, 2007.
- 22 Burger JA and Kipps TJ: CXCR4: a key receptor in the crosstalk between tumor cells and their microenvironment. *Blood* 107: 1761-1767, 2006.
- 23 Leng L, Metz CN, Fang Y, Xu J, Donnelly S, Baugh J *et al*: MIF signal transduction initiated by binding to CD74. *J Exp Med* 197: 1467-1476, 2003.
- 24 Shi X, Leng L, Wang T, Wang W, Du X, Li J *et al*: CD44 is the signaling component of the macrophage migration inhibitory factor-CD74 receptor complex. *Immunity* 25: 595-606, 2006.
- 25 Becker-Herman S, Arie G, Medvedovsky H, Kerem A and Shachar I: CD74 is a member of the regulated intramembrane proteolysis-processed protein family. *Mol Biol Cell* 16: 5061-5069, 2005.
- 26 Roger T, David J, Glauser MP and Calandra T: MIF regulates innate immune responses through modulation of Toll-like receptor 4. *Nature* 414: 920-924, 2001.
- 27 Roger T, Chanson A-L, Knaup-Reymond M and Calandra T: Macrophage migration inhibitory factor promotes innate immune responses by suppressing glucocorticoid-induced expression of mitogen-activated protein kinase phosphatase-1. *Eur J Immunol* 35: 3405-3413, 2005.
- 28 Aeberli D, Yang Y, Mansell A, Santos L, Leech M and Morand EF: Endogenous macrophage migration inhibitory factor modulates glucocorticoid sensitivity in macrophages via effects on MAP kinase phosphatase-1 and p38 MAP kinase. *FEBS Letters* 580: 974-981, 2006.
- 29 Tang Y and Eng C: PTEN autoregulates its expression by stabilization of p53 in a phosphatase-independent manner. *Cancer Res* 66: 736-742, 2006.
- 30 Guadagni F, Ferroni P, Palmirotta R, Del Monte G, Formica V and Roselli M: Non-steroidal anti-inflammatory drugs in cancer prevention and therapy. *Anticancer Res* 27: 3147-3162, 2007.
- 31 Hagemann T, Wilson J, Kuble H, Li NF, Leinster DA, Charles K *et al*: Macrophages induce invasiveness of epithelial cancer cells via NF- κ B and JNK. *J Immunol* 175: 1197-1205, 2005.
- 32 Sugimoto K, Toyoshima H, Sakai R, Miyagawa K, Hagiwara K, Ishikawa F *et al*: Frequent mutations in the p53 gene in human myeloid leukemia cell lines. *Blood* 79: 2378-2383, 1992.
- 33 Bacher M, Schrader J, Thompson N, Kuschela K, Gemsa D, Waerber G *et al*: Up-regulation of macrophage migration inhibitory factor gene and protein expression in glial tumor cells during hypoxic and hypoglycemic stress indicates a critical role for angiogenesis in glioblastoma multiforme. *Amer J Pathol* 163: 11-17, 2003.
- 34 Wu J, Cunha FQ, Liew FY and Weiser WY: IL-10 inhibits the synthesis of migration inhibitory factor and migration inhibitory factor-mediated macrophage activation. *J Immunol* 151: 4325-4332, 1993.

Received January 28, 2008

Revised May 5, 2008

Accepted May 9, 2008

Visualizing Head and Neck Tumors In Vivo Using Near-Infrared Fluorescent Transferrin Conjugate

Liang Shan, Yubin Hao, Songping Wang, Alexandru Korotcov, Renshu Zhang, Tongxin Wang, Joseph Califano, Xinbin Gu, Rajagopalan Sridhar, Zaver M. Bhujwalla, and Paul C. Wang

Abstract

Transferrin receptor (TfR) is overexpressed in human head and neck squamous cell carcinomas (HNSCCs). This study was carried out to investigate the feasibility of imaging HNSCC by targeting TfR using near-infrared fluorescent transferrin conjugate (Tf^{NIR}). Western blot analysis of four HNSCC cell lines revealed overexpression of TfR in all four lines compared with that in normal keratinocytes (OKFL). Immunocytochemistry further confirmed the expression of TfR and endocytosis of Tf^{NIR} in JHU-013 culture cells. Following intravenous administration of Tf^{NIR} (200 μ L, 0.625 μ g/ μ L), fluorescent signal was preferentially accumulated in JHU-013 tumor xenografts grown in the lower back ($n = 14$) and oral base tissues ($n = 4$) of nude mice. The signal in tumors was clearly detectable as early as 10 minutes and reached the maximum at 90 to 120 minutes postinjection. The background showed an increase, followed by a decrease at a much faster pace than tumor signal. A high fluorescent ratio of the tumor to muscle was obtained (from 1.42 to 4.15 among tumors), usually achieved within 6 hours, and correlated with the tumor size ($r = .74$, $p = .002$). Our results indicate that TfR is a promising target and that Tf^{NIR}-based optical imaging is potentially useful for noninvasive detection of early HNSCC in the clinic.

A CHALLENGE IN NEOPLASTIC DIAGNOSTICS is noninvasive detection of tumors at an early stage and providing information on treatment selection and its outcome. Molecular imaging provides opportunities to fulfill the clinical needs.^{1–3} Its advancement benefits from the identification of hundreds of biomarkers that are highly expressed in tumors.^{4,5} In theory, by detecting the differences in “molecular properties” between cancer and surrounding normal tissues, the signal to noise ratio can be significantly increased, and that should allow for detection of smaller tumors. Relative to other imaging techniques, near-infrared (NIR) fluorescence-based optical imaging

offers unique advantages for diagnostic imaging of solid tumors. Newly developed fluorescent contrast agents and highly sensitive light detection systems have made it possible to monitor the biologic activity of a wide variety of molecular targets, such as intracellular enzymes, cell surface receptors, and antigens in living subjects. NIR optical imaging is highly sensitive, with a capability to detect a molecular probe at 10^{-9} to 10^{-12} mol/L without much interference from background and does not require the use of radioactive materials.¹ Because water and biologic tissues have minimal absorbance and autofluorescence in the NIR window (650–980 nm), efficient photon penetration into and out of tissue with low intratissue scattering can be achieved with a depth of about 1 cm for reflectance and 2 to 6 cm for tomographic fluorescence.^{1,6} Although clinical application of optical imaging is limited owing to poor tissue penetration, the notable theoretical advantages include imaging a variety of molecular features based on versatile fluorescent probe design, providing dynamic, real-time in vivo images, monitoring of gene delivery, noninvasive detection of early tumors from accessible lumina by endoscopy, and real-time intraoperative visualization of tumor margins.^{7,8}

In the United States, more than 55,000 Americans develop head and neck cancer each year. Squamous cell carcinoma accounts for 90% of the head and neck

From the Departments of Radiology, Oral Diagnostic Service, and Radiation Oncology, Howard University, Washington, DC, and Departments of Otolaryngology and Radiology, Johns Hopkins University, Baltimore, MD.

This work was supported in part by Department of Defense grant USAMRMC W81XWH-05-1-0291, the Charles and Mary Latham Fund (7023185), and National Institutes of Health National Center for Research Resources/Research Centers in Minority Institutions Program grants 2G12 RR003048, 5P20 CA118770, and 5U 54CA091431.

Address reprint requests to: Paul C. Wang, PhD, Department of Radiology, Howard University, 2041 Georgia Avenue, NW, Washington, DC 20060; e-mail: pwang@howard.edu.

DOI 10.2310/7290.2008.0006

© 2008 BC Decker Inc

cancers.⁹ Head and neck squamous cell cancer (HNSCC) develops through a series of well-defined clinical and pathologic stages from atypia to carcinoma in situ and invasive lesions.^{10,11} These lesions locate superficially, which makes them ideal for early detection and evaluation of biomarker expression using optical imaging. Transferrin receptor (TfR) is a cell-membrane internalizing receptor that is responsible for almost all of the iron sequestration in mammalian cells. It is overexpressed in various malignant tumors.^{12–14} Previous work using radiolabeled transferrin (Tf) has demonstrated the feasibility of imaging mammary gland tumor xenografts with high sensitivity.^{15,16} However, targeted detection methods based on radiolabeled probes have been hampered by relatively low spatial resolution and the risk of ionizing radiation exposure. Positron emission tomography (PET) involves the generation of positron-emitting short-lived radioisotopes using a cyclotron. This limits the accessibility of PET in many locations. There are also problems associated with the time necessary for conjugating a short-lived positron emitter to biomolecules. We hypothesized that TfR would be a promising target and NIR fluorescent Tf conjugate (Tf^{NIR}) would be an ideal optical reporter for imaging HNSCC because TfR is expressed only in the parabasal and basal layers of normal squamous epithelium at a very low level and rarely in benign lesions. Importantly, TfR is overexpressed in the majority of HNSCC.^{17–19} Since HNSCCs are superficial tumors, they are ideal for early detection and evaluation of biomarker expression using optical imaging. In the present study, we investigated the feasibility of imaging HNSCC xenografts using Tf^{NIR}. A preferential accumulation of fluorescent signal was observed in tumors, and the tumor was clearly detectable in Tf^{NIR}-based optical imaging.

Materials and Methods

Cell Culture

Four HNSCC cell lines (John Hopkins University, Baltimore, MD) were analyzed for TfR expression. These cell lines were originally established from human HNSCC arising from the base of the tongue (JHU-06), larynx (JHU-011 and 022), and neck node (JHU-013) metastasis. All four cell lines were routinely maintained in RPMI 1640 medium supplemented with 10% heat-inactivated fetal bovine serum and 50 µg/mL each of penicillin, streptomycin, and neomycin (Invitrogen, Carlsbad, CA). A normal human keratinocyte line (OKFL) was used as a control and cultured in keratinocyte serum-free medium (Invitrogen, Carlsbad, CA).²⁰

Western Blot Analysis

Cells were washed twice with Dulbecco's phosphate buffered saline (DPBS) and collected in protein lysis buffer containing 50 mM Tris (pH 8.0), 150 mM NaCl, 0.1% sodium dodecyl sulfate (SDS), 0.5% sodium deoxycholate, 1% NP40, 100 µg/mL of phenylmethylsulfonyl fluoride, 2 µg/mL of aprotinin, 1 µg/mL of pepstatin, and 10 µg/mL of leupeptin. The mixture was placed on ice for 30 minutes. Following centrifugation at 15,000 rpm for 15 minutes at 4°C, the supernatant was collected. Protein concentration was determined using the Bio-Rad Protein Assay Dye Reagent Concentrate (Bio-Rad, Hercules, CA). Whole-cell lysate (30 µg) was resolved in 8% SDS-polyacrylamide gel, transferred to polyvinylidene difluoride membrane (Immobilon, Amersham Corp., Arlington Heights, IL), and probed sequentially with antibodies against TfR (Invitrogen) and β-actin (Sigma, St. Louis, MO) at 4°C overnight, separately. Blots were washed thrice (10 minutes each) with PBS + 0.1% Tween 20 and incubated with horseradish peroxidase-conjugated anti-mouse antibody (Santa Cruz Biotech, Santa Cruz, CA) for 1 hour at room temperature. Blots were developed using the ECL detection system (Bio-Rad).

Endocytosis of Tf and Immunocytochemistry of TfR

JHU-013 tumor cells at 40 to 50% confluence growing on four-chamber glass slides were used for endocytosis analysis. Cells were incubated with 6.25 µL of Alexa Fluor 488-labeled Tf (Tf⁴⁸⁸) (5 mg/mL) in 500 µL of complete medium for different durations (from 1 minute to 4 hours). After removal of the media, cells were completely washed thrice using DPBS. Cells were then fixed with 10% neutralized formalin for 10 minutes and mounted for fluorescent microscopic observation. For immunocytochemical staining of TfR, cells were first fixed using 10% neutralized formalin for 10 minutes and then incubated with anti-TfR monoclonal antibody for 2 hours at room temperature. The antibody was prepared in DPBS with a dilution of 1:200. After DPBS washing (three times, 5 minutes each), cells were incubated with Alexa Fluor 588-labeled goat antimouse immunoglobulin G (Invitrogen) for 1 hour. Negative control was stained similarly except the anti-TfR antibody was replaced by DPBS.

Animal Models and Optical Imaging of Tumors

Two solid tumor xenograft models were developed by subcutaneous inoculation of 1×10^7 subconfluent cells of

JHU-013 in 100 μ L of DPBS in the lower back or oral base tissues of athymic nude mice (8–10 weeks old; Harlan, Indianapolis, IN). Tumors were imaged when they reached certain sizes (2.4–9 mm in diameter). Fourteen tumors grown in the lower back of 12 mice, including 2 with tumors in both sides, were tested for the feasibility and fluorescent signal dynamics of Tf^{NIR}-based optical imaging. To verify the results, four tumors produced in the oral base tissues of four mice were further analyzed. Five healthy mice without tumors were used as the control.

Tf^{NIR}-based fluorescent optical imaging was performed using the IVIS 200 Imaging System (Caliper Life Sciences, Hopkinton, MA). Imaging and quantification of the signals were controlled by the acquisition and analysis software *Living Image* (Caliper Life Sciences). Mice were placed onto the warmed stage inside a light-tight camera box with continuous exposure to 2% isoflurane. Animals were given 200 μ L (0.625 μ g/ μ L) of the conjugate Tf^{NIR} through the tail vein. The entire animal was imaged every 10 to 30 minutes for at least 6 hours. The acquisition time for each image was 1 second. The light emitted from the mouse was detected, integrated, digitized, and displayed. Regions of interest from displayed images were identified and measured around the tumor sites. The signal intensity was expressed as mean flux (photons per second per centimeter squared per steradian, p/s/cm²/sr). Contralateral leg muscle was selected as normal background.

Statistical Analysis

The tumor sizes were measured using calipers, and the relationship between fluorescent signal and tumor sizes was evaluated using the statistical software *OriginPro 7.0* (OriginLab, Northampton, MA). A significant correlation was inferred if a *p* value was < .05 by correlation analysis.

Results

Expression of TfR in HNSCC Cell Lines

To better understand the expression status of TfR in HNSCC, TfR levels were analyzed in four HNSCC cell lines and one normal squamous cell line. A significantly high expression level of TfR was detected in all four HNSCC cell lines compared with that in the normal squamous cell line (Figure 1, A and B). Immunocytochemistry further confirmed the expression of TfR in JHU-013 cells. An immunoreactive signal was clearly seen in the cell

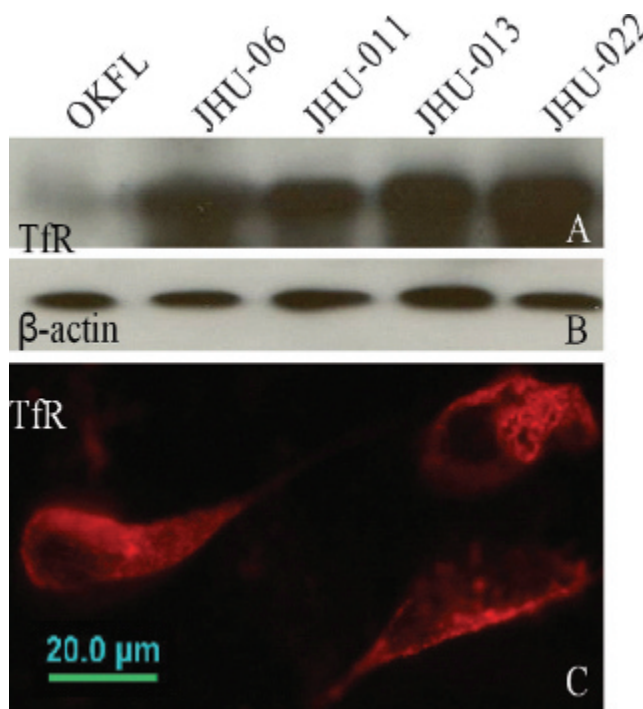


Figure 1. Transferrin receptor (TfR) expression. A, Western blot analysis of TfR expression showing overexpression of TfR in head and neck squamous cell carcinoma cell lines (JHU-06, 011, 013, 022) relative to that in a normal squamous cell line (OKFL). B, Same membrane re-probed with β -actin antibody. C, Immunocytochemistry in JHU-013 culture cells showing immunoreactive signal in cell membrane and cytoplasm.

membrane and cytoplasm (Figure 1C). Almost all of the tumor cells showed strong immunoreaction against TfR antibody. No signal was observed in the negative controls without primary antibody (data not shown).

Endocytosis and Exocytosis of Tf

The kinetics of endocytosis of Tf in JHU-013 cells was examined following incubation of fluorescence-labeled Tf (Tf⁴⁸⁸) with monolayer cell cultures (Figure 2). Binding of Tf⁴⁸⁸ with TfR on the cell membrane was observed as early as 1 to 2 minutes after incubation. With prolonged incubation, Tf⁴⁸⁸ signal was seen in the cytoplasm and cell membrane. The maximum signal in the cytoplasm was observed after 1 to 2 hours of incubation, and the signal was distributed evenly within cytoplasm. With increased incubation time (3–4 hours), signal accumulation was observed in the regions surrounding the nuclei and regions close to the cell membrane. The total fluorescence decreased gradually thereafter, indicating exocytosis of Tf⁴⁸⁸.

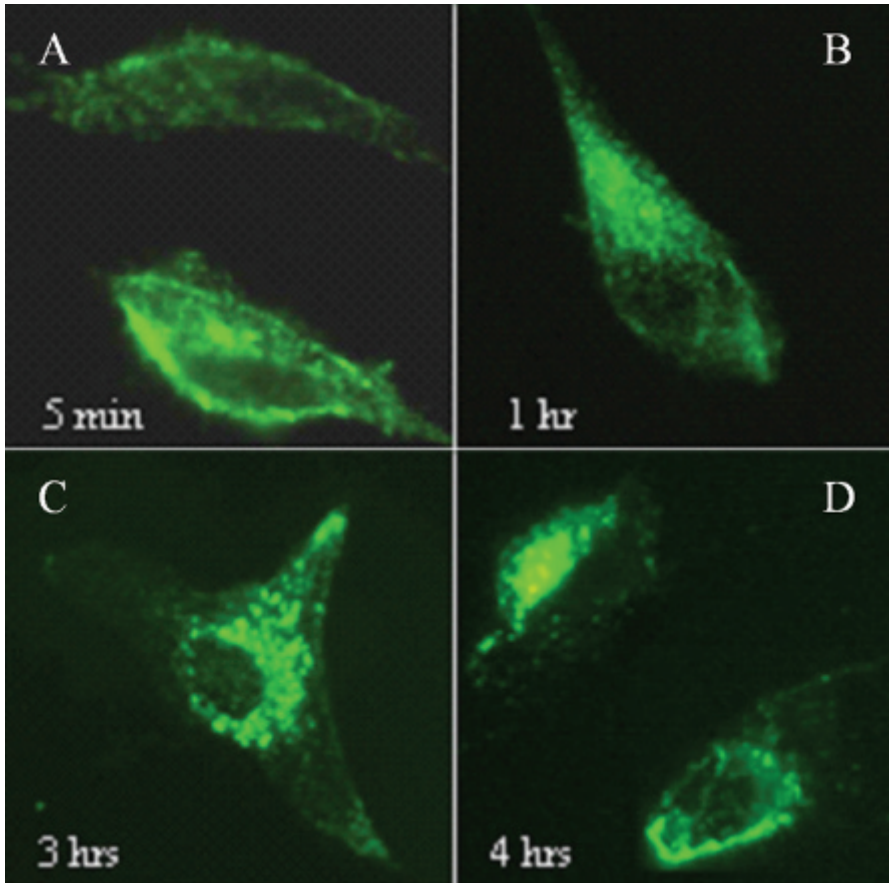


Figure 2. Different stages of transferin (Tf) endocytosis. Cells were incubated with Tf for varied times and imaged, and representative images are presented. A, Tf signal mainly in cell membrane (5 minutes). B, Signal in both cell membrane and cytoplasm with an evenly distributed pattern (1 hour incubation). Signal mainly in the perinuclear area (C; 3-hour incubation) and the peripheral area (D; 4-hour incubation). Tf was labeled with Alexa Fluor 488. The original magnification was $\times 400$.

Tf^{NIR}-Based Tumor Imaging in Animal Models of Human HNSCC

The Tf^{NIR} conjugate contains 3 mol NIR fluorescent dye (Alexa Fluor 680)/mol Tf (Invitrogen). Two hundred microliters (0.625 $\mu\text{g}/\mu\text{L}$) of the Tf conjugate as a single bolus was administered via the tail vein of mice, and the whole animal was then imaged at different times. We first tested the imaging efficiency of Tf^{NIR} in human tumor xenografts ($n = 14$) grown in the lower back of athymic nude mice (Figure 3). The tumor sizes varied from 2.4 to 9 mm in diameter. A preferential accumulation of the fluorescence was detectable as early as 10 minutes in most tumors. The fluorescent signal in the tumors showed a rapid increase followed by a gradual decrease over time. The signal was still detectable after 48 hours. Interestingly, the time to reach the maximum fluorescence varied from 90 to 300 minutes, showing significant differences among tumors in different animals. In comparison with the tumor signal, the background fluorescence increased immediately after tail vein injection of the Tf^{NIR} and decayed much faster than tumor signal. The background fluorescence was observed mainly arising from the liver, bone marrow,

brain tissue, and spleen. The fluorescent signal intensity ($\text{p/s}/\text{cm}^2/\text{sr}$) was measured from the tumors and muscles in the opposite leg. The maximum tumor to muscle fluorescent signal ratio was reached within 6 hours in the majority of the tumors. The maximum ratio varied among tumors, ranging from 1.42 to 4.15. A positive correlation was observed between this ratio and the tumor sizes (2.4–9 mm in diameter) ($r = .74$, $p = .002$) (Figure 4).

To further test the *in vivo* imaging feasibility of Tf^{NIR} in HNSCC, tumor xenografts were also established in the oral base tissues in four mice (Figure 5). In healthy mice without tumor, the fluorescent signal was observed immediately in the neck and head following administration of Tf^{NIR}. The background fluorescent signal was observed arising mainly from the large blood vessels in the neck and brain tissue (Figure 5D). The background fluorescent signal was still detectable at 2 hours after injection. Importantly, in animals with tumors, although both background and tumor fluorescent signal were observed following injection, the background fluorescence decreased rapidly and was weak, whereas the tumor signal decreased slowly and was much stronger than background. The tumor in the oral base could be clearly imaged as those

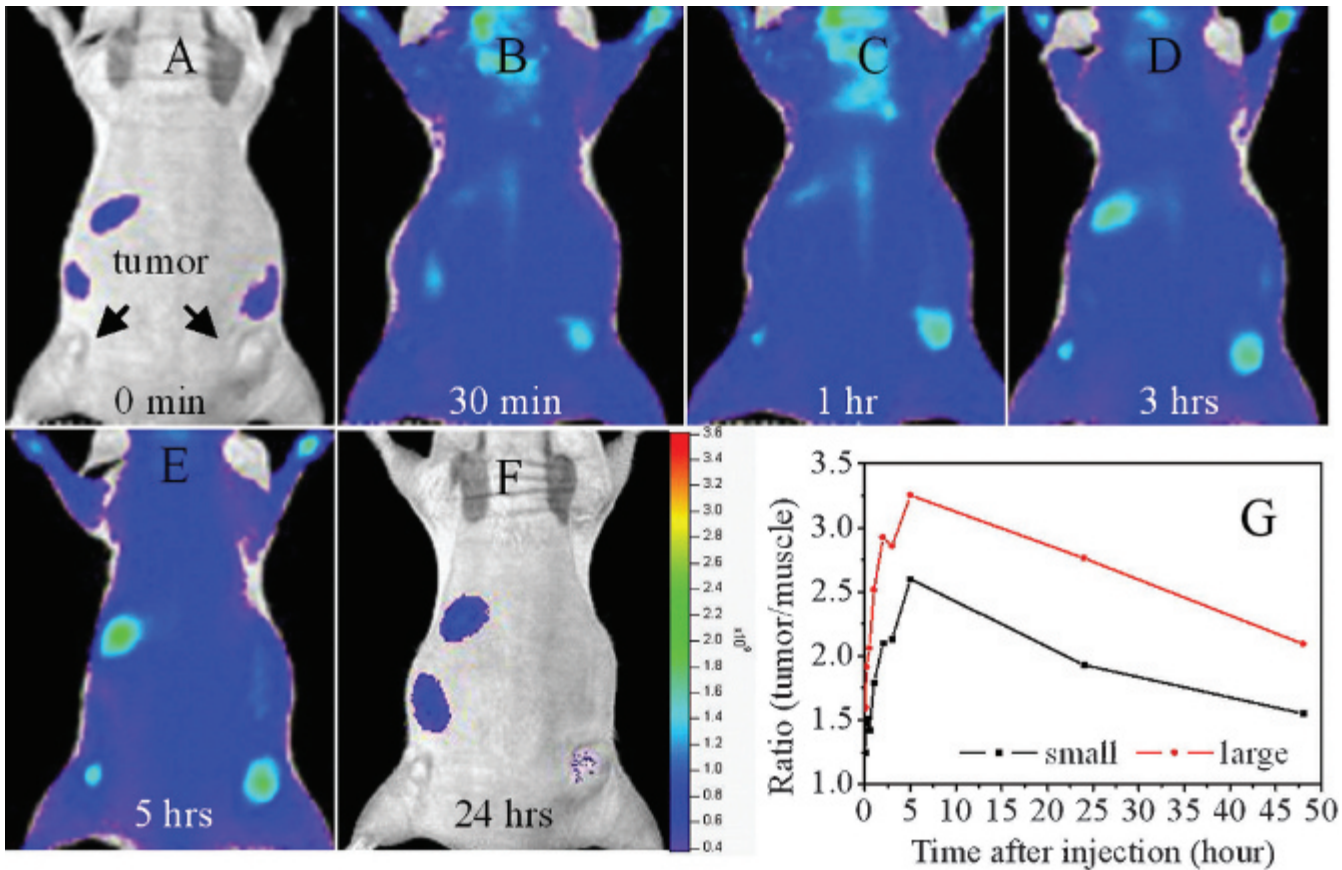


Figure 3. Whole-animal imaging following intravenous injection of near-infrared transferrin showing preferential accumulation of fluorescent signals in tumors. A to F show images taken at 0, 30 minutes, and 1, 3, 5, and 24 hours, separately. G shows change in the ratio of tumor to muscle fluorescence signal in small and large tumors over time.

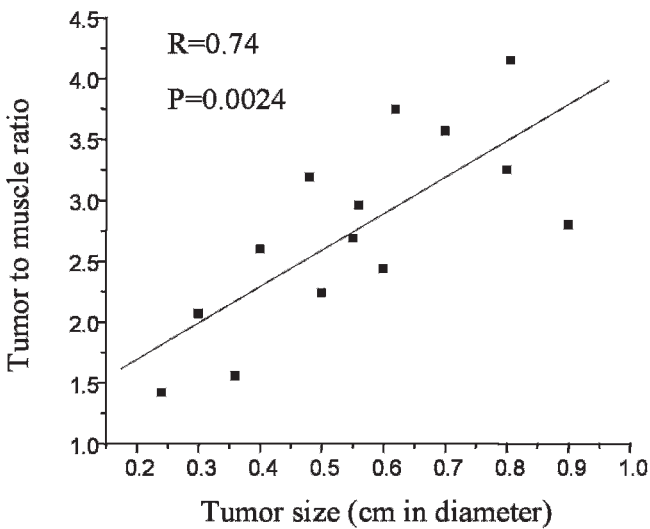


Figure 4. Positive correlation between the tumor size and the ratio of fluorescence signals from tumors to that from muscles.

in the lower back (Figure 5A–C). The background fluorescence appeared less problematic for detection of neck tumors owing to significantly weak intensity of the background compared with tumor signal.

Discussion

Theoretically, malignant tumor cells could be detected by imaging overexpressed biomarkers by taking advantage of specific binding of ligands with biomarkers and high sensitivity of optical imaging.^{1,3} Furthermore, optical assessment of the biomarker expression level is potentially helpful in assessment of tumor prognosis and drug sensitivity.^{21,22} Keeping these in mind, we tested the feasibility of tumor detection by targeted imaging of TfR using the fluorescent ligand Tf^{NIR}. TfR expression is found only in the basal layer of normal oral squamous epithelium at an extremely low level and is rarely detected in benign lesions.^{17–19} Importantly, TfR is expressed strongly in HNSCC, and a high expression level of TfR indicates high

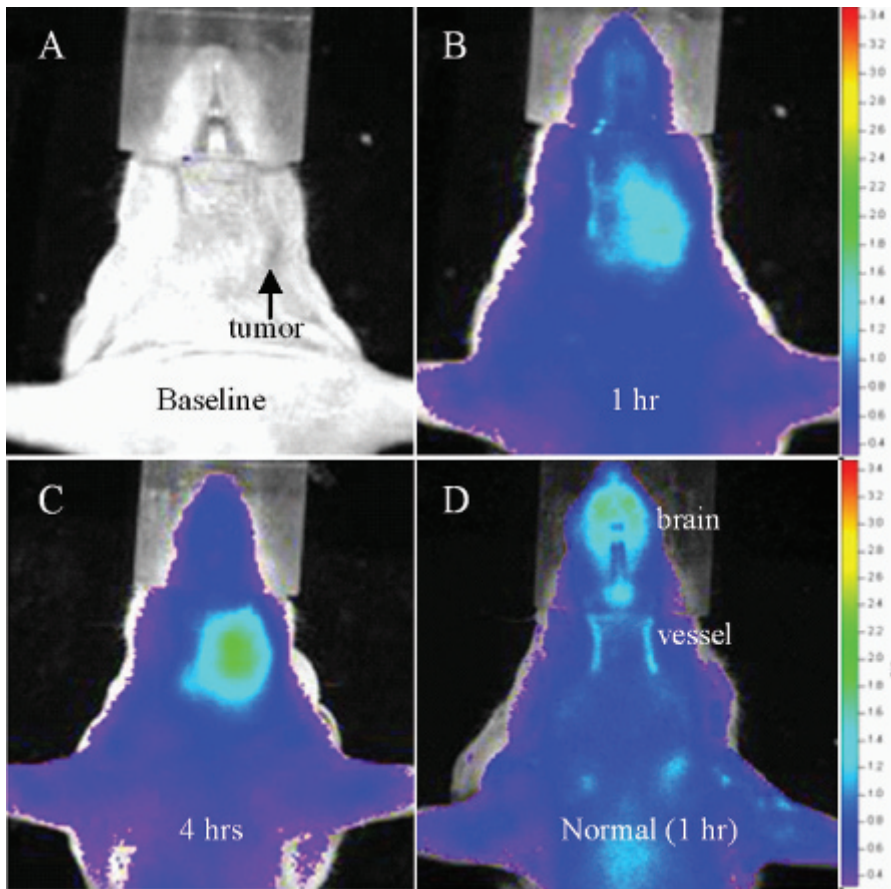


Figure 5. Near-infrared transferrin receptor (Tf^{NIR})-based imaging in healthy mice and mice with oral base tumor xenografts. A to C show images taken at 0, 1, and 4 hours, separately, following intravenous injection of Tf^{NIR} . Note the significant difference in fluorescence signals and kinetics of signal decay between tumors and background over time. D shows a healthy mouse with background signal from carotid arteries and brain tissue. The color intensity scale is the same for A, B, and C (minimum = 3.31×10^8 and maximum = 3.45×10^9). The color intensity scale for the healthy mouse in D is different (minimum = 3.83×10^8 and maximum = 2.59×10^9).

tumor malignancy and a poor prognosis.^{17–19} This specific expression pattern of TfR makes it an ideal candidate to image HNSCC. We hypothesized that the normal epithelia or benign lesions can be differentiated from malignant cells by exploring the differential expression of TfR. In the present study, overexpression of TfR was demonstrated in all HNSCC cell lines using Western blot analysis. Microscopic findings for the rapid binding of Tf^{NIR} with TfR and endocytotic activity of Tf^{NIR} in cell cultures further provided the rationale to image HNSCC in vivo using Tf^{NIR} . Specificity is critical for molecular imaging in vivo. Our previous work using MDA-MB-231 human breast cancer cells has shown that pretreatment of the cells with a threefold higher amount of unlabeled Tf (375 μ g Tf/dish) than the probe (125 μ g Tf^{NIR} /dish) resulted in a 66% decrease in the fluorescent signal.¹³ Specificity of the Tf moiety for targeting has also been demonstrated by other investigators.²³ In an in vitro study using ^{125}I -Tf in a K562 cell line, preincubation with 100-fold excess of unlabeled Tf for 5 minutes resulted in a dramatic inhibition of subsequent ^{125}I -Tf binding. A 100-fold excess of bovine serum albumin or asialo-orosomucoid (a glycoprotein) had no effect on ^{125}I -Tf binding.²³

To test our hypothesis, we first imaged HNSCC xenografts grown in the lower back of mice. Tf^{NIR} accumulated preferentially in the tumor xenografts. The maximum tumor signal to background ratio reached to 1.42 to 4.15 and could be observed within 6 hours in the majority of the tumors. The significantly high ratio enabled early detection of tumors with high sensitivity and specificity. Interestingly, the time to reach the highest signal in tumors varied among tumors and was not related to tumor sizes. This phenomenon is also observed in bioluminescent imaging following D-luciferin administration in tumors established with luciferase-expressing tumor cell lines (data not shown). The in vivo dynamic difference of Tf^{NIR} accumulation might be related to both animal individual and tumor characteristics such as tumor volume, tumor cell proliferation, vascular supply, and hypoxia.²⁴ The tumor fluorescent signal is a sum of photons from specific binding of the ligand with its receptor and nonspecific presence of the fluorescent conjugate in blood vessels and interstitial space. However, the nonspecific signal was cleared more rapidly than true tumor cell-bound signal and appeared less significant in tumor detection. Previous studies using

radiolabeled Tf showed a significant decrease in tumor signal by pretreatment with a large amount of unlabeled Tf.¹⁵ These results further indicate the importance and specificity of the Tf moiety for targeting *in vivo*. One major concern is the hypoxia and necrosis frequently presenting in large tumors.²⁵ Hypoxia and necrosis might affect both the expression of TfR and the entry, settling, and binding of Tf^{NIR}. These factors might become evident if quantitative assessment of biomarker expression or comparative analysis among tumors is performed using optical imaging, although we obtained a close correlation between the tumor to muscle fluorescent ratio and tumor size.

To further test the feasibility of HNSCC detection, we imaged the animals with and without oral base tumors. In healthy mice, fluorescent signal was observed from the large blood vessels in the neck and from brain tissue. The carotids and their branches and aorta arch are located superficially in the neck. Normal brain tissue is known to express TfR at a high level. The fluorescent background might adversely affect the detection of metastatic lesions in neck lymph nodes. Metastatic lesions might be too small to produce a stronger signal than the vessels in animal models (further study is necessary). Primary tumors can be clearly detected through the neck owing to a much stronger signal and delayed signal fading relative to background. Human HNSCC is developed and progressed through atypia to carcinoma *in situ* and then to invasive squamous cell carcinoma. These early lesions locate superficially in the wall of the oral cavity, pharynx, and esophagus. The difference in TfR expression among normal squamous epithelial cells, atypical cells, and carcinoma cells may be significant enough for optical differentiation among them through the use of Tf^{NIR}. Furthermore, development of confocal laser endomicroscopy enables analysis of *in vivo* microarchitecture.²⁶ The combination of a fluorescently labeled probe such as Tf^{NIR} and fluorescent confocal laser endomicroscopy will enable identification of early lesions, including squamous cell atypia and carcinoma *in situ*, as well as early invasive carcinomas. Our results in animal models of human HNSCC indicate that TfR is a promising target and Tf^{NIR}-based optical imaging is potentially useful for detection and localization of early HNSCC and atypical lesions in clinical practice.

Under physiologic conditions, iron-loaded Tf binds TfR on the surface of actively dividing cells. Subsequently, the Tf-TfR complex is internalized, first transported to early endosomes and then delivered to recycling endosomes. The apo-Tf is released only after the complex reaches the cell surface and then circulates until it again

comes in contact with free iron. It has been estimated that one Tf molecule could participate in this transport cycle as many as 100 times.²⁷ In the present study, the Tf was labeled with NIR fluorescent dye and the tumor was imaged based on the fluorescence of the optical reporter. The details of Tf^{NIR} recycling in tumors are unknown, and further analysis would be necessary for understanding the pharmacokinetics of Tf^{NIR} in mice.

References

1. Massoud TF, Gambhir SS. Molecular imaging in living subjects: seeing fundamental biological processes in a new light. *Gene Dev* 2003;17:545–80.
2. Graves EE, Weissleder R, Ntziachristos V. Fluorescence molecular imaging of small animal tumor models. *Curr Mol Med* 2004;4: 419–30.
3. Ntziachristos V, Bremer C, Weissleder R. Fluorescence imaging with near-infrared light: new technological advances that enable *in vivo* molecular imaging. *Eur Radiol* 2003;13:195–208.
4. Hogemann-Savellano D, Bos E, Blondet C, et al. The transferrin receptor: a potential molecular imaging marker for human cancer. *Neoplasia* 2003;5:495–506.
5. Stefflova K, Chen J, Zheng G. Using molecular beacons for cancer imaging and treatment. *Front Biosci* 2007;12:4709–21.
6. Hoffman RM. The multiple uses of fluorescent proteins to visualize cancer *in vivo*. *Nature* 2005;5:796–806.
7. Veiseh M, Gabikian P, Bahrami SB, et al. Tumor paint: a chlorotoxin: Cy5.5 bioconjugate for intraoperative visualization of cancer foci. *Cancer Res* 2007;67:6882–8.
8. Kaijzel EL, van der Pluijm G, Lowik CW. Whole-body optical imaging in animal models to assess cancer development and progression. *Clin Cancer Res* 2007;13:3490–7.
9. Greenlee RT, Hill-Harmon MB, Murray T, Thun M. Cancer statistics, 2001. *CA Cancer J Clin* 2001;51:15–36.
10. Forastiere A, Koch W, Trotti A, Sidransky D. Head and neck cancer. *N Engl J Med* 2001;345:1890–900.
11. Westra WH, Califano J. Toward early oral cancer detection using gene expression profiling of saliva: a thoroughfare or dead end? *Clin Cancer Res* 2004;10:8130–1.
12. Pirolo K, Dagata J, Wang P, et al. A tumor-targeted nanodelivery system to improve early MRI detection of cancer. *Mol Imaging* 2006;5:41–52.
13. Shan L, Wang S, Sridhar R, et al. A dual probe with fluorescent and magnetic properties for imaging solid tumor xenografts. *Mol Imaging* 2007;6:85–95.
14. Belloq NC, Pun SH, Jensen GS, Davis ME. Transferrin-containing, cyclodextrin polymer-based particles for tumor-targeted gene delivery. *Bioconjug Chem* 2003;14:1122–32.
15. Smith TA, Perkins AC, Walton PH. 99mTc-labelled human serum transferrin for tumour imaging: an *in vitro* and *in vivo* study of the complex. *Nucl Med Commun* 2004;25:387–91.
16. Vavere AL, Welch MJ. Preparation, biodistribution, and small animal PET of 45Ti-transferrin. *J Nucl Med* 2005;46:683–90.
17. Miyamoto T, Tanaka N, Eishi Y, Amagasa T. Transferrin receptor in oral tumors. *Int J Oral Maxillofac Surg* 1994;23:430–3.

18. Kearsley JH, Furlong KL, Cooke RA, Waters MJ. An immunohistochemical assessment of cellular proliferation markers in head and neck squamous cell cancers. *Br J Cancer* 1990;61:821–7.
19. Tanaka N, Miyamoto T, Saito M, et al. Transferrin receptor expression in oral tumors. *Bull Tokyo Med Dent Univ* 1991;38:19–26.
20. Dickson M, Hahn W, Ino Y, et al. Human keratinocytes that express hTERT and also bypass a p16INK4a-enforced mechanism that limits life span become immortal yet retain normal growth and differentiation characteristics. *Mol Cell Biol* 2000;20:1436–47.
21. Klausner RD, Renswoude JV, Ashwell G, et al. Receptor-mediated endocytosis of transferrin in K562 cells. *J Biol Chem* 1982;258:4715–24.
22. Zhang W, Moorthy B, Chen M, et al. A Cyp1a2-luciferase transgenic CD-1 mouse model: responses to aryl hydrocarbons similar to the humanized AhR mice. *Toxicol Sci* 2004;82:297–307.
23. Pillon A, Servant N, Vignon F, et al. *In vivo* bioluminescent imaging to evaluate estrogenic activities of endocrine disrupters. *Analyt Biochem* 2005;340:295–302.
24. Raman V, Artemov D, Pathak AP, et al. Characterizing vascular parameters in hypoxic regions: a combined magnetic resonance and optical imaging study of a human prostate cancer model. *Urol Oncol* 2007;25:358–9.
25. Kanematsu M, Semelka R, Osada S, Amaoka N. Magnetic resonance imaging and expression of vascular endothelial growth factor in hepatocellular nodules in cirrhosis and hepatocellular carcinomas. *Top Magn Reson Imaging* 2005;16:67–75.
26. Hoffman A, Goetz M, Vieth M, et al. Confocal laser endomicroscopy: technical status and current indications. *Endoscopy* 2006;38:1275–83.
27. Gomme PT, McCann KB, Bertolini J. Transferrin: structure, function and potential therapeutic actions. *Drug Discov Today* 2005;10:267–73.

BIOLUMINESCENT ANIMAL MODELS OF HUMAN BREAST CANCER FOR TUMOR BIOMASS EVALUATION AND METASTASIS DETECTION

Introduction: Convenient animal models are needed to study the progression and treatment of human tumors *in vivo*. Luciferase-based bioluminescent imaging (BLI) enables researchers to monitor tumors noninvasively and is sensitive to subtle changes in tumors.

Methods: Three human breast cancer models in nude mice were established by using luciferase-expressing MDA-MB-231-luc cells. They were subcutaneous xenografts ($n=8$), mammary gland xenografts ($n=5$), and lung metastases ($n=3$). The tumors were imaged in live mice by using a highly sensitive BLI system. The relationship between the intensity of bioluminescence from the tumor was analyzed with respect to tumor volume. Bioluminescent signals from lung metastases were studied to determine the threshold of detectability.

Results: Tumors growing in the mice's backs and mammary gland fat pads were imaged dynamically after administration of D-luciferin. The bioluminescent intensity from the tumors gradually increased and then decreased in a one-hour span. The time to reach maximum signal intensity differed significantly among tumors and was independent of tumor volume and unrelated to maximum signal intensity. A significant correlation was observed between tumor volume and maximum signal intensity in tumors from both sites. Lung metastatic lesions of .3–.5 mm in diameter were clearly detectable through the entire animal imaging process.

Conclusion: The animal models established with luciferase-expressing cancer cells in combination with BLI provide a system for rapid, noninvasive, and quantitative analysis of tumor biomass and metastasis. This biosystem simplifies *in vivo* monitoring of tumors and will be useful for noninvasive investigation of tumor growth and response to therapy. (*Ethn Dis.* 2008;18[Suppl 2]:S2-65–S2-69)

Key Words: Bioluminescent Imaging, Luciferase, Animal Models, Breast Cancer

From the Department of Radiology (LS, SW, AK, PCW), Department of Radiation Oncology (RS), Howard University, Washington, DC.

Address correspondence and reprint requests to: Paul C. Wang, PhD; Department of Radiology, Howard University; 2041 Georgia Ave, NW; Washington, DC 20060; 202-865-3711; 202-865-3722 (fax); pwang@howard.edu

Liang Shan, MD, PhD; Songping Wang, PhD; Alexandru Korotcov, PhD; Rajagopalan Sridhar, PhD; Paul C. Wang, PhD

INTRODUCTION

Bioluminescent imaging (BLI) is an optical imaging modality that enables rapid *in vivo* analyses of a variety of cellular and molecular events with extreme sensitivity.^{1–3} This imaging technique is based on light-emitting enzymes, such as luciferase, as internal biological light sources that can be detected externally as biological indicators. As a result of recent developments in techniques for high-sensitivity detection of bioluminescence, BLI has been recently tested in the detection and real-time observation of primary tumor growth and metastasis in living subjects.^{4–6} Luciferase-based light-emitting animal models have also been used to develop therapeutics that target the molecular basis of disease.⁷ Importantly, BLI provides a biosystem to test the spatial-temporal expression patterns of both target and therapeutic genes in living animals where the contextual influences of whole biological systems are intact.^{8,9} In this study, we established three bioluminescent animal models of human breast cancer using MDA-MB-231-luc cell line, which has been stably transfected with the luciferase gene. The primary and metastatic lesions were analyzed through whole-animal imaging, and the tumor volume was evaluated in relationship with the bioluminescent signal intensity.

METHODS

Cell culture and animal models

MDA-MB-231-luc human breast cancer cell line and D-luciferin were obtained from Xenogen (Alameda, Calif). This cell line has been stably transfected with

luciferase gene for luciferase-based BLI. Cells were routinely maintained in Dulbecco minimal essential medium/F-12 medium supplemented with 10% heat inactivated fetal bovine serum and 50 µg/mL each penicillin, streptomycin, and neomycin (Invitrogen, Carlsbad, Calif). Female athymic nude mice of 8–10 weeks of age ($n=16$) were purchased from Harlan (Indianapolis, Ind). Three animal models were developed. The subcutaneous solid tumor xenograft model was developed by subcutaneous injection of 1×10^7 subconfluent cells in 100 µL Dulbecco phosphate buffered saline (DPBS) in the right lower back of each mouse ($n=8$). The mammary gland fat pad tumor model was developed by injection of 1×10^7 subconfluent cells in 100 µL DPBS into the right fifth mammary gland fat pad ($n=5$). Matrigel or other anchoring matrix was not used to produce the tumors. The lung metastasis model of breast cancer was developed by tail vein injection of 1×10^6 tumor cells ($n=3$). The tumors in subcutaneous tissue and mammary gland fat pad were imaged and analyzed when they reached a certain size (3–11 mm diameter). For lung metastatic model, whole animals were checked weekly and autopsied when tumor signal from the lung region was detected.

In vivo BLI

Luciferase-based BLI was performed with a highly sensitive, cooled charge-coupled device camera mounted in a light-tight specimen box (Xenogen IVIS 200 imaging system). Imaging and quantification of signals were controlled by the acquisition and analysis software Living Image (Xenogen). Mice were placed onto the warmed stage inside the light-tight camera box with continuous exposure to 2% isoflurane. After a

baseline image was taken, animals were given the substrate D-luciferin by intraperitoneal injection at 150 mg/kg in DPBS. Then the whole animal was imaged at an interval of 2 minutes for more than one hour. Imaging time was one minute. The light emitted from the mouse was detected, integrated, digitized, and displayed by the IVIS camera system. Regions of interest from the displayed images were identified and measured around the tumor sites. The signal was quantified and expressed as photons per second by using Living Imaging software (Xenogen).

All animal protocols were conducted according to National Institutes of Health guidelines for humane use and care of animals. The animal protocols were approved by the institutional animal care and use committee of Howard University.

Histopathology

To confirm whether the detected signal from whole-animal imaging originated from the metastatic lesions in the lung, the animal was autopsied as soon as the signal was detected. The lung was examined and fixed by intrabronchial perfusion of 10% neutralized formalin solution. Paraffin-embedded sections were stained using hematoxylin and eosin for microscopic evaluation.

Statistical Analysis

Statistical analysis was performed by using statistical software OriginPro 7.0 (OriginLab, Northampton, Mass). A P value $< .05$ was considered to be a significant difference between any two sets of data.

RESULTS

Individual Difference in Dynamics of Tumor Bioluminescent Signals

After inoculation of the tumor cells into the subcutaneous tissue and mammary gland fat pads of the mouse,

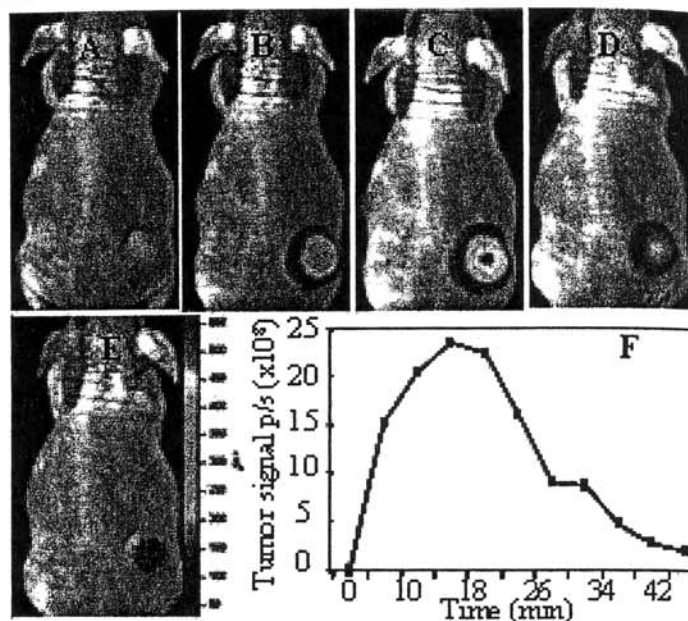


Fig 1. Dynamic change of the bioluminescent signal in tumors after administration of D-luciferin, showing gradual increase and then decrease over time. Panels A to E represent the whole animal images taken separately at 0, 10, 15, 30, and 40 minutes after luciferin administration. Panel F shows the plot of signal intensity from tumor as a function of time after injection of luciferin.

≈90% of the mice developed tumor nodules at the inoculated sites within one month. To a certain degree, the tumors varied with respect to size and rate of growth. In the present study, the tumors were allowed to grow to a desired size and used for BLI. A total of eight tumors in the subcutaneous tissue in the backs and five tumors in the mammary gland fat pads of athymic nude mice were analyzed. The maximum diameter of the 13 tumors was 3–11 mm. After administration of D-luciferin, the bioluminescent signal in tumors was clearly detectable as early as two minutes and showed a dynamic change of gradual increase and then decrease over time (Figure 1). In most of the tumors, the signal became very weak or undetectable within 60 minutes. There was a significant difference among tumors for the peak intensity time, which is defined as the time for luminescence intensity of tumor to reach the maximum, ranging from 5 to 24 minutes. A similar phenomenon

was observed for tumors located in the backs and mammary fat pads. There was no correlation between the peak intensity time and tumor volume ($R = -.13$, $P = .76$ in subcutaneous and $R = .67$, $P = .21$ in mammary gland xenografts). Also, there was no correlation between the peak intensity time and maximum tumor signal intensity ($R = -.18$, $P = .67$ in subcutaneous and $R = .74$, $P = .15$ in mammary gland xenografts). These results indicate that the dynamic change of tumor bioluminescent signal after D-luciferin administration might be related to the differences of individual mice.

Close Correlation between Bioluminescent Signal Intensity and Tumor Volume

The maximum tumor signal measured at the peak intensity time point was selected for further analysis because of the significant difference in the dynamics of tumor bioluminescent signals among mice. There was

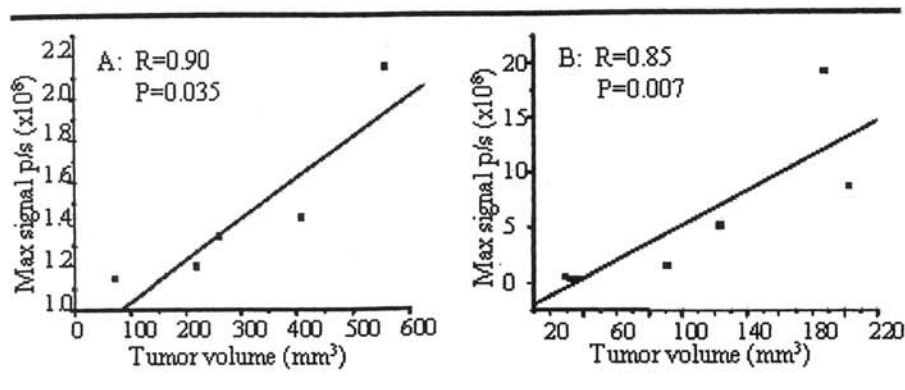


Fig 2. Close correlation between maximum signal of tumors and tumor volume. A) Solid tumor xenografts in the mammary gland fat pads of mice. B) Subcutaneous tumors in the backs of mice.

significant correlation between the maximum signal and the tumor volume for tumors located both subcutaneously ($R=.85$, $P=.007$, Figure 2B) and at the mammary gland fat pad ($R=.90$, $P=.035$, Figure 2A). This result indicates that the bioluminescent signal intensity reflects tumor size. The maximum signal intensity could be used as an indicator of tumor growth. The background signal was at a negligible level and significantly less than the signal from the tumor (Figure 1).

Highly Sensitive *in vivo* Detection of Lung Metastatic Lesions

In three mice, the tumor cells were injected through the tail vein, and whole animal imaging was performed every week. Clear signal of the tumors was first detected in the lung area at approximately one month after tail vein injection of tumor cells. After recording the images, the mice were autopsied immediately, and pathology studies of the lung were performed. In one mouse, two distinct tumor signals were observed bilaterally (Figure 3A). However, many lesions with different sizes and distributed in bilateral sides of the lung were observed under microscopy. The largest lesion located at the right lower lobe was .5 mm in diameter, corresponding to the signal on the right side

of the bioluminescent image, and the second largest lesion located at the left upper lobe was .3 mm in diameter, corresponding to the left side tumor signal in whole animal imaging (Figure 3C). In another mouse, a single tumor signal was detected, and pathology examination revealed a tumor mass of .6 mm in diameter located near the left pulmonary hilus (Figure 3B). Multiple microscopic metastatic lesions were also observed in the third mouse with very weak tumor signals. Identifying lesions <.3 mm in diameter and differ-

entiating one small lesion from another based on imaging alone was difficult.

DISCUSSION

Luciferase has served as a reporter in a number of targeted gene expression experiments in the last two decades.^{1,2} In recent years, luciferase-based BLI is becoming an important and rapidly advancing field to visualize and quantify the proliferation of tumor cells in animal models.^{10,11} Luciferase labeling is superior to other reporters, such as green fluorescent protein for tracing the progression of neoplastic growth from a few cells to extensive metastasis.^{12,13} In spite of the remarkable progress made, much more remains to be done with luciferase-based visualization of tumors *in vivo*. In the present study, we established three animal models of human breast cancer using stably luciferase-transfected cells. Regardless of the tumor sites in subcutaneous tissue or in mammary gland fat pad, the tumors could be clearly imaged with extremely low background by whole-animal imaging. Interestingly, the dynamics of the tumor signal intensity were significantly

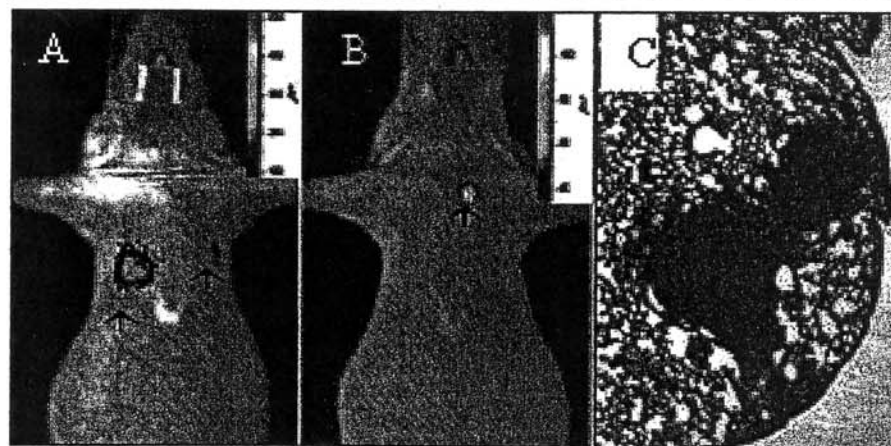


Fig 3. Detection of lung metastasis through whole animal imaging. Panel A is the image from one mouse showing signals in bilateral sides of the lung. Panel B is the image from a mouse with signal from one tumor in the left upper lobe of the lung. Panel C represents the pathologic finding of the left tumor in panel A (hematoxylin-eosin stain, $\times 40$).

different among tumors. Some tumors quickly reached the maximum intensity, whereas others took more time. The time to reach the maximum signal was independent of tumor volume and was also not related to the maximum tumor signal. There were individual differences in light emission following administration of D-luciferin. The tumor heterogeneity with respect to size, vascular density, blood supply, and other factors may affect accessibility and retention of luciferin and consequently the kinetics of light emission. Hypoxia and necrosis that are commonly observed in large tumors can lead to decreased synthesis of luciferase and ATP. The signal intensity is largely dependent on ATP and luciferase levels in the tumor and the tumor volume. In small tumors, the influence from hypoxia and necrosis may be less significant. In the present animal models, tumors <1.2 cm are more suitable for BLI because excessive necrosis was not observed under microscope. A significant correlation was observed between bioluminescent signal and tumor volume. The bioluminescent signal could be used as an indicator of tumor biomass. However, as tumors become larger, the correlation between tumor volume and bioluminescent signal becomes inferior. Another issue of concern is the selection of the time point to measure the signal intensity after luciferin administration. In the previous studies, the bioluminescent signal at the five-minute time point was arbitrarily used to represent the tumor in various analyses.^{4,5} Based on our dynamic analysis, it was clear that the signal at five-minute time point was less likely to reflect the real signal intensity of the tumors. The maximum signals at peak intensity time point may be a better indicator for tumor volume because of the strong correlation between the maximum intensity and the volume.

One potential use of BLI is the detection of metastasis in animals. The

animals can be monitored through whole-animal imaging. Wetterwald et al showed by using a bone metastasis model, that micrometastasis of .5-mm³ volume can be detected, which reveals greater sensitivity than radiographic methods.¹⁴ A study by Edinger et al using luciferase-expressing HeLa cells demonstrated that 1×10^3 cells in the peritoneal cavity, 1×10^4 cells at subcutaneous sites, and 1×10^6 circulating cells could be observed immediately after injection of the cells.¹⁵ In the present study, clear signaling from metastatic lesions could be detected when pulmonary metastatic lesions approached .3 mm in diameter. The lesions at this stage were still difficult to differentiate from the vessel spots in magnetic resonance imaging (data not shown). All of these studies with different models confirmed the high detection sensitivity of metastatic lesions using BLI. To date, the conventional methods used to test the efficacy of novel therapies on primary tumors and metastasis *in vivo* are labor intensive and time consuming. Luciferase-based BLI is highly sensitive, real-time, noninvasive, and significantly correlated with the tumor growth. These characteristics simplify such kinds of *in vivo* analysis that rely on animals.¹⁶ The therapeutic efficacy of a drug can be assessed without having to sacrifice the mice to search for tumor growth at primary and metastatic sites. Statistically significant results can be achieved by using a small number of mice, since multiple measurements can be made over time. Although metastatic lesions above a certain critical size in the lung can be detected using BLI, a major limitation of BLI is the difficulty in quantification of multiple micrometastatic lesions and comparative analysis of lesions in different parts of the body due to the photon characteristics as well as the tissue differences along the photon pathway.

ACKNOWLEDGMENTS

This work was supported in part by DoD USAMRMC W81XWH-05-1-0291 and DAMD 17-03-1-0759, DAMD 17-03-1-0123, NIH 5U54CA091431 and grant 2G12 RR003048 from the RCMI Program, Division of Research Infrastructure, National Center for Research Resources, NIH.

REFERENCES

1. Massoud TF, Gambhir SS. Molecular imaging in living subjects: seeing fundamental biological processes in a new light. *Genes Develop.* 2003;17:545-580.
2. Greer IILF, Szalay AA. Imaging of light emission from the expression of luciferases in living cells and organisms: a review. *Luminescence.* 2002;17:43-74.
3. Yu YA, Shabahang S, Timiryasova TM, et al. Visualization of tumors and metastases in live animals with bacteria and vaccinia virus encoding light-emitting proteins. *Nat Biotech.* 2003;22:313-320.
4. Jenkins DE, Hornig YS, Oei Y, Dusich J, Purchio T. Bioluminescent human breast cancer cell lines that permit rapid and sensitive *in vivo* detection of mammary tumors and multiple metastases in immune deficient mice. *Breast Cancer Res.* 2005;7:R444-R454.
5. Nogawa M, Yuasa T, Kimura S, et al. Monitoring luciferase-labeled cancer cell growth and metastasis in different *in vivo* models. *Cancer Lett.* 2005;217:243-253.
6. Sarraf-Yazdi S, Mi J, Dewhirst MW, Clary BM. Use of *in vivo* bioluminescence imaging to predict hepatic tumor burden in mice. *J Surg Res.* 2004;120:249-255.
7. Zhang W, Moorthy B, Chen M, et al. A Cyp1a2-luciferase transgenic CD-1 mouse model: responses to aryl hydrocarbons similar to the humanized AhR mice. *Toxicol Science.* 2004;82:297-307.
8. Pilon A, Servant N, Vignon F, Balaguer P, Nicolas JC. *In vivo* bioluminescent imaging to evaluate estrogenic activities of endocrine disruptors. *Analyt Biochem.* 2005;340:295-302.
9. Vooijs M, Jonkers J, Lyons S, Berns A. Noninvasive imaging of spontaneous retinoblastoma pathway-dependent tumors in mice. *Cancer Res.* 2002;62:1862-1867.
10. Ghosh M, Gambhir SS, De A, Nowels K, Goris M, Wapnir I. Bioluminescent monitoring of NIS-mediated (131I) ablative effects in MCF-xenografts. *Mol Imaging.* 2006;5:76-84.
11. Paulmurugan R, Massoud TF, Huang J, Gambhir SS. Molecular imaging of drug-modulated protein-protein interactions in living subjects. *Cancer Res.* 2004;64:2113-2119.
12. Choy G, O'Connor S, Diehn FE, et al. Comparison of noninvasive fluorescent and

- bioluminescent small animal optical imaging. *Biotechniques*. 2003;35:1022–1026.
13. Troy T, Jekic-McMullen D, Sambucetti L, Rice B. Quantitative comparison of the sensitivity of detection of fluorescent and bioluminescent reporters in animal models. *Mol Imaging*. 2004;3:9–23.
14. Wetterwald A, van der Pluijm G, Sijmons B, et al. Optical imaging of cancer metastasis to bone marrow: a mouse model of minimal residual disease. *Am J Pathol*. 2002;160:1143–1153.
15. Edinger M, Sweeney TJ, Tucker AA, Olomu AB, Negrin RS, Contag CH. Noninvasive assessment of tumor cell proliferation in animal models. *Neoplasia*. 1999;1:303–310.
16. Hardy J, Edinger M, Bachmann MH, Negrin RS, Fathman CG, Contag CH. Bioluminescence imaging of lymphocyte trafficking in vivo. *Exp Hematol*. 2001;29:1353–1360.

Inhibition of Tumor Growth by Endohedral Metallofullerenol Nanoparticles Optimized as Reactive Oxygen Species Scavenger^[S]

Jun-Jie Yin, Fang Lao, Jie Meng, Peter P. Fu, Yuliang Zhao, Gengmei Xing, Xueyun Gao, Baoyun Sun, Paul C. Wang, Chunying Chen, and Xing-Jie Liang

Division of Nanomedicine and Nanobiology, National Center for Nanosciences and Technology of China, Beijing, China (F.L., J.M., Y.Z., C.C., X.-J.L.); Center for Food Safety and Applied Nutrition, Food and Drug Administration, College Park, Maryland (J.-J.Y.); Laboratory for Bio-Environmental Effects of Nanomaterials and Nanosafety, Institute of High Energy Physics, Chinese Academy of Sciences, Beijing, China (J.M., Y.Z., G.X., X.G., B.S., C.C.); Division of Biochemical Toxicology, National Center for Toxicological Research, Food and Drug Administration, Jefferson, Arkansas (P.P.F.); and Laboratory of Molecular Imaging, Department of Radiology, Howard University, Washington, DC (P.C.W.)

Received April 28, 2008; accepted July 15, 2008

ABSTRACT

Intraperitoneal injection of [Gd@C₈₂(OH)₂₂]_n nanoparticles decreased activities of enzymes associated with the metabolism of reactive oxygen species (ROS) in the tumor-bearing mice. Several physiologically relevant ROS were directly scavenged by nanoparticles, and lipid peroxidation was inhibited in this study. [Gd@C₈₂(OH)₂₂]_n nanoparticles significantly reduced the electron spin resonance (ESR) signal of the stable 2,2-diphenyl-1-picrylhydrazyl radical measured by ESR spectroscopy. Likewise, studies using ESR with spin-trapping demonstrated efficient scavenging of superoxide radical anion, hydroxyl radical, and singlet oxygen (¹O₂) by [Gd@C₈₂(OH)₂₂]_n nanoparticles. In vitro studies using liposomes prepared from bovine liver phosphatidylcholine revealed that nanoparticles also had a strong inhibitory effect on lipid peroxidation. Consistent with their

ability to scavenge ROS and inhibit lipid peroxidation, we determined that [Gd@C₈₂(OH)₂₂]_n nanoparticles also protected cells subjected in vitro to oxidative stress. Studies using human lung adenocarcinoma cells or rat brain capillary endothelial cells demonstrated that [Gd@C₈₂(OH)₂₂]_n nanoparticles reduced H₂O₂-induced ROS formation and mitochondrial damage. [Gd@C₈₂(OH)₂₂]_n nanoparticles efficiently inhibited the growth of malignant tumors in vivo. In summary, the results obtained in this study reveal antitumor activities of [Gd@C₈₂(OH)₂₂]_n nanoparticles in vitro and in vivo. Because ROS are known to be implicated in the etiology of a wide range of human diseases, including cancer, the present findings demonstrate that the potent inhibition of [Gd@C₈₂(OH)₂₂]_n nanoparticles on tumor growth likely relates with typical capacity of scavenging reactive oxygen species.

The endohedral metallofullerenes recently attracted significant attention because of their special biomedical effect

This study was supported by the Chinese Academy of Sciences (CAS) "Hundred Talents Program" grant 07165111ZX, 973 Programs grant 2006CB705600, Natural Science Foundation of China grants 10525524 and 20751001, and the CAS Knowledge Innovation Program. This work was also supported in part by National Institutes of Health/National Center for Research Resources/Research Centers in Minority Institutions Grant 2G12RR003048, National Institutes of Health grant 5U 54CA091431, and U.S. Army Medical Research and Materiel Command grant W81XWH-05-1-0291.

Article, publication date, and citation information can be found at <http://molpharm.aspetjournals.org>.
doi:10.1124/mol.108.048348.

[S] The online version of this article (available at <http://molpharm.aspetjournals.org>) contains supplemental material.

as chemotherapeutic medicines (Cagle et al., 1999; Chen et al., 2005). Endohedral metallofullerenol nanoparticles ([Gd@C₈₂(OH)₂₂]_n) could efficiently inhibit the proliferation of tumors and decrease the activities of enzymes related to reactive oxygen species (ROS) generation in vivo, but the molecular mechanism is still unclear (Wang et al., 2006). ROS such as superoxide radical anion, hydrogen peroxide, singlet oxygen, and hydroxyl radicals have been implicated in the etiology of a wide range of acute and chronic human diseases, including amyotrophic lateral sclerosis, arthritis, cancer, cardiovascular disease, and several neurodegenerative disorders (Valko et al., 2007). Accordingly, species that have a strong capacity for scavenging ROS are of great

ABBREVIATIONS: ROS, reactive oxygen species; ESR, electron spin resonance; [Gd@C₈₂(OH)₂₂]_n nanoparticles, gadolinium endohedral metallofullerenol; HO[•], hydroxyl radical; O₂^{•-}, superoxide radical anion; ¹O₂, singlet oxygen; DPPH, 2,2-diphenyl-1-picrylhydrazyl; rBCEC, rat brain capillary endothelial cell; DMPO, 5,5-dimethyl-1-pyrroline *N*-oxide; AAPH, 2,2'-Azobis(2-amidinopropane) dihydrochloride; PBS, phosphate-buffered saline; JC-1, 5,5',6,6'-tetrachloro-1,1',3,3'-tetraethylbenzimidazole-carbocyanine iodide; ΔΨ_m, mitochondrial membrane potential; CM-H₂DCFDA, 5-(and 6-)-chloromethyl-2',7'-dichlorodihydrofluorescein diacetate, acetyl ester.

significance in biomedicine. The ability to functionalize the nanosurfaces of fullerenes and fullerene nanoparticles presents an opportunity to increase the payload of the ROS scavenger to target cells and tissues.

By using water-soluble derivatives, many investigations have measured the biological significance of fullerenes and their derivatives as prospective nanomedicines. Dugan et al. (1996) demonstrated that carboxylic acid fullerene derivatives had a potent ROS-scavenging activity and that they prevented apoptosis of cultured cortical neurons induced by exposure to *N*-methyl-D-aspartate agonists. The same derivatives protected the nigrostriatal dopaminergic system from iron-induced oxidative injury and showed effective neuroprotective antioxidant activity in vitro and in vivo. The carboxylic acid fullerene was hundreds of times more protective than vitamin E. A polyethylene glycol-conjugated fullerene (C₆₀) strongly induced tumor necrosis without any damage to the overlying normal tissue in vivo, making it an excellent candidate for targeted tumor therapy (Tabata et al., 1997). The biological effect of fullerene derivatives has been demonstrated in numerous systems, including reduction in injury after ischemic reperfusion of the intestine (Lai et al., 2000), protection of cells from undergoing apoptosis (Hsu et al., 1998; Bisaglia et al., 2000), reduction in free radical levels in organ perfusate (Chueh et al., 1999), and neuroprotective effects (Dugan et al., 1997; Lin et al., 1999). The potent biological activity of fullerene derivatives has been attributed to a combination of their unique chemical and physical characteristics. Fullerenes may therefore be particularly valuable candidates as respective nanomedicines in biological systems (Chiang et al., 1995; Tang et al., 2007b).

Endohedral metallofullerenes [i.e., compounds in which a fullerene encapsulates a metal atom(s)] have shown great promise for use in biomedical science. Although C₆₀ has been the most commonly studied fullerene in biological systems, few endohedral materials have been synthesized using C₆₀ as a cage molecule because of the limited interior volume of C₆₀. Most endohedral metallofullerenes are synthesized using C₈₂ or higher molecular weight fullerenes, and many derivatives of C₈₂ fullerenes have been synthesized in our laboratory. Gd@C₈₂ is one of the most important molecules in the metallofullerene family (Tang et al., 2007a). Gd@C₈₂(OH)₂₂ is a functionalized fullerene with gadolinium, a transition metal of lanthanide family, trapped inside a fullerene cage, and it was originally designed as a magnetic resonance imaging contrast agent for biomedical imaging (Anderson et al., 2006). We have previously reported that the chemical and physical properties of Gd@C₈₂(OH)_x are dependent on the number and position of the hydroxyl groups on the fullerene cage (Tang et al., 2007b).

In this study, electron spin resonance (ESR) spin trap technique is used to provide direct evidence that [Gd@C₈₂(OH)₂₂]_n nanoparticles can efficiently scavenge different types of ROS, including superoxide radical anion (O₂⁻), hydroxyl radical (HO[•]), and singlet oxygen (¹O₂), and the stable free radical 2,2-diphenyl-1-picrylhydrazyl (DPPH[•]). In vitro studies using liposomes prepared from bovine liver phosphatidylcholine revealed that [Gd@C₈₂(OH)₂₂]_n nanoparticles had a strong inhibitory effect on lipid peroxidation. We also determined that [Gd@C₈₂(OH)₂₂]_n nanoparticles protected cells from oxidative stress in vitro. Using human adenocarcinoma cells (A549 cells) or rat brain capillary endothelial cells (rBCECs),

we also demonstrated that [Gd@C₈₂(OH)₂₂]_n nanoparticles reduced H₂O₂-induced ROS formation and mitochondrial damage, measured as reduced mitochondrial dehydrogenase activity and membrane potential. These in vitro results correlate with the previously reported sparing effects of [Gd@C₈₂(OH)₂₂]_n nanoparticles on oxidative damage in the livers of tumor-bearing mice. [Gd@C₈₂(OH)₂₂]_n nanoparticles efficiently inhibit the growth of malignant MCF-7 solid tumor in vivo. Our overall results suggest that scavenging of ROS plays a role in the potent antitumor effects of [Gd@C₈₂(OH)₂₂]_n nanoparticles.

Materials and Methods

Materials. [Gd@C₈₂(OH)₂₂]_n nanoparticles were prepared as described previously (Xing et al., 2004; Tang et al., 2005). The nanoparticle characterizations have been described by our group (Chen et al., 2005). In brief, the average size of [Gd@C₈₂(OH)₂₂]_n particles in saline solution was 22 nm in diameter, which was measured by high-resolution atomic force microscopy and synchrotron radiation small-angle scattering. Hydrogen peroxide; xanthine; diethylenetriaminepentaacetic acid; DPPH[•]; 2,2,6,6-tetramethyl-4-piperidone; 5,5-dimethyl-1-pyrroline *N*-oxide (DMPO); and TiO₂ (anatase) were purchased from Sigma-Aldrich (St. Louis, MO). 5-Diethoxyphosphoryl-5-methyl-1-pyrroline *N*-oxide was supplied by OXIS Research, Inc. (Portland, OR). Xanthine oxidase was obtained from Roche Applied Science (Indianapolis, IN). Bovine liver phosphatidylcholine was obtained from Avanti Polar Lipids (Alabaster, AL). 2,2'-Azobis(2-amidinopropane) dihydrochloride (AAPH) was purchased from Wako Bioproducts (Richmond, VA). A Milli-Q water system (Millipore Corporation, Bedford, MA) was used to prepare ultrapure water. All of the other reagents were at least of analytical grade.

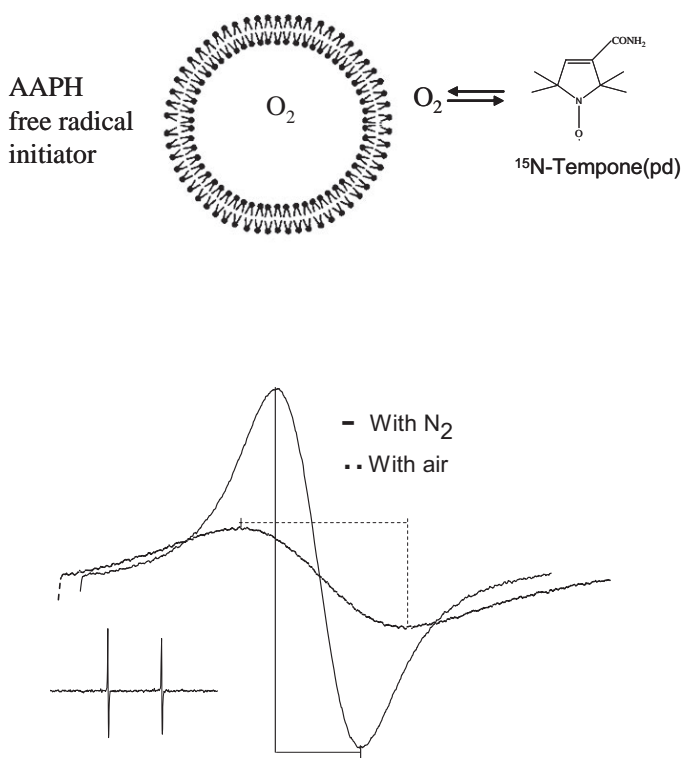
DPPH[•] Scavenging Activity. Following our previously established methodology (Yin et al., 2006), ESR spectroscopy was used to measure scavenging of the DPPH[•] free radical by [Gd@C₈₂(OH)₂₂]_n nanoparticles (Murias et al., 2005). Although DPPH[•] is a stable, nitrogen-centered radical that has no involvement in physiological processes, attenuation of the ESR signal for DPPH[•] is one of the methods widely used to demonstrate the ability of a chemical to scavenge reactive oxygen species through donation of a hydrogen atom, or, in some cases, electron transfer (Huang et al., 2005). To measure scavenging of DPPH[•], the reaction mixture contained 50 μl of [Gd@C₈₂(OH)₂₂]_n nanoparticles in 0.85% NaCl and 50 μl of 0.50 mM DPPH[•] dissolved in ethanol. The final concentration of [Gd@C₈₂(OH)₂₂]_n nanoparticles used for measurements was 0.15 mg/ml (100 μM). ESR spectra were recorded at 3, 30, 60, and 120 min after the initiation of the scavenging reaction by adding [Gd@C₈₂(OH)₂₂]_n nanoparticles. Spectra were obtained using 20-mW incident microwave power and 100-kHz field modulation of 2 G, at room temperature. The scavenging effect was determined by comparison with a control group lacking [Gd@C₈₂(OH)₂₂]_n nanoparticles.

HO[•] Scavenging Activity. The capacity of [Gd@C₈₂(OH)₂₂]_n nanoparticles to scavenge hydroxyl radical was examined by ESR spin-trapping using DMPO as a trapping agent. Hydroxyl radicals were generated by the Fenton reaction, with the reaction mixture containing freshly prepared 0.5 mM DMPO, 0.02 mM FeSO₄ (1 mM stock solution, freshly made), and 0.2 mM H₂O₂. In addition, reaction mixtures contained [Gd@C₈₂(OH)₂₂]_n nanoparticles, with final concentrations of 1.67 μM (2.5 μg/ml), 3.34 μM (5 μg/ml), 6.68 μM (10 μg/ml), and 13.34 μM (20 μg/ml), or H₂O for the blank. The ESR data were collected at ambient temperature, 6 min after initiating the formation of HO[•] by addition of FeSO₄. The following spectrometer settings were used: microwave power, 10 mW; field modulation frequency, 100 kHz; and modulation amplitude, 1 G.

Inhibition of Lipid Peroxidation. The effects of [Gd@C₈₂(OH)₂₂]_n nanoparticles on peroxidation of lipids in liposomes were measured using ESR oximetry. The ESR oximetry measurement is based on

bimolecular collision of O_2 with a spin probe. Because O_2 is paramagnetic, this collision results in spin exchange between O_2 and the spin probe, resulting in shorter relaxation times (both T_1 and T_2). Consequently, ESR signals with broader line widths are observed for the spin probe (Yin et al., 2006). Because the integrated area of the ESR signal over the scanning range is unaffected by these effects on the relaxation times, broadening of the ESR signal of the spin probe is necessarily accompanied by a decrease in the peak height of the ESR signal. In this work, the spin probe ^{15}N -Tempone (PD) (Cambridge Isotope Laboratories, Inc., Andover, MA) was used. Because the line width of this spin probe is very sensitive to O_2 concentration, decreasing oxygen concentration as a result of oxygen consumption by lipid peroxidation results in a decreasing line width of ^{15}N -Tempone (PD) spin probe. A time-dependent decrease in line width and increase in intensity of the ESR signal indicates continuous oxygen consumption. By repeated measurement of the spin probe's line widths, one can assess rate of lipid peroxidation in the sample (Scheme 1).

Liposomes were prepared as described previously (Kusumi et al., 1986). For these experiments, a suspension of 30 mg/ml bovine liver PC liposomes, and 0.1 mM ^{15}N -Tempone (PD) with or without $[Gd@C_{82}(OH)_{22}]_n$ nanoparticles (0.1–0.3 mg/ml; 66.8–200.4 μM) was added to a capillary tube. The lipid peroxidation was initiated by adding 25 mM AAPH, which is known to strongly induce lipid peroxidation in cellular and reconstituted membranes (Yin et al., 2006). The capillary tube was then sealed and positioned in the ESR instrument. ESR spectra were recorded at 4-min intervals for 28 min. Signals were obtained with 1-G scanning width, 0.5-mW incident microwave power, and 0.05-G field modulation. All ESR spectra were recorded at the low field line of ^{15}N -Tempone (PD) and at 37°C.



Scheme 1. Measurement of lipid peroxidation by ESR oximetry. Oxygen consumption is measured in a closed chamber using liposome suspensions and the spin label ^{15}N -Tempone (PD) mixed with a free radical initiator such as AAPH. The inset ESR spectra are the scans of the low field line from the ESR spectra of ^{15}N -Tempone (PD) in a nitrogen atmosphere (solid line) or air-saturated (broken line) aqueous solutions. The presence of oxygen results in a broader and less intense ESR signal for the spin probe. Spectra were recorded at 37°C, 0.5-mW microwave power, 0.05-G modulation amplitude, and 1-G scanning range.

Mitochondrial Dehydrogenase Activity in rBCEC and A549 Cells. The activity of mitochondrial dehydrogenase, a critical enzyme associated with cell survival, was measured according to a modified protocol described previously (Liang et al., 2004). In brief, rBCECs and A549 cells at 90% confluence were cultured with different concentrations of $[Gd@C_{82}(OH)_{22}]_n$ nanoparticles for 24 h. The medium was then replaced with fresh medium contained 50 μM H_2O_2 . After treatment with H_2O_2 for 2 h, cells were washed three times with PBS. The ability of mitochondria to reduce a tetrazolium salt to a formazan dye was used to assess mitochondrial dehydrogenase activity. In brief, a solution of tetrazolium salt (available in the CCK-8 kit; Dojindo Laboratories, Kumamoto, Japan) was added to the culture medium. After incubation for 1.5 h at 37°C, the absorbance at 450 nm was read using a 680 microplate spectrometer (Bio-Rad, Hercules, CA). rBCECs cells were treated with 10 μM H_2O_2 to induce oxidative damage. Each group was repeated in triplicate.

Measurement of Mitochondrial Membrane Potential. The fluorescent potentiometric dye JC-1 (Invitrogen, Carlsbad, CA) is a cationic carbocyanine compound that accumulates in mitochondria and can be used to measure mitochondrial membrane potential ($\Delta\Psi_m$). When viewed under a fluorescence microscope, JC-1 is seen as a green monomer in the cytosol and as a red aggregate in respiring mitochondria. Mitochondrial damage is measured as a reduction in $\Delta\Psi_m$ (i.e., a decrease in the red/green fluorescence ratio).

A549 or rBCECs cells (1.0×10^5 cells/ml), treated with $[Gd@C_{82}(OH)_{22}]_n$ nanoparticles and H_2O_2 as described above, were labeled with 3 μM JC-1 for 20 min in a 37°C incubator (5% CO_2). After cells were washed three times with PBS, the fluorescence was detected using a laser confocal scanning microscope (FV 500; Olympus, Tokyo, Japan). The JC-1 monomer was detected at a 530-nm emission wavelength. The fluorescence of the JC-1 aggregate was measured at 590-nm emission. The cells were also stained with Hoechst 33258 to indicate the nucleus shown in blue. Cells treated with H_2O_2 were used as the control.

Measurement of Intracellular ROS Concentration. 5-(and 6-)-Chloromethyl-2',7'-dichlorodihydrofluorescein diacetate, acetyl ester (CM-H₂DCFDA) was used to measure intracellular ROS production as reported previously (van Reyk et al., 2001). A549 and rBCECs cells were treated with $[Gd@C_{82}(OH)_{22}]_n$ nanoparticles and H_2O_2 as described above for measurement of mitochondrial dehydrogenase activity. After treatment, the samples were incubated with 5 μM CM-H₂DCFDA at 37°C for 30 min in the dark, washed three times with PBS, and then analyzed using a FACSCalibur (BD Biosciences, San Jose, CA) flow cytometer. The 488-nm excitation wavelength was used to detect the fluorescence intensity of CM-H₂DCFDA. Negative controls [without 50 μM H_2O_2 and without $[Gd@C_{82}(OH)_{22}]_n$ nanoparticles] and positive controls [with 50 μM H_2O_2 and without $[Gd@C_{82}(OH)_{22}]_n$ nanoparticles] were included in the treatment groups. Data are representative of three experiments.

Measurement of Malignant Tumor Growth in Tumor-Bearing Mice. Female tumor-bearing nude mice (six/group) were obtained from medical school of Peking University (Beijing, China). At the age of 4 weeks, mice were i.p. administered with $[Gd@C_{82}(OH)_{22}]_n$ at the concentration of 2.5 $\mu mol/kg$ (3.8 mg/ml) in saline once a day consecutively for a period of 14 days. Control animals were injected saline solution only. After animals were sacrificed, the body weight, tumor size, and tumor weight of mice administered with $[Gd@C_{82}(OH)_{22}]_n$ or saline solution were determined.

Results

Scavenging of DPPH \cdot by $[Gd@C_{82}(OH)_{22}]_n$ Nanoparticles. The scavenging activity of $[Gd@C_{82}(OH)_{22}]_n$ nanoparticles for DPPH \cdot , a stable nitrogen-centered radical, was determined. As shown in Fig. 1, DPPH \cdot produced a characteristic ESR profile. Treatment with 100 μM $[Gd@C_{82}(OH)_{22}]_n$ nano-

particles for 3 min resulted in reduction of ESR signals induced by DPPH'. Besides, addition of $[\text{Gd}@\text{C}_{82}(\text{OH})_{22}]_n$ nanoparticles caused a time-dependent decrease in the intensity of the DPPH' signal for up to 120 min. The reduction in the intensity of the ESR signal for DPPH' was 20% after 3 min and 90% at 120 min (Fig. 1) compared with the control. These results clearly indicate that under experimental conditions, the $[\text{Gd}@\text{C}_{82}(\text{OH})_{22}]_n$ nanoparticles are capable of scavenging the DPPH' stable radical in a time-dependent manner.

Scavenging of ROS by $[\text{Gd}@\text{C}_{82}(\text{OH})_{22}]_n$ Nanoparticles. To investigate the quenching of physiological ROS by $[\text{Gd}@\text{C}_{82}(\text{OH})_{22}]_n$ nanoparticles, we used the well described classic Fenton reaction involving the reaction of FeSO_4 and H_2O_2 to generate HO^\bullet radicals. Upon reaction of the spin trap DMPO with HO^\bullet , the resulting DMPO-OH adduct showed the typical 1:2:2:1 four-line ESR spectrum (with hyperfine splitting parameter $a^N = a^H = 14.9 \text{ G}$) (Fig. 2). It was observed that $[\text{Gd}@\text{C}_{82}(\text{OH})_{22}]_n$ nanoparticles at as low as $1.67 \mu\text{M}$ substantially reduced the ESR signal of the DMPO-OH adduct. Scavenging of HO^\bullet by $[\text{Gd}@\text{C}_{82}(\text{OH})_{22}]_n$ nanoparticles was concentration-dependent, with the magnitudes of the ESR signal proportionally reduced with the added $[\text{Gd}@\text{C}_{82}(\text{OH})_{22}]_n$ nanoparticles increased from 1.67, 3.34, 6.68, and up to $13.34 \mu\text{M}$. It resulted in a greater than 95% reduction in ESR signal for the DMPO-OH adduct when $13.34 \mu\text{M}$ $[\text{Gd}@\text{C}_{82}(\text{OH})_{22}]_n$ nanoparticles were added (Fig. 2).

O_2^\bullet and $^1\text{O}_2$, the other two ROS, were also reduced by

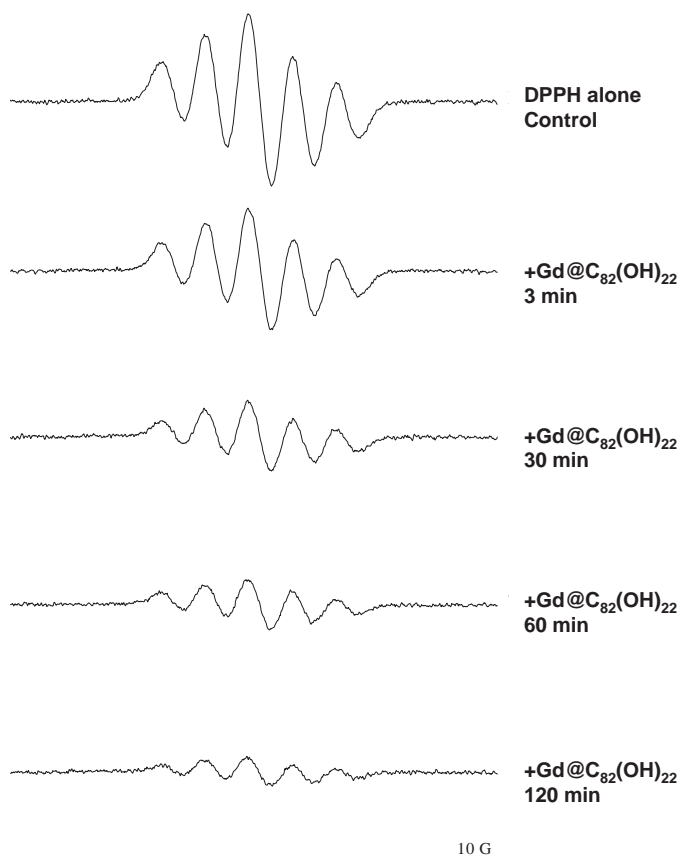


Fig. 1. Scavenging of DPPH' generated ESR signals by $[\text{Gd}@\text{C}_{82}(\text{OH})_{22}]_n$ nanoparticles ($100 \mu\text{M}$) recorded at 0, 3, 30, 60, and 120 min. The ESR settings were as follows: field setting, 3328 G; sweep width, 100 G; modulation amplitude, 2 G; and microwave power, 15 mW.

$[\text{Gd}@\text{C}_{82}(\text{OH})_{22}]_n$ nanoparticles, respectively. The reduction in the ESR signals for $^1\text{O}_2$ and O_2^\bullet was dependent on the concentration of $[\text{Gd}@\text{C}_{82}(\text{OH})_{22}]_n$ nanoparticles (Supplemental Figs. 1 and 2).

Inhibition of Lipid Peroxidation in Liposomes by $[\text{Gd}@\text{C}_{82}(\text{OH})_{22}]_n$ Nanoparticles. Reactive oxygen radicals are known to produce a time-dependent peroxidation of the polyunsaturated lipids in plasma membrane. In our study, lipid peroxidation was initiated by AAPH. Inhibition of lipid peroxidation by $[\text{Gd}@\text{C}_{82}(\text{OH})_{22}]_n$ nanoparticles was assessed using ESR oximetry recorded at 4-min intervals for 28 min. The consumption of oxygen-accompanying lipid peroxidation was measured as a time-dependent narrowing of the ESR signal for the spin probe ^{15}N -Tempone (PD). As shown in Fig. 3A, narrowing of the ESR signal was necessarily accompanied by an increase in the peak height of the ESR signal within the scanning range. The results of inhibition of lipid peroxidation by $[\text{Gd}@\text{C}_{82}(\text{OH})_{22}]_n$ nanoparticles at concentrations of 66.8, 133.6, and $200.4 \mu\text{M}$ are shown in Fig. 3, B–D, respectively; the ESR signal intensities were approximately 80, 75, and 70% of the control (Fig. 3A). All resulted in lower consumption rates of oxygen seen as smaller peak heights in the ESR signal as a result of lower rates of line narrowing of the spin probe. Increasing the concentration of $[\text{Gd}@\text{C}_{82}(\text{OH})_{22}]_n$ nanoparticles from 66.8 to $200.4 \mu\text{M}$ resulted in an increased inhibition of lipid peroxidation measured as retardation of line narrowing, and an increase in the ESR signal formed by interaction with the spin probe (Fig. 3, B–D). The progressive increases in peak-to-peak signal intensity (and accompanying progressive narrowing of line width) in each panel were due to time-dependent oxygen consumption resulting from lipid peroxidation.

Biological Activity of $[\text{Gd}@\text{C}_{82}(\text{OH})_{22}]_n$ Nanoparticles in Normal (rBCEC) and Cancer (A549) Cells under Oxidative Stress. The protective effects of $[\text{Gd}@\text{C}_{82}(\text{OH})_{22}]_n$ nanoparticles against cellular oxidative damage were investigated. Treatment of adenocarcinoma (A549) cells or rBCECs with H_2O_2 for 2 h resulted in significant cellular damage, measured as loss of mitochondrial dehydrogenase activity (Fig. 4A). Pretreatment of cells with up to $66.8 \mu\text{M}$ $[\text{Gd}@\text{C}_{82}(\text{OH})_{22}]_n$ nanoparticles significantly reduced oxidative injury to cellular mitochondria. This protective effect in adenocarcinoma A549 cells was similar to the protection in rBCECs under same pretreatment with $[\text{Gd}@\text{C}_{82}(\text{OH})_{22}]_n$ nanoparticles (Fig. 4A).

The $[\text{Gd}@\text{C}_{82}(\text{OH})_{22}]_n$ nanoparticles were also evaluated for their ability to protect against H_2O_2 -induced mitochondrial damage, measured as a reduction in the $\Delta\Psi_m$. Mitochondrial membrane potential is important for oxidative phosphorylation through electron transfer chain in mitochondria. Dysfunction of mitochondria could enhance the electron leak and ROS generation in cells treated with H_2O_2 . The $\Delta\Psi_m$, an indicator of mitochondrial damage level, was measured with the JC-1 probe by flow cytometry. In cells untreated with H_2O_2 , the JC-1 probe was seen primarily as red aggregates, indicating substantial uptake by respiring mitochondria (Fig. 4B, A and D). For both rBCEC and A549 cells, treatment with H_2O_2 resulted in a decrease in red aggregates of the JC-1 probe in mitochondria and an increase in green monomers of the JC-1 probe in the cytoplasm (Fig. 4B, B and E). These results demonstrate H_2O_2 -induced mitochondrial damage and a reduction in $\Delta\Psi_m$. Pretreatment of cells with $[\text{Gd}@\text{C}_{82}(\text{OH})_{22}]_n$ nanoparticles resulted in partial

restoration of mitochondrial uptake of the JC-1, indicating a protective effect against oxidative injury to cellular mitochondria (Fig. 4B, C and F). Protection of mitochondria measured by $\Delta\Psi_m$ is consistent with the measurement of mitochondrial dehydrogenase activity in rBCEC and A549 cells pretreated with $[\text{Gd}@\text{C}_{82}(\text{OH})_{22}]_n$ nanoparticles.

Figure 4C shows the effects $[\text{Gd}@\text{C}_{82}(\text{OH})_{22}]_n$ nanoparticles on the levels of H_2O_2 -induced intracellular ROS. Treatment of rBCEC or A549 cells with H_2O_2 resulted in a significant increase in intracellular ROS. Pretreatment with $[\text{Gd}@\text{C}_{82}(\text{OH})_{22}]_n$ nanoparticles significantly ($P < 0.05$) reduced the levels of H_2O_2 -induced ROS in both cell types. The total inhibition percentage in A549 cells was $29.7 \pm 2.23\%$

and in rBCECs was $11.9 \pm 1.85\%$, respectively. These results demonstrate a correlation between the bioeffects of $[\text{Gd}@\text{C}_{82}(\text{OH})_{22}]_n$ nanoparticles and their ability to scavenge physiological ROS.

Inhibitory Efficacy of $[\text{Gd}@\text{C}_{82}(\text{OH})_{22}]_n$ Nanoparticles on Tumor Growth in Nude Mice. The growth of human breast carcinomas in mice treated with $[\text{Gd}@\text{C}_{82}(\text{OH})_{22}]_n$ nanoparticles and saline for a period of 14 days was determined. As shown in Fig. 5A, tumor size of mice treated with $[\text{Gd}@\text{C}_{82}(\text{OH})_{22}]_n$ nanoparticles was much smaller than that of control animals. The tumor weight of mice treated with $2.5 \mu\text{mol/kg}$ $[\text{Gd}@\text{C}_{82}(\text{OH})_{22}]_n$ nanoparticles and with saline is shown in Fig. 5B. The nanoparticle showed significant inhib-

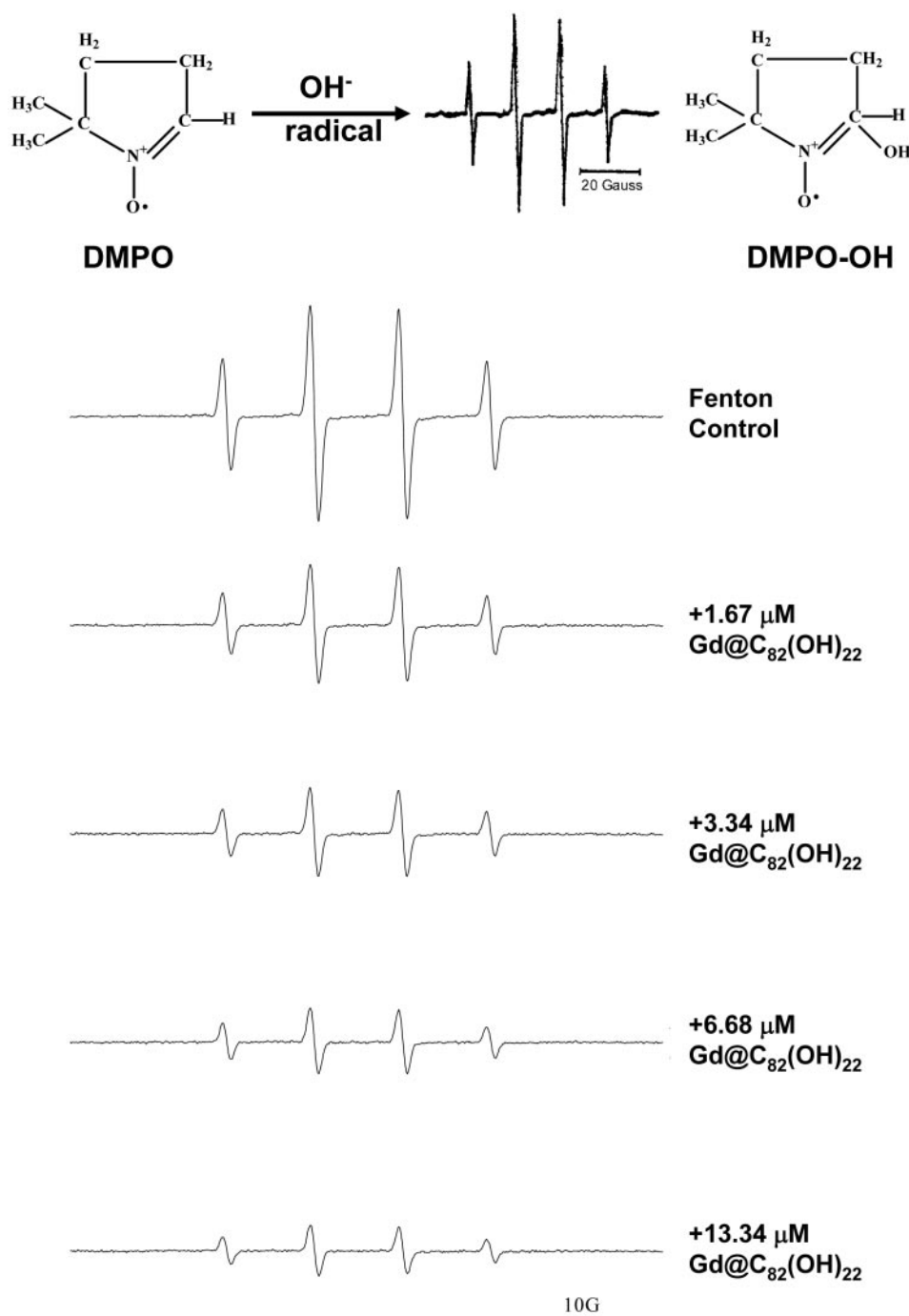


Fig. 2. ESR signals of hydroxyl radicals generated by Fenton reaction and scavenged by $[\text{Gd}@\text{C}_{82}(\text{OH})_{22}]_n$ nanoparticles measured at 6 min after initiating generation of HO^\cdot . The ESR settings were as follows: field setting, 3328 G; sweep width, 100 G; modulation amplitude, 1 G; and microwave power, 15 mW.

itory effect 6 days after treatment. In addition, there was less mortality of mice treated with $[\text{Gd}@\text{C}_{82}(\text{OH})_{22}]_n$ nanoparticles than the saline-treated group (data not shown).

Discussion

In this study, we used the ESR technique to provide direct evidence that $[\text{Gd}@\text{C}_{82}(\text{OH})_{22}]_n$ nanoparticles can markedly scavenge different types of ROS. These results are consistent with the previously reported sparing effects of $[\text{Gd}@\text{C}_{82}(\text{OH})_{22}]_n$ nanoparticles on oxidative damage in the livers of tumor-bearing mice (Chen et al., 2005). $[\text{Gd}@\text{C}_{82}(\text{OH})_{22}]_n$ nanoparticles reduced H_2O_2 -induced ROS formation and mitochondrial damage, measured as reduced mitochondrial dehydrogenase activity and mem-

brane potential in adenocarcinoma cells or rat brain capillary endothelial cells, $[\text{Gd}@\text{C}_{82}(\text{OH})_{22}]_n$ nanoparticles also efficiently inhibit the growth of malignant solid tumors in vivo. The overall data suggest that scavenging of reactive oxygen species by $[\text{Gd}@\text{C}_{82}(\text{OH})_{22}]_n$ nanoparticles plays a vital role in the inhibition of tumor growth.

Similar to most of chemotherapeutic agents used in clinic, the development of fullereneol nanoparticles for tumor treatment is hampered by their high cytotoxicity. There are modulation factors that can determine whether the developed fullereneol nanoparticles exhibit high therapeutic efficiency and low toxicity (Nishibori et al., 2004). ROS are known to be important factors to initiate the progress of tumor proliferation. In this study, we demonstrate that $[\text{Gd}@\text{C}_{82}(\text{OH})_{22}]_n$

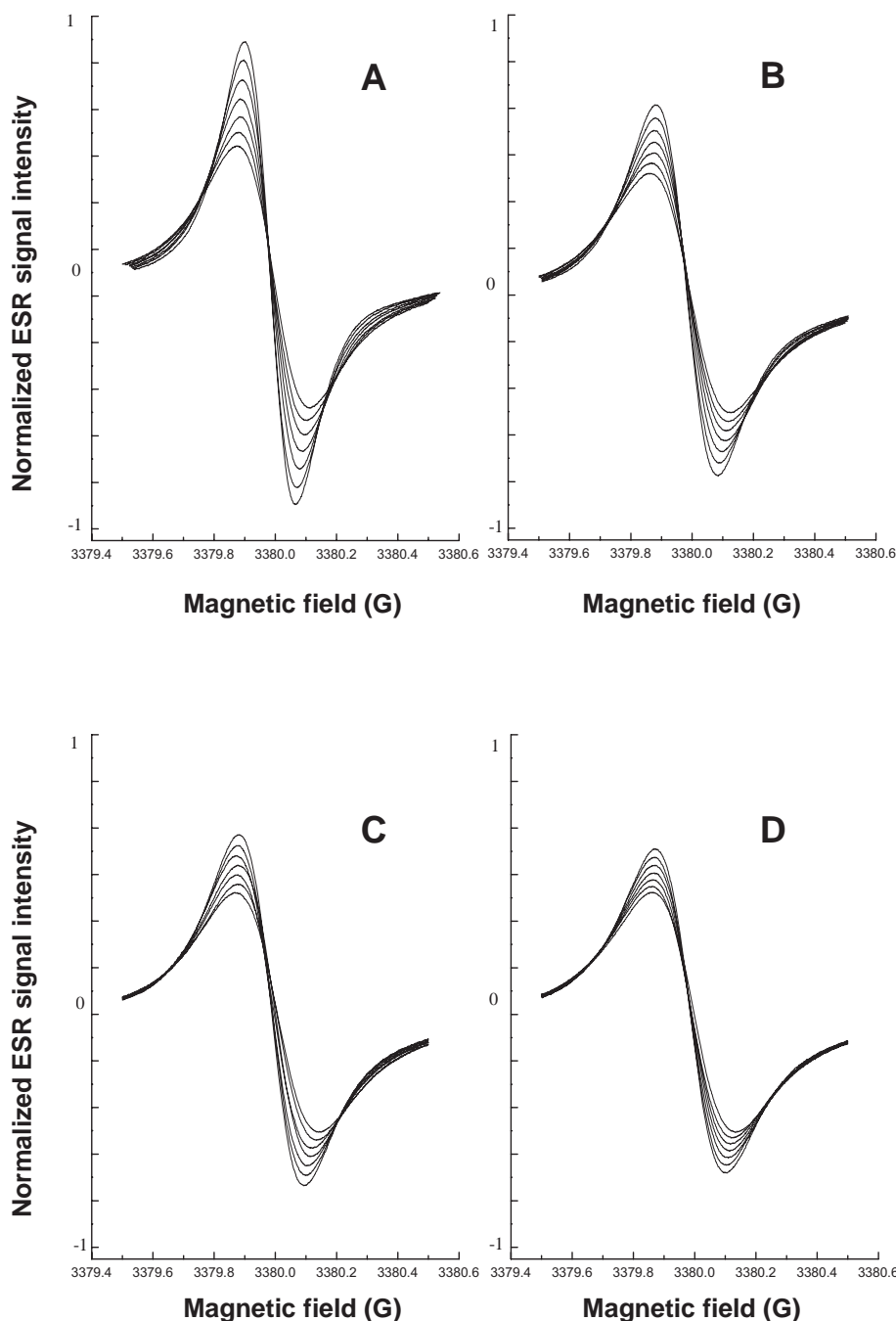


Fig. 3. Inhibition of lipid peroxidation by $[\text{Gd}@\text{C}_{82}(\text{OH})_{22}]_n$ nanoparticles. Lipid peroxidation was initiated by 25 mM AAPH (A) and inhibited by 66.8 μM (B), 133.6 μM (C), and 200.4 μM (D) $[\text{Gd}@\text{C}_{82}(\text{OH})_{22}]_n$ nanoparticles. The ESR spectra were recorded at 4-min intervals for 28 min with a Varian E-109 X-band spectrometer (Varian, Inc., Palo Alto, CA) equipped with a variable temperature controller accessory. Signals were obtained with 0.5-mW incident microwave power and with 0.05-G field modulation at 37°C.

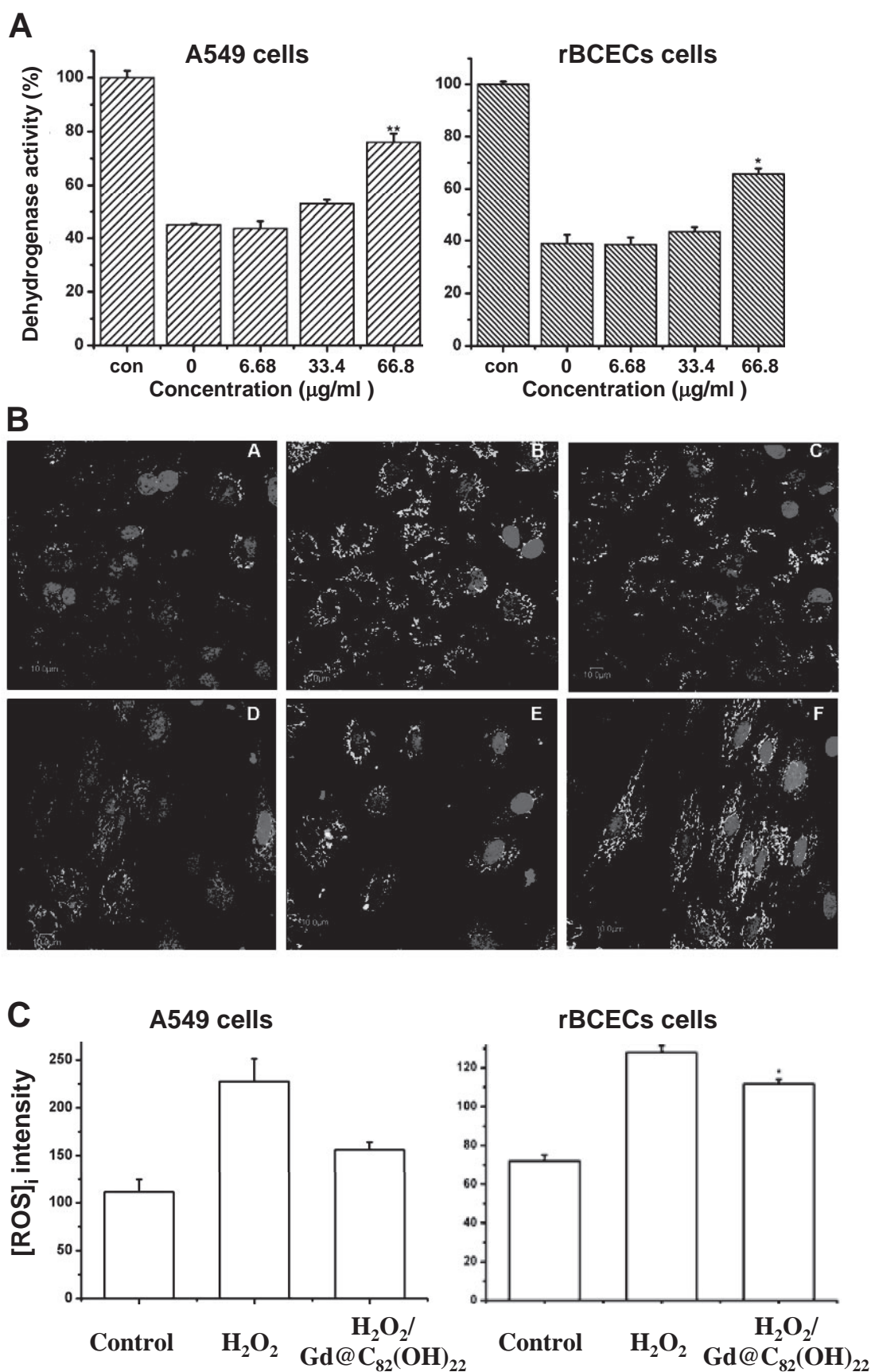


Fig. 4. $[\text{Gd@C}_{82}(\text{OH})_{22}]_n$ nanoparticles reduced intracellular ROS in rBCEC and A549 cells. A, reduction of mitochondrial dehydrogenase activity by 6.68 μM (10 $\mu\text{g/ml}$), 33.4 μM (50 $\mu\text{g/ml}$), and 66.8 μM (100 $\mu\text{g/ml}$) of $[\text{Gd@C}_{82}(\text{OH})_{22}]_n$ nanoparticles incorporated in A549 cells and rBCECs. Statistical significance was observed when treated with 100 $\mu\text{g/ml}$ $[\text{Gd@C}_{82}(\text{OH})_{22}]_n$ nanoparticles (significance noted as *, $P < 0.05$ and **, $P < 0.01$). B, protection against H_2O_2 -induced mitochondrial damage by 66.8 μM (100 $\mu\text{g/ml}$) $[\text{Gd@C}_{82}(\text{OH})_{22}]_n$ nanoparticles measured as a reduction in $\Delta\Psi_m$. A and D, untreated cells; B and E, H_2O_2 -treated cells; and C and F, cells pretreated with $[\text{Gd@C}_{82}(\text{OH})_{22}]_n$ nanoparticles. A to C represent A549 cells. D to F represent rBCECs. C, reduction of H_2O_2 -induced intracellular ROS by 66.8 μM (100 $\mu\text{g/ml}$) $[\text{Gd@C}_{82}(\text{OH})_{22}]_n$ nanoparticles.

nanoparticles inhibit tumor growth by efficiently scavenging ROS, which promotes tumor proliferation.

With support of our experimental results, we hypothesize that $\text{Gd@C}_{82}(\text{OH})_{22}$ nanoparticles scavenge ROS through electron-electron polarization, forming a semicharge transfer complex with free radicals. The Gd@C_{82} metallofullerene has a C_{82} cage and a C_{2v} point group symmetry. The encapsulated gadolinium atom located in the vicinity of the highly conjugated carbon-carbon double bonds of the cage effectively polarizes electron distribution on the carbon cage around the encapsulated gadolinium atom (Nishibori et al., 2004). Our theoretical calculations by an ab initio method (Takabayashi et al., 2004) revealed that the highest occupied molecular orbitals in $\text{Gd@C}_{82}(\text{OH})_{22}$ are localized mainly on the carbon atoms away from the gadolinium atom, whereas almost no frontier orbital distributes on the carbon cage close to the gadolinium atom (Tang et al., 2007a). Thus, encapsulation of the gadolinium transition atom inside of the fullerene cage facilitates polarization of the electrons on the cage, rendering

it more accessible for forming the charge-transfer complex with reactive oxygen radicals. Boltalina et al. (1997) reported the electron affinity of several gadolinium metallofullerenes, ranging from C_{74} up to C_{82} , and determined that in all cases, encapsulation of gadolinium atom inside of the fullerene cage gives rise to an increase in electron affinity (Boltalina et al., 1997). Although the electron affinity of C_{82} is 3.14 ± 0.06 eV, the electron affinity of Gd@C_{82} is higher, with a value of 3.3 ± 0.1 eV. Thus, encapsulation of a gadolinium atom inside of the C_{82} cage enhances the interaction with free radicals through an electron polarization mode.

As shown from our theoretical calculations, besides the effect of the encaged gadolinium atom, the multihydroxyl groups of $\text{Gd@C}_{82}(\text{OH})_{22}$ nanoparticles also induce electron-deficient areas on the cage surface of the molecules, rendering them highly susceptible for attack by the nucleophilic free radicals, such as the hydroxyl radical. The hydroxyl radical polarized toward the $\text{Gd@C}_{82}(\text{OH})_{22}$ cage surface partially loses its electron density, but it can be stabilized (compensated) through forming hydrogen bonding with the proximate hydroxyl proton(s) of $\text{Gd@C}_{82}(\text{OH})_{22}$. Because of its highly electronic deficient and very large cage surface area, the hydroxyl radical-bounded $\text{Gd@C}_{82}(\text{OH})_{22}$ can absorb (trap) another hydroxyl radical through similar electron polarization. The complex species is water-soluble, moves freely within the cells, and is susceptible for interaction with mediums, particularly water, resulting in the chemical formation of hydrogen peroxide, hydroxide, hydrogen molecule, and the recovered intact $\text{Gd@C}_{82}(\text{OH})_{22}$ molecule. The recovered $\text{Gd@C}_{82}(\text{OH})_{22}$ is intact; thus, it can continuously proceed free radical scavenging through the same mechanism. As such, $\text{Gd@C}_{82}(\text{OH})_{22}$ nanoparticles serve as a converter to destroy free radicals into other species but without destroying $\text{Gd@C}_{82}(\text{OH})_{22}$ itself.

We hypothesize that this mechanism to scavenge ROS may be general. Our proposed mechanism suggests that $\text{Gd@C}_{82}(\text{OH})_{22}$ can act as an ROS scavenging sponge, capable of wiping out (scavenging) all types of ROS. Intracellular ROS are known to induce DNA mutation, including the formation of DNA strand breaks and modification DNA bases (Halliwell and Aruoma, 1991; Dizdaroglu, 1992). Therefore, $\text{Gd@C}_{82}(\text{OH})_{22}$ that can scavenge all types of reactive oxygen radicals should possess important biological consequences, including inhibition of tumor cell growth. Investigators are examining the biomedical uses for fullerenes as antioxidants, which can effectively scavenge active radicals or suppress ROS in organ or tissue and reducing oxidative stress caused by tumor progression. Therefore, an increase in antioxidant capacity and ROS scavenging activity would reduce the physiological deterioration and enhance the organism resistance to tumor initiation and promotion. Chemical modifications to alter the surface properties of endohedral metallofullerenol are widely applied to modulate their biological effects, in particular, to reduce or eliminate the nanotoxicity of metallofullerenol in vivo or in vitro (Sayes et al., 2004; Wang et al., 2004). Our study provides new insight in developing novel kinds of nanoparticles as effective chemotherapeutic agents. More research is needed to support the chemotherapeutic mechanism of endohedral metallofullerenes, including $[\text{Gd@C}_{82}(\text{OH})_{22}]_n$ nanoparticles, to fully exploit them in biomedicine.

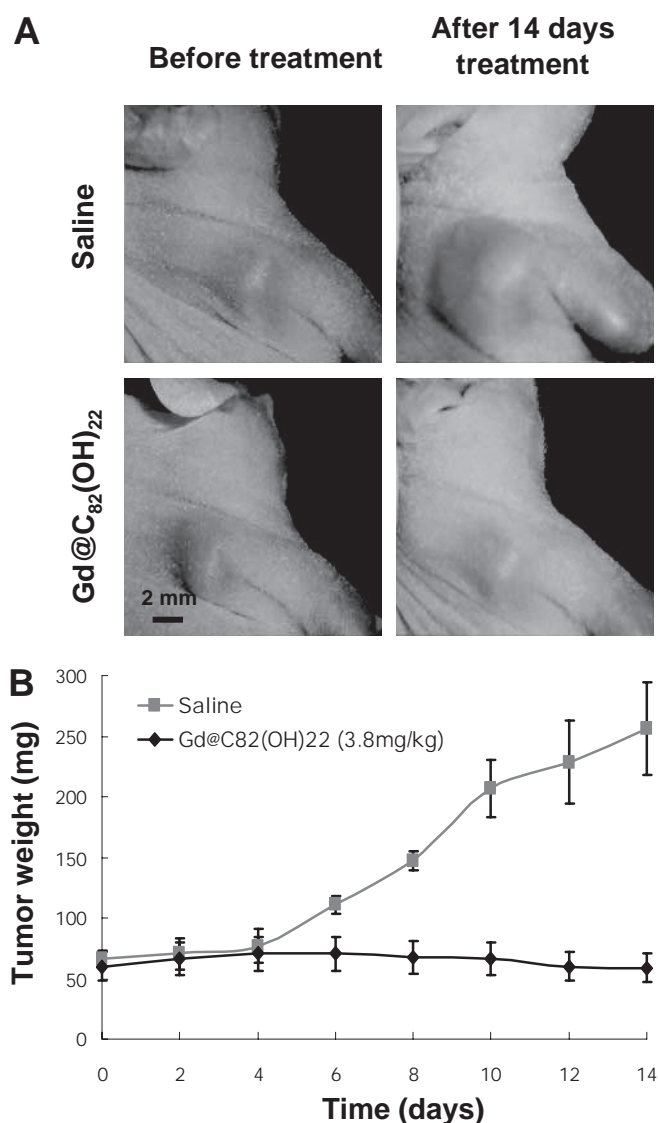


Fig. 5. Inhibition of tumor growth in nude mice by $[\text{Gd@C}_{82}(\text{OH})_{22}]_n$ nanoparticles. **A**, photographs of tumor size. **B**, tumor growth inhibition by $[\text{Gd@C}_{82}(\text{OH})_{22}]_n$ nanoparticles (●) compared with saline group (■). ***, $P = 0.001$, two-tailed Student's t test, nanoparticles versus saline.

Acknowledgments

We gratefully acknowledge the comments of Wayne Wamer (Center for Food Safety & Applied Nutrition/U.S. Food and Drug Administration) during the preparation of this manuscript.

References

- Anderson SA, Lee KK, and Frank JA (2006) Gadolinium-fullerenol as a paramagnetic contrast agent for cellular imaging. *Invest Radiol* **41**:332–338.
- Bisaglia M, Natalini B, Pellicciari R, Straface E, Malorni W, Monti D, Franceschi C, and Schettini G (2000) C3-Fullero-tris-methanodicarboxylic acid protects cerebellar granule cells from apoptosis. *J Neurochem* **74**:1197–1204.
- Boltalina O, Ioffe IN, Sorokin ID, and Sidorov LN (1997) Electron affinity of some endohedral lanthanide fullerenes. *J Phys Chem A* **101**:9561–9563.
- Cagle DW, Kennel SJ, Mirzadeh S, Alford JM, and Wilson LJ (1999) In vivo studies of fullerene-based materials using endohedral metallofullerene radiotracers. *Proc Natl Acad Sci U S A* **96**:5182–5187.
- Chen C, Xing G, Wang J, Zhao Y, Li B, Tang J, Jia G, Wang T, Sun J, Xing L, et al. (2005) Multihydroxylated [Gd@C82(OH)22]n nanoparticles: antineoplastic activity of high efficiency and low toxicity. *Nano Lett* **5**:2050–2057.
- Chiang LY, Lu FJ, and Lin JT (1995) Free radical scavenging activity of water-soluble fullerenols. *J Chem Soc Chem Commun* **1**:1283–1284.
- Chueh SC, Lai MK, Lee MS, Chiang LY, Ho TI, and Chen SC (1999) Decrease of free radical level in organ perfusate by a novel water-soluble carbon-sixty, hexa(sulfoethyl)fullerenes. *Transplant Proc* **31**:1976–1977.
- Dizdaroğlu M (1992) Oxidative damage to DNA in mammalian chromatin. *Mutat Res* **275**:331–342.
- Dugan LL, Gabrielsen JK, Yu SP, Lin TS, and Choi DW (1996) Buckminsterfullerenol free radical scavengers reduce excitotoxic and apoptotic death of cultured cortical neurons. *Neurobiol Dis* **3**:129–135.
- Dugan LL, Turetsky DM, Du C, Lobner D, Wheeler M, Almlı CR, Shen CK, Luh TY, Choi DW, and Lin TS (1997) Carboxyfullerenes as neuroprotective agents. *Proc Natl Acad Sci U S A* **94**:9434–9439.
- Halliwell B and Aruoma OI (1991) DNA damage by oxygen-derived species. Its mechanism and measurement in mammalian systems. *FEBS Lett* **281**:9–19.
- Hsu SC, Wu CC, Luh TY, Chou CK, Han SH, and Lai MZ (1998) Apoptotic signal of Fas is not mediated by ceramide. *Blood* **91**:2658–2663.
- Huang D, Ou B, and Prior RL (2005) The chemistry behind antioxidant capacity assays. *J Agric Food Chem* **53**:1841–1856.
- Kusumi A, Subczynski WK, Pasenkiewicz-Gierula M, Hyde JS, and Merkle H (1986) Spin-label studies on phosphatidylcholine-cholesterol membranes: effects of alkyl chain length and unsaturation in the fluid phase. *Biochim Biophys Acta* **854**:307–317.
- Lai HS, Chen WJ, and Chiang LY (2000) Free radical scavenging activity of fullerenol on the ischemia-reperfusion intestine in dogs. *World J Surg* **24**:450–454.
- Liang XJ, Shen DW, and Gottesman MM (2004) Down-regulation and altered localization of γ -catenin in cisplatin-resistant adenocarcinoma cells. *Mol Pharmacol* **65**:1217–1224.
- Lin AM, Chyi BY, Wang SD, Yu HH, Kanakamma PP, Luh TY, Chou CK, and Ho LT (1999) Carboxyfullerene prevents iron-induced oxidative stress in rat brain. *J Neurochem* **72**:1634–1640.
- Murias M, Jäger W, Handler N, Erker T, Horvath Z, Szekeres T, Nohl H, and Gille L (2005) Antioxidant, prooxidant and cytotoxic activity of hydroxylated resveratrol analogues: structure-activity relationship. *Biochem Pharmacol* **69**:903–912.
- Nishibori E, Iwata K, and Sakata M (2004) Anomalous endohedral structure of Gd@C82 metallofullerenes. *Phys Rev B* **69**:113412.
- Sayes CM, Guo W, Lyon D, Byd AM, Ausman KD, Tao YJ, Sitharaman B, Wilson LJ, Hughes JB, West JL, et al. (2004) The differential cytotoxicity of water-soluble fullerenes. *Nano Lett* **4**:1881–1887.
- Tabata Y, Murakami Y, and Ikada Y (1997) Photodynamic effect of polyethylene glycol-modified fullerene on tumor. *Jpn J Cancer Res* **88**:1108–1116.
- Takabayashi Y, Rikiishi Y, Hosokawa T, Shibata K, and Kubozono Y (2004) Preferred location of the Dy ion in the minor isomer of Dy@C82 determined by Dy LIII-edge EXAFS. *Chem Phys Lett* **388**:23–26.
- Tang J, Xing G, Yuan H, Cao WB, Jing L, Gao X, Qu L, Cheng Y, Ye C, Zhao Y, et al. (2005) Tuning electronic properties of metallic atom in bondage to a nanospace. *J Phys Chem B* **109**:8779–8785.
- Tang J, Xing G, Zhao F, Yuan H, and Zhao Y (2007a) Modulation of structural and electronic properties of fullerene and metallofullerenes by surface chemical modifications. *J Nanosci Nanotechnol* **7**:1085–1101.
- Tang J, Xing J, Zhao Y, Jing L, Yuan H, Zhao F, Gao X, Qian H, Su R, Ibrahim K, et al. (2007b) Switchable semiconductive property of the polyhydroxylated metallofullerene. *J Phys Chem B* **111**:11929–11934.
- Valko M, Leibfritz D, Moncol J, Cronin MT, Mazur M, and Telser J (2007) Free radicals and antioxidants in normal physiological functions and human disease. *Int J Biochem Cell Biol* **39**:44–84.
- van Reyk DM, King NJ, Dinauer MC, and Hunt NH (2001) The intracellular oxidation of 2',7'-dichlorofluorescein in murine T lymphocytes. *Free Radic Biol Med* **30**:82–88.
- Wang H, Wang J, Deng X, Sun H, Shi Z, Gu Z, Liu Y, and Zhao Y (2004) Biodistribution of carbon single-wall carbon nanotubes in mice. *J Nanosci Nanotechnol* **4**:1019–1024.
- Wang J, Chen C, Li B, Yu H, Zhao Y, Sun J, Li Y, Xing G, Yuan H, Tang J, et al. (2006) Antioxidative function and biodistribution of [Gd@C82(OH)22]n nanoparticles in tumor-bearing mice. *Biochem Pharmacol* **71**:872–881.
- Xing G, Zhao YL, Tang J, Zhang B, and Gao XF (2004) Influence of structural properties on stability of fullerenols. *J Phys Chem B* **108**:11473–11479.
- Yin JJ, Kramer JK, Yurawecz MP, Eynard AR, Mossoba MM, and Yu L (2006) Effects of conjugated linoleic acid (CLA) isomers on oxygen diffusion-concentration products in liposomes and phospholipid solutions. *J Agric Food Chem* **54**:7287–7293.

Address correspondence to: Dr. Xing-Jie Liang, Laboratory of Nanobiomedicine and Nanosafety, Division of Nanomedicine and Nanobiology, National Center for Nanoscience and Technology of China, 11, First North Rd., Zhongguancun, Beijing, People's Republic of China, 100190. E-mail: liangxj@nanoctr.cn



Image-based evaluation of the molecular events underlying HC11 mammary epithelial cell differentiation

Liang Shan^a, Renshu Zhang^b, Wanghai Zhang^c, Edward Lee^c, Rajagopalan Sridhar^b, Elizabeth G. Snyderwine^d, Paul C. Wang^{a,*}

^a Department of Radiology, Howard University, Washington, DC 20060, USA

^b Department of Radiation Oncology, Howard University, Washington, DC 20060, USA

^c Department of Pathology, Howard University, Washington, DC 20060, USA

^d National Cancer Institute, National Institutes of Health, Bethesda, MD 20892, USA

ARTICLE INFO

Article history:

Received 24 July 2008

Available online 8 August 2008

Keywords:

Mammary epithelial cells

Differentiation

Signal pathways

Optical imaging

ABSTRACT

We have developed an image-based technique for signal pathway analysis, target validation, and compound screening related to mammary epithelial cell differentiation. This technique used the advantages of optical imaging and the HC11-Lux model system. The HC11-Lux cell line is a subclone of HC11 mammary epithelial cells transfected stably with a luciferase construct of the β -casein gene promoter (p-344/-1 β c-Lux). The promoter activity was imaged optically in real time following lactogenic induction. The imaging signal intensity was closely correlated with that measured using a luminometer following protein extraction ($R = 0.99$, $P < 0.0001$) and consistent with the messenger RNA (mRNA) level of the endogenous β -casein gene. Using this technique, we examined the roles of JAK2/Stat5A, Raf-1/MEK/MAKP, and PI3K/Akt signal pathways with respect to differentiation. The imaging studies showed that treatment of the cells with epidermal growth factor (EGF), AG490 (JAK2-specific inhibitor), and LY294002 (PI3K-specific inhibitor) blocked lactogenic differentiation in a dose-dependent manner. PD98059 (MEK-specific inhibitor) could reverse EGF-mediated differentiation arrest. These results indicate that these pathways are essential in cell differentiation. This simple, sensitive, and reproducible technique permits visualization and real-time evaluation of the molecular events related to milk protein production. It can be adopted for high-throughput screening of small molecules for their effects on mammary epithelial cell growth, differentiation, and carcinogenesis.

© 2008 Elsevier Inc. All rights reserved.

The mammary gland undergoes a physiological cycle of lobuloalveolar development and differentiation from the virgin state to pregnancy and lactation. This cycle involves a complex interplay of both hormones and growth factors [1–3]. Abnormal development is an important factor in breast carcinogenesis. Hormones, including estrogen and prolactin, are strongly associated with an increase in breast cancer risk, with evidence of a dose-response relationship [4–6]. In addition, exposure to certain chemicals and hormone-mimicking or endocrine-disrupting compounds leads to breast carcinogenesis, precocious puberty, or inability to produce sufficient breast milk [7,8]. To date, approximately 200 chemical compounds have been recognized as risk factors in human breast carcinogenesis, but most of the chemicals to which people are routinely exposed remain to be tested for carcinogenic risk. The conventional analytic methods for molecular delineation and compound screening are generally time-consuming and need DNA, RNA, and/or protein extraction as the first step. To under-

stand the complex interplay of hormones, growth factors, and environmental compounds on the growth and differentiation of mammary epithelial cells, it is critical to develop a simple and sensitive method with the capability of high-throughput screening (HTS)¹ [9,10].

The HC11 mammary epithelial cell line was originally derived from midpregnant BALB/c mouse mammary gland tissue. HC11 cells have retained the characteristics of normal mammary epithelial stem cells. After growth to confluence in the presence of insulin and epidermal growth factor (EGF), HC11 cells become competent and respond to stimulation by the lactogenic hormones dexamethasone, insulin, and prolactin (DIP). The cells will undergo differentiation with synthesis of milk proteins such as β -casein, a marker of

* Corresponding author. Fax: +1 202 865 3722.

E-mail address: pwang@howard.edu (P.C. Wang).

¹ Abbreviations used: HTS, high-throughput screening; EGF, epidermal growth factor; DIP, dexamethasone, insulin, and prolactin; GM, growth medium; DMEM, Dulbecco's modified Eagle's medium; FBS, fetal bovine serum; DM, differentiation medium; CCD, charge-coupled device; p/s, photons per second; BCA, bicinchoninic acid; cDNA, complementary DNA; PCR, polymerase chain reaction; EtBr, ethidium bromide; UV, ultraviolet; RT, reverse transcriptase; mRNA, messenger RNA; ATP, adenosine triphosphate; MAO, monoamine oxidase.

mammary gland terminal differentiation [7,11]. On the other hand, transplantation of HC11 cells transfected with certain oncogenes can result in tumor development in nude mice [12]. Because of these unique features, HC11 cells provide a well-established in vitro model system for studying signal transduction pathways and hormonal/growth factor regulation of mammary epithelial cell differentiation [7,13–16]. The current study describes a simple and sensitive method for optical imaging of the molecular events leading to differentiation of HC11 mammary epithelial cells. The HC11 cells are stably transfected with a β -casein promoter luciferase construct (p-344/-1 β c-Lux) (HC11-Lux). When the cells grow to confluence in the presence of EGF and insulin in the medium, they become competent and are ready to respond to DIP. The competent HC11-Lux cells show extremely high β -casein promoter activity when stimulated with DIP. The β -casein promoter activity could be detected on the basis of light emission and imaged in real time using an optical imaging system. The light signal intensity was closely correlated with the cell differentiation state. Using this system, we successfully imaged the time-dependent changes during DIP-induced differentiation. We investigated the role of several key signal transduction pathways using pathway-specific inhibitors. The image-based method maximizes the information, simplifies the traditional techniques, and is potentially useful for developing a rapid and robust HTS method for signal pathway analysis, target validation, and small-molecule screening.

Materials and methods

HC11-Lux cell culture

The HC11-Lux mammary epithelial cell line (a subclone of COMMA-1D cells) was kindly provided by David S. Salomon (National Cancer Institute, Bethesda, MD, USA) and Nancy E. Hynes (Friedrich Miescher Institute, Basel, Switzerland) [15,16]. The cells

are stably transfected with a β -casein promoter luciferase construct (p-344/-1 β c-Lux). Cells were routinely maintained in growth medium (GM) that consisted of Dulbecco's modified Eagle's medium (DMEM)/F-12 medium, 10% heat-inactivated fetal bovine serum (FBS), 5 μ g/ml bovine insulin, 10 ng/ml EGF, and 50 μ g/ml each of penicillin, streptomycin, and neomycin. The culture medium, FBS, insulin, EGF, and antibiotics all were purchased from Invitrogen (Carlsbad, CA, USA). To induce differentiation, cells were seeded in 96-well microplates and allowed to grow to 100% confluence. The cells were maintained in GM for 1 to 2 more days to become competent. The competent cells were then stimulated with differentiation medium (DM) for various times. The DM contained DMEM/F-12, 10% heat-inactivated FBS, 5 μ g/ml bovine insulin, 1 μ M dexamethasone (Sigma, St. Louis, MO, USA), 5 μ g/ml bovine prolactin (Sigma), and 50 μ g/ml each of penicillin, streptomycin, and neomycin.

Bioluminescent optical imaging

Luciferase-based bioluminescent optical imaging was performed using a Xenogen IVIS 200 imaging system (Caliper Life Sciences, Hopkinton, MA, USA). The system is equipped with a highly sensitive, cooled charge-coupled device (CCD) camera and a light-tight specimen box. Imaging and quantification of signals were controlled by the acquisition and analysis software Living Image 3.0 (Caliper Life Sciences). To image the event of differentiation, d-luciferin was added to each well and mixed gently (final concentration of 150 μ g/ml). The microplates were then placed on the stage of the specimen box. The temperature of the stage inside the box was maintained at 37 °C. Images were captured at 5 min after adding d-luciferin. The image acquisition time was 1 min. The bioluminescent signal from the cells in each well was measured and expressed as total flux (photons per second [p/s]). At least five replicates were performed in all experiments, and each

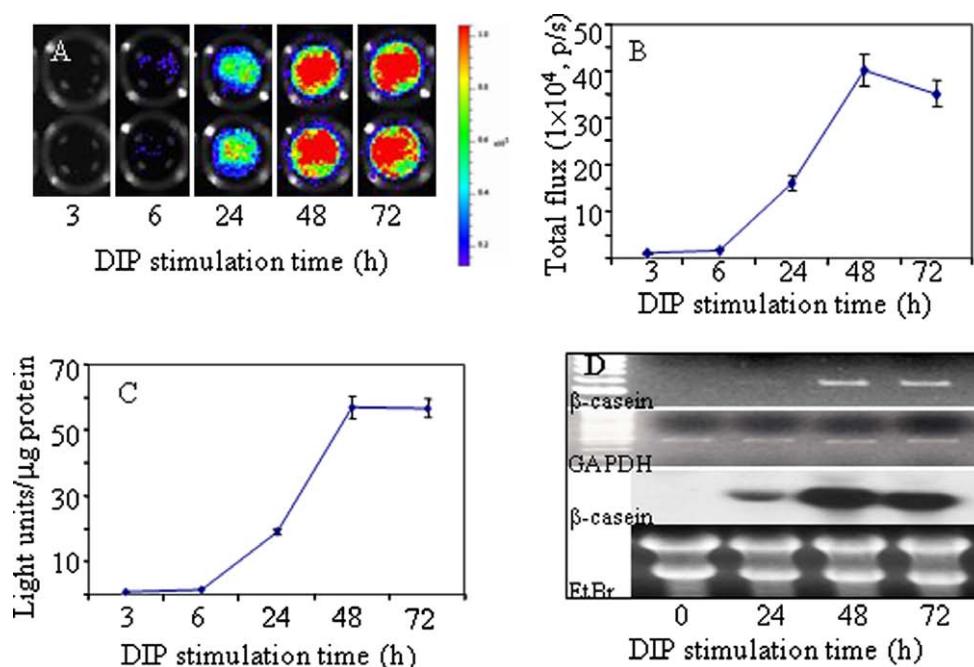


Fig. 1. Imaging of DIP-induced differentiation and comparison with traditional methods. (A) Representative images of the cells at different times following DIP induction. (B) Quantification of the light signals from the images. (C) β -Casein promoter activity measured using single-tube luminometer following protein extraction. A close correlation was obtained between image-based and luminometer measurements for β -casein promoter activity ($R = 0.99$, $P < 0.001$). (D) Semiquantitative RT-PCR and Northern blot analysis of the endogenous β -casein gene mRNA level, showing consistency with imaging findings. Cells were seeded in 96-well microplates in GM, maintained for 2 days after 100% confluence, and then stimulated with DIP and imaged. For protein and RNA extraction, 24- or 6-well plates were used. Values are the means and standard deviations of five replicates. GAPDH is used as the internal control.

experiment was repeated at least three times. The representative data are presented.

β -Casein gene promoter activity measurement using luminometric assay

HC11-Lux cells were cultured in 24-well plates and harvested at different times after DM stimulation and other treatments. The total protein was extracted from cells, and the β -casein gene promoter activity was assayed on triplicate samples using the luciferase assay system (Promega, Madison, WI, USA). Protein concentration was determined using the bicinchoninic acid (BCA) protein assay kit (Pierce, Rockford, IL, USA). The light emission (expressed as light units) was measured on a single-tube luminometer. The β -casein promoter activity was expressed as light units/microgram protein.

Semiquantitative RT-PCR and Northern blot analysis

Cells were cultured and treated on 6-well plates. Total RNA was isolated from HC11-Lux cells using TRIzol extraction reagent (Invitrogen). From each sample, 1 μ g of total RNA was used to synthesize the first-strand complementary DNA (cDNA) in a final volume of 20 μ l using the SuperScript First-Strand Synthesis Kit (Invitrogen). Also, 0.5 μ l of the cDNA was used to amplify a segment of the β -casein gene using the primers 5'-ACTGTATCCTCTGAGACTG-3' and 5'-TCTAGGTACTGCAGAAGTC-3'. An amplified fragment of the GAPDH gene was used as an internal control, and the primers were purchased from Invitrogen. The polymerase chain reaction (PCR) was carried out for 20 cycles, with each cycle consisting of a denaturing step for 45 s at 94 °C, an annealing step for 45 s at 58 °C, and a polymerization step for 45 s at 72 °C. The PCR product was separated on 2% agarose gel containing ethidium

bromide (EtBr) and was photographed under ultraviolet (UV) illumination. For Northern blot analysis, 30 μ g of total RNA were separated on 1% agarose-formaldehyde gel. Loading of the RNA was evaluated with EtBr staining. The RNA was transferred to nylon membranes (Micron Separations, Westboro, MA, USA) and hybridized overnight to the β -casein probe. The β -casein probe was a fragment generated by reverse transcriptase (RT)-PCR as described above and was 32 P-labeled using the Ready-To-Go DNA Labeling Beads (-dCTP) (Amersham Biosciences, Piscataway, NJ, USA).

Statistical analysis

The results were analyzed using the statistical software Origin-Pro 7.0 (OriginLab, Northampton, MA, USA). A *P* value of 0.05 was considered as a significant correlation for the β -casein gene promoter activity between the image-based method and the luminometer measurement following protein extraction.

Results

Imaging of DIP-induced cell differentiation

To image the differentiation event, cells were seeded on 96-well microplates, allowed to grow to 100% confluence, maintained for 2 more days in the GM, and then stimulated with DM. Cells were imaged at 3, 6, 24, 48 and 72 h separately using a Xenogen optical imaging system (Alameda, CA, USA) (Figs. 1A and B). The light signal from the cells could be detected as early as 6 h, although the signal was weak. A significantly higher light signal was detected at 24 h, and the signal reached the highest levels at 48 and 72 h. When confluent cells were maintained for a relatively long period in the GM (e.g., ≥ 2 days), a stronger light signal from cells was usually detected at 48 h than at 72 h following DIP stimulation.

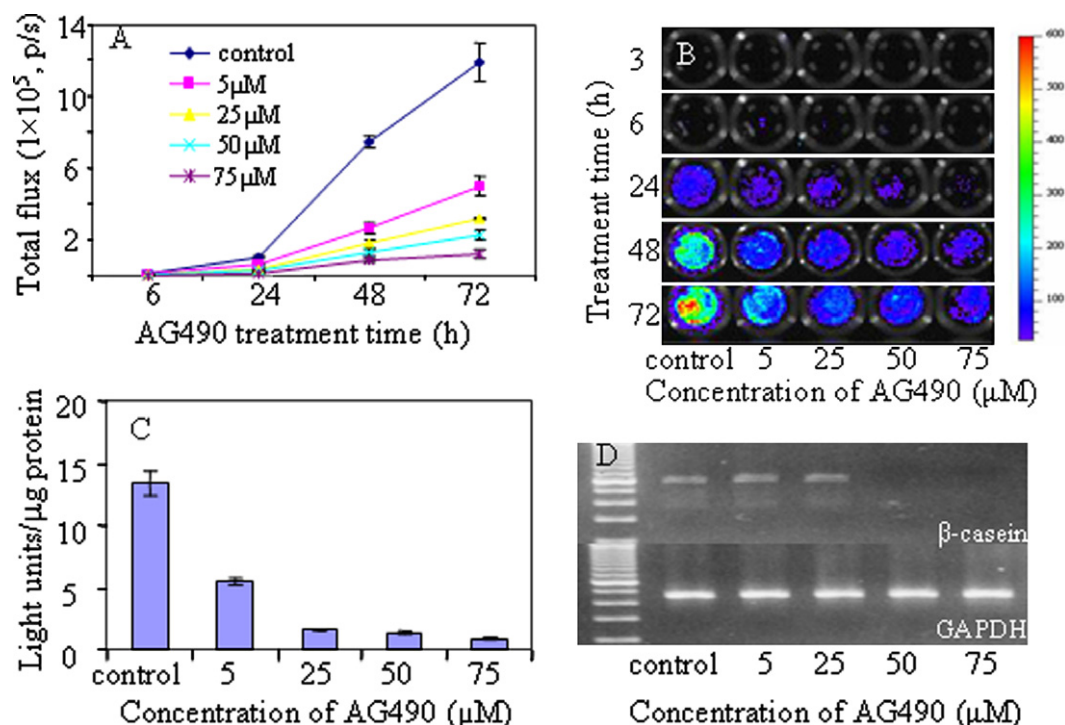


Fig. 2. Imaging of cell differentiation inhibition following inhibition of JAK2 using specific inhibitor AG490. Confluent cells were maintained for 1 day in GM and then stimulated using DM with AG490 at different concentrations. (A,B) Representative images and quantitative results showing dose-dependent decrease of light signals and indicating inhibition of cell differentiation. (C) β -Casein promoter activity at 48 h time point measured using luminometer. (D) Semiquantitative RT-PCR of endogenous β -casein gene mRNA at 48 h time point. There was a close correlation between imaging findings and luminometer measurement and consistency with the β -casein mRNA level. GAPDH is used as the internal control. Control: DM alone.

This phenomenon might be related to the different status of cell proliferation activity. To confirm the imaging results, we also measured the β -casein gene promoter activity using the luminometric assay following protein extraction (Fig. 1C). Luminometric results were similar to those of optical imaging, and a close correlation for the β -casein gene promoter activity was obtained between the two methods ($R = 0.99$, $P = 0.0008$). Both techniques demonstrated that the HC11-Lux cells underwent differentiation following DIP stimulation. To verify whether the β -casein gene promoter activity represented the differentiation status, the messenger RNA (mRNA) level of the endogenous β -casein gene was analyzed using semiquantitative RT-PCR (Fig. 1D, upper two panels) and Northern blot analysis (Fig. 1D, lower two panels). Both methods demonstrated a detectable mRNA level at 24 h, and the level became higher at 48 and 72 h following DIP stimulation. The imaging results were consistent with those from RT-PCR and Northern blot analysis. Optical imaging is simple and superior to these traditional methods for real-time visualization and evaluation of the cell differentiation. Imaging and image process could be completed within a few minutes.

Imaging of differentiation inhibition by blocking JAK2/Stat5A signal pathway

The JAK2/Stat5A signal pathway is the major mechanism of DIP-induced mammary cell differentiation. AG490 is a JAK2-selective inhibitor [17]. To image the effect of AG490 on differentiation, AG490 was added into DM at various concentrations when GM was replaced by DM. Cells were imaged at different time points. A dose-dependent inhibition of the β -casein gene promoter activity was clearly imaged (Figs. 2A and B). The cells emitted a significantly lower light signal than the control without AG490 treatment ($P < 0.01$). At the concentration of 5 μ M AG490, the β -casein gene promoter activity decreased to less than half of the control. These results indicate that blockage of the JAK2/Stat5A signal pathway led to failure of the cell differentiation. When β -casein gene promoter activity at the 48-h time point was measured using the luminometric assay following protein extraction, similar results were obtained, with a close correlation between the two methods ($R = 0.99$, $P = 0.001$). The optical imaging results were also consistent with the mRNA level of the endogenous β -casein gene from RT-PCR analysis (Fig. 2D), indicating the reliability of optical imaging for detecting differentiation status.

Imaging the role of Raf-1/MEK/MAKP signal pathway

Activation of the Raf-1/MEK/MAKP signal pathway is responsible for mammary epithelial cell growth [16]. Previous studies demonstrated that activation of this pathway by DIP is important for optimization of DIP-induced differentiation. However, overactivation of this pathway plays an important role in mammary gland carcinogenesis. We imaged the significance of this signal pathway in the mammary cell differentiation. EGF is well known to activate this pathway. When the competent HC11-Lux cells were treated with both DIP and EGF, the imaging showed that EGF effectively inhibited the β -casein promoter activity even at a concentration as low as 0.5 ng/ml (Figs. 3A and B). This inhibitory effect in imaging was consistent with the β -casein mRNA expression by RT-PCR (Fig. 3C). These cells exhibited undetectable levels of β -casein mRNA expression at 48 h. On the contrary, the control cells without EGF showed both high β -casein promoter activity and high β -casein mRNA level. PD98059 is a specific MEK inhibitor that can selectively block MEK activation in response to different growth factors, including EGF [16]. As competent HC11-Lux cells were treated with

PD98059 and DIP together, PD98059 enhanced the DIP-induced β -casein promoter activity (Figs. 4A and B). At the concentration of 10 μ M, PD98059 showed the most effective enhancement, with twofold higher β -casein promoter activity than DIP alone. In the presence of EGF (1 ng/ml) in DM, PD98059 reversed the inhibitory effect of EGF in a dose-dependent manner (Figs. 4C and D). At the concentrations of 5 to 20 μ M, more than 50% recovery of the activity was obtained for the EGF-induced inhibition. These results suggest that EGF could block the DIP-induced differentiation and that activation of the raf-1/MEK/MAKP pathway is one of the major mechanisms of differentiation arrest.

Imaging of PI3K/Akt signal pathway

PI3K/Akt is another important signal pathway in DIP-induced HC11 differentiation [18]. We inhibited the PI3K/Akt pathway using the PI3K-specific inhibitor LY294002 (Fig. 5) [18]. When LY294002 was added into the DM, the DIP-induced cell differentiation was significantly inhibited, presenting a dose-dependent inhibitory pattern. At the concentration of 10 μ M, the light signal

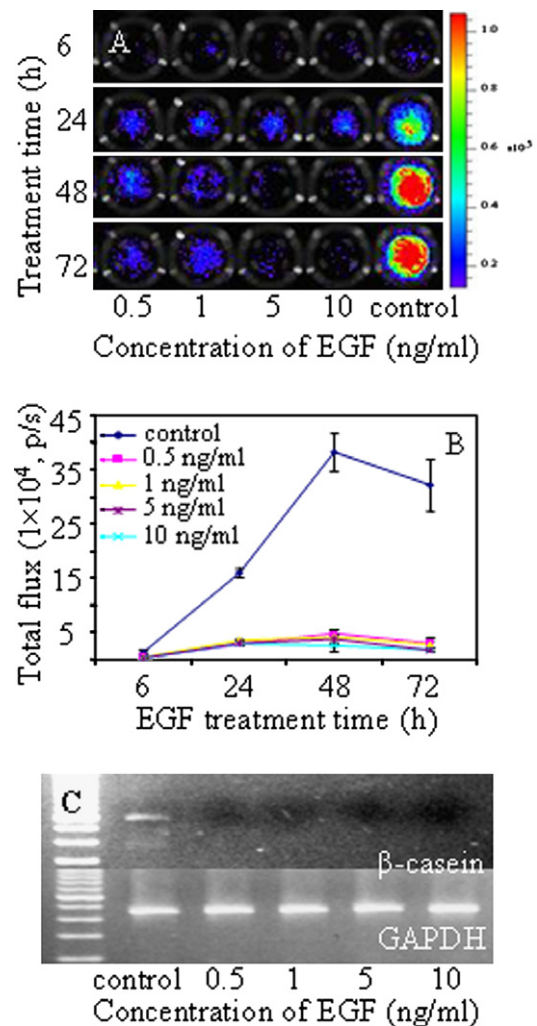


Fig. 3. Imaging of cell differentiation arrest following overactivation of Raf-1/MEK/MAKP pathway by adding EGF into DM. (A,B) Representative images and quantitative results showing complete differentiation arrest by EGF. (C) Semiquantitative RT-PCR of endogenous β -casein gene mRNA at 48 h time point showing undetectable β -casein mRNA that was consistent with imaging findings. GAPDH is used as the internal control. Control: DM alone.

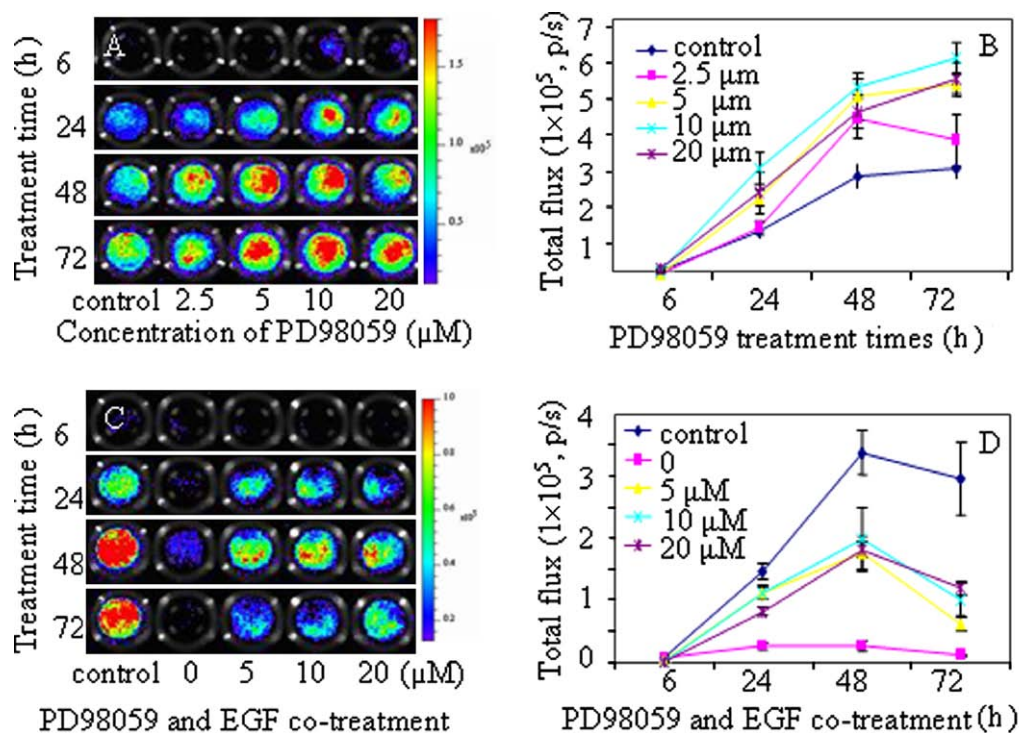


Fig. 4. Imaging of the cell differentiation alteration following inhibition of Raf-1/MEK/MAKP pathway using MEK-specific inhibitor PD98059 and its reversal effect of EGF-induced differentiation arrest. (A,B) Representative images and quantitative results showing enhancement of DIP-induced differentiation by PD98059. (C,D) Cotreatment of cells using PD98059 and EGF showing partial reversal of EGF-induced arrest. Control: DM alone. In other samples, EGF was added at the concentration of 1 ng/ml and PD98059 was added as indicated in panels C and D.

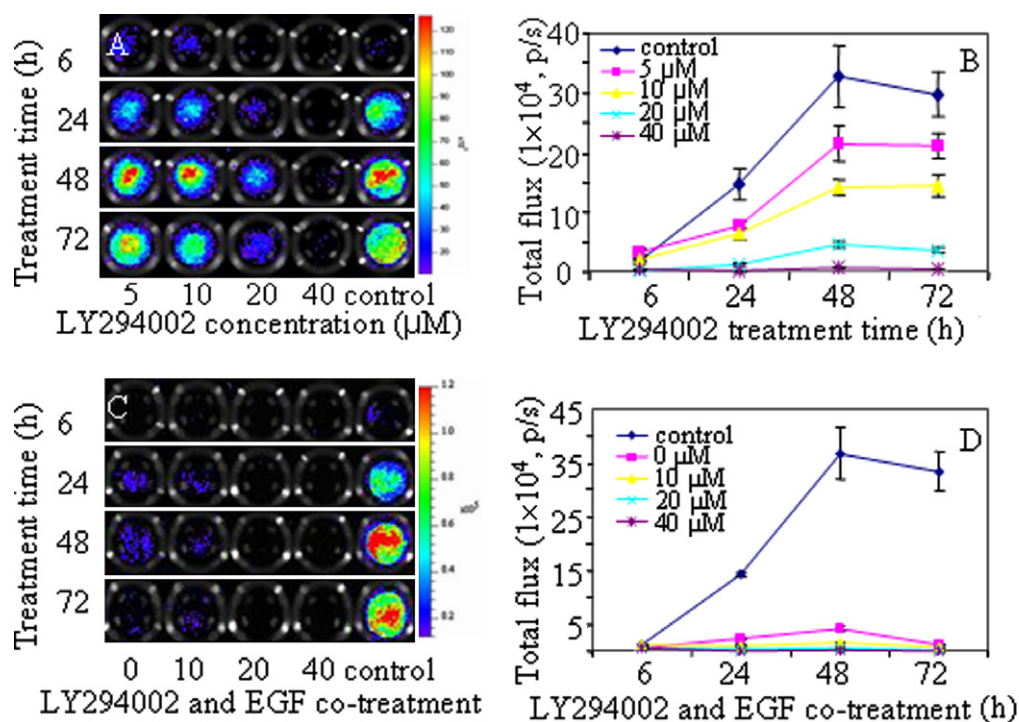


Fig. 5. Imaging of cell differentiation following inhibition of PI3K/Akt pathway using PI3K-specific inhibitor LY294002. LY294002 was added into DM at different concentrations before treatment. (A,B) Representative images and quantitative results showing dose-dependent inhibition of DIP-induced differentiation. (C,D) Cotreatment of cells using LY294002 and EGF showing complete arrest of DIP-induced differentiation. Control: DM alone. In other samples, EGF was added at the concentration of 1 ng/ml and LY294002 was added as indicated in panels C and D.

intensity was only approximately 40% of the controls at different treatment time points (24, 48, and 72 h). At the concentration higher than 20 μM, the light signal intensity was significantly

lower, indicating that DIP-induced differentiation was nearly completely arrested. When the cells were treated with LY294002 in the presence of EGF, the imaging results revealed

that the cell differentiation was completely inhibited even at very low concentrations of both EGF (1 ng/ml) and LY294002 (5 μ M/ml). EGF and LY294002 had an additive or synergistic effect on the inhibition of DIP-induced mammary epithelial cell differentiation. These results suggest that the PI3K/Akt pathway plays an important role in DIP-induced β -casein expression.

Discussion

Recent technological advances have made it feasible to conduct HTS of gene expression changes and small molecules based on visual phenotypes of individual cells or functional reporters using automated imaging [9,10]. Luciferase-based bioluminescent imaging is cost-effective and easy to use, with an extremely high signal-to-noise ratio relative to other imaging techniques. In the presence of oxygen, Mg^{2+} , and adenosine triphosphate (ATP), luciferase catalyzes the conversion of d-luciferin to oxyluciferin, which is accompanied by release of a photon. This article has described a simple and sensitive image-based method that is reproducible and permits real-time evaluation and visualization of the molecular events related to milk protein production. We tested the feasibility of this technique for imaging DIP-induced differentiation and underlying signal pathways. The hallmark of mammary gland differentiation is secretion of milk protein, including β -casein. Transcription of the β -casein gene is highly dependent on prolactin. Insulin and dexamethasone increase prolactin-stimulated β -casein mRNA transcription and stability. The close correlation between the image findings and β -casein promoter activity as measured following protein extraction indicates that this method was precise in quantification. The consistency of the image-based findings with the endogenous β -casein mRNA expression level suggests that findings in imaging indeed reflected the status of cell differentiation. DIP-induced differentiation involves JAK2/Stat5A, Raf-1/MEK/MAKP, and PI3K/Akt pathways [15–17]. On normal mammary epithelial cells, JAK2/Stat5A mediates growth-suppressive and differentiation-inducing effects, whereas the Raf-1/MEK/MAKP pathway plays a key role in cell proliferation and the PI3K/Akt pathway contributes to cell survival. In mammary gland carcinogenesis, JAK2/Stat5A signaling plays a dual role in breast cancer initiation and progression [19–21]. Aberrant activation of the Raf-1/MEK/MAKP pathway is related to development of various cancers, including breast cancer [22]. The PI3K/Akt pathway contributes to resistance of mammary gland tumors to chemotherapy [18]. We imaged the role of the three key pathways in DIP-induced cell differentiation. Inhibition of the JAK2/Stat5A and PI3K/Akt pathways using specific inhibitors and overactivation of Raf-1/MEK/MAKP using EGF all led to failure of differentiation, presenting significant low light signal in optical imaging. Close correlation or consistency for the findings between the image-based technique and conventional methods demonstrates that this technique is reliable.

Compared with conventional methods, the significant advantage of the image-based method is that it is simple, is rapid, and permits real-time visualization and evaluation of cell differentiation status. These features make the image-based technique ideal for laboratory automation. This method can be extended to robust HTS of natural or human-made small molecules for their effects on mammary differentiation, carcinogenesis, or drug development. Analysis using signal pathway-specific inhibitors demonstrated the potential as an HTS technique. HTS primarily aims to systematically test hundreds of small molecules to find candidates. Recently developed and more complex phenotypic assays, such as cell-based and whole-organism-based ones, precede HTS to validate new targets and characterize new lead com-

pounds in cellular contexts [23]. The cell-based phenotypic assay is an upcoming methodology for the investigation of cellular processes and their alteration by multiple chemical or genetic perturbations [24,25]. Cell-based screens use genetic engineering to narrow the field of targets in an attempt to reduce their complexity to that of a biochemical assay. Ding and coworkers developed a method using a neuronal-specific promoter luciferase construct in embryonic stem cells to screen compounds that can induce neuron differentiation [26]. This embryonic stem cell system allows compounds to induce complex phenotypic change, differentiation of cells into neurons, without prior knowledge of the mechanism underlying this transformation. Valley and coworkers described a two-step homogeneous bioluminescent assay for monoamine oxidase (MAO) and screened small molecules to find MAO inhibitors [27]. With the help of automated fluorescent microscopy, Li and coworkers identified some blockers of gap junction communication between cells by coculturing donor cells (preloaded with a membrane-impermeable dye) and acceptor cells and measuring junction-dependent transfer of fluorescence into acceptor cells [28]. In contrast to biochemical screening, these assays detect the responses within the context of intercellular structural and functional networks of normal and diseased cells, respectively. However, high variation of many cell-based assays and not yet fully satisfying solutions for quantitative image analysis are limitations of the technology. The method described in the current study used the characteristics of the HC11 cell system and highly sensitive bioluminescent imaging to visualize and quantify the mammary epithelial cell differentiation. To our knowledge, it is the first image-based system for signal pathway analysis, target validation, and compound screening related to mammary epithelial cell differentiation.

Acknowledgments

We thank Drs. David S. Salomon and Nancy E. Hynes for providing HC11-Lux cell line. This work was supported in part by USAMRMC W81XWH-05-1-0291, Charles and Mary Latham Fund (#7023185), NIH 5P20 CA118770. This work was also supported in part by grant 2 G12 RR003048 from the RCMI Program Division of Research Infrastructure, National Center for Research Resources, NIH.

References

- [1] C. Briskin, Hormonal control of alveolar development and its implications for breast carcinogenesis, *J. Mammary Gland Biol. Neoplasia* 7 (2002) 39–48.
- [2] V. Goffin, N. Binart, P. Touraine, P.A. Kelly, Prolactin: The new biology of an old hormone, *Annu. Rev. Physiol.* 64 (2002) 47–67.
- [3] N. Binart, C.J. Ormandy, P.A. Kelly, Mammary gland development and the prolactin receptor, *Adv. Exp. Med. Biol.* 480 (2000) 85–92.
- [4] E. Cavalieri, D. Chakravarti, J. Guttenplan, E. Hart, J. Ingel, R. Jankowiak, P. Muti, E. Rogan, J. Russo, R. Santen, T. Sutter, Catechol estrogen quinones as initiators of breast and other human cancers: Implications for biomarkers of susceptibility and cancer prevention, *Biochim. Biophys. Acta* 1766 (2006) 63–78.
- [5] J. Russo, L.M. Hasan, G. Balogh, S. Guo, I.H. Russo, Estrogen and its metabolites are carcinogenic agents in human breast epithelial cells, *J. Steroid Biochem. Mol. Biol.* 87 (2003) 1–25.
- [6] L. Shan, S.A. Rouhani, H.A.J. Schut, E.G. Snyderwine, 2-Amino-1-methyl-6-phenylimidazo[4,5-b]pyridine (PhIP) modulates lactogenic hormone-mediated differentiation and gene expression in HC11 mouse mammary epithelial cells, *Cell Growth Differ.* 12 (2001) 649–656.
- [7] L. Shan, M. Yu, E.G. Snyderwine, Gene expression profiling of chemically-induced rat mammary gland cancer, *Carcinogenesis* 26 (2005) 503–509.
- [8] S.E. Fenton, Endocrine-disrupting compounds and mammary gland development: Early exposure and later life consequences, *Endocrinology* 147 (Suppl. 6) (2006) S18–S24.
- [9] P.A. Clemons, Complex phenotypic assays in high-throughput screening, *Curr. Opin. Chem. Biol.* 8 (2004) 334–338.
- [10] S.A. Sundberg, High-throughput and ultra-high-throughput screening: Solution- and cell-based approaches, *Curr. Opin. Biotechnol.* 11 (2000) 47–53.

- [11] L. Shan, M. Yu, C. Qiu, E.G. Snyderwine, Id4 regulates mammary epithelial cell growth and differentiation and is overexpressed in rat mammary gland carcinomas, *Am. J. Pathol.* 163 (2003) 2495–2502.
- [12] A. Raafat, A. Zoltan-Jones, L. Strizzi, S. Bargo, K. Kimura, D. Salomon, R. Callahan, Kit and PDGFR- activities are necessary for Notch4/Int3-induced tumorigenesis, *Oncogene* 26 (2007) 662–672.
- [13] N. Chughtai, S. Schimchowitsch, J.J. Lebrun, S. Ali, Prolactin induces SHP-2 association with Stat5 nuclear translocation and binding to the -casein gene promoter in mammary cells, *J. Biol. Chem.* 277 (2002) 31107–31114.
- [14] T. Galbaugh, M.G. Cerrito, C.C. Jose, M.L. Cutler, EGF-induced activation of Akt results in mTOR-dependent p70S6 kinase phosphorylation and inhibition of HC11 cell lactogenic differentiation, *BMC Cell Biol.* 7 (2006) 34.
- [15] B.M. Marte, T. Meyer, S. Stabel, G.J. Standke, S. Jaken, D. Fabbro, N.E. Hynes, Protein kinase C and mammary cell differentiation: Involvement of protein kinase C alpha in the induction of -casein expression, *Cell Growth Differ.* 5 (1994) 239–247.
- [16] M.G. Cerrito, T. Galbaugh, W. Wang, T. Chopp, D. Salomon, M.L. Cutler, Dominant negative Ras enhances lactogenic hormone-induced differentiation by blocking activation of the Raf-Mek-Erk signal transduction pathway, *J. Cell Physiol.* 201 (2004) 244–258.
- [17] J. Xie, M.J. LeBaron, M.T. Nevalainen, H. Rui, Role of tyrosine kinase Jak2 in prolactin-induced differentiation and growth of mammary epithelial cells, *J. Biol. Chem.* 277 (2002) 14020–14030.
- [18] R.L. Dillon, D.E. White, W.J. Muller, The phosphatidylinositol 3-kinase signaling network: Implications for human breast cancer, *Oncogene* 26 (2007) 1338–1345.
- [19] C. Briskin, A. Ayyanan, W. Doppler, Prolactin signaling and Stat5: Going their own separate ways? *Breast Cancer Res.* 4 (2002) 209–212.
- [20] L. Shan, M. Yu, B. Clark, E.G. Snyderwine, Possible role of Stat5a in rat mammary gland carcinogenesis, *Breast Cancer Res. Treat.* 88 (2004) 263–272.
- [21] K.U. Wagner, H. Rui, Jak2/Stat5 signaling in mammaryogenesis, breast cancer initiation, and progression, *J. Mammary Gland Biol. Neoplasia* 13 (2008) 93–103.
- [22] J.A. McCubrey, L.S. Steelman, W.H. Chappell, S.L. Abrams, E.W. Wong, F. Chang, B. Lehmann, D.M. Terrian, M. Milella, A. Tafuri, F. Stivala, M. Libra, J. Basecke, C. Evangelisti, A.M. Martelli, R.A. Franklin, Roles of the Raf/MEK/ERK pathway in cell growth, malignant transformation, and drug resistance, *Biochim. Biophys. Acta* 1773 (2007) 1263–1284.
- [23] M.J. Evans, A. Saghatelian, E.J. Sorensen, B.F. Cravatt, Target discovery in small-molecule cell-based screens by in situ proteome reactivity profiling, *Nat. Biotechnol.* 23 (2005) 1303–1307.
- [24] J.J. Cali, A. Niles, M.P. Valley, M.A. O'Brien, T.L. Riss, J. Schultz, Bioluminescent assays for ADMET, *Expert Opin. Drug Metab. Toxicol.* 4 (2008) 103–120.
- [25] K. Korn, E. Krausz, Cell-based high-content screening of small-molecule libraries, *Curr. Opin. Chem. Biol.* 11 (2007) 503–510.
- [26] S. Ding, T.Y. Wu, A. Brinker, E.C. Peters, W. Hur, N.S. Gray, P.G. Schultz, Synthetic small molecules that control stem cell fate, *Proc. Natl. Acad. Sci. USA* 100 (2003) 7632–7637.
- [27] M.P. Valley, W. Zhou, E.M. Hawkins, J. Shultz, J.J. Cali, T. Worzella, L. Bernad, T. Good, D. Good, T.L. Riss, D.H. Klaubert, K.V. Wood, A bioluminescent assay for monoamine oxidase activity, *Anal. Biochem.* 359 (2006) 238–246.
- [28] Z. Li, Y. Yan, E.A. Powers, X. Ying, K. Janjua, T. Garyantes, B. Baron, Identification of gap junction blockers using automated fluorescence microscopy imaging, *J. Biomol. Screen.* 8 (2003) 489–499.

转铁蛋白导向脂质体核磁造影剂纳米粒子 ($\text{Tf}^{\text{NR}}\text{-Lip}^{\text{NBD}}\text{-Magnevist}$) ——一种肿瘤靶向磁共振造影剂

王秩秋¹, 单良¹, 王颂平¹, Alexandru Korotcov¹, 梁兴杰^{1,2}

(1. Molecular Imaging Laboratory, Department of Radiology, Howard University, Washington DC;

2. 中国国家纳米科学中心, 北京 100080)

摘要: 造影剂辅助的核磁共振成像是目前肿瘤诊断的最好方法之一。但是由于核磁共振成像内在的低灵敏性以及造影剂的非特异性, 导致肿瘤早期诊断较为困难。文章将一种新的肿瘤靶向核磁造影剂纳米粒子应用于早期肿瘤的影像诊断。这种新的肿瘤靶向核磁造影剂纳米粒子由配体转铁蛋白 (Tf)、纳米水平的正电脂质体 (Lip) 载体和临床常用的造影剂 Magnevist ($\text{Tf}^{\text{NR}}\text{-Lip}^{\text{NBD}}\text{-Magnevist}$) 三部分构成。另外转铁蛋白和脂质体粒子上, 亦标记了荧光物质用于确定转铁蛋白-脂质体-造影剂纳米粒子的靶向性, 以及肿瘤的光学影像诊断。在体外实验中, 利用激光共聚焦显微镜和光学影像证明了靶向纳米粒子介导的细胞内吞和特异性结合。在裸鼠肿瘤模型中, 造影剂纳米粒子 $\text{Tf}^{\text{NR}}\text{-Lip}^{\text{NBD}}\text{-Magnevist}$ 经尾静脉注入后, 显著增强了肿瘤内信号与周围组织的对比度。由造影剂纳米粒子介导的肿瘤内信号显著强于单独 Magnevist 辅助的肿瘤内信号。同时, 利用光学影像方法, 在肿瘤内检测到特异的荧光信号。其结果进一步支持了转铁蛋白-脂质体-造影剂 ($\text{Tf}^{\text{NR}}\text{-Lip}^{\text{NBD}}\text{-Magnevist}$) 纳米粒子的靶向性和肿瘤影像诊断的有效性。

关键词: 核磁共振; 肿瘤诊断; 转铁蛋白; 纳米粒子; 靶向性; 光学成像

中图分类号: Q6-33

0 引言

核磁共振成像因其具有无创、快速、高解析率、高对比度等特点, 在临床上广为使用。特别是在肿瘤的诊断中, 该技术利用病变组织和正常组织物理特性的不同而获得的结构、功能影像, 已经成为原发肿瘤和肿瘤转移早期诊断中不可或缺的重要依据^[1]。肿瘤的形成是长时间、多因素控制、多步骤、多基因突变的复杂变化过程。大多数恶性肿瘤都是单克隆起源, 呈现无控制性生长。在临床上, 相当一部分患者寻求医治时, 疾病已经进入中、晚期, 丧失了最佳的治疗时间, 这是肿瘤死亡率居高不下的原因之一。核磁共振成像虽然具备上述种种优点, 但因其较低的灵敏度却不能满足肿瘤早期诊断的要求。这是因为, 早期肿瘤和正常组织在物理特性上差异较小 (例如 T_1 和 T_2), 这种微小的物理特性差异不足以产生肿瘤和正常组织的影像对比^[2-4]。为了解决这一难题, 人们应用核磁共振造影剂来增强肿瘤和正常组织影像的对比度以利于肿瘤的早期诊断。然而, 现有的造影剂 (如: Gd-DTPA) 主要是经呈高渗透状态的肿瘤血管, 被动

扩散到肿瘤组织的细胞间质, 这种非特异造影剂难以达到另人满意的对比成像效果, 在使用中受到一定限制。

随着靶向药物的不断发展, 科学家希望通过特异性生物分子介导, 合成出一类具有肿瘤靶向性的造影剂, 以进一步降低核磁共振成像技术的检测极限, 用于肿瘤的早期诊断^[5-7]。肿瘤靶向造影剂主要由配体、造影剂载体和造影剂三部分构成。从理论上讲, 由于肿瘤表面抗原过度表达, 肿瘤靶向造影剂可以特异性地聚集在肿瘤细胞表面, 从而增强微小肿瘤病灶的核磁信号, 实现肿瘤早期诊断。文献报道, 纳米尺度的阳离子脂质体 (Lip) 可被用作药物或基因治疗的载体^[8]。在脂质体的表面修饰上如叶酸、转铁蛋白 (Tf) 或抗肿瘤表面抗原抗体

收稿日期: 2008-05-30

基金项目: NIH/NCRR/RCMI 2G12RR003048, USAMRMC W81XWH-05-1-0291, and NIH 5U54CA091431

通讯作者: 王秩秋, E-mail: pwang@howard.edu;

<http://www.howard.edu/medicine/radiology/mil/>

等靶向配体, 就可以特异性引导造影剂到达癌细胞。用于肿瘤靶向的靶向基团一般需要具有体积小、毒性低、对肿瘤特异性结合能力强、无免疫原性等特性。肿瘤靶向脂质体粒子不但能选择性地运载药物或基因到癌细胞, 而且更增加了脂质体的转染效率。转铁蛋白受体在许多肿瘤, 包括口腔、前列腺、乳腺、胰腺等癌细胞表面呈现高表达^[9-14]。比如, 有研究表明在 74% 的乳腺癌、76% 的肺腺癌、93% 的肺鳞癌中转铁蛋白受体呈现高表达。且转铁蛋白受体的表达水平与肿瘤的增长速度及预后成正比^[14]。因此, 近年来基于转铁蛋白的肿瘤靶向药物研发十分活跃, 转铁蛋白、转铁蛋白受体的抗体、或单链抗体片段等被用来作靶向的基团^[15]。

本文利用阳性脂质体粒子、转铁蛋白和临床上使用的核磁造影剂 Magnevist 构建了转铁蛋白-脂质体-Magnevist 肿瘤靶向纳米粒子 (Tf^{NR}-Lip^{NBD}-Magnevist), 来增强核磁共振影像的对比度, 用于肿瘤的早期诊断。为了研究方便, 我们还在转铁蛋白上标记了近红外荧光物质。在实验中, 采用光学成像的方法, 确定转铁蛋白-脂质体-造影剂纳米粒子的生物分布。光学成像方法简易, 检测灵敏度高 (可达 10^{-9} ~ 10^{-12} mol/L), 没有放射性, 因此在动物模型观察基因表达、基因传递, 以及手术中确定肿瘤的边界上已有很好的应用^[16-18]。光学影像受限制于荧光在体内有限的穿透力, 目前仅能提供较好的二维空间的影像。如果核磁共振高解析度成像和高灵敏度的光学成像相组合, 可在分子水平上显示某疾病特殊丰富的影像表位^[19-21]。一系列实验表明, 通过转铁蛋白介导的靶向型核磁造影剂纳米粒子, 特异性地富集于肿瘤组织, 显著增强了核磁共振影像的对比度^[22,23]。

1 材料与方法

1.1 双重标记靶向纳米核磁造影剂 Tf^{NR}-Lip^{NBD}-Magnevist 的制备

阳离子脂质体 1,2-dioleoyl-sn-glycero-3-phosphoethanolamine (DOPE) 和 1,2-dioleoyl-3-trimethylammonium-propane (DOTAP) 按 1:1 的比例 (重量) 混合溶解在氯仿溶液中 (Lip), 或在 DOTAP:DOPE 中再加入 0.1% NBD-DOPE (荧光标记脂质体 DOPE-N-(7-nitro-2,1,3-benzoxadiazol-4-yl)(Avanti Polar Lipids, Alabaster, AL)) 构建带有 NBD 荧光标记的脂质体 (Lip^{NBD})。取 3.6 μ l (精

确度只能到 0.1 μ l) Lip^{NBD} 混合液经氮气吹干后加入 50 μ l 含 12 μ l Magnevist 造影剂 (Berlex, Wayne, NJ) 的水溶液重新水化 Lip^{NBD}。每微升 Magnevist 造影剂含 469.01 μ g gadopentatate dimeglumine。震荡 10 分钟后用水调至 175 μ l。将此混合液先用超声降解 (80-90 W, 10 min), 然后分别经孔径为 0.2 μ m 和 0.1 μ m 的聚碳酸酯薄膜过滤。最后加入 25 μ l 荧光剂 Alexa 680 标记的人转铁蛋白 (Tf^{NR}, 5 mg/mL) (Invitrogen, Carlsbad, CA), 混匀后静置 10 分钟以上。所有实验都用新鲜制备的探针。最终反应物的体积为 200 μ l。脂质体、人转铁蛋白与 Magnevist 的比例为 10:12.5:0.56 (nmol/ μ g/mg)。另外, 为研究探针的细胞内吞作用, 用近红外 Alexa 680 荧光剂替代核磁共振造影剂构建了 Tf-Lip^{NBD}-dye 探针。浓度为 200 μ l 探针内含 2 μ l Alexa 680 荧光剂。

1.2 细胞培养和动物模型

我们用人乳腺癌 MDA-MB-231-luc (Caliper Life Sciences, Hopkinton, MA) 培养细胞和动物模型来测试我们新构建的靶向纳米核磁造影剂的有效性。MDA-MB-231-luc 细胞转染了北美萤火虫荧光素酶基因, 表达高水平的转铁蛋白受体。细胞常规培养在含 10% 小牛血清的 DMEM/F-12 培养基中。8 到 10 周左右的胸腺缺陷型雌性裸鼠 (Harlan, Indianapolis, IN) 用于制作皮下肿瘤模型。 1×10^7 个细胞悬浮于 100 μ l DPBS 中注射于裸鼠后背皮下。直径 0.4 至 1.2 cm 的肿瘤用于试验。

1.3 共聚焦显微镜观察

MDA-MB-231-luc 细胞培养在 8 孔细胞培养板上, 培养 24 小时达到 40% 至 50% 后, 吸去原培养基, 加入 150 μ l 含 25 μ l 探针 (Tf^{NR}-Lip^{NBD}-Magnevist, Tf-Lip^{NBD}-dye 或单独 Alexa 680) 的无血清、无抗生素培养基, 分别培养 5、30、60、120 分钟。之后, 用 PBS 溶液洗 3 次, 用 10% 的福尔马林溶液固定 10 分钟。细胞核用 4,6-二氨基-2-苯吡啶 (DAPI) 复染。细胞在 Zeiss LSM 510 共聚焦显微镜下观察。用激发波长 633 nm 和发射波 650 nm 来观察 Tf^{NR} 或 Alexa 680 荧光剂, 用激发波长 488 nm 和发射波 505~550 nm filter 来观察 Lip^{NBD} 绿色荧光, 并用激发波长 364 nm 和发射波 385~470 nm filter 检验 DAPI 蓝色荧光。

1.4 靶向纳米造影剂 Tf^{NR}-Lip^{NBD}-Magnevist 体外靶向特异性影像分析

细胞培养在 10 cm 直径的培养皿中, 至细胞占

据 80% 面积, 吸去培养液, 加入 3 ml 含 200 μ l 各种不同探针 (Tf^{NIR}-Lip^{NBD}-Magnevist, Tf-Lip^{NBD}-dye, Lip^{NBD}-dye, Magnevist 或 Alexa 680) 的培养基, 培养 60 分钟。用 PBS 溶液洗 3 次后, 收集细胞并调节至相同数目。经离心后, 细胞团块通过 Xenogen IVIS200 光学成像仪 (Caliper Life Science, Hopkinton, MA) 成像并定量荧光强度。不同探针处理的细胞荧光强度用微软 Excel 软件做统计分析。在核磁共振成像, 用 150 cm² 培养瓶培养细胞, 吸去培养液, 加入 10 ml 含 600 μ l 探针的培养液。培养 60 分钟后, 用 PBS 溶液洗 3 次, 收集细胞并调节至相同数目。离心后, 细胞团块用 Bruker 400MHz 的核磁共振仪, spin-echo (SE)、T1-weighted 成像方法检测。成像参数是 echo time (TE)=11.416 ms、repetition time (TR) =500 ms, 采样重复 4 次, 影像尺寸为 20 mm \times 20 mm, matrix size=256 \times 128, 影像厚度为 2 mm。T1 测量方法用 FISP-T1 (fast imaging steady state precession imaging sequence) 程序, 参数是: TE =1.5 ms、TR=3 ms, 采样重复 8 次, 16 frames, 32 segments, inversion delay 49.2 ms, repetition time 2572 ms。核磁共振的影像取自微离心管内细胞团块的中段。所有的成像最终用 Bruker 公司图像分析软件来分析。每项体外实验至少重复 3 次。

1.5 靶向纳米造影剂 Tf^{NIR}-Lip^{NBD}-Magnevist 体内靶向特异性及有效性影像分析

为了评价 Tf^{NIR}-Lip^{NBD}-Magnevist 的肿瘤靶向性, 在 MDA-MB-231-luc 肿瘤模型, 首先用 Xenogen IVIS 200 光学呈像仪进行光学成像。成像和信号的定量由 Living Image (Caliper Life Science, Hopkinton, MA) 软件控制。小鼠放置于避光的 Xenogen 机器内的保温平台上, 用 2% 异氟烷持续麻醉小鼠。小鼠通过尾静脉注射 200 μ l Tf^{NIR}-Lip^{NBD}-Magnevist 探针 (含 12 μ l Magnevist)。每 10~30 分钟成像一次, 连续成像至 6 小时。每次呈像时间 1 秒。然后, 测定肿瘤部位荧光信号强度。信号强度用平均流量 (光子/(秒 \cdot cm² \cdot 球面度), p/(s \cdot cm² \cdot sr)) 表示。对侧腿部肌肉作为对照。

对于核磁共振成像研究, 从尾静脉给予 200 μ l Tf^{NIR}-Lip^{NBD}-Magnevist 探针 (含 12 μ l Magnevist)。为了进行比较, 同一个动物亦静脉给予相同剂量的 Lip-Magnevist 或 Magnevist。两次核磁共振成像研究间隔至少三天, 以避免前次的造影剂残留造成影响。核磁共振成像采用 multislice

multiecho T1-weighted spin-echo sequence 成像方法, 扫描参数为 TR=800 ms、TE=11.4 ms, 影像切片厚度 1 mm。每一个动物首先在注射探针前作一次肿瘤扫描, 然后在静脉注射后 3 小时内, 每隔 10 分钟对肿瘤进行次序扫描。

2 结 果

2.1 Tf^{NIR}-Lip^{NBD}-Magnevist 的细胞内吞共聚焦显微镜观察

细胞和 Tf^{NIR}-Lip^{NBD}-Magnevist 或 Magnevist 分别培养 5 分钟至 2 小时。Tf^{NIR}-Lip^{NBD}-Magnevist 孵育的细胞显示很强的 Tf^{NIR} 近红外荧光信号 (图 1 A, D1) 和绿色 Lip^{NBD} 信号 (图 1B, E1)。在和 Magnevist 孵育的细胞中检测不到任何荧光信号 (图 1 D2, E2)。Lip^{NBD} (绿色) 和荧光染料 (红色) 在孵育 5 分钟后即能观察到其在胞浆中的信号。荧光强度不断增加, 直至 1 小时后达到最大值。之后, Lip^{NBD} 和染料蓄积形成多个内含体。这些内含体主要位于胞浆的周边区域。在 2 小时后更加明显。相对仅有染料孵育的对照组, 细胞对染料的摄取并不明显。利用光学成像进一步确定了探针在肿瘤细胞中的摄取。

利用核磁共振成像, 当探针 Tf^{NIR}-Lip^{NBD}-Magnevist 或 Lip^{NBD}-Magnevist 与细胞共孵育后, 相对于 Magnevist, 细胞显示明显的信号增强和 T1 短缩。T1 在与 Tf^{NIR}-Lip^{NBD}-Magnevist 探针孵育时减短至 366 ms, 在与探针 Lip^{NBD}-Magnevist 孵育时为 374 ms, 而与 Magnevist 孵育时为 408 ms。与 Tf^{NIR}-Lip^{NBD}-Magnevist 孵育的细胞较与 Lip^{NBD}-Magnevist 孵育的细胞显示更高的信号强度。这些结果证明, Tf 对于探针经靶向性细胞的内存, 具有重要作用。Lip^{NBD}-Magnevist 和仅 Magnevist 介导产生的核磁信号强度和 T1 不同, 反应了肿瘤细胞膜和脂质体的有效融合。

2.2 Tf^{NIR}-Lip^{NBD}-Magnevist 介导的肿瘤影像对比度增强

为了研究探针是否在体内能够特异性的富集在肿瘤, 我们首先进行了以 Tf^{NIR} 肿瘤内积聚为目标的光学成像。在静脉注射探针 Tf^{NIR}-Lip^{NBD}-Magnevist 后, 近红外荧光信号在 10 分钟时便清晰可辨, 90 分钟至 2 小时荧光的强度达到最大 (图 2)。荧光强度和肿瘤的大小成正比, 大的肿瘤 (0.8 cm 直径) 在注射 2 天后仍可测到明显的荧光

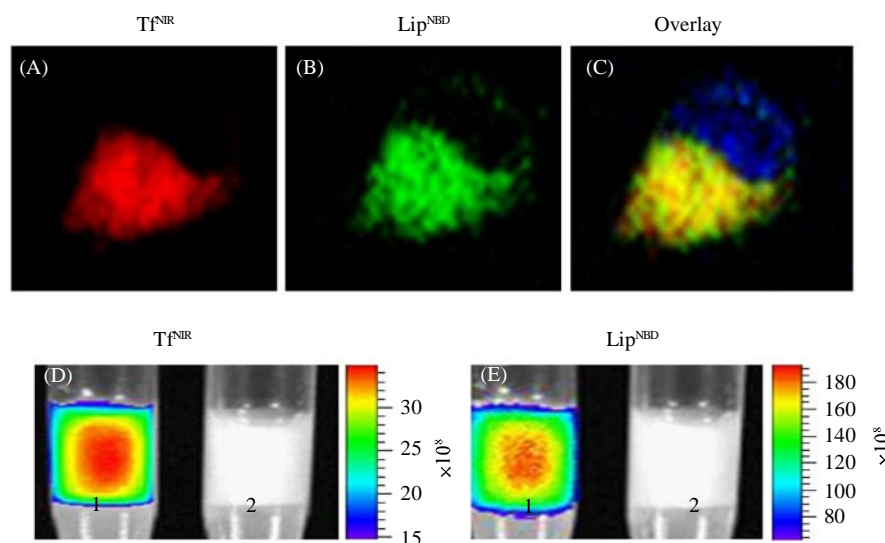


Fig.1 Confocal and optical detection of the reporters in cells incubated with the probe Tf^{NIR} - Lip^{NBD} -CA or Magnevist alone for one hour. Panels A-C are representative confocal microscopic images, showing cytoplasmic distribution of Tf^{NIR} (A) and Lip^{NBD} (B) and their co-localization (C). Panels D-E are optical images of the cell pellets. Strong fluorescent signals of Tf^{NIR} (D, lane 1) and Lip^{NBD} (E, lane 1) are detected in cells incubated with Tf^{NIR} - Lip^{NBD} -CA, but not in cells incubated with Magnevist alone (D and E, lane 2)

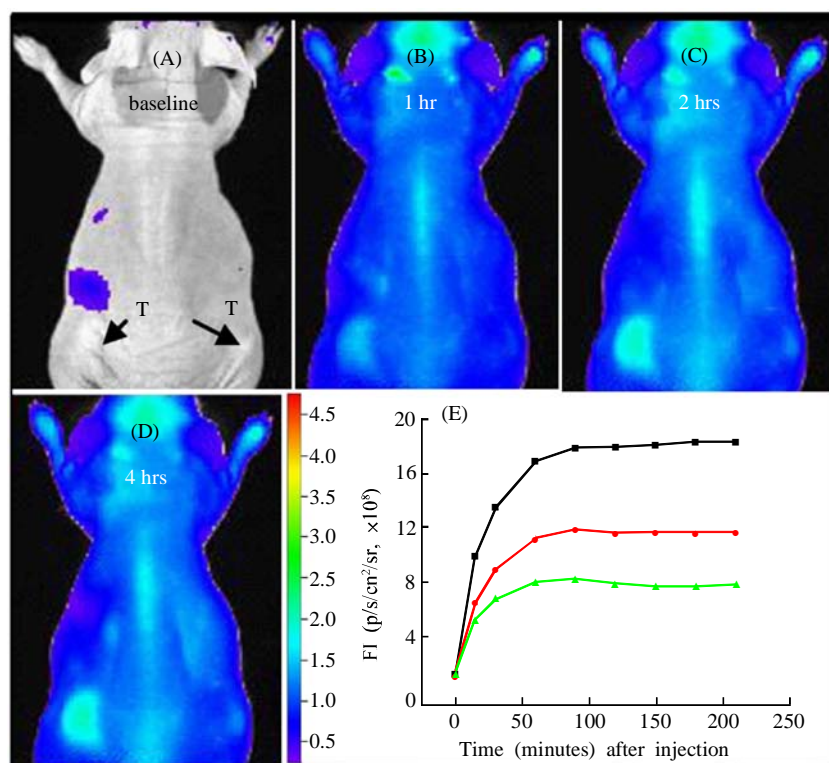


Fig.2 Optical imaging of the tumors following i.v. administration of the Tf^{NIR} - Lip^{NBD} -CA, showing preferential accumulation of the fluorescent signal of Tf^{NIR} in tumors (panels A-D). The fluorescence signal was detectable as early as 10 min and reached a maximum at about 2 h and then decreased gradually. Panel E shows the plot of time versus signal intensity obtained from the tumor and the contralateral muscle. The signal intensity is expressed as $\text{p}/(\text{s} \cdot \text{cm}^2 \cdot \text{sr})$. —■—: Large tumor; —●—: Small tumor; —▲—: Muscle

信号。小的肿瘤,其荧光强度在24小时后已很微弱。虽然Lip^{NBD}能够在体外被清晰地检测到,但因绿色荧光较差的穿透能力,在体内无法被检测到。组织自发荧光也是体内检测Lip^{NBD}困难的另一个重要原因。在静脉注射探针后,探针快速地分布到全身,并且很快被血流丰富的器官吸收,如肝、脾、肺、脑和骨髓。然而,探针很快从这些器官中代谢出去,与之不同的是,在肿瘤中探针衰退的过程非常缓慢。肿瘤对探针的摄取,因转铁蛋白和转铁蛋白受体的结合而增强。背景荧光在最初的快速增强之后,其背景也快速下降(图2)。根据肿瘤的大小不同,在不同的时间点上(10分钟至48小时)肿瘤的荧光强度和正常组织(对侧腿肌肉)的荧光强度比为1.3至3.4。小于3 mm直径的肿瘤显示较弱的荧光信号,可能是由血管系统差异造成的。含有荧光染料的Lip而没有Tf交联的探针并没有使肿瘤组织的荧光增强。

在无胸腺裸鼠实体瘤动物模型同样表明了核磁共振成像信号的增强。肿瘤直径大小从0.4至1.2 cm不等(共10只动物)。相同的小鼠用来比较探针和仅用Magnevist时信号增强的不同。使用Tf^{NR}-Lip^{NBD}-Magnevist探针或仅用Magnevist的实验相隔至少三天。静脉注射Tf^{NR}-Lip^{NBD}-Magnevist探针明显增强了肿瘤成像对比度(图3)。在注入10

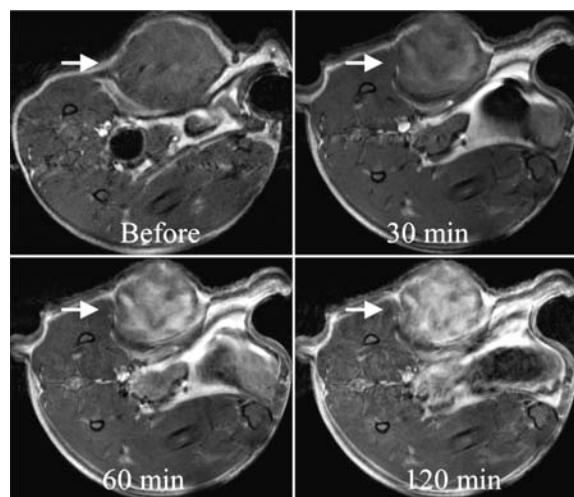


Fig.3 A time course of the *in vivo* tumor MRI imaging following i.v. injection of the probe Tf^{NR}-Lip^{NBD}-CA. The images show gradually increased enhancement of the tumor signals (arrow) and heterogeneous enhancement pattern within the tumor. The MRI parameters are TE=11.416 ms, TR=800 ms, number of average=4, field of view=(28×30) mm², matrix size=256×192, and slice thickness=1.0 mm

分钟后可观测到增强信号,并不断增强,在90分钟至2小时信号达到高峰(图3),达到高峰的时间与肿瘤的大小有关。之后,信号逐渐减弱。在肿瘤内不同部位信号增强有很大的差异。在1至3小时内,信号增强的形态分布渐趋稳定。肿瘤的一些区域增强很快,而另一些区域增强较慢。小的肿瘤,信号的增强在整个肿瘤中比较均匀。通常增强从周边开始。使用Magnevist造影剂进行核磁共振成像,肿瘤的影像对比度在给予Magnevist后比无造影剂的影像有轻微的增强(图4)。最大增强效果通常在注入30至60分钟后观测到。信号增强度在3小时内逐渐下降并回至给与造影剂之前的水平。单纯Magnevist的药物动力学和Tf^{NR}-Lip^{NBD}-Magnevist探针表现不同。含Magnevist但无Tf交联的脂质体,相对于Magnevist或Tf^{NR}-Lip^{NBD}-Magnevist表现出更弱的信号增强作用。

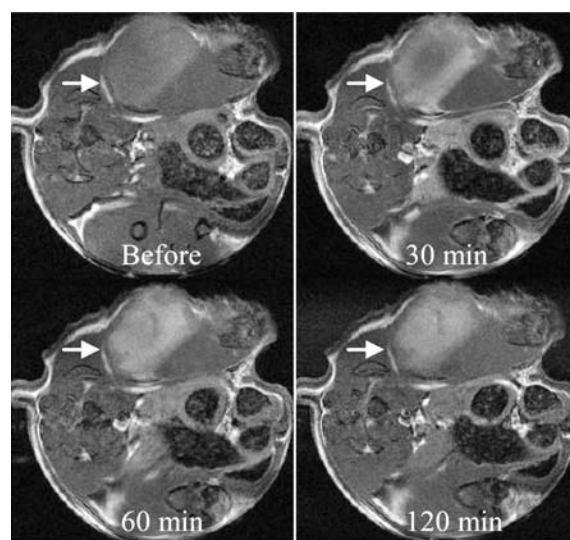


Fig.4 Magnevist-mediated signal enhancement. The images show that the enhancement starts from tumor peripheral area and gradually increases to the center over time. The enhancement is relatively homogenous and it is weaker than the enhancement by the probe, Tf^{NR}-Lip^{NBD}-CA

3 讨 论

肿瘤细胞生长异常迅速,不仅在形态学上与正常细胞大不相同,而且在细胞表面蛋白空间分布及绝对数量上也与正常细胞存在巨大差异。这种特殊的病理生理微环境差异为肿瘤的早期诊断和靶向治疗提供了很大空间。本文报道了利用转铁蛋白修饰

的靶向型核磁共振造影剂的合成与应用, TfR 在恶性肿瘤中高表达是功能化纳米粒子的设计依据。如前所述, 从结构上看, 转铁蛋白-脂质体-造影剂纳米粒子可以分为三个部分, 每个部分都各具特点: 1) 转铁蛋白特异性好, 与转铁蛋白受体特异性结合, 有效避免了非特异性结合带来的“误靶向”; 2) 阳离子脂质体有很多优势, 比如高包装容量、低免疫原性, 和较低生物毒性, 通过连接配体可以增强转染效率; 3) $Gd-DTPA$ 被进一步修饰后, 由于空间位阻效应阻碍了重金属原子与生命体系的直接接触, 降低了重金属毒性。另外, 由于近红外光较可见光对体内组织的穿透力好, 可提高该探针的深度分辨率^[17,18]。用近红外荧光分子标记亦将正常组织的自发荧光干扰减少到最小。通过激光共聚焦显微镜对两种荧光分子的观察我们可以得出结论, 本文报道的靶向型核磁造影剂稳定性良好, 可有效地标定癌细胞。

靶向纳米核磁造影剂的合成是后续成像研究的基础, 因此纳米颗粒合成过程中有以下部分需要注意: 1) 我们直接把吹干了的脂质体薄膜附以造影剂浓缩液, 并在和 Tf 连接前, 经超声降解法和反复通过微孔膜来缩小 $Lip-Magnevist$ 复合物的尺寸。结合文献报道合成工艺^[24-28], 我们将 Lip 和 Tf 以 10:12.5 比例混合, 这样可以得到理想的靶向效果。我们先前的研究通过扫描电子显微镜方法和扫描探针显微镜方法, 证实用脂质体可以有效地包裹 $Magnevist$ 造影剂^[29]。2) 人转铁蛋白、阳离子脂质体和 $Magnevist$ 复合物是通过电荷的相互作用相连, 所以使用前新鲜制备效果更为理想。文献报道, Tf 和 $Lip-DNA$ 复合物的直径只有 50 至 90 nm^[24,27], 所以, 我们推测在经过超声降解法后反复通过 200 和 100 nm 孔径的聚碳酸酯薄膜只会造成不到 10% 的探针损失。通过测量, 主要的探针材料大小都在 100 nm 以内。肿瘤毛细血管一般存在孔状结构, 孔的大小在 200 nm 左右^[30]。还有科学家用荧光显微镜法观察脂质体进入肿瘤时发现, 那些固体肿瘤内的小孔大小为 400 nm^[31]。从尺寸效应上看, 我们有理由认为, 本文所述探针不会超过肿瘤脉管系统的尺寸而影响它的传输过程。

靶向型纳米粒子在体内外的稳定性问题一直是人们关注的焦点之一, 这是因为科学家担心那些结构复杂且通过非键作用力相连的纳米粒子可能在生物环境下降解, 不能实现人们预期的功能。我们首先评估在体外环境下探针摄入的效率。为了视觉观

察和量化这个效率, 我们分别设计了几组不同成分的探针。通过共聚焦显微镜法发现, Tf^{NIR} 、 Lip^{NBD} 和 NIR 染料标记共同分布在肿瘤细胞的细胞质。他们在细胞质的外围积聚形成内涵体。Lee 和 Kim^[32]已报道过有关 $Tf-Lip$ 介导的质粒 DNA 转染, 也会形成类似的内涵体。利用光学成像法我们进一步证实了共聚焦实验的结果。细胞摄入与 Tf 和 Lip 的介导有关, 拮抗 TfR 会导致细胞摄入明显降低。 NIR 染料和细胞共培养, 并没有看到荧光信号也排除了游离 NIR 染料的非特异性结合或进入细胞的可能。没有 Tf 相联的 $Lip^{NBD-dye}$ 探针, 在细胞中的高摄取并不意外。有两种机制可以将造影剂引入细胞, 一种是脂质体的有效转染而介导的细胞膜融合, 进而导致的细胞内吞^[26], 另一种是经 Tf 与 TfR 的特异性结合。对 Tf 的预处理并不能如预期那样阻止拥有融合细胞膜功能的脂质体发生细胞内吞作用。通过我们的定量分析和拮抗分析, Tf 和 Lip 在探针摄入细胞时起了协同作用。通过细胞团块的核磁共振成像, 我们也发现了一个同样的现象: 造影剂经由 Tf 和 Lip 的引介进入细胞内。协同作用首先是 Tf 和 TfR 在细胞膜表面发生特异性结合, 然后是阳离子脂质体和细胞膜表面的阴离子发生互相作用, 最后是受体和脂质体-细胞膜融合共同调节内吞作用^[33]。在核磁共振成像上 $T1$ 的短缩, 取决于探针累聚的程度, 而这种造影剂积聚又与肿瘤的生理环境密切相关。与体外实验结果一致, 通过光学成像和核磁共振成像我们能看到体内探针具有靶向性。共聚焦成像、光学荧光成像和核磁共振成像影像的对比增强速度具有很高的一致性。在肿瘤内荧光强度大约在给药 90 分钟后达到最大, 并在随后的 1 到 3 小时之间达到峰值。而核磁共振成像对照组在 45 分钟时达到高峰, 并在造影剂注射入 3 小时内回到基线水平。双重探针释放的磁共振信号远比单单加入 CA 探针的信号要强。这些结果和在基因治疗时发现 Tf 介导的 Lip 系统有高基因转染效率是一致的^[27,28]。更有趣的是, 肿瘤内不同部位的特异性增强与肿瘤的病理变化一致。如果只用 CA , 虽可增强成像对比, 但增强程度很弱, 且信号几乎是均匀分布的。核磁共振不均匀分布和肿瘤病理组织的相互印证具有潜在的实用价值。通过分子成像得到的结果, 我们可以给医生提供更多的信息, 而不用再依赖传统的活组织深度切片检查技术。当给予没有螯合 Tf 的 $Lip-Magnevist$ 探针时, 我们没有观察到肿瘤内造影剂

或荧光染色的累积。大部分 Lip 积聚在血流丰富的器官中, 例如肝、脾、骨髓和肺等。我们的探针亦可用来做光学成像检查肿瘤, 并通过 TfR 的表达水平推测肿瘤细胞的生长。虽然对于一些深层组织的肿瘤, 荧光穿透的局限性仍然是一个问题, 但这些参数对于病人的选择治疗和预后治疗有很大的价值。显然, 可用于多种成像方法的探针比单一性的探针更有优势^[22,23]。

总之, 我们构建了一种包含核磁共振造影和荧光标记的双重纳米分子探针, 体内和体外实验均证实了该探针具有很好的靶向性, 并成功应用于核磁共振和光学成像。对于核磁共振成像来说, 该探针增强影像对比程度, 在现有设备下提高了肿瘤诊断的灵敏度, 有利于肿瘤早期诊断。由于探针里含有近红外荧光物, 我们还可以使用该探针进行光学成像, 且近红外荧光物质具有很好的穿透力, 为肿瘤诊断提供了很好的深度分辨率。此外, 我们还提供了用肿瘤细胞能表达的特异生物标记物, 对肿瘤细胞进行定量的检测, 可以有助于检测病人的治疗反应和预后情况。

致谢: 感谢中国国家纳米科学中心孟幻博士对文稿的编辑整理。

参考文献:

- [1] Gillies RJ, Bhujwalla ZM, Evelhoch J, Garwood M, Neeman M, Robinson SP, Sotak CH, van Der SB. Applications of magnetic resonance in model systems: tumor biology and physiology. *Neoplasia*, 2000,2:139~151
- [2] Pautler RG. Mouse MRI: concepts and applications in physiology. *Physiol*, 2004,19:168~175
- [3] Hornak JP. The basics of MRI. <http://www.cis.rit.edu/people/faculty/hornak/>
- [4] Persigehl T, Heindel W, Bremer C. MR and optical approaches to molecular imaging. *Abdom Imaging*, 2005,30:342~354
- [5] Artemov D. Molecular magnetic resonance imaging with targeted contrast agent. *J Cell Biochem*, 2003,90:518~524
- [6] Massoud TF, Gambhir SS. Molecular imaging in living subjects: seeing fundamental biological processes in a new light. *Gene Dev*, 2003,17:545~580
- [7] Blasberg RG. Molecular imaging and cancer. *Mol Cancer Ther*, 2003,2:335~345
- [8] Nobs L, Buchegger F, Gurny R, Allemann E. Current methods for attaching targeting ligands to liposomes and nanoparticles. *J Pharm Sci*, 2004,93:1980~1992
- [9] Keer HN, Kozlowski JM, Tsai YC, Lee C, McEwan RN, Grayhack JT. Elevated transferrin receptor content in human prostate cancer cell lines assessed *in vitro* and *in vivo*. *J Urol*, 1990,143:381~385
- [10] Rossi MC, Zetter BR. Selective stimulation of prostatic carcinoma cell proliferation by transferrin. *Proc Natl Acad Sci USA*, 1992,89:6197~6201
- [11] Qian ZM, Li HY, Sun HZ, Ho KW. Targeted drug delivery via the transferrin receptor-Mediated endocytosis pathway. *Pharm Rev*, 2002,54:562~582
- [12] Thorstensen K, Romslo I. The transferrin receptor: its diagnostic value and its potential as therapeutic target. *Scand J Clin Lab Invest*, 1993,215(suppl):113~120
- [13] Li HY, Qian ZM. Transferrin/transferrin receptor mediated drug delivery. *Med Res Rev*, 2002,22:225~250
- [14] Ponka P, Lok CN. The transferrin receptor: role in health and disease. *Int J Biochem Cell Biol*, 1999,31:1111~1137
- [15] Jain RK, Baxter LT. Mechanisms of heterogenous distribution of monoclonal antibodies and other macro-molecules in tumors: significance of elevated interstitial pressure. *Cancer Res*, 1998,48:7022~7032
- [16] Graves EE, Weissleder R, Ntziachristos V. Fluorescence molecular imaging of small animal tumor models. *Curr Mol Med*, 2004, 4:419~430
- [17] Ntziachristos V, Bremer C, Weissleder R. Fluorescence imaging with near-infrared light: new technological advances that enable *in vivo* molecular imaging. *Eur Radiol*, 2003,13:195~208
- [18] Hoffman RM. The multiple uses of fluorescent proteins to visualize cancer *in vivo*. *Nature*, 2005,5:796~806
- [19] Schellenberger EA, Sosnovik D, Weissleder R, Josephson L. Magneto/optical annexin V, a multimodal protein. *Bioconjug Chem*, 2004,15:1062~1067
- [20] Blasberg RG. *In vivo* molecular-genetic imaging: multimodality nuclear and optical combinations. *Nucl Med Biol*, 2003,30:879~888
- [21] Veisheh O, Sun C, Gunn J, Kohler N, Gabikian P, Lee D, Bhattarai N, Ellenbogen R, Sze R, Hallahan A, Olson J, Zhang M. Optical and MRI multifunctional nanoprobe for targeting gliomas. *Nano Lett*, 2005,5:1003~1008
- [22] Artemov D, Mori N, Okolie B, Bhujwalla ZM. MR molecular imaging of HER-2/neu receptor in breast cancer cells using targeted iron oxide nanoparticles. *Magn Reson Med*, 2003,49:403~408
- [23] Modo MMJ, Bulte JWM (ed). Molecular and cellular MR imaging. Boca Raton, Florida, USA: CRC Press, 2007
- [24] Xu L, Frederik P, Pirolo KF, Tang W, Rait A, Xiang L, Huang W, Cruz I, Yin Y, Chang EH. Self-assembly of a virus-mimicking nanostructure system for efficient tumor-targeted gene delivery. *Hum Gene Ther*, 2002,13:469~481
- [25] Kurs M, Walker GF, Roessler V, Ogris M, Roedel W, Kircheis R, Wagner E. Novel shielded transferring-polyethylene glycol-polyethylenimine/DNA complexes for

- systemic tumor-targeted gene transfer. *Bioconjug Chem*, 2003,14:222~231
- [26] Simoes S, Pires P, Duzgunes N, Pedroso de Lima M. Cationic liposomes as gene transfer vectors: barriers to successful application in gene therapy. *Curr Opin Mol Theory*, 1999,1:147~157
- [27] Nakase M, Inui M, Okumura K, Kamei T, Nakamura S, Tagawa T. p53 gene therapy of human osteosarcoma using a transferring-modified cationic liposome. *Mol Cancer Ther*, 2005,4:625~631
- [28] Pirollo KF, Xu L, Chang EH. Non-viral gene delivery for p53. *Curr Opin Mol Ther*, 2002,2:168~175
- [29] Pirollo K, Dagata J, Wang P, Freedman M, Vladar A, Fricke S, Ileva L, Zhou Q, Chang EH. A tumor-targeted nanodelivery system to improve early MRI detection of cancer. *Mol Imaging*, 2006,5:41~52
- [30] Hobbs SK, Monsky WL, Yuan F, Roberts WG, Griffith L, Torchilin VP, Jain RK. Regulation of transport pathways in tumor vessels: role of tumor type and microenvironment. *Proc Natl Acad Sci USA*, 1998,95:4607~4612
- [31] Unezaki S, Maruyama K, Hosoda JI, Nagae I, Koyanagi Y, Nakata M, Ishida O, Iwatsuru M, Tsuchiya S. Direct measurement of extravasation of poly-ethyleneglycol-coated liposomes into solid tumor tissue by *in vivo* fluorescence microscopy. *Int J Pharm*, 1996,144:11~17
- [32] Lee SM, Kim JS. Intracellular trafficking of transferring-conjugated liposome/DNA complexes by confocal microscopy. *Arch Pharm Res*, 2005,28:93~99
- [33] Yin J, Lin AJ, Buckett PD, Wessling-Resnick M, Golan DE, Ealsh CT. Single-cell FRET imaging of transferrin receptor trafficking dynamics by sfp-catalyzed, site-specific protein labeling. *Chem Biol*, 2005,12:999~1006

TRANSFERRIN LIPOSOME NANOPARTICLE (Tf^{NIR}-Lip^{NBD}-MAGNEVIST) — A TUMOR TARGETING MRI CONTRAST AGENT

WANG Paul C¹, SHAN Liang¹, WANG Song-ping¹, KOROTCOV Alexandru¹, LIANG Xing-jie^{1,2}

1. Molecular Imaging Laboratory, Department of Radiology, Howard University, Washington DC, USA;

2. Laboratory of Nanomedicine and Nanobiology, National Center for
Nanoscience Technology of China, Beijing 100080, China)

Abstract: Magnetic resonance imaging (MRI) with contrast agent enhancement is one of the best imaging method for tumor diagnosis. However, due to the low sensitivity and nonspecific deposition of contrast agent in tissue, early detection of tumor by MRI is still challenging. In this paper, the authors present a new targeted nanosized MRI contrast agent for early detection of tumor. This targeted MRI contrast agent nanoparticle is composed of three components: transferrin (Tf) as ligand, cationic liposome as carrier, and a clinically used MRI contrast agent, Magnevist, as payload (Tf^{NIR}-Lip^{NBD}-Magnevist). The Tf and liposome are labeled with fluorescent dyes for evaluation of targeting efficiency by optical imaging. Confocal microscopy and optical imaging *in vitro* have shown that the endocytosis of the nanoparticle occurs via specific binding to transferrin receptor. A significant MR image contrast enhancement in tumor was achieved by i.v. injection of Tf^{NIR}-Lip^{NBD}-Magnevist into tumor bearing nude mouse. The contrast enhancement is much stronger with the nanosized MRI contrast agent than with Magnevist alone. Meanwhile, specific fluorescent signals from the dyes were also detected using optical imaging technique. These results further support the targeting property of the Tf^{NIR}-Lip^{NBD}-Magnevist nanoparticle as well as the efficacy of the probe to be used for tumor diagnosis.

Key Words: Magnetic resonance imaging; Tumor diagnosis; Transferrin; Nanoparticle; Targeting property; Optical imaging

This work was supported by grants from NIH/NCRR/RCMI 2G12RR003048, USAMRMC W81XWH-05-1-0291, and NIH 5U54CA091431

Received: May 30, 2008

Corresponding author: WANG Paul C, E-mail: pwang@howard.edu; <http://www.howard.edu/medicine/radiology/mil/>

Biopharmaceutics and Therapeutic Potential of Engineered Nanomaterials

Xing-Jie Liang^{1,*}, Chunying Chen^{1,2}, Yuliang Zhao^{1,2,*}, Lee Jia³ and Paul C. Wang⁴

¹Laboratory of Nanobiomedicine and Nanosafety, Division of Nanomedicine and Nanobiology, National Center for Nanosciences and Technology of China, Beijing 100190, P.R. China; ²Laboratory for Bio-Environmental Effects of Nanomaterials and Nanosafety, Institute of High Energy Physics, Chinese Academy of Sciences, Beijing 100049, P.R. China; ³Toxicology & Pharmacology Branch, Division of Cancer Treatment and Diagnosis, National Cancer Institute/NIH, Rockville, MD 20852, USA; ⁴Laboratory of Molecular Imaging, Department of Radiology, Howard University, Washington DC 20060, USA

Abstract: Engineered nanomaterials are at the leading edge of the rapidly developing nanosciences and are founding an important class of new materials with specific physicochemical properties different from bulk materials with the same compositions. The potential for nanomaterials is rapidly expanding with novel applications constantly being explored in different areas. The unique size-dependent properties of nanomaterials make them very attractive for pharmaceutical applications. Investigations of physical, chemical and biological properties of engineered nanomaterials have yielded valuable information. Cytotoxic effects of certain engineered nanomaterials towards malignant cells form the basis for one aspect of nanomedicine. It is inferred that size, three dimensional shape, hydrophobicity and electronic configurations make them an appealing subject in medicinal chemistry. Their unique structure coupled with immense scope for derivatization forms a base for exciting developments in therapeutics. This review article addresses the fate of absorption, distribution, metabolism and excretion (ADME) of engineered nanoparticles *in vitro* and *in vivo*. It updates the distinctive methodology used for studying the biopharmaceutics of nanoparticles. This review addresses the future potential and safety concerns and genotoxicity of nanoparticle formulations in general. It particularly emphasizes the effects of nanoparticles on metabolic enzymes as well as the parenteral or inhalation administration routes of nanoparticle formulations. This paper illustrates the potential of nanomedicine by discussing biopharmaceutics of fullerene derivatives and their suitability for diagnostic and therapeutic purposes. Future direction is discussed as well.

Keywords: Metabolism, engineered nanomaterials, nanomedicine, fullerenol, carbon nanotube, titanium dioxide (TiO₂), silica dioxide (SiO₂), magnetic nanoparticles.

1. INTRODUCTION

Full-scale research and development initiatives for nanotechnology in many countries were spawned by the National Nanotechnology Initiative (NNI) in the USA (<http://www.nano.gov>), announced in January 2000 under Clinton's administration [1]. The NNI stresses long-term research looking 20 to 30 years ahead, on the conviction that prioritizing basic and challenging research will lead to breakthrough technological developments. The USA's 21st Century Nanotechnology Research and Development Act (passed in 2003) allocated almost \$3.7 billion to fund nanotechnologies during 2005-2008, which excludes a substantial defense-related expenditure. Since the NNI, the American Government's nanotechnology research funding has increased by more than ten times, starting from \$116 million in 1997 to the actual budget of \$1,425 million in 2007.

Chinese government is also investing and committing to nanotechnology. In the past years the number of publications on nanotechnology originating from China rose to several hundreds per year, which is exceeded only by the United States. The high number of papers at recent nanotechnology conferences in China provides evidence of vigorous research and development that is being carried out by Chinese researchers, and shows the extensive commercialization efforts being made around Shanghai and Beijing. The establishment of the National Center for Nanoscience and Technology of China at Beijing and the National Engineering Research Center for Nanotechnology at Shanghai are good indicators of the high level of interest [1]. There is special interest in combining nanotechnology with traditional Chinese medicine, because nanoformulations may greatly increase therapeutic efficacy of traditional Chinese medicine, and improve its standardization, modernization, and internationalization.

Over the last decade or so, nanomaterials have been broadly studied because of their unique size-dependent physical and chemical properties [1, 2]. Nanomaterials are substances with one or more external dimensions, or an internal structure, on the nanoscale, which could exhibit distinct novel characteristics that the same material at large size may not feature. Nanoparticles, such as carbon lattices, nanotubes, metal oxides, liposomes, micelles and polymers etc., are made of a wide variety of nanomaterials with a diameter of less than 100nm (0.1μm). Nanoparticles can be mainly divided into two groups: (I) labile nanoparticles which disintegrate into many molecular components upon application (e.g. liposomes, micelles, polymers, nanoemulsions), and (II) insoluble nanoparticles such as titanium dioxide (TiO₂), silica dioxide (SiO₂), fullerenes and quantum dots (QD) (e.g. carbon lattices, nanotubes, metal oxides), which remain intact. Three principal factors, the increased relative surface area, nano-scale size and the quantum effects (in some instances), distinguish the properties of nanomaterials from those of bulk materials. Due to their unique properties, applications of nanomaterials in various areas are increasing rapidly. There are many industrial and consumer products (such as cosmetics, sunscreens, paints, textiles, toothpastes, sanitary ware coatings and even food products, etc.), which contain nanomaterials and many more are still under development [3]. As nanoscience is experiencing massive investment worldwide [4], a further increase in biological and medical products developed from nanomaterials is foreseeable [5].

The accumulating investments and efforts in nanotechnology are expected to lead to new technological breakthroughs and increase in the applications of nanomaterials in medicine in the near future [6]. Engineered nanomaterials are being exploited in many different biological and medical fields due to their unequaled photo-, electro-chemical and physical properties. Multifunctional nanoparticles play important roles in cancer diagnostics and therapeutics. Particles and their aggregates can be broken down to even smaller particles via milling and/or dispersion—a distinct process to generate nanoscale particles rather than solvated materials [7]. The translocation and distribution of nanoparticles in the body is size-dependent. Hence, the adverse effects of nanoparticles may not be

*Address correspondence to these author at the Division of Nanomedicine and Nanobiology, National Center for Nanoscience and Technology of China, Beijing 100190, and Lab. for Bio-Environmental Effects of Nanomaterials and Nanosafety, Institute of High Energy Physics, Chinese Academy of Sciences, Beijing 100049, P.R. China; Tel: +086-010-8254-5569; Fax: +086-010-6265-6765; E-mail: liangxj@nanocenter.cn; zhaoyuliang@mail.ihep.ac.cn

easily predicted or derived from the known toxicity of the same chemical constituent at micro-size [8-10]. There is a need for the information on the biopharmaceutics (ADME) of these man-made nanoparticles. Dissolution, translocation, deposition or excretion is critical for nanoparticles to exert their biological effects within the body. The present paper reviews metabolic properties and pharmacological effects of bioengineered nanoparticles known today and their uses in medicine.

2. DISTINCTIVE METHODOLOGIES FOR BIOPHARMACEUTICAL STUDIES ON NANOPARTICLES

Bulk materials may show unexpected novel properties when they are miniaturized to nanosize. This spurs great interests in exploiting physicochemical consequences from the change in size of the materials and utilizing the resulting changes for applications to benefit human services. Keeping the mass unchanged, a decrease in size of particles will result in an increase in total surface area of particles [8, 11, 12] (See Table 1). This increase in surface area would cause chemical modifications at the surface and generate additional physico-chemical and /or biological activities that the corresponding large particles may not possess. Furthermore the increase in particle surface would allow insoluble, labile particles or even particle core to carry more reactive molecule species, and ultimately produce either beneficial or adverse biological effects.

Metabolism of many nanomaterials has not been studied in detail. Most metabolic studies on nanomaterials employed the traditional analytical methods to compare the results from the nanoscale with the non-nanoscale materials. For example, isotope labeling of nanoparticles has been broadly used to determine their distribution and translocation *in vivo*. Liu et al detected ^{59}Fe , ^{13}C , ^{14}C , ^{125}I -labeled carbon nanotube (CNT) for measurement of the tissue distribution and metabolism of CNT in animal model [13]. Fluorescent labeling is also a useful method to determine the location and trafficking of nanoparticles in biological systems by detecting fluorescence intensity of the fluorophors. Inductively coupled plasma-mass spectroscopy (ICP-MS) is another method used for quantitative measurement of the concentration of metal nanoparticles. It is difficult to detect and quantify the metabolism of nanomaterials by a single analytical technology. The most commonly used analytical methods are based on chromatography, mass spectrometry (MS) and NMR. Although the requirements for studying the biodistribution /toxicokinetics and mutagenicity/genotoxicity of nanoparticles are similar to those used for studying conventional micro or macro sized materials, the specific characteristics of nanoparticles may require additional considerations of methodologies to measure the unique features of distribution and metabolism of nanoparticles. For example, the present genotoxicity tests for novel chemotherapeutic agents *in vivo* do not cover the expected target organs or tissues where nanoparticles deposit. In addition, the broadly used cell diffusion chamber incorporating a microporous membrane is a standard device for estimating percutaneous absorption of commonly-used medical and consumer products. Having stated that, the conventional models may not be appropriate for estimating the unique biological capability of nanoparticles for medical application. Therefore, new methodologies to assess the metabolic pathways (penetration, dissolution, translocation, and deposition et al) of

nanoparticles are needed for characterizing the properties of engineered nanomaterials.

3. IMPROVED PHARMACEUTICAL PROPERTIES OF COMPOUNDS MODIFIED BY NANOTECHNOLOGY

Currently, in the early stage of drug discovery, most of compounds formulated for *in vivo* experiments are frequently lipophilic or sparingly soluble in water. Typical intravenous formulations for these compounds at neutral pH require the presence of multi-solvent, surfactant, or in mixed micellar solutions, or nanosuspensions[14]. It is complicated to determine the intrinsic pharmacokinetic behavior of nanopreparation of a new drug entity from pharmacokinetic behavior of the same drug that is formulated using micro or macro form of the drug entity. The complication may result from various situations such as slow or incomplete dissolution of injected nanoparticles, precipitation of the compounds or particles in the bloodstream, delayed release of the compounds from the dosing vehicle, competition between the compounds and formulation ingredients for transport, metabolism and binding to proteins and other blood and tissue components. The strategies used in pharmaceutical industry may be applied to improve the solubility of these compounds without alteration of their properties while developing nanoformulations. The entrapped dosage of the compound in terms of loading capacity of the drug vehicle and the kinetics of release of the entrapped compound are important determinants for the success of developing a 'non-interfering' vehicle for the dosage formulation. If an analytical technique used to determine drug concentration in the body is sensitive enough to detect compounds at low doses, screening for formulations at relatively low concentrations may be feasible. Nanoparticles may be employed to solve this critical problem due to their unique physical, chemical, electronic, and magnetic characteristics. Some nanoformulations can be monitored by virtue of photostable optical intensity of the compounds for clinical measurement. The low concentration of compounds can be detected by the electronic, magnetic or optical signals of nanoparticles. In this way, the metabolism and pharmacokinetic behavior of these compounds can be quantitatively measured *in vivo*, and the pharmacokinetic behavior of the compounds can be evaluated by monitoring the nanoparticle vehicle used in the pharmaceutical preparation[15].

Conventional formulations of the highly lipophilic taxane, paclitaxel (Taxol) for intravenous use contain cremaphor as a solvent. Toxicity due to cremaphor contributes to adverse effects of this versatile anticancer drug. Abraxane is a nanoformulation of paclitaxel conjugated to nano-bead protein structure. It is noteworthy that abraxane is one in a small list of FDA approved for the treatment of breast cancer. Paclitaxel is a very effective anticancer drug. The nano-bead protein conjugated formulation increased water solubility allowing for elimination of the toxicity associated with the solvent vehicle (cremaphor) and improved therapeutic index. Nanoparticles (such as TiO_2) have been used as carrier to increase the photostability of the pharmacologically active payload. The nanoparticulate multilayer of nanoparticles was used as an optical filter to protect the drug from damage by light exposure. The increased hydrophilicity of TiO_2 nanoparticles increases the aqueous wettability by preventing aggregation in the dispersion medium.

Table 1. The Correlated Proportion of Particle Size and Particle Surface Area

Particle diameter (nm)	Particle number (number/pound)	Particle surface area (mm^2/pound)
1000	10^{15}	3×10^9
100	10^{18}	3×10^{10}
10	10^{21}	3×10^{11}

This increases the dissolution rate of the entrapped photoprotected cargo molecules in the nanoformulation by facilitating the maximal exposure of compounds' surface area to the dispersion medium[16].

4. POTENTIAL MEDICAL APPLICATIONS AND BIOLOGICAL EFFECTS OF NANOMATERIALS

Carbon nanotubes comprise an important class of nanomaterials. A hydrophilic functionalized soluble single-walled carbon nanotube (SWNT) is of special interest because of its wide use as a highly effective means of transporting molecular cargo of various sizes and types across the cell membrane to the therapeutic cellular target. SWNT has been demonstrated to carry smaller molecules into cells through a variety of energy -dependent and/or -independent processes [17-19]. Therapeutic drug molecules or diagnostic sensor molecules are usually linked covalently to functionalized SWNT through ester or disulfide bonds. Upon cellular entry, SWNTs encounter the acidic reducing environment of lysosomes or endosomes, where the disulfide and ester bonds are cleaved to selectively release their cargo [20]. There are several studies employing CNTs for nanoformulations designed for intracellular transport and controlled release of pharmaceuticals including cancer chemotherapeutic agents. For example, the full clinical potential of the highly effective anti-cancer drug is not achieved because of inadequate delivery to the targeted tumor *in vivo*. Lippard *et al.* [21] combined cisplatin with SWNTs due to their proven capacity to act as a longboat, shuttling smaller molecules across tumor cell membranes. They demonstrated that nanoformulations of SWNTs conjugated to platinum(IV) could effectively deliver a lethal dose of the anti-cancer drug inside the malignant cancer cells[21]. However, these studies have to be viewed with some caution because of potential toxicity of nanotubes[22]. The potential hazards of CNTs to humans and other biological systems was assessed by measuring DNA damage caused by CNTs in mouse embryonic stem (ES) cells[23]. Many experiments have demonstrated the adverse pulmonary effects of SWNTs *in vivo* after intratracheal instillation, in both rats and mice. Further studies indicate that if CNT reach the lungs, they are much more toxic than carbon black or quartz[24, 25]. It is noteworthy that the report of National Institute for Occupational Safety and Health (NIOSH) states that none or only a small fraction of the CNT enters in the lung through inhalation at the workplace [26]. SWNT induced oxidative stress, which is exemplified by the formation of free radicals, accumulation of peroxidative products, antioxidant depletion, and cytotoxicity in human keratinocytes [27, 28]. In addition, Moller *et al.* showed that other carbon nanomaterial such as ultrafine carbon black particles could impair phagosome transport and cause cytoskeletal dysfunctions with a transient increase of intracellular calcium signal[29].

Bioeffect of nanoparticles in the body depends not only on the amount of nanoparticles but also the size and surface of nanoparticles. It has been demonstrated that the ultrafine nanoparticles were deposited in lungs and other organs, when rats were subjected to chronic inhalation of TiO₂ nanoparticles of different sizes, for 3 months. These studies showed more translocation of nanoscale TiO₂ to interstitial sites and regional lymph nodes when compared to the fine TiO₂ nanoparticles. By comparing carbon black or CNT particles of similar size and composition but with significant difference of specific surface area, it was found that the biological effects (inflammation, genotoxicity, and tissue damage as indicated by histopathologic examination) of nanoparticles were determined by specific surface area, not by particle mass. Similar findings were reported in earlier studies on the tumorigenic effects of other nanoparticles. It has been shown that tumor incidence was correlated better with specific surface area than with particle mass[30].

Liposomes have been used as an effective vehicle for drugs, such as for cisplatin, paclitaxel, daunomycin, doxorubicin and amphotericin *et al.* Nanocarriers for medical applications are made of relatively safe materials, including synthetic biodegradable poly-

mers, lipids and polysaccharides. Administration of doxorubicin encapsulated into PEG-PE micelles increased doxorubicin accumulation and penetration in tumors, compared to the much lower levels of drug achieved with doxorubicin itself without nanotechnological modification. *In vitro* and *in vivo* pulmonary deposition of nano liposomes has been performed using Andersen Cascade Impactor and intratracheal instillation in rats, respectively. Liposomes were prepared by thin film evaporation technique and liposomal dispersion was passed through high pressure homogenizer. Nanoliposomes (NLs) were harvested by centrifugation and characterized by scanning electronic microscopy (SEM). NLs were dispersed in phosphate buffered saline (PBS) at pH 7.4. The dispersion was spray-dried and sizes of powders were measured by atomic force microscopy (AFM). *In vivo* studies revealed significant retention of nanoliposome-trapped medicine after 24 hours, suggesting slow clearance of NLs in biological system. The encapsulated nanoliposome provides a practical approach for direct delivery of compounds for controlled and prolonged retention at the targeted site of action. It may play a promising role as effective therapeutic drug delivery system in reducing the risk of acute and chronic toxicity[31]. Nano-sized particles are more likely to increase the bioavailability, which could result in improved chemotherapeutic effects. It is important to note that specific particle surface area may be a better indication for maximum tolerated exposure level of nanoparticles. Recent publications on the pulmonary effects of CNT confirm the intuitive assumption that nano-sized nanotube can induce a rather general non-specific pulmonary response[22, 24, 26, 32].

5. POTENTIAL THERAPEUTIC STRATEGY BASED ON GENOTOXICITY OF NANOPARTICLES

Some of the adverse biological effects of nanoparticles *in vivo* have linked to the inflammatory response with exacerbation of airways disease, cardiovascular events caused by hypercoagulability or atherosclerotic plaque destabilization[33, 34]. Many of these conclusions are derived from studies on nanoscale particles that can cause inflammatory response or inflammation and these conclusions may not be extrapolatable to nanoparticles in general, and they may be less relevant for engineered nanomaterials. Nanoparticles that readily cross cellular membranes can be expected to be able to reach the nucleus and DNA, which is important when genotoxic effects are considered. For instance, functionalized SWCN have been reported to reach the cell nucleus[18, 35]. Even if nanoparticles do not go through the nuclear envelope, they would eventually have access to the nucleus in dividing cells, because the nuclear envelope dissolves during mitosis leading to cell division. For most nanoparticles, it is unknown whether they interact directly with DNA or the mitotic spindle, and what size and/or charge of nanoparticles could lead to defects in DNA transcription and chromosomal damage and aberration. However, there are indications that certain types of nanoparticles are capable of causing DNA damage.. Surface area and charge density of nanotubes are considered to be critical in determining their electrostatic complex formation with DNA[36]. Therefore, cationic functionalized CNTs are frequently used for binding to DNA and widely used for cell specific delivery of functional DNA and siRNA to specifically modify the expression of the targeted gene. The composition and the coating of nanoparticles are probably the key factors in determining their genotoxic effects. Nanotubes coated with a positively charged polyelectrolyte, functioning as a counterpart for negatively-charged DNA, have been wrapped with DNA to generate DNA sensors[37]. The property of various types of nanoparticles complexed with DNA has been utilized for cellular and nuclear delivery of DNA and oligonucleotides [38-40]. In addition, SWNT can bind with single- and double stranded DNA, and/or peptide amino acid (PAA)[41-44]. QDs, such as cadmium selenide (CdSe), have been used for tracking and monitoring biological molecular process and function *in vitro* and *vivo*. CdSe is usually capped with a shell of

PEG, with biotin surface functionality for broad biological application *in vivo*. Water-soluble semiconductor QDs can also cause bond breakage in DNA strands due to photogenerated and surfaceoxide-generated free radicals [45].

In principle, genotoxicity of nanoparticles can be assessed using *in vitro* assays on mammalian cells. However, the timing of the tests has to be long enough to ensure that the nanomaterial can reach the nucleus. In the *in vitro* chromosome aberration test which was related to sample prep/ agglomeration state, it is necessary to examine two post-treatment metaphases by allowing two rounds of cell replication. In the cytokinesis-block micronucleus test *in vitro*, the treatment with nanoparticle should occur in one cell cycle without cytochalasin B (Cyt-B), followed by another cycle with the presence of Cyt-B, to examine the cells after the 2nd post-treatment mitosis. If the genotoxic effects of nanoparticles are related with inflammation, simple *in vitro* assays may not be adequate for demonstrating the genotoxic potential of nanoparticles. In general, the relationship between inflammation and genotoxic effects is still not well understood for many types of nanoparticles including weakly soluble nanoparticles. Depending on the endpoint of study, demonstration of an association between inflammation and genotoxic effects may require relatively long-term experiments, which may be impractical. In rats, intratracheal instillation of nanosized carbon black, fine TiO₂ (anatase) and fine α -quartz (SiO₂) resulted in an increase of *hprt* mutations in alveolar cells after 15 months treatment [30]. It appears that basic studies on the association between inflammation and genotoxicity are necessary before conclusions can be drawn on the importance of inflammation-related genotoxicity of nanoparticles. *In vivo*, actively dividing cells are expected to be the primary targets of genotoxic effects of nanoparticles, as genotoxicity can be fixed only when the cell divides. The widely used *in vivo* genotoxicity tests, the bone marrow micronucleus test and the liver UDS (Unscheduled DNA Synthesis) test, have been employed to detect DNA damaging effects of nanoparticles that reach the bone marrow and the liver, respectively, or that have systemic genotoxic effects. Currently, there is no validated standard method for assessing genotoxic effects on dividing cells associated with carcinogenesis in the expected target tissues *in vivo*. However, techniques such as the comet assay, micronucleus test, and gene mutation analysis in transgenic animals could probably yield valuable results for studying the effects of nanoparticles on DNA.

6. TRANSLOCATION OF NANOPARTICLES IN BIOLOGICAL SYSTEM

There is a tendency for accumulation of insoluble nanoparticles in the body and the biological effects would be dependent on the properties and dose of nanoparticles, as well as the site of accumulation. Nanoscale particles may affect movement of endogenous substances (proteins, enzymes) or exhibit increased reactions with biological molecules. Autonomic nervous system may also be a target for the adverse effects of inhaled particulates. In the *in vivo* evaluation of the biological effects of nanoparticles, the translocation to the systemic circulation is an important aspect. The possible translocation of nanoparticles has not been studied extensively, although the importance of nanoparticle transport and translocation in biological systems, in pharmacology and delivery of biomolecular drugs [46]. Characterizing the status of the component molecule of nanoparticle, and understanding the processes of translocation, dissolution, and possible nanoparticle-receptor interactions are key challenges to define the biological effects of nanoparticles *in vivo*.

Nanomaterials are expected to dissolve faster than larger sized materials of the same mass based on surface area considerations alone—although other factors such as surface curvature/roughness also play a role. In addition to phagocytosis, which is mostly for cellular ingestion of relatively large particles, translocation of insoluble particles into cells is most likely to be dependent on processes of endocytosis, mainly pinocytosis and phagocytosis, or re-

ceptor-mediated endocytosis[47]. Similarly, expulsion of nanoparticles from live cells may occur predominantly by exocytosis. Dissolution, even over the period of weeks or months, may significantly enhance clearance of nanoparticles. Diffusional movement of nanoparticles through cell membranes is likely to be limited under normal conditions [48]. More research in diffusional movement may provide a better understanding of nanoscale particle translocation processes. Several authors have reported on the movement of nanoscale particles from the lung to the blood[49]. Nemmar *et al* [50] have studied the translocation of inhaled technetium (^{99m}Tc) labeled carbon nanoparticles to the blood. The authors concluded that phagocytosis by macrophages and/or endocytosis by epithelial and endothelial cells was responsible for carbon nanoparticle-translocation to the blood but other routes must also exist.

Particles up to 25 μ m size were found in the foot dermis of elephantiasis patients with impaired lymphatic drainage in the lower legs. These particles were located either in the phagosomes of macrophages, or in the cytoplasm of other cells. The failure of conducting lymph to the node produces a permanent deposit of particles in the dermal tissues. This indicates that particles, which penetrate normal or damaged skin, are removed via the lymphatic system of healthy people[12]. Micro-sized and even submicron sized liposomes do not easily penetrate into the viable epidermis, while nano-sized liposomes with an average diameter up to 272 nm have been found to reach into the viable epidermis and some in the dermis. Smaller sized liposomes of 116 and 71 nm have been found in higher concentrations in the dermis. Liposomal emulsion particles with diameter of 50 nm to 1 micron, have been detected in the epidermis in association with the cell membranes after topical application to human skin[51]. In subsequent studies, it has been shown that formulations containing nanoliposomal microspheres allow penetration of nanoliposome spheres into melanoma cells, and even into the nucleus.

New degradable nanomaterials such as polyanhydrides were used for preparing controlled release formulations of proteins and peptides. Some of these formulations can be utilized for delivering proteins and peptide through the skin and lungs[52]. Some conclusions regarding nanoparticles penetration of skin by nanoparticles can be drawn from the rather limited literature on the subject. Firstly, penetration through the skin barrier is dependent on particle size. Nano-sized particles are more likely to penetrate deeper into the skin than larger ones. Secondly, nanomaterials, which can dissolve, or leak from a nanoparticle (e.g. metals), or break into smaller parts (e.g. liposomes), can possibly penetrate the skin. There is no clear indication that nanoparticles, which had penetrated the skin, also entered the systemic circulation. However, it has been observed that nanoparticles can be phagocitized by macrophages, Langerhans cells or other cells.

7. EVALUATION OF BIOLOGICAL EFFECTS OF NANOPARTICLES

Nanoparticles, because of their ultrahigh reactive surface sites and quantum effects, are being widely used in the traditional industries, such as dyes, paints, medical diagnosis, sunscreens and cosmetics. There are certain principles for biological and medical evaluation of potential nanoparticles (See Table 2). Metal nanoparticles have found uses in biological and medical studies[53]. Increased numbers of neutrophils and phagocytes in lung fluid and the deposition of nanoparticles in alveolar cells were observed in rats and hamsters following inhalation of silver or gold nanoparticles. Acute pulmonary reaction in response to administration of nanoparticles such as carbon black, TiO₂, and iron oxide revealed rapid translocation of nanoparticles across the epithelium after deposition. It was found that severe effect on renal function could occur in the metal nanoparticles-treated mice, without significant change in biochemical profile of blood. Blood-element test showed that in the rats treated with metal nanoparticles (such as Zn- or Cu),

red cell distribution width, corpuscular volume and blood platelet significantly increased, and hemoglobin as well as haematocrit significantly decreased. The study indicated that metal nanoparticles could cause anemia in animal model. Besides the pathological lesions in the liver, renal, and heart tissue, only slight stomach and intestinal inflammation was evident in all the metal-treated mice, without significant pathological effects in other organs[54, 55].

Table 2. Biological and Medical Evaluation of Nanoparticle

Subjects of evaluation	Aspects of evaluation
Biodistribution	Whole organism, tissue and organ level
Localization	Different intracellular vesicle, organelles, cell level
Metabolic routes	Absorption, distribution, metabolism and excretion (ADME)
Immunological properties	IgG/IgM specific Abs, cytokine induction, T cell activation
<i>In vivo</i> degradation	Enzyme digestion, lysosomal decomposition
Biocompatibility	Biological environment and adverse health effect <i>in vivo</i>
Toxicological characters	Chemical composition, particle size, reactivity, structure/ properties, surface coating modification
Chemotherapeutic concerns	Therapeutic index of nanomedicines and their delivery systems relates with clinical administration
Etc	Other unclear consequence associated with nanomedicines

TiO₂ nanoparticles are widely used for a variety of applications. Pulmonary inflammatory response was observed for 20 nm TiO₂, but not for 250 nm TiO₂ particles[56]. In order to evaluate the biological effect of TiO₂ particles, the acute biological reaction caused by nano-sized TiO₂ particles in adult mice was compared with that resulting from fine TiO₂ particles [56]. Due to the low toxicity, a fixed large dose of TiO₂ nanosuspensions was administered to mice by a single oral gavage. TiO₂ particles showed no obvious acute toxicity in 2 weeks, however, female mice showed high accumulation of the nano-sized nanoparticles in liver. In the assessment of acute biological effects of TiO₂ particles, abnormal activities were not observed in these mice, and there were no cancer and carcinogenic symptoms after autopsy because of the short exposure period. Different laboratories have reported that the retention half-life of TiO₂ particles *in vivo* was long because of inefficient and slow rates of excretion. Oberdorster *et al.* [57] reported that the retention half-times of TiO₂ in rat lung were 117 days for fine particles and 541 days for ultrafine particles. After intravenous injection of rats with 200-400nm TiO₂ nanoparticles, about 69% of the injected TiO₂ nanoparticles at 5 min and 80% at 15 min were accumulated in the rat liver[58]. The 80 nm TiO₂ *in vivo* may directly result in the nanoparticle deposition in the liver and lead to hepatic lesion. Surprisingly, the 25 nm TiO₂, the same as the fine particles, are not retained in the liver, but accumulate mainly in the spleen, kidneys, and lung tissues.

Biodistribution, penetration through tissue, phagocytosis and endocytosis of nanosized materials are all likely to have an impact on potential toxicity of nanoparticles. These processes are most likely dependent on surface characters of nanoparticles. The complex pathways involved in exposure and uptake, translocation and metabolism, and elimination of nanoparticles in biological systems are depicted (Fig. 1). The liver, as a main detoxification organ, is activated to eliminate the side effects induced by most of the mass ingested nanoparticles. Following oral intake, a part of these nanoparticles are excreted through the kidneys. However, the small size and difficult clearance resulted in prolonged retention of nanoparticles *in vivo* and damage to the liver and kidneys. The

changes of serum biochemical parameters including bilirubin levels (TBIL), alkaline phosphatase (ALP), alanine aminotransferase (ALT) and aspartate aminotransferase (AST) and other pathological characteristics of liver were mostly used to evaluate the effect of nanoparticles on liver function, which was usually indicated by measurement of hydropic degeneration around the central vein and the spotty necrosis of hepatocytes. In addition, the nephrotoxicity could be assessed by measurement of activities of creatine kinase (CK), lactate dehydrogenase (LDH) and alpha-hydroxybutyrate dehydrogenase (HBDH). The myocardial damage was shown by change of serum LDH and alpha-HBDH caused by treatment with nanoparticles. For example, increase in levels of uric acid (UA), blood urea nitrogen (BUN) and creatinine were accompanied by pathological changes in the kidneys of experimental animals treated with TiO₂ nanoparticles. However, there were no abnormal or pathological changes in the heart, lung, testicle (ovary), and spleen tissues. Biodistribution studies showed that TiO₂ nanoparticles were retained mainly in the liver, spleen, kidneys, and lung tissues, which indicated that TiO₂ particles could be transported to other tissues and organs after uptake from the gastrointestinal tract after oral dosing.

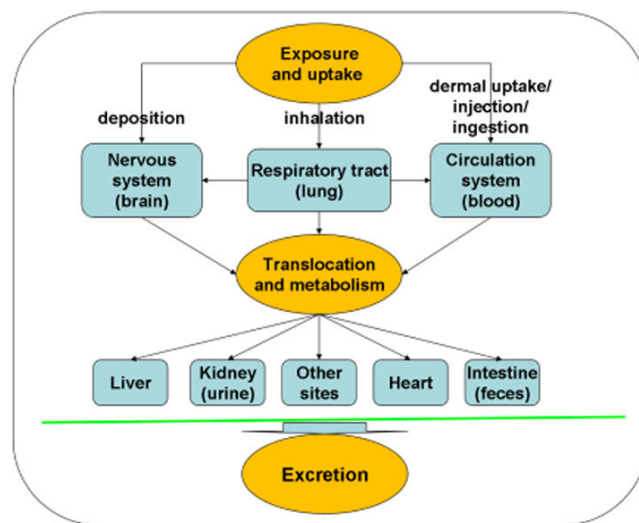


Fig. (1). Possible routes for translocation and metabolism of nanoparticles in biological system.

There are many pathways for systemic exposure, translocation and excretion of nanoparticles, which were proposed in published literatures. The exact pathways for transport and metabolism of nanoparticles are not clear. Further *in vitro* and *in vivo* investigations are necessary.

Although the levels of AST, ALT, and TBIL enzymes for liver function did not change much, the ratio of ALT/AST (as a more sensitive indicator for hepatic injury) could be measured for bioevaluation of liver function after oral ingestion of nanoparticles. The changed liver weight and the hepatocyte necrosis in the pathological examination were helpful to estimate liver injury caused by administration of nanoparticles. In addition, test of LDH in serum is often used to detect tissue alterations and diagnose heart attack, anemia, and liver diseases. Generally, high LDH level shows the myocardial lesion when combined with data for CK and alpha-HBDH, and the hepatocellular damage are expressed when combined with AST and ALT enzymes. The high LDH and alpha-HBDH enzyme levels implied that nanoparticles resulted in more myocardial damage although the pathological change was not observed in cardiac tissue. From the changes of biochemical parameters, such as ALT/AST, BUN, and LDH, it was clear that nanoparticles affected the functions of liver and kidneys in female mice. In summary, administered nanoparticles were retained mainly in liver,

kidneys, spleen, and lung. The obvious hepatic injury caused by nanoparticles could be seen by hydropic degeneration around the central vein and the spotty necrosis of hepatocytes, and the kidney damage was inferred from histopathological examination of the renal tubule and observation of swelling in the renal glomerulus [56].

8. BIOLOGICAL REACTION OF NANOPARTICLES IN RESPIRATORY SYSTEM

Because lung has extensive, location-specific defense systems such as mucociliary clearance in the upper airways and macrophage clearance in the lower, unciliated part of the respiratory tract, most of the nanoparticles in the dosage could be found in lung after the inhaled administration to rats or mice. Deposition of nanosized particles less than 0.5 μm diameter in the respiratory tract is mainly determined by diffusion. The diffusional deposition of nanosized particle during breathing is affected by: (1) dynamics of nanoparticles and their size and shape; (2) geometry of the branching airways and the alveolar structures; (3) breathing pattern, either nose or mouth breathing; and (4) airflow velocity and the residence time in the respiratory tract [59]. Some of the nanoparticles from the administered dose can remain in the airway for a long time. Nanoparticle transport from the alveolar region toward the larynx in humans is mediated through macrophages. This is a slow process even under normal conditions, and serves to eliminate only a part of the nanoparticles deposited in the peripheral lung. The remainder may accumulate in lung surfactant or interstitial fluid unless the nanoparticles are biodegradable or cleared by simple chemical dissolution. Therefore, it can lead to a different cumulative dose for a given deposited dose of nanoparticles with different durability and resistance to dissolution or degradation. The kinetics of dissolution of inhaled nanoparticles is the most important factor in determining whether a low-toxicity nanoparticle, such as amorphous silica (SiO_2), could be eliminated in the epithelial lining fluid or whether nanoparticles such as carbon blacks or iron oxides are engulfed by alveolar macrophages. Thus, solubility of nanoparticles is a key driver for the mechanisms of their biological metabolism including their clearance *in vivo*.

On the epithelium walls of the respiratory tract, nanoparticles first come into contact with the mucous or serous lining fluid and its surfactant layer. Therefore, the destiny of particle compounds that are soluble in this lining fluid is different from the slower dissolving or insoluble compounds [59]. Soluble nanoparticle could dissolve and often be metabolized in the lining fluid, eventually be transferred to the blood, and undergo further metabolism. In this way, particle compounds may have the potential to reach organs far from the original site of entry and to produce biological effects. On the other hand, the slower-dissolving and insoluble nanoparticles deposited on the wall of airway will only be moved by ciliated cells shuffling, coughing, and swallowing. There is evidence that a significant fraction of nanoparticles is retained in the respiratory tract. The slow dissolving and insoluble nanoparticles deposited in alveoli will be taken up by macrophages under normal physiological conditions. However, for the nanoparticles able to penetrate into interstitium, the macrophage uptake is less likely.

The alveolar macrophage plays an important role in the response of the lung to inhaled nanoparticles. Their essential function is phagocytosis and clearance of inhaled nanoparticles. The alveolar cells could produce surfactant by cellular secretion, which contain significant quantities of biotransformation enzymes, particularly cytochrome P450-dependent mono-oxygenases, which participate in detoxification reactions for overcoming nanoparticle toxicity. In addition, macrophages also carry out several other metabolic functions, such as the active uptake of endogenous and exogenous compounds, permeability functions and immunologic functions. The kinetics of nanoparticle metabolism *in vivo* may also be affected by differences in the pH of subcellular compartments [60]. If nanopar-

ticle is neither soluble nor degradable in the biological environment, it is likely to have high biostability with a strong tendency for accumulation upon constant administration. In addition to the known biological effects of nanomaterials with low-solubility, disposition factors of nanoparticles may also influence their biological effects and applications *in vivo*.

Macrophage-mediated nanoparticle removal may be impaired especially for the young and the old people, and persons with lung diseases. As noted above, nanoparticles that escape phagocytosis by macrophages may interact with cells lining the epithelium. In general larger nanoparticles are phagotized, while smaller particles escape uptake by macrophages. The large surface area of nanoparticle presents a reactive interface with cells. Depending on the nature of their molecular surface, nanoparticles may have a greater capacity to induce or mediate adverse effects than larger particles, not only in the respiratory system, but also in the cardiovascular system, the central nervous system and the immune system [8].

9. BIOLOGICAL REACTION OF NANOPARTICLES IN NERVOUS SYSTEM

The absorption of nanoparticles in olfactory nervous system has been studied in connection with the development of drug-delivery systems. Some drug-delivery systems might circumvent the blood-brain barrier in order to enable penetration of diagnostics or medical therapeutics to the brain [61, 62]. Because of the smaller diameter, larger surface area and increased number of nanoparticles compared with non-nanoscale particles in a fixed volume and amount, nanoparticles could carry more reactive materials such as free radicals, transition metals, or chemotherapeutic compounds to the deep organs, and increase drug accumulation in body. Although ingestion is possible when dust accumulates on mucosa surfaces of the oropharynx and nasopharynx or from contaminated food, inhalation is still the most common route for exposure of nanoparticle in biological system. Nanoparticle could be translocated into the central nervous system (CNS) via the olfactory pathway. There is evidence that an increased Mn^{++} concentration was observed in the brain of rats after inhalation of manganese phosphate or manganese sulfate. Also, there was an increase of ^{13}C concentration in the olfactory bulb, cerebrum and cerebellum of rat brain after exposure to ^{13}C labeled carbon nanoparticles [63]. Severe damage to brain tissue was also observed when large mouth bass lived in the water containing 500 ppb buckyballs [64].

Nanoparticles, such as TiO_2 particles, can be taken up by the olfactory bulb via the primary olfactory neurons and accumulated in the olfactory nerve layer, olfactory ventricle, and granular cell layer of the olfactory bulb. The distribution areas of larger TiO_2 particles were wider than those of nano-sized TiO_2 in the olfactory bulb, indicating that larger TiO_2 particles entered more easily into the olfactory bulb through olfactory tract than nano-sized TiO_2 . This is likely because nanosized TiO_2 particles might be adsorbed in the nasal cavity and/or mucosa and only a small fraction of particles were translocated into the olfactory bulb and brain through the respiratory tract and olfactory nerve system.

Because nanoparticles can be translocated to the olfactory bulb through the olfactory nerve system after nasal inhalation by mice, translocation of nanoparticles could influence the micro-distributions of Fe, Cu, and Zn in the olfactory bulb [65]. The changes in micro distribution patterns of metal would influence the normal metabolism of substance and energy in organism. In brain, Zn is one of the most prevalent trace elements and is highly enriched in the hippocampus. Zn is also known to influence the synthesis and the metabolism of proteins and nucleic acids. The concentration of trace metals in brain also shows a close relationship with Alzheimer's disease, Parkinson's disease and multiple sclerosis. Numbers of segmented neutrophils and lymphocytes, protein carbonyl levels, and interstitial fibrosis were higher in golden hamsters exposed to carbon black, TiO_2 , and SiO_2 [66]. Nanoparticles do

not rest at the original site after inhalation, and they could be transferred to the surrounding tissues and other areas, such as, epithelial, interstitial, and endothelial sites of lung, and enter the blood circulation[56]. Therefore, nanoparticles could migrate via the secondary and tertiary olfactory pathways to most parts of brain. The subsequent influence on neuron and brain functions could be induced by the invasion of nanoparticles.

10. METABOLIC FATE AND DIPOSITION OF FULLERENE IN BIOLOGICAL SYSTEMS

There have been very few studies on the destiny, distribution, metabolism and bioaccumulation of nanoparticles in humans. Following exposure to nanoparticles *in vivo*, the target organs and resultant biological responses need to be identified, and realistic exposure levels for effect assessment should be determined. These include dose response data for the target organs, and knowledge of the subcellular locations of nanoparticles, and the mechanism of their interactions at the cellular level. For ordinary chemical substances, pharmacokinetic and pharmacodynamic information to assess the effectiveness of the compound is generally already available or can be predicted on the basis of existing data from tests on analogous compounds. For nanoparticles, however, this information is scarce or even non-existent. Due to lack of information, appropriate assessment of biological effects of nanoparticles is accompanied by large uncertainties. Both pharmacodynamic and pharmacokinetic studies are necessary for various types of nanoparticles on a "case by case" basis to assess the impacts of their biological applications, before more general assumptions can be made with respect to all nanoparticles.

Although the types of nanomaterials are increasing rapidly, many are particles containing organic molecules as building materials and inorganic elements (usually metals) as cores. Fullerenes have attracted considerable attention in various disciplines of nanotechnology and nanoscience. Investigations of chemical, physical and biological properties of fullerenes have yielded promising information. The unique carbon cage structure coupled with immense scope for derivatization makes fullerenes attractive for pharmaceutical applications.

Fullerene was first reported by Dr. Kroto *et al.* twenty years ago [67]. Before their discovery in 1985, graphite and diamond were the only two known allotropic forms of carbon. Dr. Kroto *et al.* [67] discovered a novel allotrope of carbon, which they called buckminsterfullerene due to its geodesic structure. Buckminsterfullerene is well known by its shortened name fullerene. Fullerene is known with 60 carbon atoms arranged as a truncated icosahedron, with 60 vertices and 32 faces. Twelve of the 32 faces are pentagonal and 20 hexagonal. The pentagons are necessary in order to allow curvature and eventual closure of the surface. The crystal and molecular structure of C_{60} fullerene have been resolved using single-crystal x-ray diffraction methods [68]. Considerable research activities have followed after the procedures of preparing fullerene in workable quantities were developed [69]. Biological and pharmacological activities of fullerenes have been investigated for evaluating their therapeutic potential. These include anti-HIV protease activity, photodynamic DNA cleavage, free radical scavenging action, and antimicrobial action as well as the utility of fullerenes as diagnostic agents [70-74]. Fullerene molecule can fit inside the hydrophobic cavity of HIV proteases and block the access of substrates to the catalytic site of enzyme. Fullerenes can be used as radical scavengers and antioxidants. Photosensitization of fullerenes can produce singlet oxygen in high quantum yields. This action, together with direct electron transfer from excited state of fullerene and DNA bases, can be used to cleave DNA. In addition, fullerenes have also been used as carriers for gene and drug delivery systems. Meanwhile, they are used for serum protein profiling as MELDI material for biomarker discovery through MALDITOF mass spectrometry.

Even though most fullerenes are man-made synthetic compounds, naturally occurring fullerene has also been reported in the geological environment of Shunga, a town in the lake region of Karwelia in Russia [75]. Synthetic fullerenes are produced by high temperature vaporization of solid graphitic rods by resistive heating in the presence of a few to several torr of rare gas. The soot produced by vaporization contains various levels of fullerene, depending on the vaporization conditions. However, the majority of the fullerenes produced are C_{60} and C_{70} , with C_{60} being more abundant. The fullerenes are extracted by placing the soot with a solvent in which the fullerenes are soluble. The solution is then filtered and allowed to evaporate to yield fullerene powders.

Endohedral metallofullerenes, i.e., compounds in which a fullerene encapsulates a metal atom(s), have shown great promise for biomedical applications. Although C_{60} has been the most commonly studied fullerene in biological systems, few endohedral materials have been synthesized using C_{60} as a cage molecule because of the limited interior volume of C_{60} . Most endohedral metallofullerenes are synthesized using C_{82} or higher molecular weight fullerenes, and many more derivatives of C_{82} fullerenes have been synthesized currently. $Gd@C_{82}$ is one of the most important molecules in the metallofullerene family [76]. Gadolinium endohedral metallofullerenol (e.g., $Gd@C_{82}(OH)_{22}$) is a functionalized fullerene with gadolinium, a transition metal of lanthanide family, trapped inside fullerene cage and was originally designed as a contrast agent for magnetic resonance imaging (MRI) [72]. It has been previously reported that the chemical and physical properties of gadolinium endohedral metallofullerenols are dependent on the number and position of the hydroxyl groups on the fullerene cage [76-78]. The results have shown that modifying the outer cage of $Gd@C_{82}$ with a number of hydroxyl groups alters the electronic properties of inner metal atom as well as the electron density and polarizability of the electrons in the cage surface. Although $Gd@C_{82}(OH)_{22}$ was originally studied as a novel highly efficient contrast agent for MRI, it has been demonstrated that aggregates of $Gd@C_{82}(OH)_{22}$, $Gd@C_{82}(OH)_{22}$ nanoparticles, also inhibit tumor growth in animals [79]. It has been shown that intraperitoneal injection of $Gd@C_{82}(OH)_{22}$ nanoparticles efficiently inhibited the growth of hepatoma cells implanted subcutaneously in the legs of mice. Further studies suggested that inhibition of tumor growth involved reduction in tumor-induced oxidative stress rather than direct cytotoxicity to tumor cells [79]. The potential of $Gd@C_{82}(OH)_{22}$ nanoparticles for advances in cancer therapeutics will be discussed in following sections.

11. MEDICAL APPLICATION OF ENDOHEDRAL METALLOFULLERENE

Water-soluble endohedral metallofullerenols have been extensively studied over the last decade for their potential in using endohedral metallofullerene derivatives in biological systems. Generally, the endohedral metallofullerenols can be synthesized using procedures similar to C_{60} hydroxylation. In 2000, Hirahara *et al.* reported the synthesis of a multi-hydroxylated fullerene, $Gd@C_{82}(OH)_n$ ($n = 30-40$), using TBAOH (tetrabutylammonium hydroxide) as a transfer agent [80]. Although available only in small quantities now, endohedral metallofullerene derivatives have demonstrated potential as a novel MRI contrast agent for diagnostic use [78], and as therapeutic agents [81, 82]. Endohedral metallofullerene contains unique features including all-carbon shell with a large surface, a hollow core capable of accommodating ions, a cage structure that protects entrapped metal ions from being released into biological system. These compounds are especially interesting because of the proven chemical reactivity of surface carbon atoms that can be used for introducing reactive functional groups for possible conjugation to additional chemotherapeutic payloads. These unique properties distinguish endohedral metallofullerenes from all other contrast agents for delivering metal ions *in vivo*.

11.1. Magnetic Nanoparticles as MRI Contrast Agents

Nanotechnologies based on magnetic nanoparticles (MNPs) have been applied to biological systems for diagnostic or therapeutic purposes. Magnetic resonance imaging (MRI) was employed to obtain images by magnetic characteristics of MNPs as a disturbance of the proton resonance by paramagnetic interaction with nearby MNP[83]. In addition to the use of magnetic nanoparticles as MRI contrast agents, magnetic nanoparticles can be used for magnet guided targeting of the nanoparticles themselves or of cells containing these nanoparticles for a variety of applications. Such targeting techniques are a promising approach for efficient delivery of drugs to localized disease sites, such as tumors[84]. Currently, MRI is still one of the most important diagnostic applications of magnetic nanoparticles as contrast agents.

MRI is one of the main diagnostic tools used in medicine. MRI contrast agents are used to change the relaxation times of protons in water to provide an increased image contrast between the target tissue and the surrounding background tissues. Magnevist™ (Gd-DTPA) and Omniscan™ (Gd(DTPA-BMA)) are the most commonly used MRI contrast agents. These two agents are highly soluble in water and contain Gd, a paramagnetic metal. Gadolinium is responsible for shortening the spin-lattice relaxation time, T1, of hydrogen in water and produces a brighter image in the T1 weighted MRI scan. However, there are several problems associated with the use of these agents. These agents may dissociate and release toxic Gd metal to the surrounding tissues. In addition, [Gd(DTPA)(H₂O)]₂ is unstable in acidic conditions. These problems prompted the need for a new class of MRI contrast agents. The new contrast agents must meet certain requirements: (1) enhance the proton relaxation rate significantly; (2) localize in the target tissue for a period of time and (3) possess good stability and be non-toxic. Also, the new contrast agents must be water-soluble to enhance the relaxation of water protons.

Water-soluble Gd-based endohedral metallofullerenes have potential to be a new generation of MRI contrast agents. Several groups have reported that Gd@C₈₂(OH)_x, a new metallofullerol, demonstrated a proton magnetic relaxation rate (1/T1) much higher than that of the commercial compounds [85]. Since the surrounding water molecules will not directly interact with the gadolinium metal inside the cage, the higher relaxation rate is suggested due to the electronic interactions between the water molecules and paramagnetic cage of the metallofullerol. The large surface area of the paramagnetic cage interacting with numerous water molecules simultaneously via hydrogen bonding makes the spin-lattice relaxation process faster and the T1 relaxation time shorter.

11.2. Medical Application and Biological Effects of Fullerenols

Proliferation, viability, metabolism, and differentiation capacity have been measured in mesenchymal stem cell (MSC) cultured with Gd@C₈₂ fullerol. Gd@C₈₂ fullerenols were taken up by cells and distributed in endosomes in the cytoplasm of MSC and macrophages as shown by light and electron microscopy. It was demonstrated that cellular labeling with Gd@C₈₂ is feasible and can produce T1 contrast enhancement on MRI. This study suggests that further investigation of Gd fullerol for tracking viable cells, including stem cells, is warranted.

Fullerenes are effective photosensitizers. Under photoirradiation, fullerenes can induce DNA cleavage, mutations, cancer initiation, and cytotoxicity. In rat, microsomes exposed to UV and visible light, fullerene (as a cyclodextrin complex) induced time- and concentration dependent oxidative injuries seen as lipid peroxidation and protein damage. While a slight genotoxic effect was seen in the somatic mutation and recombination test (SMART) in *Drosophila* at the highest concentration of fullerene tested, fullerene gave negative results in the SOS chromosome test in *Escherichia coli* (bacterial genotoxicity test indicating DNA damage). Fullerene dissolved in polyvinylpyrrolidone was mutagenic to *Salmonella*

typhimurium tester strains in the presence of rat liver microsomes when irradiated by visible light. Mutation was probably due to the generation of oxidized phospholipids by the action of reactive oxygen species. The photo-induced bioactivities of fullerene were suggested to be caused by reactive oxygen species (superoxide radical and OH⁻) generated by electron transfer reaction of fullerene with molecular oxygen [72]. On the other hand, C₆₀(OH)₂₂ fullerol was found to be a potent hydroxyl radical scavenger in human breast cancer cell lines [86]. This type of water-soluble fullerols had excellent anti-oxidant capacity in cultured cortical neurons[87] and prevented hydrogen peroxide- and cumene hydroperoxide-elicited changes in rat hippocampus *in vitro*[88].

Intraperitoneal injection of gadolinium endohedral metallofullerenol ([Gd@C₈₂(OH)₂₂]_n nanoparticles) could decrease activities of enzymes associated with the metabolism of reactive oxygen species (ROS) in tumor-bearing mice[79]. Gd@C₈₂(OH)₂₂ administration can efficiently restore the functions of damaged liver and kidney of the tumor-bearing mice. It has shown that Gd@C₈₂(OH)₂₂ nanoparticles were delivered to almost all types of tissues in mice after intraperitoneal administration and mainly aggregated in bone, kidneys, stomach, liver, spleen, pancreas and thymus. The fullerene cage can not be destroyed during metabolism in organisms and the internal Gd³⁺ was not liberated and distributed to the tissues. The presence of Gd *in vivo* represents the exact distribution of [Gd@C₈₂(OH)₂₂]_n nanoparticles *in vivo*. Watanabe *et al.* found that the accumulation of Gd in liver was higher than that in tumor when they investigated the accumulation of Gd-incorporating nanoemulsion in mice tumor for neutron-capture study [89]. Polyhydroxylated fullerene derivatives could be entrapped in the reticuloendothelial system (RES) and transported to all tissues by blood circulation *in vivo*, and retained in bone, liver, spleen and kidney[90]. Intravenous administration of Gd@C₈₂(OH)₄₀ to mice resulted mainly in delivery to lung, liver, spleen and kidney [90]. The prothrombin time (PT), thrombin time (TT), active partial thromboplastin time (APTT) and fibrinogen (Fbg) in plasma were measured after [Gd@C₈₂(OH)₂₂]_n administration. The prolongation of APTT and increased fibrinogen were observed due to [Gd@C₈₂(OH)₂₂]_n treatment, and the PT was shortened. A possible link with fibrinogen/ fibrin and tumor growth and dissemination has been clarified using tumor-bearing fibrinogen-deficient mice. The tumor cells directly or indirectly influence the coagulation system by interacting with blood cells (monocytes, platelets, neutrophils) and vascular endothelial cells. The shortened PT and increased Fbg are indications of thrombus. Moreover, blood clotting can be accelerated not only by tissue factor, but also by thrombin-antithrombin (TAT) complexes. One might suspect the increased levels of TAT are induced by the changes of one or more coagulation factors within the cascades after injection of [Gd@C₈₂(OH)₂₂]_n particles in mice. For mice inoculated with H22 hepatoma, which induced the metabolic imbalance of detoxification, the functions of liver and spleen of experimental mice were deteriorated. Surprisingly, in the [Gd@C₈₂(OH)₂₂]_n-treated nude mice, hepatomegaly and splenomegaly were less. This indicates that the liver damage was inhibited. It is in agreement with the serum enzyme profiles reported before, in which, the serum AST and ALT activities, the sensitive biochemical parameters for hepatocellular damage, were significantly decreased by i.p. injection of [Gd@C₈₂(OH)₂₂]_n. Based on renal function tests, markers of kidney damage were restored to the normal level by nanoparticle-treatments.

The activities of hepatic superoxide dismutase (SOD), glutathione peroxidase (GSH-Px), glutathione S-transferase (GST) and catalase were measured in mice administered with [Gd@C₈₂(OH)₂₂]_n nanoparticles, the GSH-Px, CAT and SOD activities were downregulated after treatment with [Gd@C₈₂(OH)₂₂]_n nanoparticles. Additionally, the levels of glutathione, protein bound thiols and malondialdehyde were also lower. Hydroxylated fullerene derivatives might be novel antioxidants *in vivo*. [Gd@

$\text{C}_{82}(\text{OH})_{22}\text{n}$ nanoparticles help to maintain the antioxidant-oxidant balance during tumor growth in mice. GST is a member of a family of detoxification enzymes that metabolize a variety of carcinogens by conjugating lipophilic electrophiles to GSH for excretion as mercapturic acid derivatives and thioethers and thioesters. GSH plays a vital role in the protection of cells against oxidative stress and acts as an important water-phase non-enzymatic antioxidant and an essential cofactor for antioxidant enzymes taking part in cellular redox reactions [91]. Their reduction with the $[\text{Gd}@\text{C}_{82}(\text{OH})_{22}\text{n}]$ nanoparticle treatment could be attributed to the elimination of ROS *in vivo* and alleviating the burden of liver detoxification.

In addition, to measure the biological effect of $[\text{Gd}@\text{C}_{82}(\text{OH})_{22}\text{n}]$ nanoparticles as ROS scavenger *in vitro*, electron spin resonance (ESR) spectroscopy was used to measure direct scavenging of several physiologically relevant ROS made by $[\text{Gd}@\text{C}_{82}(\text{OH})_{22}\text{n}]$ nanoparticles and inhibitory effects on lipid peroxidation. $[\text{Gd}@\text{C}_{82}(\text{OH})_{22}\text{n}]$ nanoparticles significantly reduced the ESR signal of the stable free radical, 2,2-diphenyl-1-picrylhydrazyl radical (DPPH $^{\bullet}$). Similarly, studies using ESR with spin-trapping demonstrated efficient scavenging of superoxide radical anion ($\text{O}_2^{\bullet-}$), hydroxyl radical (HO^{\bullet}) and singlet oxygen ($^1\text{O}_2$) by $[\text{Gd}@\text{C}_{82}(\text{OH})_{22}\text{n}]$ nanoparticles. *In vitro* studies using liposomes prepared from bovine liver phosphatidylcholine revealed that $[\text{Gd}@\text{C}_{82}(\text{OH})_{22}\text{n}]$ nanoparticles also had a strong inhibitory effect on lipid peroxidation. Consistent with their ability to scavenge free radicals and inhibit lipid peroxidation, $[\text{Gd}@\text{C}_{82}(\text{OH})_{22}\text{n}]$ nanoparticles also protected cells subjected *in vitro* to oxidative stress. Studies using human lung adenocarcinoma cells or rat brain capillary endothelial cells demonstrated that $[\text{Gd}@\text{C}_{82}(\text{OH})_{22}\text{n}]$ nanoparticles reduced H_2O_2 -induced free radical formation and mitochondrial damage. In summary, the results revealed strong free radical-scavenging activities of $[\text{Gd}@\text{C}_{82}(\text{OH})_{22}\text{n}]$ nanoparticles *in vitro* and *in vivo*. As these ROS have been implicated in the etiology of a wide range of human diseases, including cancer, the present findings demonstrated that the potent inhibition of $[\text{Gd}@\text{C}_{82}(\text{OH})_{22}\text{n}]$ nanoparticles on tumor growth likely related to the high free radical scavenging capacity. $[\text{Gd}@\text{C}_{82}(\text{OH})_{22}\text{n}]$ nanoparticles may exhibit antitumor activity by enabling recovery of hepatic and renal functions and by regulating oxidative stress in tumor cells. In the future some appropriate modifications to the unique surface of $[\text{Gd}@\text{C}_{82}(\text{OH})_{22}\text{n}]$ nanoparticles may lead to modified properties suitable for diagnostic and therapeutic applications.

12. POTENTIAL APPLICATION OF NANOMATERIALS IN NANOMEDICINE

Nanomedicine is the science and technology of diagnosing, treating and preventing disease and improving human health. From the standpoint of nanomedicine, there is an urgent need to understand the metabolic implications of nanomaterials in relationship to specific nanoscale properties. Once nanoparticles are absorbed by the gastrointestinal tract, these particles will be transported directly to the liver via the portal vein. The liver is able to actively remove compounds from the blood. Currently, there is no evidence that hepatic elimination affects the bioavailability of absorbed nanoparticles in the body.

Although there are few studies on metabolism of nanoparticles, it is considered unlikely that inert nanoparticles such as gold and silver particles, fullerenes and CNT, can be metabolized effectively by enzymes in the body. However, it is likely that nanoparticles with functionalized groups can be metabolized. For instance, the protein cap of a functionalized QD could be cleaved by proteases [92]. Also the metallic core of QDs and other metal oxides could be sequestered by metallothionein and excreted. These enzymes, present in liver and kidney, can bind metal and restore the cellular metal homeostasis [93]. In addition, nanoparticle drug-delivery systems consisting of liposomes are able to fuse with cell membranes and enable intracellular delivery of nanoparticles. The

intracellular load of nanoparticles could then be metabolized according to the normal metabolic pathways described for the conventionally formulated drugs.

Dendrimers, another kind of nanoparticles, are characterized by a combination of high degree of end-group functionality and a compact, precisely defined molecular structure. These characteristics can be used in biomedical applications for the amplification or multiplication of effects on a molecular level, or to create extremely high local concentrations of drugs, molecular labels, or probe moieties. In diagnostics, dendrimers that bear GdIII complexes are used as contrast agents in magnetic resonance imaging. DNA dendrimers have potential for routine use in high-throughput functional genomic analysis, and as DNA biosensors. Dendrimers are also being investigated for therapeutics, for example, as carriers for controlled drug delivery, in gene transfection, as well as in neutron-capture therapy.

The ability of tracing a single molecule at both light microscopic and ultrastructural levels is a powerful tool in understanding the dynamics of cellular function. The search for optimal techniques for tracing QDs at light microscopic and ultrastructural levels is being actively pursued. QD probes are nanometer-sized semiconductors with fluorescent properties suitable for biological imaging of the tagged molecules [94]. QD sized 5–10 nm have been suggested to be more photo stable than conventional fluorophores [95, 96]. The most commonly used ODs are Cd–Se, Zn–S, Cd–Te, Cd–S and Pb–S nanocrystals and they are all commercially available. QDs offer a favorable compromise between small fluorophores and large beads for single molecule experiments in living cells. QDs will be invaluable tools for ultrasensitive studies of the dynamics of cellular metabolism [97].

Micronised particles with a diameter of about 15 nm are known to be used in sunscreens as physical UV filter. As potential therapy, penetration of micronised Ti, Zn and Si oxides into the skin was investigated due to their small particle size. Coated nanoparticles were found in the epidermis and dermis of the treated human skin samples taken during surgery. It is suggested that nanoparticles could pass through the uppermost horny skin layer (*stratum corneum*) via intercellular channels and penetrate into deeper vital skin layers. In addition, TiO_2 nanoparticles photoexcited by UV irradiation could suppress the growth of tumor cells implanted in nude mice. This cytotoxic effect of photoexcited TiO_2 particles is associated with the generation of strong reactive oxygen species such as OH^{\bullet} and H_2O_2 on the surface of TiO_2 nanoparticles. This radical generating property of TiO_2 nanoparticles makes them ideal candidates for cancer treatment. The cell killing effect of TiO_2 nanoparticles could be adapted to an anticancer modality by the local or regional administration of TiO_2 nanoparticles to the tumor, followed by light irradiation focusing on the tumor, especially for the treatment of superficial tumors in an organ appropriate for light exposure such as skin, oral cavity, trachea, and urinary bladder. It may be possible to modify the surface characteristics of TiO_2 or other nanoparticles to produce stronger and more extensive anticancer effects without troublesome side effects.

It will be important to be aware of the potential issues to safely and efficiently propel nanotechnology forward into clinical application. At the National Institute of Health, USA, the National Cancer Institute (NCI) led a National Nanotechnology Initiative and supported a Nanotechnology Characterization Laboratory to perform preclinical toxicology and other studies. In addition, the National Institute for Environmental Health and Safety (NIEHS) also funded a Nanotechnology Safety Initiative through the National Toxicology program. It will be essential to develop a systematic program of nanotechnology for long-term safety and clinical application of nanomaterials.

CONCLUSIONS

The metabolism of nanoparticles in the body strongly depends on the surface characteristics of the nanomaterials. A threshold

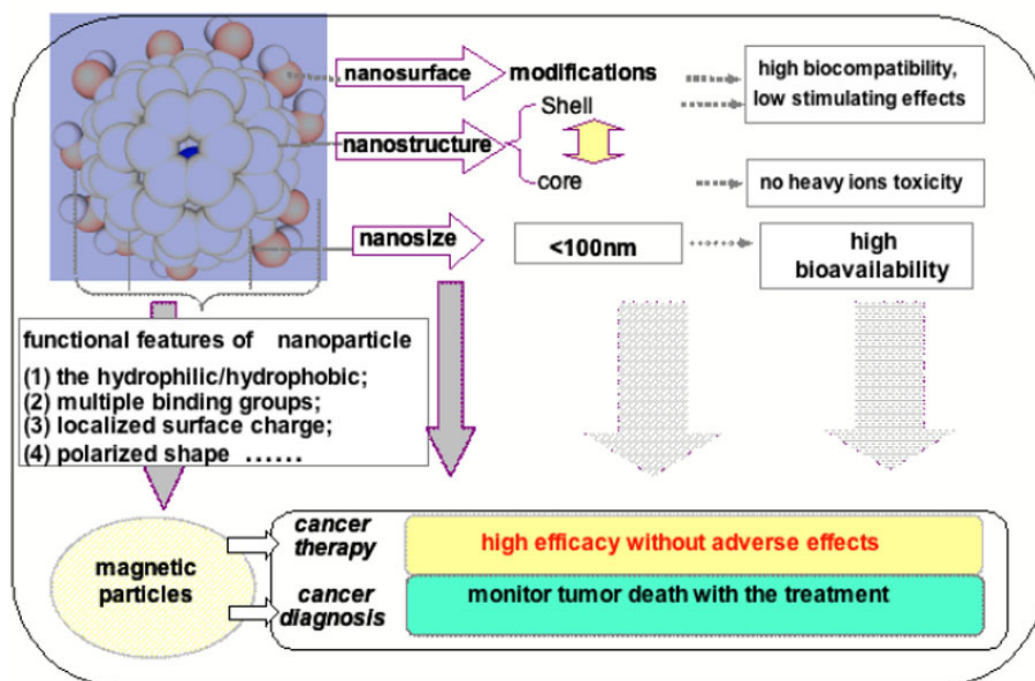


Fig. (2). Unique structural and surface features of nanoparticles.

This sandwich-type nanostructure carries a potent anticancer nanomedicine that may produce little side-effects to normal tissues *in vivo* and nearly no cytotoxicity to normal cells *in vitro*. The inner core with or without heavy metallic atom, the type and number of outer surrounded functional-groups can be changed to generate different series of relatively non toxic anticancer nanomedicine. The size of individual particle is at nanolevel (less than 100 nm). The paramagnetic metallic atom inside the cage can serve as an MRI contrast agent to simultaneously monitor the chemotherapeutic effects during treatment of tumor.

limited size of nanoparticles may exist for restricting the movement of nanoparticles in various parts of body. The pharmacokinetic behaviors of different types of nanoparticles require thorough investigation. The biological effects associated with different nanoparticles should be studied at the target organs, tissues and cellular levels. The assessment of biological effects in cardiopulmonary system is necessary for every new nanoparticle to be used for medical application. There is no universal "nanoparticle" to fit for all needs. Each nanomaterial should be treated individually for evaluation of biological effects. It is challenging to put together a set of high throughput and low cost tests for assessing biological effects of nanoparticles without compromising efficiency and reliability. Nanoparticles designed for drug delivery or as nanomedicine need special attention.

This is particularly important for nanoparticles than for larger particles because of the difference in their surface area and the resulting changes in their physico-chemical properties (Fig. 2). The available information on most nanoparticles indicates that certain nanoparticles may be genotoxic and phototoxic and photogenotoxic. There is need for more data on toxicokinetics and toxicodynamics of insoluble nanoparticles with respect to different uptake routes. There are only a few long term studies reported that are related to nanomaterials including SiO₂, CNT, and TiO₂. Nanoparticles may have potential for generating free radicals and exhibit oxidative tendency depending on their surface characteristics. The toxicokinetics and metabolism of nanomaterials have not been studied in detail[98]. Therefore, it is difficult to model the metabolism of nanomaterials. In particular, there is limited information about how the physico-chemical parameters of nanoparticles affect their absorption and transport across barriers of skin, gut, lungs and eye, and their entry into systemic circulation, metabolism, accumulation in secondary target organs and excretion. Because the current static imaging technology used for *in vivo* investigations on biodistribution of nanoparticles can not detect small fractions of nanoparticles in vascular bed, blood stream and inner organs of body, we need to

develop better methods to quantitate more precisely the unique metabolism of nanoparticles in biological systems.

ACKNOWLEDGEMENTS

This work is financially supported by the Chinese Academy of Sciences (CAS) "Hundred Talents Program" (07165111ZX), MOST 2006CB705600, and in part by NIH/NCRR/RCMI 2G12RR003048, NIH 5U 54CA091431, and USAMRMC W81XWH-05-1-0291 grants.

LIST OF ABBREVIATIONS:

NNI	= National Nanotechnology Initiative
ADME	= Absorption, distribution, metabolism and excretion
CNT	= Carbon nanotube
SWNT	= Single-walled carbon nanotube
ICP-MS	= Inductively couple plasma-mass spectroscopy
TiO ₂	= Titanium dioxide
SiO ₂	= Silicon dioxide
NLs	= Nano-liposomes
SEM	= Scanning electronic microscopy
AFM	= Atomic force microscopy
QD	= Quantum dots
CdSe	= Cadmium selenide
Cyt-B	= Cytochalasin B
TBIL	= Total bilirubin levels
ALP	= Alkaline phosphatase
ALT	= Alanine aminotransferase
AST	= Aspartate aminotransferase
CK	= Creatine kinase

LDH	= Lactate dehydrogenase
HBBDH	= Alpha-hydroxybutyrate dehydrogenase
UA	= Uric acid
BUN	= Blood urea nitrogen
CNS	= Central nervous system
AD	= Alzheimer's disease
PD	= Parkinson's disease
MS	= Multiple sclerosis
TBAOH	= Tetrabutylammonium hydroxide
SMART	= Somatic mutation and recombination test
ROS	= Reactive oxygen species
RES	= Reticuloendothelial system
SOD	= Superoxide dismutase
GSH-Px	= Glutathione peroxidase
GST	= Glutathione S-transferase
ESR	= Electron spin resonance

REFERENCES

- Jia, L. (2005) Global governmental investment in nanotechnologies. *Curr. NanoScience.*, **3**, 263-6.
- Whitesides, G. M. (2003) The 'right' size in nanobiotechnology. *Nat Biotechnol.*, **21**, 1161-5.
- Seaton, A. and Donaldson, K. (2005) Nanoscience, nanotoxicology, and the need to think small. *Lancet.*, **365**, 923-4.
- Mazzola, L. (2003) Commercializing nanotechnology. *Nat Biotechnol.*, **21**, 1137-43.
- Paull, R.; Wolfe, J.; Hebert, P. and Sinkula, M. (2003) Investing in nanotechnology. *Nat Biotechnol.*, **21**, 1144-7.
- Roszek, B.; de Jong, W.H.; Geertsma, R.E. (2005) Nanotechnology in medical applications: state-of-the-art in materials and devices. *RIVM report 265001001/2005*.
- Jia, L. (2005) Nanoparticle formulation Increases oral bioavailability of poorly soluble drugs: experimental evidences, theory, and approaches. *Curr. NanoScience.*, **3**(1), 237-43.
- Oberdorster G, O. E.; Oberdorster J. (2005b) Nanotoxicology: An Emerging Discipline Evolving from Studies of Ultrafine Particles. *Environ Health Perspect.*, **113**, 823-39.
- de Jong, W. H.; Roszek, B.; Geertsma, R.E. (2005) Nanotechnology in medical applications: possible risks for human health. *RIVM report 265001002/2005*.
- Zhao, Y. and Nalwa, H. S. (2007) *Nanotoxicology.*, American Scientific Publishers, California, 2007.
- Nel, A.; Xia, T.; Madler, L. and Li, N. (2006) Toxic potential of materials at the nanolevel. *Science.*, **311**, 622-7.
- Hoet, P. H.; Bruske-Hohlfeld, I. and Salata, O. V. (2004) Nanoparticles - known and unknown health risks. *J Nanobiotechnology.*, **2**, 12.
- Liu, Y. and Wang., H. F. (2007) Nanotechnology tackles tumours. *Nature Nanotechnol.*, **2** (1), 20-1.
- Jia, L. W.; Cerna, C.; Weitman, S. (2002) Effect of nanonization on absorption of 301029: Ex vivo and in vivo pharmacokinetic correlations determined by LC/MS. *Pharm. Res.*, **14**, 1091-6.
- Bittner, B. and Mountfield, R. J. (2002) Intravenous administration of poorly soluble new drug entities in early drug discovery: the potential impact of formulation on pharmacokinetic parameters. *Curr Opin Drug Discov Devel.*, **5**, 59-71.
- Li, N.; Kommireddy, D. S.; Lvov, Y.; Liebenberg, W.; Tiedt, L. R. and De Villiers, M. M. (2006) Nanoparticle multilayers: surface modification of photosensitive drug microparticles for increased stability and in vitro bioavailability. *J Nanosci Nanotechnol.*, **6**, 3252-60.
- Kam, N. W.; O'Connell, M.; Wisdom, J. A., and Dai, H. (2005) Carbon nanotubes as multifunctional biological transporters and near-infrared agents for selective cancer cell destruction. *Proc Natl Acad Sci U S A.*, **102**, 11600-5.
- Pantarotto, D.; Briand, J. P.; Prato, M. and Bianco, A. (2004) Translocation of bioactive peptides across cell membranes by carbon nanotubes. *Chem Commun (Camb).*, **1**, 16-7.
- Kostarelos, K. L. L.; Pastorin, G.; Wu, W.; Wieckowski, S.; Luangsivilay, J.; Godefroy, S.; Pantarotto, D.; Briand, J.; Muller, S.; Prato, M.; Bianco, A. (2007) Cellular uptake of functionalized carbon nanotubes is independent of functional group and cell type. *Nat. Nanotech.*, **2**, 108-13.
- Arunachalam, B.; Phan, U. T.; Geuze, H. J. and Cresswell, P. (2000) Enzymatic reduction of disulfide bonds in lysosomes: characterization of a gamma-interferon-inducible lysosomal thiol reductase (GILT). *Proc Natl Acad Sci U S A.*, **97**, 745-50.
- Feazell, R. P.; Nakayama-Ratchford, N.; Dai, H. and Lippard, S. J. (2007) Soluble single-walled carbon nanotubes as longboat delivery systems for platinum(IV) anticancer drug design. *J Am Chem Soc.*, **129**, 8438-9.
- Service, R. F. (2003) American Chemical Society meeting. Nanomaterials show signs of toxicity. *Science.*, **300**, 243.
- Zhu, L.; Chang, D. W.; Dai, L. and Hong, Y. (2007) DNA damage induced by multiwalled carbon nanotubes in mouse embryonic stem cells. *Nano Lett.*, **7**, 3592-7.
- Lam, C. W.; James, J. T.; McCluskey, R. and Hunter, R. L. (2004) Pulmonary toxicity of single-wall carbon nanotubes in mice 7 and 90 days after intratracheal instillation. *Toxicol Sci.*, **77**, 126-34.
- Liu, A.; Sun, K.; Yang, J.; Zhao, D. (2008) Toxicological effects of multi-wall carbon nanotubes in rats. *J Nanopart Res.*, DOI10.1007/s11051-008-9369-0.
- Maynard, A. D.; Baron, P. A.; Foley, M.; Shvedova, A. A.; Kisin, E. R. and Castranova, V. (2004) Exposure to carbon nanotube material: aerosol release during the handling of unrefined single-walled carbon nanotube material. *J Toxicol Environ Health A.*, **67**, 87-107.
- Shedova, A. A.; Castranova, V.; Kisin, E.R.; Schwegler-Berry, D.; Murray, A.R.; Gandelsman, and V.Z.; M.; A.; Baron, P. (2003) Exposure to carbon nanotube material: assessment of nanotube cytotoxicity using human keratinocyte cells. *J Toxicol Environ Health A.*, **66**, 1909-26.
- Deng, X. J.; G; Wang, H.; Sun, H.; Wang, X.; Yang, S.; Wang, T.; Liu, Y. (2007) Translocation and fate of multi-walled carbon nanotubes in vivo. *Carbon.*, **45**, 1419-24.
- Moller, W.; Brown, D. M.; Kreyling, W. G.; and Stone, V. (2005) Ultrafine particles cause cytoskeletal dysfunctions in macrophages: role of intracellular calcium. *Part Fibre Toxicol.*, **2**, 7.
- Driscoll, K. E.; Deyo, L. C.; Carter, J. M.; Howard, B. W.; Hassenbein, D. G. and Bertram, T. A. (1997) Effects of particle exposure and particle-elicited inflammatory cells on mutation in rat alveolar epithelial cells. *Carcinogenesis.*, **18**, 423-30.
- Chougule, M.; Padhi, B. and Misra, A. (2007) Nano-liposomal dry powder inhaler of tacrolimus: preparation, characterization, and pulmonary pharmacokinetics. *Int J Nanomedicine.*, **2**, 675-88.
- Warheit, D. B.; Laurence, B. R.; Reed, K. L.; Roach, D. H.; Reynolds, G. A. and Webb, T. R. (2004) Comparative pulmonary toxicity assessment of single-wall carbon nanotubes in rats. *Toxicol Sci.*, **77**, 117-25.
- Pope, C. A.; 3rd, Burnett, R. T.; Thurston, G. D.; Thun, M. J.; Calle, E. E.; Krewski, D. and Godleski, J. J. (2004) Cardiovascular mortality and long-term exposure to particulate air pollution: epidemiological evidence of general pathophysiological pathways of disease. *Circulation.*, **109**, 71-7.
- Borm, P. J.; Schins, R. P. and Albrecht, C. (2004) Inhaled particles and lung cancer, part B: paradigms and risk assessment. *Int J Cancer.*, **110**, 3-14.
- Pantarotto, D.; Singh, R.; McCarthy, D.; Erhardt, M.; Briand, J. P.; Prato, M.; Kostarelos, K. and Bianco, A. (2004) Functionalized carbon nanotubes for plasmid DNA gene delivery. *Angew Chem Int Ed Engl.*, **43**, 5242-6.
- Singh, R.; Pantarotto, D.; McCarthy, D.; Chaloin, O.; Hoebeke, J.; Partidos, C. D.; Briand, J. P.; Prato, M.; Bianco, A. and Kostarelos, K. (2005) Binding and condensation of plasmid DNA onto functionalized carbon nanotubes: toward the construction of nanotube-based gene delivery vectors. *J Am Chem Soc.*, **127**, 4388-96.
- He, P. and Bayachou, M. (2005) Layer-by-layer fabrication and characterization of DNA-wrapped single-walled carbon nanotube particles. *Langmuir.*, **21**, 6086-92.

- [38] Tan, Y.; Whitmore, M.; Li, S.; Frederik, P. and Huang, L. (2002) LPD nanoparticles—novel nonviral vector for efficient gene delivery. *Methods Mol Med.*, **69**, 73-81.
- [39] Gemeinhart, R. A.; Luo, D. and Saltzman, W. M. (2005) Cellular fate of a modular DNA delivery system mediated by silica nanoparticles. *Biotechnol Prog.*, **21**, 532-7.
- [40] Bejjani, R. A.; BenEzra, D.; Cohen, H.; Rieger, J.; Andrieu, C.; Jeanny, J. C.; Gollomb, G. and Behar-Cohen, F. F. (2005) Nanoparticles for gene delivery to retinal pigment epithelial cells. *Mol Vis.*, **11**, 124-32.
- [41] Zheng, M.; Jagota, A.; Semke, E. D.; Diner, B. A.; McLean, R. S.; Lustig, S. R.; Richardson, R. E. and Tassi, N. G. (2003) DNA-assisted dispersion and separation of carbon nanotubes. *Nat Mater.*, **2**, 338-42.
- [42] Rajendra, J.; Baxendale, M.; Dit Rap, L. G. and Rodger, A. (2004) Flow linear dichroism to probe binding of aromatic molecules and DNA to single-walled carbon nanotubes. *J Am Chem Soc.*, **126**, 11182-8.
- [43] Rajendra, J. and Rodger, A. (2005) The binding of single-stranded DNA and PNA to single-walled carbon nanotubes probed by flow linear dichroism. *Chemistry.*, **11**, 4841-7.
- [44] Audette, G. F.; van Schaik, J.; Hazes, B.; Irvin, R.T. (2004). DNA-binding protein nanotubes. *Nano Lett.*, **4**, 1897-902.
- [45] Green, M. and Howman, E. (2005) Semiconductor quantum dots and free radical induced DNA nicking. *Chem Commun (Camb).*, **7**(1), 121-3.
- [46] Florence, A. T. and Hussain, N. (2001) Transcytosis of nanoparticle and dendrimer delivery systems: evolving vistas. *Adv Drug Deliv Rev.*, **50 Suppl 1**, S69-89.
- [47] Li, W. C.; Ye, C.; Wei, T.; Zhao, Y.; Lao, F.; Chen, Z.; Meng, H.; Gao, Y.; Yuan, H.; Xing, G.; Zhao, F.; Chai, Z.; Zhao, Y.; Yang, F.; Han, D.; Tang, X.; Zhang, Y. (2008) The translocation of Fullerene nanoparticles into lysosome via the pathway of clathrin-mediated endocytosis. *Nanotechnology.*, **19**, doi:10.1088/0957-4484/19/14/145102.
- [48] Heckel, K.; Kieffmann, R.; Dorger, M.; Stoeckelhuber, M. and Goetz, A. E. (2004) Colloidal gold particles as a new *in vivo* marker of early acute lung injury. *Am J Physiol Lung Cell Mol Physiol.*, **287**, L867-78.
- [49] Nemmar, A.; Hoet, P. H.; Vanquickenborne, B.; Dinsdale, D.; Thomeer, M.; Hoylaerts, M. F.; Vanbilloen, H.; Mortelmans, L. and Nemery, B. (2002) Passage of inhaled particles into the blood circulation in humans. *Circulation.*, **105**, 411-4.
- [50] Nemmar, A.; Vanbilloen, H.; Hoylaerts, M. F.; Hoet, P. H.; Verbruggen, A. and Nemery, B. (2001) Passage of intratracheally instilled ultrafine particles from the lung into the systemic circulation in hamster. *Am J Respir Crit Care Med.*, **164**, 1665-8.
- [51] Verma, D. D.; Verma, S.; Blume, G. and Fahr, A. (2003) Particle size of liposomes influences dermal delivery of substances into skin. *Int J Pharm.*, **258**, 141-51.
- [52] Langer, R. (2000) Biomaterials in drug delivery and tissue engineering: one laboratory's experience. *Acc Chem Res.*, **33**, 94-101.
- [53] Meng, H.; Chen, Z.; Xing, G.; Yuan, H.; Chen, C.; Zhao, F.; Zhang, C. and Zhao, Y. (2007) Ultrahigh reactivity provokes nanotoxicity: explanation of oral toxicity of nano-copper particles. *Toxicol Lett.*, **175**, 102-10.
- [54] Wang, B.; Feng, W. Y.; Wang, T. C.; Jia, G.; Wang, M.; Shi, J. W.; Zhang, F.; Zhao, Y. L. and Chai, Z. F. (2006) Acute toxicity of nano-and micro-scale zinc powder in healthy adult mice. *Toxicol Lett.*, **161**, 115-23.
- [55] Chen, Z.; Meng, H.; Xing, G.; Chen, C.; Zhao, Y.; Jia, G.; Wang, T.; Yuan, H.; Ye, C.; Zhao, F.; Chai, Z.; Zhu, C.; Fang, X.; Ma, B. and Wan, L. (2006) Acute toxicological effects of copper nanoparticles *in vivo*. *Toxicol Lett.*, **163**, 109-20.
- [56] Wang, J.; Zhou, G.; Chen, C.; Yu, H.; Wang, T.; Ma, Y.; Jia, G.; Gao, Y.; Li, B.; Sun, J.; Li, Y.; Jiao, F.; Zhao, Y. and Chai, Z. (2007) Acute toxicity and biodistribution of different sized titanium dioxide particles in mice after oral administration. *Toxicol Lett.*, **168**, 176-85.
- [57] Oberdorster, G.; Ferin, J. and Lehnert, B. E. (1994) Correlation between particle size, *in vivo* particle persistence, and lung injury. *Environ Health Perspect.*, **102 Suppl 5**, 173-9.
- [58] Huggins, C. B. and Froehlich, J. P. (1966) High concentration of injected titanium dioxide in abdominal lymph nodes. *J Exp Med.*, **124**, 1099-106.
- [59] Kreyling, W. G.; Semmler-Behnke, M. and Moller, W. (2006) Ultrafine particle-lung interactions: does size matter? *J Aerosol Med.*, **19**, 74-83.
- [60] Borm, P.; Klaessig, F. C.; Landry, T. D.; Moudgil, B.; Pauluhn, J.; Thomas, K.; Trotter, R. and Wood, S. (2006) Research strategies for safety evaluation of nanomaterials, part V: role of dissolution in biological fate and effects of nanoscale particles. *Toxicol Sci.*, **90**, 23-32.
- [61] Olivier, J. C. (2005) Drug transport to brain with targeted nanoparticles. *NeuroRx.*, **2**, 108-19.
- [62] Boffetta, P.; Soutar, A.; Cherrie, J. W.; Granath, F.; Andersen, A.; Anttila, A.; Blettner, M.; Gaborieau, V.; Klug, S. J.; Langard, S.; Luce, D.; Merletti, F.; Miller, B.; Mirabelli, D.; Pukkala, E.; Adami, H. O. and Weiderpass, E. (2004) Mortality among workers employed in the titanium dioxide production industry in Europe. *Cancer Causes Control.*, **15**, 697-706.
- [63] Oberdorster, G.; Sharp, Z.; Atudorei, V.; Elder, A.; Gelein, R.; Kreyling, W. and Cox, C. (2004) Translocation of inhaled ultrafine particles to the brain. *Inhal Toxicol.*, **16**, 437-45.
- [64] Oberdorster, E. (2004) Manufactured nanomaterials (fullerenes, C60) induce oxidative stress in the brain of juvenile largemouth bass. *Environ Health Perspect.*, **112**, 1058-62.
- [65] Wang, J. C.; Yu, H.; Sun, J.; Li, B.; Li, Y.; Gao, Y.; Chai, Z.; He, W.; Huang, Y.; Zhao, Y. (2007) Distribution of TiO₂ particles in the olfactory bulb of mice after nasal inhalation using microbeam SRXRF mapping techniques. *Journal of Radioanalytical and Nuclear Chemistry.*, **272**(3), 527-31.
- [66] Oberdorster, G.; Oberdorster, E. and Oberdorster, J. (2005) Nanotoxicology: an emerging discipline evolving from studies of ultrafine particles. *Environ Health Perspect.*, **113**, 823-39.
- [67] Kroto H. W.; H. J. R.; O'Brien S. C.; Curl R. F. and Smalley R. E. (1985) C₆₀: Buckminsterfullerene. *Nature.*, **318**, 162-3.
- [68] Liu, S.; Lu, Y. J.; Kappes, M. M. and Ibers, J. A. (1991) The Structure of the C₆₀ Molecule: X-Ray Crystal Structure Determination of a Twin at 110 K. *Science.*, **254**, 408-10.
- [69] W. Kratschmer, L. D. L.; K. Fostiropoulos and D.R. Huffman (1990) Solid C₆₀: a new form of carbon. *Nature.*, **347**, 354-7.
- [70] Qiao, R.; Roberts, A. P.; Mount, A. S.; Klaine, S. J. and Ke, P. C. (2007) Translocation of C₆₀ and its derivatives across a lipid bilayer. *Nano Lett.*, **7**, 614-9.
- [71] Satoh, M. and Takayanagi, I. (2006) Pharmacological studies on fullerene (C₆₀), a novel carbon allotrope, and its derivatives. *J Pharmacol Sci.*, **100**, 513-8.
- [72] Yamakoshi, Y.; Umezawa, N.; Ryu, A.; Arakane, K.; Miyata, N.; Goda, Y.; Masumizu, T. and Nagano, T. (2003) Active oxygen species generated from photoexcited fullerene (C₆₀) as potential medicines: O₂-* versus ¹O₂. *J Am Chem Soc.*, **125**, 12803-9.
- [73] Zhao, X.; Striolo, A. and Cummings, P. T. (2005) C₆₀ binds to and deforms nucleotides. *Biophys J.*, **89**, 3856-62.
- [74] Friedman, S. H. D.; D.L.; Sijbesma, R.P.; Srdanov, G.; Wudl, F.; Kenyon, G.L (1993) Inhibition of HIV-1 Protease by Fullerene Derivatives: Model Building Studies and Experimental Verification. *J. Am. Chem. Soc.*, **115**, 6505-9.
- [75] Buseck, P. R.; Tsipursky, S. J. and Hettich, R. (1992) Fullerenes from the Geological Environment. *Science.*, **257**, 215-7.
- [76] Tang, J.; Xing, G.; Zhao, F.; Yuan, H. and Zhao, Y. (2007) Modulation of structural and electronic properties of fullerene and metallofullerenes by surface chemical modifications. *J Nanosci Nanotechnol.*, **7**, 1085-101.
- [77] Tang, J.; Xing, G.; Zhao, Y.; Jing, L.; Gao, X.; Cheng, Y.; Yuan, H.; Zhao, F.; Chen, Z.; Meng, H.; Zhang, H.; Qian, H.; Su, R.; Ibrahim, K. (2006) Periodical variation of electronic properties in polyhydroxylated metallofullerene materials. *Advanced Materials.*, **18**, 1458-62.
- [78] Chen, C.; Xing, G.; Wang, J.; Zhao, Y.; Li, B.; Tang, J.; Jia, G.; Wang, T.; Sun, J.; Xing, L.; Yuan, H.; Gao, Y.; Meng, H.; Chen, Z.; Zhao, F.; Chai, Z. and Fang, X. (2005) Antioxidative function and biodistribution of [Gd@C₈₂(OH)₂₂]n nanoparticles in tumor-bearing mice. *Nano Lett.*, **5**, 2050-7.
- [79] Wang, J.; Chen, C.; Li, B.; Yu, H.; Zhao, Y.; Sun, J.; Li, Y.; Xing, G.; Yuan, H.; Tang, J.; Chen, Z.; Meng, H.; Gao, Y.; Ye, C.; Chai,

- Z.; Zhu, C.; Ma, B.; Fang, X. and Wan, L. (2006) One-dimensional metallofullerene crystal generated inside single-walled carbon nanotubes. *Biochem Pharmacol.*, **71**, 872-81.
- [80] Hirahara, K.; Suenaga, K.; Bandow, S.; Kato, H.; Okazaki, T.; Shinohara, H. and Iijima, S. (2000) *In vivo* studies of fullerene-based materials using endohedral metallofullerene radiotracers. *Phys Rev Lett.*, **85**, 5384-7.
- [81] Cagle, D. W.; Kennel, S. J.; Mirzadeh, S.; Alford, J. M. and Wilson, L. J. (1999) The structural determination of endohedral metallofullerene Gd@C(82) by XANES. *Proc Natl Acad Sci U S A.*, **96**, 5182-7.
- [82] Liu, L.; Gao, B.; Chu, W.; Chen, D.; Hu, T.; Wang, C.; Dunsch, L.; Marcelli, A.; Luo, Y. and Wu, Z. (2008) Magnetic Nanoparticles for Cancer Therapy. *Chem Commun (Camb.)*, **28**(4), 474-6.
- [83] Goya, G. F. G. V.; Ibarra, M. R. (2008) Magnetically modulated therapeutic systems. *Curr. NanoScience.*, **4**(1), 1-16.
- [84] Häfeli, U. I. J. P. (2004) Antioxidant, prooxidant and cytotoxic activity of hydroxylated resveratrol analogues: structure-activity relationship. *Int J. Pharm.*, **277**, 19-24.
- [85] Murias, M.; Jager, W.; Handler, N.; Erker, T.; Horvath, Z.; Szekeres, T.; Nohl, H. and Gille, L. (2005) A biologically effective fullerene (C60) derivative with superoxide dismutase mimetic properties. *Biochem Pharmacol.*, **69**, 903-12.
- [86] Zhu, X.; Zhu, L.; Li, Y.; Duan, Z.; Chen, W. and Alvarez, P. J. (2007) Developmental toxicity in zebrafish (*Danio rerio*) embryos after exposure to manufactured nanomaterials: buckminsterfullerene aggregates (nC60) and fullerol. *Environ Toxicol Chem.*, **26**, 976-9.
- [87] Dugan, L. L.; Gabrielsen, J. K.; Yu, S. P.; Lin, T. S.; and Choi, D. W. (1996) Buckminsterfullerenol free radical scavengers reduce excitotoxic and apoptotic death of cultured cortical neurons. *Neurobiol Dis.*, **3**, 129-35.
- [88] Tsai, M. C.; Chen, Y. H. and Chiang, L. Y. (1997) Polyhydroxylated C60, fulleranol, a novel free-radical trapper, prevented hydrogen peroxide- and cumene hydroperoxide-elicited changes in rat hippocampus in-vitro. *J Pharm Pharmacol.*, **49**, 438-45.
- [89] Watanabe, T.; Ichikawa, H. and Fukumori, Y. (2002) Tumor accumulation of gadolinium in lipid-nanoparticles intravenously injected for neutron-capture therapy of cancer. *Eur J Pharm Biopharm.*, **54**, 119-24.
- [90] Mikawa, M.; Kato, H.; Okumura, M.; Narazaki, M.; Kanazawa, Y.; Miwa, N. and Shinohara, H. (2001) Paramagnetic water-soluble metallofullerenes having the highest relaxivity for MRI contrast agents. *Bioconj Chem.*, **12**, 510-4.
- [91] Sies, H. (1999) Glutathione and its role in cellular functions. *Free Radic Biol Med.*, **27**, 916-21.
- [92] Hardman, R. (2006) A toxicologic review of quantum dots: toxicity depends on physicochemical and environmental factors. *Environ Health Perspect.*, **114**, 165-72.
- [93] Coyle, P.; Philcox, J. C.; Carey, L. C. and Roife, A. M. (2002) Metallothionein: the multipurpose protein. *Cell Mol Life Sci.*, **59**, 627-47.
- [94] Yacoby, A.; Heiblum, M.; Mahalu, D. and Shtrikman, H. (1995) Coherence and Phase Sensitive Measurements in a Quantum Dot. *Phys Rev Lett.*, **74**, 4047-50.
- [95] Chan, W. C.; Maxwell, D. J.; Gao, X.; Bailey, R. E.; Han, M. and Nie, S. (2002) Luminescent quantum dots for multiplexed biological detection and imaging. *Curr Opin Biotechnol.*, **13**, 40-6.
- [96] Wu, X.; Liu, H.; Liu, J.; Haley, K. N.; Treadway, J. A.; Larson, J. P.; Ge, N.; Peale, F. and Bruchez, M. P. (2003) Immunofluorescent labeling of cancer marker Her2 and other cellular targets with semiconductor quantum dots. *Nat Biotechnol.*, **21**, 41-6.
- [97] Dahan, M.; Levi, S.; Luccardini, C.; Rostaing, P.; Riveau, B. and Triller, A. (2003) Diffusion dynamics of glycine receptors revealed by single-quantum dot tracking. *Science.*, **302**, 442-5.
- [98] Chen, Z.; Meng, H.; Xing, G.; Chen, C.; Zhao, Y. (2007) Toxicological and biological effects of nanomaterials. *International Journal of Nanotechnology.*, **4**(1/2), 179-96.



The scavenging of reactive oxygen species and the potential for cell protection by functionalized fullerene materials

Jun-Jie Yin^{b,1}, Fang Lao^{a,1}, Peter P. Fu^d, Wayne G. Wamer^b, Yuliang Zhao^{a,c,*}, Paul C. Wang^f, Yang Qiu^a, Baoyun Sun^c, Gengmei Xing^c, Jinquan Dong^c, Xing-Jie Liang^{a,**}, Chunying Chen^{a,c,*}

^a Division of Nanomedicine and Nanobiology, National Center for Nanoscience and Technology of China, Beijing 100190, China

^b Center for Food Safety and Applied Nutrition, Food and Drug Administration, College Park, MD 20740, USA

^c Laboratory for Bio-Environmental Effects of Nanomaterials and Nanosafety, Institute of High Energy Physics, Chinese Academy of Sciences, Beijing 100049, China

^d Division of Biochemical Toxicology, National Center for Toxicological Research, Food and Drug Administration, Jefferson, AR 72079, USA

^f Laboratory of Molecular Imaging, Department of Radiology, Howard University, Washington, DC 20060, USA

ARTICLE INFO

Article history:

Received 1 August 2008

Accepted 23 September 2008

Available online 4 November 2008

Keywords:

Gadolinium endohedral metallofullerene

Fullerenol

Carboxyfullerene

Scavenging activity

Cytoprotection

Reactive oxygen species

ABSTRACT

We demonstrated that three different types of water-soluble fullerenes materials can intercept all of the major physiologically relevant ROS. $C_{60}(C(COOH)_2)_2$, $C_{60}(OH)_{22}$, and $Gd@C_{82}(OH)_{22}$ can protect cells against H_2O_2 -induced oxidative damage, stabilize the mitochondrial membrane potential and reduce intracellular ROS production with the following relative potencies: $Gd@C_{82}(OH)_{22} \geq C_{60}(OH)_{22} > C_{60}(C(COOH)_2)_2$. Consistent with their cytoprotective abilities, these derivatives can scavenge the stable 2,2-diphenyl-1-picrylhydrazyl radical (DPPH), and the reactive oxygen species (ROS) superoxide radical anion ($O_2^{\cdot-}$), singlet oxygen, and hydroxyl radical (HO^{\cdot}), and can also efficiently inhibit lipid peroxidation *in vitro*. The observed differences in free radical-scavenging capabilities support the hypothesis that both chemical properties, such as surface chemistry induced differences in electron affinity, and physical properties, such as degree of aggregation, influence the biological and biomedical activities of functionalized fullerenes. This represents the first report that different types of fullerene derivatives can scavenge all physiologically relevant ROS. The role of oxidative stress and damage in the etiology and progression of many diseases suggests that these fullerene derivatives may be valuable *in vivo* cytoprotective and therapeutic agents.

© 2008 Elsevier Ltd. All rights reserved.

1. Introduction

A large number of *in vitro* and *in vivo* studies suggest that oxidative stress is linked to either the primary or secondary mechanisms of progression for many acute and chronic diseases. As mediators of oxidative stress, reactive oxygen species (ROS), which include superoxide radical anion ($O_2^{\cdot-}$), hydroxyl radical (HO^{\cdot}), singlet oxygen (1O_2), and hydrogen peroxide, have been implicated in the etiology of several human diseases, including amyotrophic lateral sclerosis, arthritis, cancer, cardiovascular disease, and a number of neurodegenerative disorders [1,2]. Cellular targets of ROS include DNA, proteins and lipids. Damage to these cellular targets has been associated with aging and several human diseases

including cancer, atherosclerosis, ischemia, inflammation, and liver injury [3–5]. In addition, it has been determined that compared to normal cells, cancer cells are under increased oxidative stress, which is associated with increased generation of ROS and can result in stimulation of cellular proliferation, mutations, and genetic instability [6–8]. Thus, chemical species that potently scavenge ROS may be of great significance in biomedicine both for maintaining health and for use in cancer chemotherapy.

It is well established that fullerenes and their derivatives possess a unique capacity for scavenging ROS [9–11]. Because underivatized fullerenes are insoluble in water and biological systems, hydroxylated and other derivatized fullerenes have been utilized due to their increased water solubility and resulting increase in payload of ROS-scavenging activity to target cells and tissues. Demonstrated protective effects of water-soluble fullerene derivatives include reduction of injury on ischemic reperfusion of the intestine [10], a decrease in numbers of cells undergoing apoptosis [11], reduction in free radical levels in organ perfusate [12], and neuroprotective effects [13].

Hydroxylated fullerenes (fullerenols) and malonic acid-substituted fullerenes (carboxyfullerenes) are two major groups in

* Corresponding authors. Division of Nanomedicine and Nanobiology, National Center for Nanoscience and Technology of China, No. 11 Beiyitiao Zhongguancun, Beijing 100190, China. Tel.: +86 10 8254 5560; fax: +86 10 6265 6765.

** Corresponding author.

E-mail addresses: zhaoyuliang@ihep.ac.cn (Y. Zhao), liangxj@nanoctr.cn (X.-J. Liang), chenchy@nanoctr.cn (C. Chen).

¹ Both authors are contributed equally.

water-soluble fullerene materials, which were found to possess biological significance as free radical scavengers [9–15]. For example, Dugan et al. [14,15] demonstrated that carboxylic acid-substituted C_{60} derivatives had potent ROS-scavenging activity. These fullerene derivatives prevented apoptosis of cultured cortical neurons induced by exposure to N-methyl D-aspartate (NMDA)-agonists, protected the nigrostriatal dopaminergic system from iron-induced oxidative injury, and showed effective neuro-protective antioxidant activity *in vitro* and *in vivo*. Fullerenols have also been demonstrated to be particularly valuable candidates for use as free radical scavengers or water-soluble antioxidants in biological systems [16].

Endohedral metallofullerenes, i.e. compounds in which a fullerene encapsulates a metal atom(s), have shown great promise for use in biomedical science. Although C_{60} has been the most commonly studied fullerene in biological systems, few endohedral materials have been synthesized using C_{60} as a cage molecule because of the limited interior volume of C_{60} . Therefore, most endohedral metallofullerenes are synthesized using C_{82} or higher molecular weight fullerenes, and many derivatives of C_{82} fullerenes have been synthesized in our laboratory. $Gd@C_{82}$ is one of the most important molecules in the metallofullerene family [17]. Gadolinium endohedral metallofullerenol (e.g., $Gd@C_{82}(OH)_{22}$) is a functionalized fullerene with gadolinium, a transition metal in the lanthanide family, trapped inside the C_{82} fullerene cage. We have previously reported that the chemical and physical properties of gadolinium endohedral metallofullerenols are dependent on the number and position of the hydroxyl groups on the fullerene cage [17]. These results demonstrated that modifying the outer cage of $Gd@C_{82}$ with a number of hydroxyl groups tunes the electronic properties of the inner metal atom as well as the electron density and polarizability of the electrons at the fullerene's surface.

Gadolinium endohedral metallofullerenols were originally designed as magnetic resonance imaging (MRI) contrast agents for biomedical imaging [18]. These materials have additionally attracted attention due to their potential use in chemotherapy [18,19]. We have recently reported that aggregates of $Gd@C_{82}(OH)_{22}$, i.e. $Gd@C_{82}(OH)_{22}$ nanoparticles, inhibited the proliferation of tumors and decreased the induction of antioxidant defenses *in vivo* [18,19]. We have also determined that intraperitoneally injected $[Gd@C_{82}(OH)_{22}]_n$ nanoparticles efficiently inhibited the growth of hepatoma cells implanted into the legs of mice and that inhibition of tumor growth involved reduction in tumor-induced oxidative stress rather than direct cytotoxicity to tumor cells [19]. However, the molecular mechanisms underlying these protective effects are still unclear.

It has been shown that a number of fullerenes, fullerenols, and endohedral metallofullerenols are capable of reacting with and/or scavenging free radicals [15,16,20]. However, much less is known about the protective role of $Gd@C_{82}(OH)_{22}$ nanoparticles. It has not been determined if the ROS-scavenging capability of $[Gd@C_{82}(OH)_{22}]_n$ nanoparticles is higher than the other functionalized fullerenes (e.g., functionalized C_{60} -fullerenols and C_{60} -carboxyfullerenes). In this study we employ the electron spin resonance (ESR) spin trap technique to provide direct *in vitro* evidence that $Gd@C_{82}(OH)_{22}$, a fullerenol ($C_{60}(OH)_{22}$), and a carboxyfullerene ($C_{60}(C(COOH)_2)_2$), can efficiently scavenge different types of free radicals and inhibit lipid peroxidation. Both ROS, i.e. superoxide radical anion (O_2^-), hydroxyl radical (HO^\bullet) and singlet oxygen (1O_2), and the stable, nitrogen-centered free radical, DPPH $^\bullet$ were intercepted by these fullerene derivatives. Using human lung adenocarcinoma A549 cells or rat brain capillary endothelial cells (rBCECs), we further demonstrate that these fullerene derivatives reduce H_2O_2 -induced cytotoxicity, free radical formation and mitochondrial damage.

2. Materials and methods

2.1. Preparation and characterization of water-soluble fullerene derivatives

Highly purified hydroxylated and malonic acid-substituted derivatives of C_{60} were prepared by previously published methods [21,22]. Although the diameter of an isolated C_{60} molecule is about 0.7 nm, fullerene derivatives readily aggregate and form nanoparticles in aqueous solution. Additional physical and chemical properties of $C_{60}(OH)_{22}$ and $C_{60}(C(COOH)_2)_2$ can be found in the previous reports [21,22]. The synthesis and characterization of $Gd@C_{82}(OH)_{22}$ have been previously described [18]. The nanoparticles' sizes were characterized in water using a field emission scanning electron microscope (FE-SEM, Hitachi S-4800, Japan). To investigate their particle sizes in the matrix used for ESR studies, we additionally measured their particle size distribution in phosphate buffered saline (PBS, 20 mM phosphate, 0.8% NaCl, pH 7.4) using dynamic light scattering (DLS) (Nano ZS90, Malvern). The DLS data were in agreement with those obtained by SEM (data not shown).

The fullerene derivatives used for ESR detection were prepared according to the experimental requirements (see materials and methods below). For cell experiments, nanoparticles of fullerene derivatives were diluted as needed with PBS prior to use. We further compared the spectra of different fullerenes, which were recorded between 200 nm and 600 nm using a UV–Vis spectrophotometer (CARY 100 Bio, Varian, Inc., USA) at room temperature of 20–25 °C.

2.2. Reagents

Hydrogen peroxide (H_2O_2), xanthine, diethylenetriaminepentaacetic acid (DTPA), 1,1-diphenyl-2-picrylhydrazyl radical (DPPH $^\bullet$) and 2,2,6,6-tetramethyl-4-piperidone (TEMP) were purchased from Sigma Aldrich (St. Louis, MO) 5-tert-Butoxycarbonyl-5-methyl-1-pyrroline-N-oxide (BMPPO) and 5-diethoxyphosphoryl-5-methyl-1-pyrroline N-oxide (DEPMPO) were supplied by Oxis International (Portland, OR). Basic endothelial cell growth factor (bECGF) and xanthine oxidase were obtained from Roche Applied Science (Indianapolis, IN). Egg phosphatidylcholine was obtained from Avanti Polar Lipids, Inc. (Alabaster, AL). 2,2'-Azobis(2-amidinopropane) dihydrochloride (AAPH) was purchased from Wako Chemicals (Richmond, VA). All reagents used in cell culture were obtained from HyClone Co. (Logan, UT) unless otherwise stated. Fluorescent probes JC-1 (5,5',6,6'-tetrachloro-1,1',3,3'-tetraethylbenzimidazolylcarbocyanine iodide) and CM-H $_2$ DCFDA (5-(and-6)-chloromethyl-2',7'-dichlorodihydrofluorescein diacetate, acetyl ester) were purchased from Invitrogen Co. (Molecular Probes, Eugene, OR). All other reagents used were at least of analytical grade.

2.3. Cell cultures

rBCECs were prepared following a modified protocol of Deli et al. [23]. In brief, four Wistar rats (85–90 g) were sacrificed by cervical dislocation, the forebrains were collected, meninges were removed and the grey matter was minced and digested with type II collagenase. The cell pellets were resuspended in Dulbecco's modified Eagle's medium (DMEM) and centrifuged at 1500 rpm for 5 min. After three cycles of suspension and centrifugation, the pellet containing capillary endothelial cells was collected and cultured in DMEM medium with 20% fetal bovine serum (FBS), supplemented with 10 U/mL heparin (Sigma–Aldrich Co., St. Louis, MO), 100 U/mL penicillin–streptomycin solution and 150 µg/mL endothelial cell growth factor (bECGF). All experiments used rBCECs cells in the third passage. A549 cells from the American Type Culture Collection (ATCC) (Manassas, VA) were maintained in DMEM supplemented with 10% FBS and antibiotics (100 U/mL, penicillin–streptomycin) at 37 °C in 5% CO_2 . Experiments were performed at least 3 times.

2.4. Cell viability assessment

The activity of mitochondrial dehydrogenase, a critical measure of mitochondrial function, and cellular toxicity, was determined according to a protocol previously described. Briefly, rBCECs or A549 cells at 90% confluence were cultured with different concentrations of fullerene derivative nanoparticles (10, 50, 100 µM) for 24 h. The medium was then replaced with fresh medium containing 50 µM H_2O_2 (Chemical Reagents Co., Beijing). After treatment with H_2O_2 for 2 h, cells were washed three times with PBS. The mitochondria's ability to reduce a tetrazolium salt to a formazan dye was used to assess mitochondrial dehydrogenase activity. Briefly, a certain volume of solution containing tetrazolium salt (available in the CCK-8 Kit from Dojindo Laboratories, Japan) was added to the culture medium. After incubation for 1.5 h at 37 °C, the absorbance at 450 nm was read using a Bio-Rad 680 microplate reader (Bio-Rad, Hercules, CA). Measurement for each treatment was repeated in triplicate.

2.5. Measurement of mitochondrial membrane potential

The fluorescent potentiometric dye JC-1 is a cationic carbocyanine compound that accumulates in mitochondria and can be used to measure the mitochondrial membrane potential ($\Delta\Psi_m$). In intact cells, JC-1 accumulates in the mitochondria as aggregates and exhibits a fluorescence emission shift from green (~525 nm), the

monomeric form, to red (~ 600 nm), the aggregate. When viewed under a fluorescence microscope, JC-1 is seen as a green monomer in the cytosol and as a red aggregate in respiring mitochondria. Mitochondrial damage is measured as a reduction in $\Delta\Psi_m$, i.e. a decrease in the red/green fluorescence ratio.

A549 or rBCECs cells (1.0×10^5 cells/ml), treated with fullerene derivative nanoparticles and H_2O_2 as described above, were labeled with $3 \mu M$ JC-1 for 20 min in a $37^\circ C$ incubator (5% CO_2). After cells were washed three times with PBS, the fluorescence was detected using a laser confocal scanning microscope (Olympus FV 500). The JC-1 monomer was detected at a 530-nm emission wavelength. The fluorescence of the JC-1 aggregate was measured at 590 nm emission. The cells were also stained with Hoechst 33258 to show the nuclei as blue. Cells treated with H_2O_2 only were used as the positive control.

2.6. Measurement of intracellular ROS concentration

CM- H_2 DCFDA was used to measure intracellular ROS production as previously reported [24]. A549 or rBCECs cells were treated with fullerene derivative nanoparticles and H_2O_2 as described above for measurement of mitochondrial dehydrogenase activity. After treatment, the samples were incubated with $5 \mu M$ CM- H_2 DCFDA at $37^\circ C$ for 30 min in the dark, washed three times with PBS, and then analyzed using a FACSCalibur flow cytometer (Becton Dickinson, San Jose, CA). The 488-nm excitation and 515-nm emission wavelengths were used to measure the fluorescence intensity of CM- H_2 DCFDA. Negative controls (without $50 \mu M$ H_2O_2 and $100 \mu M$ nanoparticles) and positive controls (with $50 \mu M$ H_2O_2 and without nanoparticles) were included in the treatment groups with $100 \mu M$ nanoparticles. Data are representative of three experiments.

2.7. Electron spin resonance (ESR) spectroscopic measurements

All ESR measurements were carried out at ambient temperature ($27^\circ C$) using a Varian E-109 X-Band ESR Spectrometer (Varian Inc., Palo Alto, CA). To analyze the free radical-scavenging capability of fullerene derivatives, cell-free radical producing systems were used for measurement of DPPH $^\bullet$, superoxide radical anion, hydroxyl radical and singlet oxygen. In addition, lipid peroxidation was measured using a cell-free, *in vitro* system. The concentration of fullerene derivatives nanoparticles was varied in order to determine the maximal scavenging efficacy for each radical studied. Each experiment was repeated at least three times.

2.8. DPPH $^\bullet$ scavenging activity

DPPH $^\bullet$ is a stable, nitrogen-centered free radical. While DPPH $^\bullet$ has no involvement in physiological processes, attenuation of the ESR signal for DPPH $^\bullet$ is one of the methods widely used to demonstrate a chemical's ability to scavenge free radicals through donation of a hydrogen atom or, in some cases, electron transfer [25]. The effect of each fullerene derivative on the ESR spectrum of DPPH $^\bullet$ was examined. All samples contained $100 \mu M$ DPPH $^\bullet$ in a mixture of 20% ethanol in PBS. To examine scavenging of DPPH $^\bullet$, samples also contained $100 \mu M$ of the selected fullerene derivative. ESR spectra were recorded 5 min after addition of the fullerene derivative. Spectra were obtained using 15 mW incident microwave power and 100 kHz field modulation of 2 G. The scavenging effect was determined by comparison with a control group lacking nanoparticles.

2.9. Superoxide radical anion ($O_2^{\bullet -}$) scavenging activity

BMPO was used to trap and detect $O_2^{\bullet -}$ by ESR spectroscopy. Superoxide radical anion was generated using the xanthine/xanthine oxidase system. The scavenger-radical reaction was initiated by addition of xanthine oxidase solution (XOD). The reaction contained $100 \mu M$ xanthine, 20 mM BMPO, $50 \mu M$ DTPA, 0.1 U/ml XOD and $150 \mu M$ of a fullerene derivative. The ESR spectra were recorded at 1.5 min after initiating the generation of $O_2^{\bullet -}$ by addition of XOD. The following instrument settings were used for collecting ESR spectra: microwave power of 10 mW, field modulation frequency of 100 kHz, and modulation amplitude of 1 G.

2.10. Hydroxyl radical (HO^\bullet) scavenging activity

Interception of hydroxyl radicals by each fullerene derivative was determined by the ESR spin-trapping technique [26]. The ESR assay was based on the competition between the trapping agent, DEPMPO, and the fullerene derivative nanoparticles for HO^\bullet . Hydroxyl radicals were generated by the classical Fenton reaction with the reaction mixture containing freshly prepared $500 \mu M$ DEPMPO, $20 \mu M$ $FeSO_4$ ($1000 \mu M$ stock solution, freshly made) and $200 \mu M$ H_2O_2 with or without $100 \mu M$ of a fullerene derivative. The ESR data were collected at ambient temperature, 2 min after initiating the formation of HO^\bullet by addition of $FeSO_4$. Spectra were recorded using the same spectrometer settings as those used for detecting $O_2^{\bullet -}$.

2.11. Singlet oxygen (1O_2) scavenging activity

The spin trap TEMP was used to determine the three nanoparticles' abilities to scavenge 1O_2 . Singlet oxygen was generated by photoexcitation of Rose Bengal at 560 nm. ESR data were collected for samples containing 10 mM TEMP and 0.1 mM

Rose Bengal with or without fullerene nanoparticles (0.2 mM). Samples were irradiated at ambient temperature in the ESR microwave cavity using a 1-kW xenon lamp (Schoeffel, Kratos Inc., Westwood, NJ) with a single monochromator (GM 252, Schoeffel, Kratos Inc., Westwood, NJ) set at 560 nm. The instrument settings for obtaining ESR spectra of the TEMP- 1O_2 adduct were: 15 mW microwave power and 1 G field modulation. The time dependence of the ESR signal for the formation of the TEMP- 1O_2 adduct was measured using the time dependent intensity of the center line of the ESR spectrum during irradiation of the sample (typically 30 min).

2.12. Inhibition of lipid peroxidation

The effects of fullerene derivatives on peroxidation of lipids in liposomes were measured using ESR oximetry. The ESR oximetry measurement is based on changes in the relaxation time of the spin probe due to the bimolecular collision of O_2 with the spin probe. Because O_2 is paramagnetic, this collision results in spin exchange between O_2 and the spin probe, resulting in shorter relaxation times (both T_1 and T_2). Consequently, at higher concentrations of dissolved O_2 , broader ESR signals are observed for the spin probe [27,28]. Since the integrated area of the ESR signal over the scanning range is unaffected by these effects on the relaxation times, broadening of the spin probe's ESR signal is necessarily accompanied by a decrease in the peak height of the ESR signal. This can be readily seen for the ESR signal measured for ^{15}N -Tempone (^{15}N -PDT) under N_2 and O_2 atmospheres (Fig. 7A). When the ESR signal is measured under a N_2 atmosphere, a narrower, line width and higher peak intensity is observed compared to measurement of the ESR signal under an O_2 atmosphere. Under conditions where the levels of dissolved O_2 vary, a time dependent decrease in line width and increase in the peak intensity of the ESR signal indicate continuous O_2 consumption.

Liposomes were prepared as previously described [27]. Briefly, a suspension of 30 mg/mL egg PC liposomes, 0.1 mM ^{15}N -Tempone (^{15}N -PDT) with or without fullerene derivatives (0.2 mM $Gd@C_{82}(OH)_{22}$, 0.2 mM $C_{60}(OH)_{22}$ or 0.3 mM $C_{60}(C(COOH)_2)_2$) was added to a capillary tube. The lipid peroxidation was initiated by adding 25 mM AAPH, which is known to strongly induce lipid peroxidation in cellular and reconstituted membranes [26]. The capillary tube was then sealed and positioned in the ESR instrument. ESR spectra were then recorded at 4 min intervals for 24 min. Signals were obtained with a 1 G scanning width, 1 mW incident microwave power and with 100 kHz field modulation. All ESR spectra were recorded at the low field line of ^{15}N -Tempone (^{15}N -PDT) and at $37^\circ C$.

2.13. Statistical analysis

All data are expressed as the mean \pm S.D. For analysis of results from studies on cultured cells, the unpaired Student's *t* test was applied to identify significant differences between the groups treated with fullerene derivatives and non-treated as controls. For the ESR experiments, a one-way analysis of variance (ANOVA) followed by a *post hoc* Fisher protected least-significant-difference test was applied. $P < 0.05$ was considered to be a significant difference.

3. Results

3.1. Characterizations

Prior to studies on the scavenging of ROS, field emission scanning electron microscopy (FE-SEM) was employed for characterization of $Gd@C_{82}(OH)_{22}$, $C_{60}(OH)_{22}$, and $C_{60}(C(COOH)_2)_2$ in PBS solution (Fig. 1). These fullerene derivatives readily aggregate and form nanoparticles in aqueous solution. To further investigate their particle sizes in the matrix used for biological experiments and ESR studies, we measured their size distribution in physiological saline using dynamic light scattering (DLS). The DLS data closely match with those obtained by SEM. The average diameter of $Gd@C_{82}(OH)_{22}$, $C_{60}(OH)_{22}$, and $C_{60}(C(COOH)_2)_2$ nanoparticles determined by DLS are 78 ± 5.3 , 123 ± 14.2 , and 170 ± 14.7 nm, respectively. Thus, nanoparticles formed from fullerene encapsulating Gd (i.e. $Gd@C_{82}(OH)_{22}$) are significantly smaller than nanoparticles from metal-free fullerenes (i.e. $C_{60}(OH)_{22}$, and $C_{60}(C(COOH)_2)_2$). As seen in Fig. 1, the UV-Vis spectra of hydroxylated fullerenes ($Gd@C_{82}(OH)_{22}$ and $C_{60}(OH)_{22}$) differ significantly from the spectra of $Gd@C_{82}$ and C_{60} . C_{60} exhibit a marked absorption band with a maximum at 340 nm, while $Gd@C_{82}$ shows an obvious shoulder at 310–330 nm. Concentration dependent changes in the DLS data (data not shown) and UV spectroscopy of aqueous solutions of these water-soluble fullerenes revealed evidence of the formation of aggregates or clusters at the concentration of $200 \mu M$.

3.2. Protective effect against cellular oxidative stress

The protective effects of water-soluble fullerene derivatives were investigated using two cellular systems. Treatment of A549 cells or rBCECs with 50 μM H_2O_2 for 2 h resulted in significant cellular toxicity, measured as loss of mitochondrial dehydrogenase activity (Fig. 2). Pretreatment with fullerene derivatives, 24 h prior to addition of H_2O_2 , resulted in protection against cellular toxicity (Fig. 2). Concentration dependent protection against cytotoxicity was observed following treatment with each of the fullerene derivatives. The protective effects of the fullerenes against cytotoxicity are further summarized in Table 1. As shown in Fig. 2 and summarized in Table 1, $\text{Gd@C}_{82}(\text{OH})_{22}$ nanoparticles exhibit the greatest protective effects against H_2O_2 -induced cytotoxicity, followed by $\text{C}_{60}(\text{OH})_{22}$ nanoparticles, with $\text{C}_{60}(\text{C}(\text{COOH})_2)_2$ nanoparticles the least protective.

The fullerene derivatives were also evaluated for their ability to protect against H_2O_2 -induced mitochondrial damage measured as a reduction in the mitochondrial membrane potential ($\Delta\Psi_{\text{m}}$). In cells untreated with H_2O_2 , the JC-1 probe was seen primarily as red aggregates, indicating substantial uptake by respiring mitochondria

(Fig. 3A). For both rBCECs and A549 cells, treatment with 50 μM H_2O_2 for 2 h resulted in a decrease in red aggregates of the JC-1 probe in mitochondria and an increase in green monomers of the JC-1 probe in the cytoplasm (Fig. 3B). This result demonstrates H_2O_2 -induced mitochondrial damage and a reduction in $\Delta\Psi_{\text{m}}$. Samples pre-treated with 100 $\mu\text{mol/L}$ $\text{C}_{60}(\text{C}(\text{COOH})_2)_2$, $\text{C}_{60}(\text{OH})_{22}$, and $\text{Gd@C}_{82}(\text{OH})_{22}$ demonstrate an increase in red fluorescence compared to the untreated. Pretreating cells with $\text{Gd@C}_{82}(\text{OH})_{22}$ nanoparticles (Fig. 3E) resulted in partial restoration of mitochondrial uptake of the JC-1. The restoration of mitochondrial uptake observed following pretreatment with $\text{Gd@C}_{82}(\text{OH})_{22}$ was higher than that observed following pretreatment with $\text{C}_{60}(\text{C}(\text{COOH})_2)_2$ (Fig. 3C) or $\text{C}_{60}(\text{OH})_{22}$ (Fig. 3D). This result indicates that $\text{Gd@C}_{82}(\text{OH})_{22}$ protects against oxidative injury to cellular mitochondria better than $\text{C}_{60}(\text{C}(\text{COOH})_2)_2$ and $\text{C}_{60}(\text{OH})_{22}$ fullerene derivatives.

The total intracellular levels of ROS, resulting from treatment of cells with 50 μM H_2O_2 for 2 h, was measured by flow cytometry in A549 cells and rBCECs cells labeled with CM- H_2DCFDA . Fig. 4 shows the effects of $\text{C}_{60}(\text{C}(\text{COOH})_2)_2$, $\text{C}_{60}(\text{OH})_{22}$, and $\text{Gd@C}_{82}(\text{OH})_{22}$ nanoparticles on the levels of H_2O_2 -induced intracellular ROS.

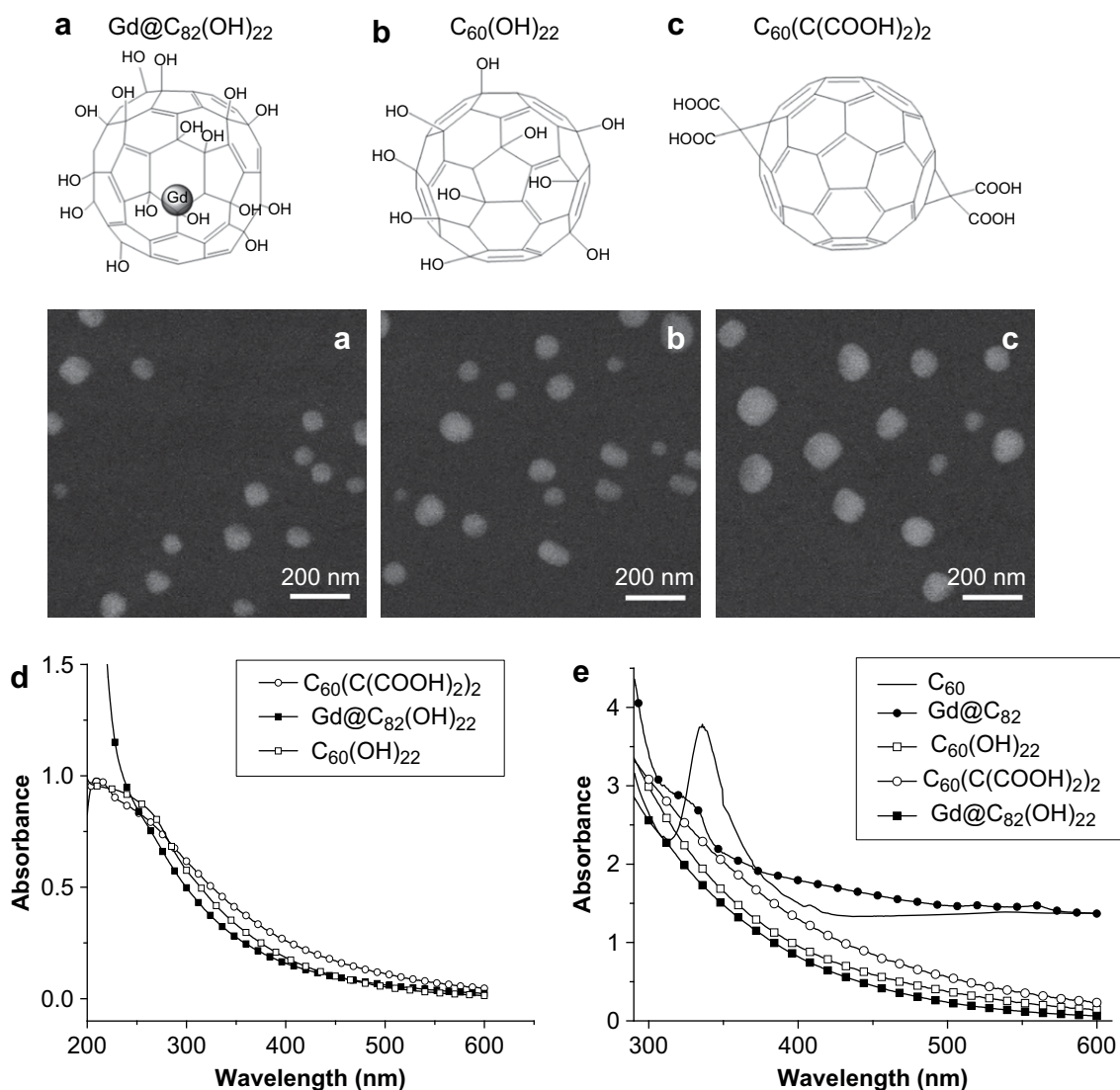


Fig. 1. Structures and FE-SEM images of the three fullerenes: (a) $\text{Gd@C}_{82}(\text{OH})_{22}$, (b) $\text{C}_{60}(\text{OH})_{22}$, (c) $\text{C}_{60}(\text{C}(\text{COOH})_2)_2$, and (d) UV-Vis absorption spectra of water-soluble fullerenes: ($\text{Gd@C}_{82}(\text{OH})_{22}$, $\text{C}_{60}(\text{OH})_{22}$, and $\text{C}_{60}(\text{C}(\text{COOH})_2)_2$ at 200 μM in PBS solution and (e) UV-Vis absorption spectra of $\text{Gd@C}_{82}(\text{OH})_{22}$, $\text{C}_{60}(\text{OH})_{22}$, $\text{C}_{60}(\text{C}(\text{COOH})_2)_2$, Gd@C_{82} , and C_{60} . Gd@C_{82} and C_{60} were prepared at 1 mM in toluene solutions.

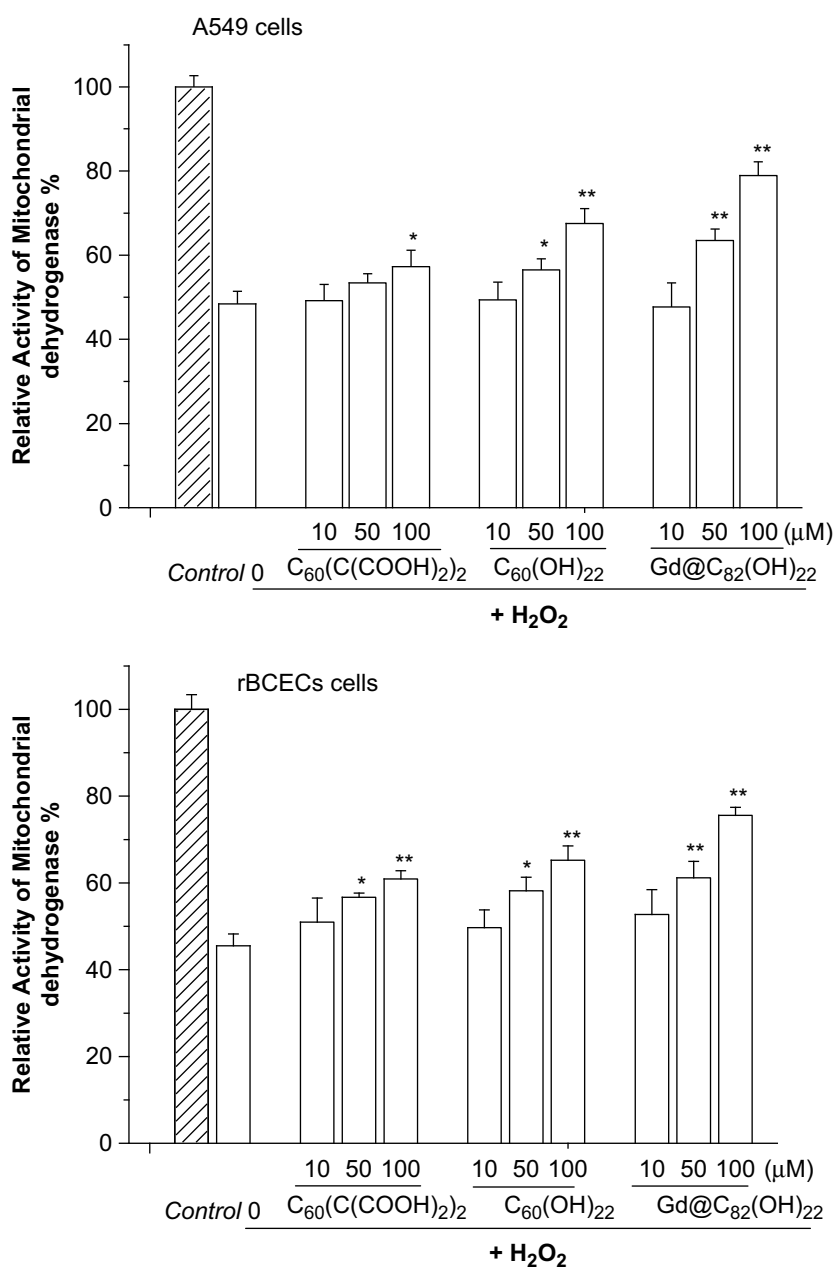


Fig. 2. Protective effects of three fullerene derivatives: Gd@C₈₂(OH)₂₂, C₆₀(OH)₂₂, and C₆₀(C(COOH)₂)₂ against H₂O₂-induced damage in A549 cells and rBCECs cells. The cells were treated with 10–100 μM fullerene derivatives before incubation with 50 μM H₂O₂. **P* < 0.05 and ***P* < 0.01 vs. H₂O₂-treated control.

Treatment of rBCECs or A549 cells with H₂O₂ resulted in a significant increase in intracellular ROS. Pretreatment with nanoparticles

Table 1

Comparison of protective effects of three fullerene derivatives Gd@C₈₂(OH)₂₂, C₆₀(OH)₂₂, and C₆₀(C(COOH)₂)₂ on H₂O₂-induced cytotoxicity and intracellular ROS generation in A549 cells or rBCEC cells.

Percentage of inhibition (%)	Cell viability		Total ROS Level	
	A549	rBCECs	A549	rBCECs
Gd@C ₈₂ (OH) ₂₂	59.1 ± 3.3	54.1 ± 1.9	94.6 ± 2.6	93.5 ± 3.4
C ₆₀ (OH) ₂₂	37.1 ± 3.5	35.5 ± 3.3	74.1 ± 3.5	72.7 ± 2.9
C ₆₀ (C(COOH) ₂) ₂	17.2 ± 3.8	27.8 ± 1.9	47.2 ± 2.2	20.4 ± 1.8

Note: For measuring effects on cell viability, the cells were treated with 100 μmol/ml fullerene derivatives before incubation with 50 μM H₂O₂. Cell viability was assessed by measurement of mitochondrial dehydrogenase activity. For measurement of intracellular ROS, the same conditions for incubation with H₂O₂ were used. Levels of intracellular ROS were determined by flow cytometry.

of fullerene derivatives significantly reduced the levels of H₂O₂-induced ROS in both cell types. Pretreatment with Gd@C₈₂(OH)₂₂ or C₆₀(OH)₂₂ nanoparticles resulted in greater reduction of H₂O₂-induced intracellular ROS levels than pretreatment with C₆₀(C(COOH)₂)₂ nanoparticles (Fig. 4 and Table 1). The effects of three fullerene derivatives on levels of intracellular ROS are further summarized in Table 1. The results shown in Table 1 demonstrate a correlation between the cellular protective effects of fullerene derivatives and their ability to scavenge intracellular ROS. Hydroxylated fullerenols were stronger ROS scavenger than malonic acid derivatives.

3.3. DPPH[•] radical-scavenging activities

To determine whether or not these fullerene derivatives can scavenge nitrogen-centered radicals, experiments were performed using the stable, nitrogen-centered free radical, DPPH[•]. The effects

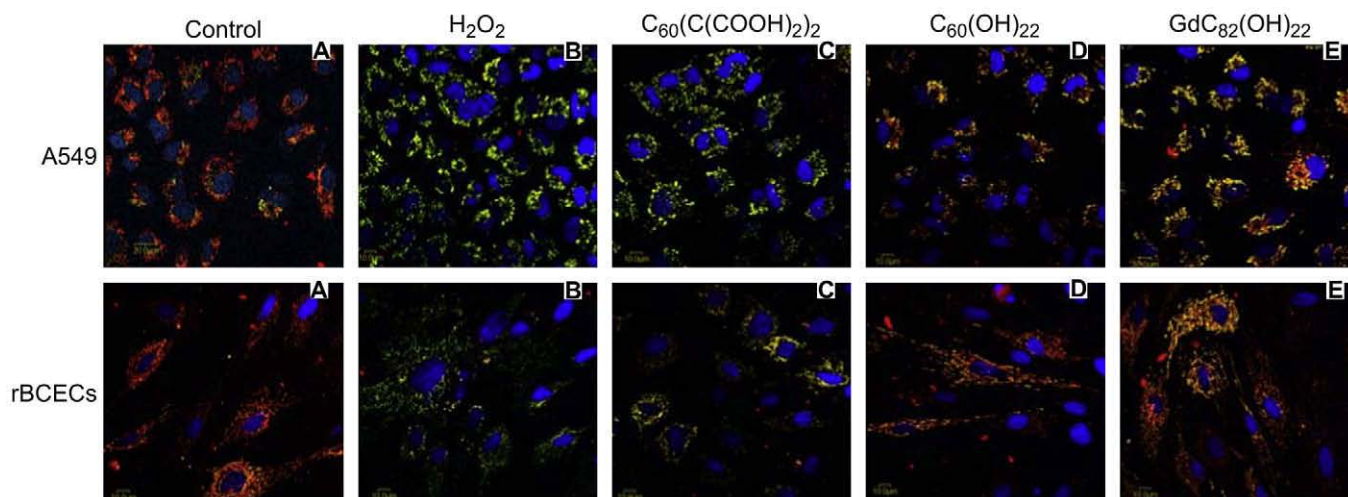


Fig. 3. The protective effects three fullerene derivatives $\text{Gd@C}_{82}(\text{OH})_{22}$, $\text{C}_{60}(\text{OH})_{22}$, and $\text{C}_{60}(\text{C}(\text{COOH})_2)_2$ against H_2O_2 -induced mitochondrial damage in A549 cells, and rBCEC cells. The cells were treated with $100\ \mu\text{M}$ fullerene derivatives before incubation with $50\ \mu\text{M}$ H_2O_2 . Aggregation of the dye, JC-1, seen as red fluorescence, indicates integrity of the mitochondrial membrane.

of the three water-soluble fullerene derivatives on the ESR spectra of DPPH $^{\bullet}$ are shown in Fig. 5A. A characteristic one-line spectrum was obtained for solutions of $100\ \mu\text{M}$ DPPH $^{\bullet}$ in 20% ethanol. A reduction in signal intensity was associated with the addition of any of the three fullerene derivatives. However, the radical-scavenging activity of the fullerene derivatives differed. $\text{Gd@C}_{82}(\text{OH})_{22}$ was significantly more efficient in quenching DPPH $^{\bullet}$ than $\text{C}_{60}(\text{OH})_{22}$. $\text{C}_{60}(\text{C}(\text{COOH})_2)_2$ had the weakest ability in scavenging DPPH $^{\bullet}$. All fullerenes were present at a concentration of $100\ \mu\text{M}$. The inhibitory effects of three fullerene derivatives are further summarized in Table 2. As shown in Fig. 5 and summarized in Table 2, $\text{Gd@C}_{82}(\text{OH})_{22}$ nanoparticles exhibit the highest capability to eliminate DPPH $^{\bullet}$ radical, followed by $\text{C}_{60}(\text{OH})_{22}$ nanoparticles, with $\text{C}_{60}(\text{C}(\text{COOH})_2)_2$ nanoparticles the least effective ($P < 0.05$).

3.4. Superoxide radical anion ($\text{O}_2^{\bullet-}$) scavenging capability

The relative scavenging abilities of the fullerene derivatives for $\text{O}_2^{\bullet-}$, generated by the xanthine/xanthine oxidase system, are seen in Fig. 5B. The typical ESR spectrum for the spin adduct between $\text{O}_2^{\bullet-}$ and the spin trap, BMPO, was observed. All of the fullerene derivatives, at a final concentration of $150\ \mu\text{M}$, reduced the spin adduct's signal intensity. The relative scavenging abilities of the fullerenes for $\text{O}_2^{\bullet-}$ were similar to those observed for scavenging of DPPH $^{\bullet}$, i.e. $\text{Gd@C}_{82}(\text{OH})_{22} \approx \text{C}_{60}(\text{OH})_{22} > \text{C}_{60}(\text{C}(\text{COOH})_2)_2$. The inhibitory effects of three fullerene derivatives are further summarized in Table 2.

3.5. Hydroxyl radical (HO^{\bullet}) scavenging capability

Hydroxyl radicals were generated by the classical Fenton reaction involving the reaction of FeSO_4 and H_2O_2 [29]. The Fenton reaction was started by the addition of $\text{Fe}(\text{II})$ ($200\ \mu\text{M}$ final concentration), $200\ \mu\text{M}$ H_2O_2 and $500\ \mu\text{M}$ DEPMPO. The signal intensity of the spin adduct was reduced by addition of each fullerene derivative at a final concentration of $100\ \mu\text{M}$ (Fig. 5C). The relative efficiencies for quenching the HO^{\bullet} were similar to those observed for quenching DPPH $^{\bullet}$ and $\text{O}_2^{\bullet-}$. Reductions in signal intensities were approximately 55%, 67% and 88% for $\text{C}_{60}(\text{C}(\text{COOH})_2)_2$, $\text{C}_{60}(\text{OH})_{22}$ and $\text{Gd@C}_{82}(\text{OH})_{22}$, respectively. The inhibitory effects of three fullerene derivatives are further summarized in Table 2.

3.6. Singlet oxygen ($^1\text{O}_2$) scavenging activity

The spin trap TEMP was used to demonstrate the ability of $\text{Gd@C}_{82}(\text{OH})_{22}$, $\text{C}_{60}(\text{OH})_{22}$, and $\text{C}_{60}(\text{C}(\text{COOH})_2)_2$ to scavenge $^1\text{O}_2$. These three fullerene derivatives exhibit UV–Visible spectral absorption in the range of 200–350 nm (Fig. 1D). To avoid photo-excitation of these compounds, singlet oxygen was generated by irradiation of Rose Bengal at 560 nm for 30 min. In the presence of TEMP, the ESR signal of TEMPO adduct was observed (Fig. 6). The ESR signal of TEMPO adduct intensity was reduced by addition of each of the fullerene derivatives (Fig. 6). Again, $\text{Gd@C}_{82}(\text{OH})_{22}$ showed the strongest inhibition and $\text{C}_{60}(\text{C}(\text{COOH})_2)_2$ exhibited the least. The efficiencies of $\text{C}_{60}(\text{C}(\text{COOH})_2)_2$, $\text{C}_{60}(\text{OH})_{22}$ and $\text{Gd@C}_{82}(\text{OH})_{22}$ in inhibiting formation of TEMPO are 9.1%, 38.2%, and 58.2%, respectively (Table 2).

3.7. Inhibition of lipid peroxidation in liposomes

2,2'-Azobis(2-amidinopropane) dihydrochloride (AAPH) is a strong inducer of lipid peroxidation [27]. The impact of radical-scavenging activity by the fullerene nanoparticles was further examined by measuring the ability of fullerene nanoparticles to inhibit lipid peroxidation induced by AAPH. Free radicals, generated through the decomposition of AAPH, produce a time dependent peroxidation of polyunsaturated lipids in liposomes. Using ESR oximetry, the consumption of oxygen accompanying lipid peroxidation is measured as a time dependent narrowing of the ESR signal for the spin probe, ^{15}N -Tempone. Since the area beneath the signal intensity vs. magnetic field curve remains constant, this narrowing of the ESR signal is necessarily accompanied by an increase in the peak height of the ESR signal within the scanning range (Fig. 7A). $25,000\ \mu\text{M}$ AAPH was added to initiate the lipid peroxidation. The control sample, with egg PC alone, showed a sharp spectral peak for ^{15}N -Tempone, while addition of fullerene derivatives resulted in lower consumption rates of oxygen seen as smaller peak heights in the ESR signal due to lower rates of line narrowing of the spin probe. Addition of $\text{Gd@C}_{82}(\text{OH})_{22}$ (Fig. 7B) resulted in strongest inhibition of lipid peroxidation measured as retardation of line narrowing, and corresponding retardation in the growth of the ESR signal's intensity, compared to $\text{C}_{60}(\text{C}(\text{COOH})_2)_2$ and $\text{C}_{60}(\text{OH})_{22}$ (Fig. 7B). The inhibitory effects of three fullerene derivatives on lipid peroxidation are further summarized in Table 2.

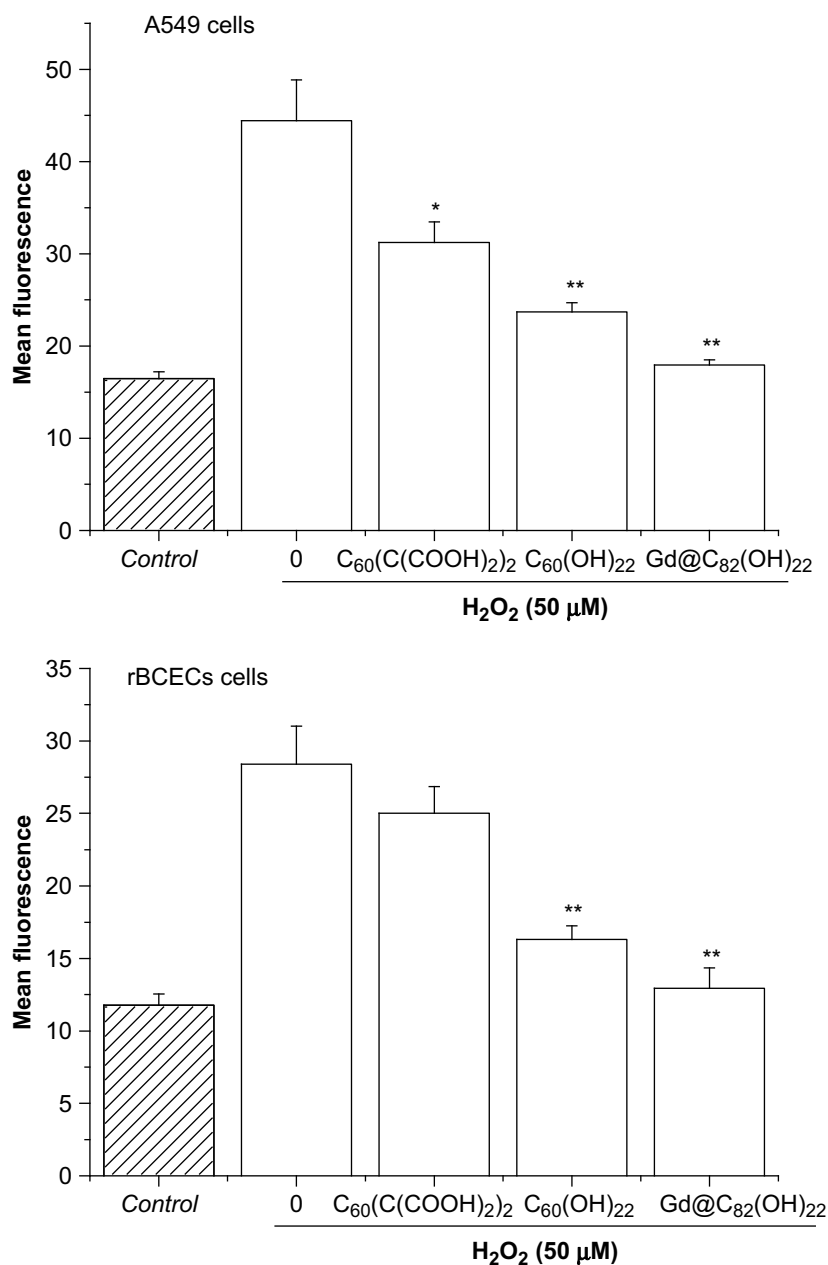


Fig. 4. Protective effects of fullerene derivatives, $Gd@C_{82}(OH)_{22}$, $C_{60}(OH)_{22}$, and $C_{60}(C(COOH)_2)_2$, against H_2O_2 -induced ROS generation in A549 cells or rBCECs cells. The cells were treated with 100 μM fullerene derivatives before incubation with 50 μM H_2O_2 . * $P < 0.05$ and ** $P < 0.01$ vs. H_2O_2 -treated control.

4. Discussion

In this study we employ ESR techniques to systematically provide direct evidence that $Gd@C_{82}(OH)_{22}$, $C_{60}(OH)_{22}$, and $C_{60}(C(COOH)_2)_2$ nanoparticles can effectively scavenge different types of free radicals/ROS. This represents the first report that several different types of fullerene derivatives can scavenge all physiologically relevant ROS. Consistent with these results, we also determined that these fullerene derivatives can inhibit lipid peroxidation. Our study also shows that these nanoparticles protect A549 cells and normal rBCECs against H_2O_2 -induced cytotoxicity (Figs. 2–4).

In contrast to water-soluble C_{60} derivatives, nanoparticles of underivatized C_{60} appear to lack significant cytoprotective properties. Indeed, investigators have shown that underivatized C_{60} can elicit cytotoxicity, the formation of ROS and lipid peroxidation

[30–34]. Sayes et al. have reported that aqueous suspensions containing nanoparticles of underivatized C_{60} are cytotoxic to human dermal fibroblasts at low levels ($LC_{50} = 20$ ppb) and can generate ROS such as O_2^- [33]. Sayes et al. have also observed that the cytotoxicity of underivatized C_{60} is associated with lipid peroxidation [33]. It is noteworthy that derivatization of the fullerene cage with carboxyl and hydroxyl groups results in a dramatic decrease in the cytotoxicity and generation of ROS [33,34].

We have demonstrated that Gd-encaged fullerenes are much stronger ROS scavenger than hollow fullerenes, though they all can intercept all of the major physiologically relevant ROS. These radical-scavenging abilities of fullerenes may be attributed to several molecular properties. Foremost is the large electron affinity of fullerenes. The electron affinity of C_{60} has been reported to be 2.7 eV while the larger fullerene, C_{82} , has an electron affinity of 3.14 eV [35,36]. Insertion of Gd into the C_{82} fullerene further

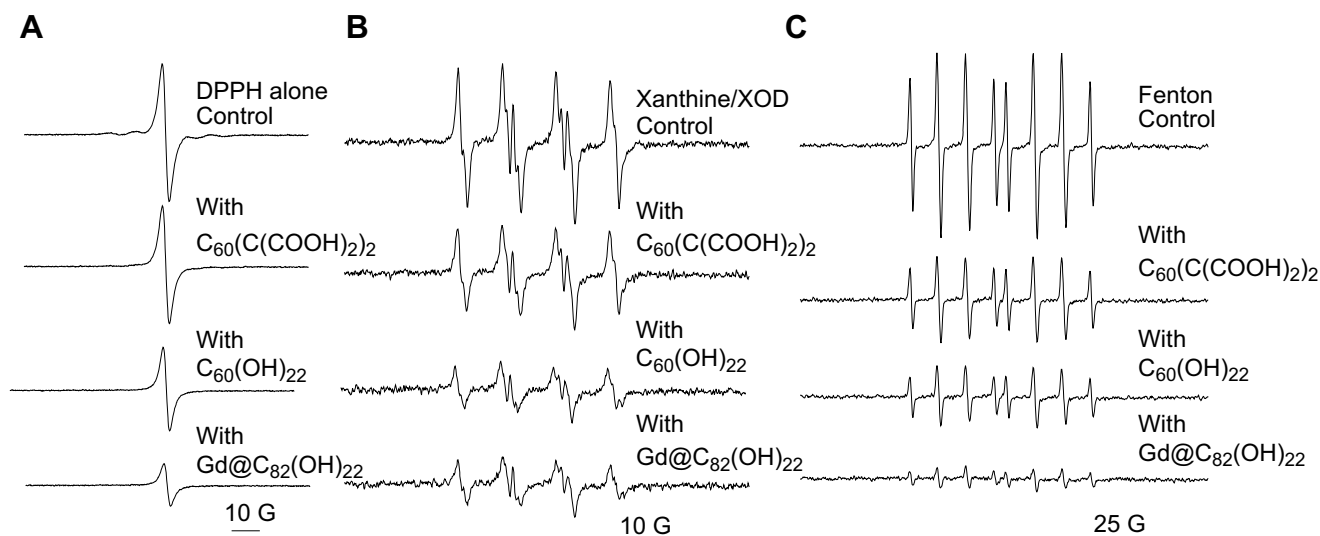


Fig. 5. Scavenging of DPPH[•] (A), superoxide radical anions (B) and hydroxyl radicals (C) by three fullerenes, C₆₀(C(COOH)₂)₂, C₆₀(OH)₂₂, and Gd@C₈₂(OH)₂₂. For DPPH[•] (A), samples contained 100 μM fullerenes, and 0.1 mM DPPH in 20% ethanol; and ESR spectra were recorded 5 min after sample mixing at room temperature. For superoxide radical anions (B), samples contained 20 mM BMPO, with and without 150 μM fullerenes, mixed with 1 mM xanthine, 0.05 mM DTPA and 0.1 unit/ml xanthine oxidase. Data were recorded 1.5 min after addition of XOD at room temperature. For hydroxyl radicals (C), samples contained 0.5 mM DEPMPO, with and without 100 μM fullerenes, 0.2 mM H₂O₂ and 0.02 mM Fe²⁺. Data were recorded 5 min after addition of Fe²⁺ at room temperature.

increases the electron affinity. Boltalina et al. have measured the electron affinity of Gd@C₈₂ to be 3.3 ± 0.1 eV [36]. Differences in electron affinities may contribute to the relative efficiencies (Gd@C₈₂(OH)₂₂ > C₆₀(OH)₂₂ > C₆₀(C(COOH)₂)₂) which we observe for radical scavenging and cytoprotection. Adding to the effects of electron affinity is the large polarizability of fullerenes, which further facilitates attachment of electrons and radicals to the nanosurface of fullerenes [37]. A second factor contributing to broad-based radical-scavenging activity is derivatization of the fullerene's nanosurface. Ali et al. have demonstrated that derivatizing a C₆₀ fullerene with *tris*-malonic acid results in electron deficient areas on the fullerene's surface which facilitates binding of O₂^{•−} [38]. Binding of a second O₂^{•−} to an adjacent electron deficient area results in destruction of O₂^{•−}, production of H₂O₂, and regeneration of the fullerene in a reaction similar to that catalyzed by superoxide dismutase. Derivatizing with hydroxyl groups similarly induces electron deficient areas on the fullerene's surface and may lead to similar catalytic activity for polyhydroxylated fullerenes such as [Gd@C₈₂(OH)₂₂]_n. Indeed, the potent scavenging of O₂^{•−} that we and other investigators have observed strongly suggests that polyhydroxylated fullerenes possess a superoxide dismutase activity [16,38]. A similar catalytic sequence of events appears to result in scavenging of ¹O₂ by fullerenes. Although fullerenes are not good substrates for oxidation by ¹O₂, we and others have observed that they are efficient quenchers of ¹O₂ [39,40]. While the mechanism is not yet completely elucidated, it appears that association of O₂ with the fullerene surface, which has been reported by several investigators, is the initial step in

deactivation of ¹O₂ by fullerenes [41,42]. Binding of ¹O₂ is accompanied by formation of a charge-transfer complex leading to deactivation of ¹O₂. It has been reported that the rate of deactivation of ¹O₂ by endohedral metallofullerenes, such as Ce@C₈₂, is similar to the diffusion controlled rate for quenching ¹O₂ in benzene [40]. The scavenging of more reactive radicals, such as HO[•], is expected to be mechanistically simpler, involving

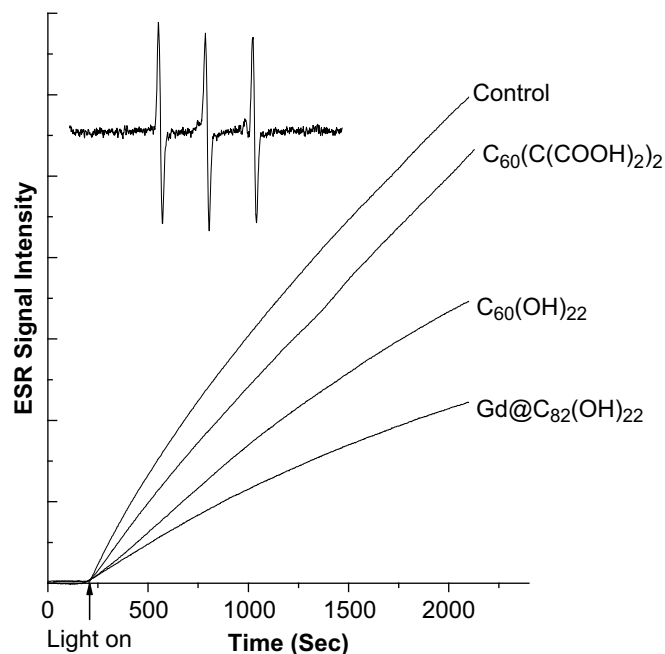


Fig. 6. Time dependence of ESR signal for the formation of TEMP-¹O₂ adducts. ¹O₂ was generated by irradiation of Rose Bengal with visible light (560 nm) at ambient temperature. Samples contained 10 mM TEMP and 0.1 mM Rose Bengal, with and without a fullerene derivative (200 μM). The inset is the ESR spectrum of the TEMP-¹O₂ adduct observed in all the cases. The time scans of ESR signal intensity were obtained with fixed field position (the peak position of the center line of ESR spectrum), 15 mW microwave power and 1 G field modulation.

Table 2

Scavenging of DPPH[•] radical, superoxide radical anion, singlet oxygen, hydroxyl radical, and inhibition of lipid peroxidation by three fullerene derivatives, C₆₀(C(COOH)₂)₂, C₆₀(OH)₂₂, and Gd@C₈₂(OH)₂₂.

Percentage of Scavenging or Inhibition (%)	DPPH [•]	O ₂ ^{•−}	¹ O ₂	OH [•]	Lipid peroxidation
Gd@C ₈₂ (OH) ₂₂	75	65.8	58.2	88.1	56.1
C ₆₀ (OH) ₂₂	45.5	65.8	38.2	66.7	44.6
C ₆₀ (C(COOH) ₂) ₂	13.6	31.6	9.1	54.8	39.2

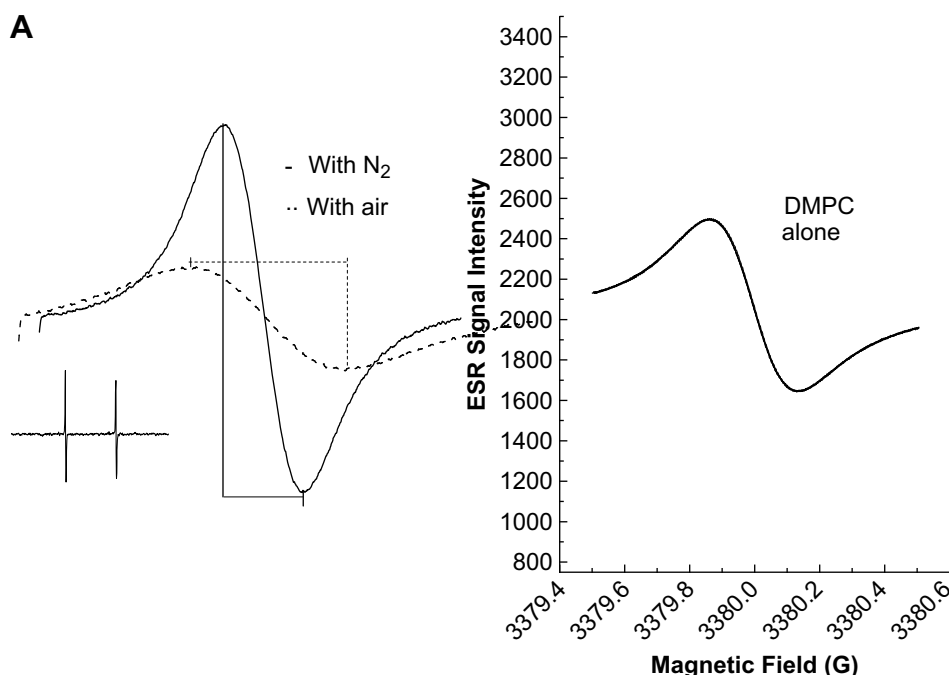


Fig. 7. Effect of fullerene derivatives on lipid peroxidation in liposomes. **A.** Oxygen consumption is measured in a closed chamber using liposome suspensions and the spin label ^{15}N -Tempone mixed with a free radical initiator such as AAPH. The left panel shows ESR spectra of the scans of the low field line of ^{15}N -Tempone in a nitrogen atmosphere (solid line) or air-saturated (broken line) aqueous solutions. The presence of oxygen results in a broader and less intense ESR signal for the spin probe. Lipid peroxidation was measured in the control experiment (left panel) with saturated lipid, DMPC, where there is no oxygen consumption because no lipid peroxidation involved. Spectra were recorded at 37°C ; 0.5 mW microwave power, 0.05 G modulation amplitude, and 1 G scanning range. **B.** Lipid peroxidation was inhibited by fullerene nanoparticles. Lipid peroxidation was assessed using ESR oximetry. The samples contained liposomes (30 mg/mL egg phosphatidylcholine) and 0.1 mM ^{15}N -Tempone (PD) spin label. Fullerene nanoparticles were also added to some samples (Panel a, no fullerene; Panel b, $300\ \mu\text{M}\ \text{C}_{60}(\text{C}(\text{COOH})_2)_2$; Panel c, $200\ \mu\text{M}\ \text{C}_{60}(\text{OH})_{20}$; Panel d $200\ \mu\text{M}\ \text{Gd}@\text{C}_{82}(\text{OH})_{22}$). Lipid peroxidation was initiated by adding 25 mM AAPH. After the sample was sealed in a capillary, the ESR spectrum was recorded 7 times at 4 min intervals with a Varian E-109 X-band spectrometer with a variable temperature controller accessory as described in the Experimental Section. Signals were obtained with 0.5 mW incident microwave power and with 0.05 G field modulation at 37°C . The progressive increases in peak to peak signal intensity (and accompanying progressive narrowing of line width) in each panel are due to time-dependent oxygen consumption resulting from lipid peroxidation. The inhibitory effects of fullerene nanoparticles on lipid peroxidation may be seen as smaller changes in peak to peak signal intensities seen in panels b, c and d compared to panel a.

stoichiometric addition of the radical to the fullerene [43]. Analogous scavenging of highly reactive radicals has been observed by Krusic et al. [44]. These investigators determined that one C_{60} molecule may scavenge as many as 15 benzyl radicals. This ability of certain water-soluble fullerenes to efficiently scavenge a wide range of reactive species has led to them being called “radical sponges” [45].

In addition to the mentioned molecular properties, supramolecular properties involving aggregation into nanoparticles/nanostructure may also contribute to the radical-scavenging capacity of water-soluble fullerenes. It is well established that the size and structure of nanoparticles of endohedral metallofullerenes, such as $\text{Gd}@\text{C}_{82}(\text{OH})_{22}$, affect their performance as MRI contrast agents [46]. This effect derives from the relationship between nanoparticle size, nanoparticle rotation rate in biological media and spin interactions resulting in MRI contrast enhancement [47]. However, little is known about the effects of nanoparticle size on the antioxidant and radical quenching activities of fullerenes. We determined that nanoparticles of $\text{Gd}@\text{C}_{82}(\text{OH})_{22}$, $\text{C}_{82}(\text{OH})_{22}$, and $\text{C}_{60}(\text{C}(\text{COOH})_2)_2$ differed in average size (78 nm, 123 nm and 170 nm, respectively). A suspension of larger nanoparticles would provide smaller total surface area for interaction with the biological environment, namely, provide less reactive sites for the ROS, thus reducing the efficiency of scavenging reactive species. This factor may contribute to the relative efficiencies (i.e., $\text{Gd}@\text{C}_{82}(\text{OH})_{22} \geq \text{C}_{82}(\text{OH})_{22} > \text{C}_{60}(\text{C}(\text{COOH})_2)_2$) we note in their cytoprotection, radical scavenging and inhibition of lipid peroxidation. In addition, size may influence the distribution of nanoparticles in cells and in tissues.

We have demonstrated the biological significance of fullerenes’ antioxidant and radical-scavenging activities by showing their ability to protect against oxidant-induced cytotoxicity and mitochondrial damage *in vitro*. The role of oxidative stress and damage in the etiology and progression of many diseases suggests that fullerenes may be valuable *in vivo* protective and therapeutic agents. Indeed, it has been shown that intraperitoneally injected nanoparticles of $\text{Gd}@\text{C}_{82}(\text{OH})_{22}$ are extremely effective in shrinking tumors induced by implantation of hepatoma cells in mice [18]. This therapeutic effect was correlated with lowering markers of tumor-induced oxidative stress [19]. Gharbi et al. have reported that intraperitoneally pre-treating mice with C_{60} resulted in reduced acute liver toxicity induced by CCl_4 [48]. This protective effect was attributed to antioxidant protection against CCl_4 -induced oxidative damage. Recently, Quick et al. have found that an orally administered carboxyfullerene derivative protected transgenic mice, which were deficient in superoxide dismutase [49]. Protective effects included increases in lifespan, learning, and memory. Biochemical measurements demonstrated a correlation between these observed protective effects and antioxidant protection. These studies, and others, demonstrate that the antioxidant activities of fullerenes are linked to protective and therapeutic effects. *In vitro* antioxidant and radical-scavenging activities, such as those reported here, may be viewed as easily measured surrogate markers for therapeutic effects. These profiles of a fullerene’s antioxidant activity should be valuable for developing highly effective fullerene derivatives for use in biomedicine.

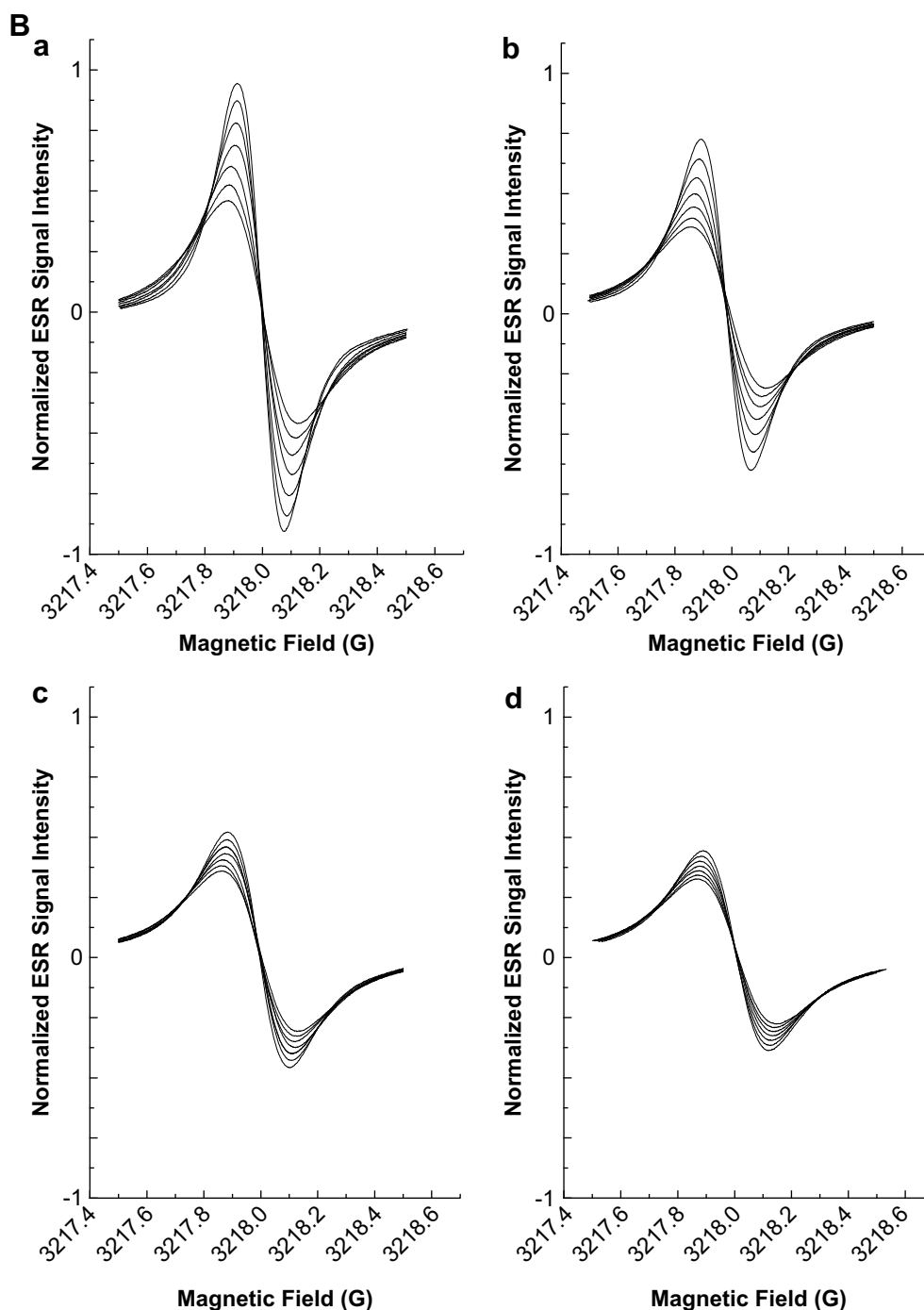


Fig. 7. (continued).

5. Conclusion

We investigated the protective effects of three fullerene nanomaterials as the inhibitors of reactive oxygen species (antioxidants and free radical scavengers). The ESR spin trap technique provided direct *in vitro* evidence that the three fullerene derivatives, gadolinium endohedral metallofullerenol ($\text{Gd}@\text{C}_{82}(\text{OH})_{22}$), fulleranol ($\text{C}_{60}(\text{OH})_{22}$), and carboxyfullerene ($\text{C}_{60}(\text{C}(\text{COOH})_2)_2$), can efficiently scavenge different types of free radicals and inhibit lipid peroxidation. Both of the reactive oxygen species and the nitrogen-centered free radical were intercepted by these fullerene materials. We demonstrated *in vitro* by using human lung adenocarcinoma cell line A549 or rat brain capillary endothelial cell line (rBCECs)

that they could reduce H_2O_2 -induced cytotoxicity, free radical formation and mitochondrial damage. These nanomaterials have great potential in biomedical applications, for examples, gadolinium endohedral metallofullerenols can be used for both of MRI imaging and chemotherapy. The present findings provide a molecular basis of the diseases for which oxidative stress may play a key role.

Acknowledgements

This work is financially supported by the Chinese Academy of Sciences (CAS) "Hundred Talents Program" (07165111ZX), the National Basic Research Program of China (2006CB705603,

2007CB935604), the Natural Science Foundation of China (NSFC) (10525524, 20751001, and 10490180), and the CAS Knowledge Innovation Program. This work was also supported in part by NIH/NCRR/RCMI 2G12RR003048, NIH 5U 54CA091431, and USAMRMC W81XWH-05-1-0291 grants.

This article is not an official U.S. Food and Drug Administration (FDA) guidance or policy statement. No official support or endorsement by the U.S. FDA is intended or should be inferred.

Appendix

Figures with essential colour discrimination. Fig. 3 in this article is difficult to interpret in black and white. The full colour images can be found in the on-line version, at doi:10.1016/j.biomaterials.2008.09.061.

References

- Halliwell B, Gutteridge J. Free radicals in biology and medicine. New York: Oxford University Press; 1989.
- Valko M, Leibfritz D, Moncol J, Cronin MT, Mazur M, Telser J. Free radicals and antioxidants in normal physiological functions and human disease. *Int J Biochem Cell Biol* 2007;39:44–84.
- Aust SD, Chignell CF, Bray TM, Kalyanaram B, Mason RP. Free radicals in toxicology. *Toxicol Appl Pharmacol* 1993;120:168–78.
- Loft S, Poulsen HE. Cancer risk and oxidative DNA damage in man. *J Mol Med* 1996;74:297–312.
- Stadtman ER, Berlett BS. Reactive oxygen-mediated protein oxidation in aging and disease. *Chem Res Toxicol* 1997;10:485–94.
- Toyokuni S, Okamoto K, Yodoi J, Hiai H. Persistent oxidative stress in cancer. *Febs Lett* 1995;358:1–3.
- Hileman EA, Achanta G, Huang P. Superoxide dismutase: an emerging target for cancer therapeutics. *Expert Opin Ther Targets* 2001;5:697–710.
- Pelicano H, Carney D, Huang P. ROS stress in cancer cells and therapeutic implications. *Drug Resist Updat* 2004;7:97–110.
- Tsai MC, Chen YH, Chiang LY. Polyhydroxylated C60, fullereneol, a novel free-radical trapper, prevented hydrogen peroxide- and cumene hydroperoxide-elicited changes in rat hippocampus in-vitro. *J Pharm Pharmacol* 1997;49:438–45.
- Bisaglia M, Natalini B, Pellicciari R, Straface E, Malorni W, Monti D, et al. C3-fullerene-tris-methanodicarboxylic acid protects cerebellar granule cells from apoptosis. *J Neurochem* 2000;74:1197–204.
- Lai HS, Chen WJ, Chiang LY. Free radical scavenging activity of fullereneol on the ischemia-reperfusion intestine in dogs. *World J Surg* 2000;24:450–4.
- Chueh SC, Lai MK, Lee MS, Chiang LY, Ho TI, Chen SC. Decrease of free radical level in organ perfusate by a novel water-soluble carbon-sixty, hexa-(sulfobutyl)fullerenes. *Transplant Proc* 1999;31:1976–7.
- Dugan LL, Turetsky DM, Du C, Lobner D, Wheeler M, Almli CR, et al. Carboxyfullerenes as neuroprotective agents. *Proc Natl Acad Sci U S A* 1997;94:9434–9.
- Ali SS, Hardt JJ, Quick KL, Kim-Han JS, Erlanger BF, Huang T-T, et al. A biologically effective fullerene (C₆₀) derivative with superoxide dismutase mimetic properties. *Free Radic Biol Med* 2004;37:1191–202.
- Dugan LL, Gabrielsen JK, Yu SP, Lin TS, Choi DW. Buckminsterfullereneol free radical scavengers reduce excitotoxic and apoptotic death of cultured cortical neurons. *Neurobiol Dis* 1996;3:129–35.
- Chiang LY, Lu FJ, Lin JT. Free-radical scavenging activity of water-soluble fullereneols. *J Chem Soc Chem Commun* 1995:1283–4.
- Tang J, Xing GM, Zhao F, Yuan H, Zhao YL. Modulation of structural and electronic properties of fullerene and metallofullerenes by surface chemical modifications. *J Nanosci Nanotechnol* 2007;7:1085–101.
- Chen CY, Xing GM, Wang JX, Zhao YL, Li B, Tang J, et al. Multihydroxylated [Gd@C₈₂(OH)₂₂]_n nanoparticles: antineoplastic activity of high efficiency and low toxicity. *Nano Lett* 2005;5:2050–7.
- Wang JX, Chen CY, Li B, Yu H, Zhao YL, Sun J, et al. Antioxidative function and biodistribution of [Gd@C₈₂(OH)₂₂]_n nanoparticles in tumor-bearing mice. *Biochem Pharmacol* 2006;71:872–81.
- Yin JJ, Lao F, Meng J, Fu PP, Zhao YL, Xing GM, et al. Superior capability of eliminating free radicals by polyhydroxylated endohedral metallofullereneol optimized as ROS species scavenger. *Mol Pharmacol* 2008;74:1132–40.
- Xing GM, Zhao J, Zhao YL, Tang J, Zhang B, Gao XF, et al. Influences of structural properties on stability of fullereneols. *J Phys Chem B* 2004;108:11473–9.
- Li W, Chen CY, Ye C, Wei TT, Zhao YL, Lao F, et al. The translocation of fullerene nanoparticles into lysosome via the pathway of clathrin-mediated endocytosis. *Nanotechnology* 2008;19. doi:10.1088/0957-4484/19/14/145102.
- Deli MA, Abraham CS, Niwa M, Falus A. N,N-diethyl-2-[4-(phenylmethyl)-phenoxy]ethanamine increases the permeability of primary mouse cerebral endothelial cell monolayers. *Inflamm Res* 2003;52(Suppl. 1):S39–40.
- Nishikawa T, Edelstein D, Du XL, Yamagishi S, Matsumura T, Kaneda Y, et al. Normalizing mitochondrial superoxide production blocks three pathways of hyperglycaemic damage. *Nature* 2000;404:787–90.
- Basly JP, Basly I, Bernard M. ESR spectroscopy applied to the study of pharmaceuticals radiosterilization: cefoperazone. *J Pharm Biomed Anal* 1998;17:871–5.
- Kadirov MK, Bosnjakovic A, Schlick S. Membrane-derived fluorinated radicals detected by electron spin resonance in UV-irradiated Nafion and Dow ionomers: effect of counterions and H₂O₂. *J Phys Chem B Condens Matter Mater Surf Interfaces Biophys* 2005;109:7664–70.
- Yin JJ, Kramer JK, Yurawecz MP, Eynard AR, Mossoba MM, Yu L. Effects of conjugated linoleic acid (CLA) isomers on oxygen diffusion-concentration products in liposomes and phospholipid solutions. *J Agric Food Chem* 2006;54:7287–93.
- Kusumi A, Subczynski WK, Pasenkiewicz-Gierula M, Hyde JS, Merkle H. Spin-label studies on phosphatidylcholine-cholesterol membranes: effects of alkyl chain length and unsaturation in the fluid phase. *Biochim Biophys Acta* 1986;854:307–17.
- Burkitt MJ, Gilbert BC. The autoxidation of iron(II) in aqueous systems: the effects of iron chelation by physiological, non-physiological and therapeutic chelators on the generation of reactive oxygen species and the induction of biomolecular damage. *Free Radic Res Commun* 1991;14:107–23.
- Yamakoshi Y, Umezawa N, Ryu A, Arakane K, Miyata N, Goda Y, et al. Active oxygen species generated from photoexcited fullerene (C₆₀) as potential medicines: O₂^{•−} versus ¹O₂. *J Am Chem Soc* 2003;125:12803–9.
- Markovic Z, Todorovic-Markovic B, Kleut D, Nikolic N, Vranjes-Djuric S, Misiric P, et al. The mechanism of cell-damaging reactive oxygen generation by colloidal fullerenes. *Biomaterials* 2007;28:5437–48.
- Markovic Z, Trajkovic V. Biomedical potential of the reactive oxygen species generation and quenching by fullerenes (C₆₀). *Biomaterials* 2008;29:3561–73.
- Sayes CM, Gobin AM, Ausman KD, Mendez J, West JL, Colvin VL. Nano-C₆₀ cytotoxicity is due to lipid peroxidation. *Biomaterials* 2005;26:7587–95.
- Sayes CM, Fortner JD, Guo W, Lyon D, Boyd AM, Ausman KD, et al. The differential cytotoxicity of water-soluble fullerenes. *Nano Lett* 2004;4:1881–7.
- Wang L-S, Conceicao J, Changming J, Smalley RE. Threshold photodetachment of cold C₆₀. *Chem Phys Lett* 1991;182:5–11.
- Boltalina OV, Ioffe IN, Sorokin ID, Sidorov LN. Electron affinity of some endohedral lanthanide fullerenes. *J Phys Chem A* 1997;101:9561–3.
- Ptasińska S, Echt O, Denifl S, Stano M, Sulzer P, Zappa F, et al. Electron attachment to high fullerenes and to Sc₃N@C₈₀. *J Phys Chem A* 2006;110:8451–6.
- Ali SS, Hardt JJ, Quick KL, Kim-Han JS, Erlanger BF, Huang TT, et al. A biologically effective fullerene (C₆₀) derivative with superoxide dismutase mimetic properties. *Free Radical Bio Med* 2004;37:1191–202.
- Arbogast JW, Darmannan AP, Foote CS, Rubin Y, Diedrich FN, Alvarez MM, et al. Photophysical properties of C₆₀. *J Phys Chem* 1991;95:11–2.
- Yanagi K, Okubo S, Okazaki T, Kataura H. Endohedral metallofullerenes as strong single oxygen quenchers. *Chem Phys Lett* 2007;435:306–10.
- Werner H, Wohlers M, Bublak D, Blöcker J, Schlögl R. Interaction of molecular oxygen with solid C₆₀. *Fullerenes Nanotubes Carbon Nanostructures* 1993;1:457–74.
- Kopylov VB, Gavronskaya YY. Electronic and vibrational spectra of fullerenes in contact with oxygen. *Russian J Gen Chem* 2001;71:1589–92.
- Bensasson RV, Brettreich M, Frederiksen J, Göttinger H, Hirsch A, Land EJ, et al. Reactions of e[−](aq), CO₂^{•−}, HO₂[•], O₂^{•−}, O₂(¹Δ_g) with a dendro[60]fullerene and C₆₀[C(COOH)₂]_(n) (n = 2–6). *Free Radical Bio Med* 2000;29:26–33.
- Krusic PJ, Wasserman E, Keizer PN, Morton JR, Preston KF. Radical reactions of C₆₀. *Science* 1991;254:1183–5.
- Xiao L, Takada H, Gan X, Miwa N. The water-soluble fullerene derivative “Radical Sponge” exerts cytoprotective action against UVA irradiation but not visible-light-catalyzed cytotoxicity in human skin keratinocytes. *Bioorg Med Chem Lett* 2006;16:1590–5.
- Xing GM, Yuan H, He R, Gao XY, Jing L, Zhao F, et al. The strong MRI relaxivity of paramagnetic nanoparticles. *J Phys Chem B* 2008;112:6288–91.
- Tóth E, Bolcska RD, Borel A, González, Helm L, Merbach AE, et al. Water-soluble gadofullerenes: toward high-relaxivity, pH-responsive MRI contrast agents. *J Am Chem Soc* 2004;127:799–805.
- Gharbi N, Pressac M, Hadchouel M, Szwarc H, Wilson SR, Moussa F. [60]fullerene is a powerful antioxidant *in vivo* with no acute or subacute toxicity. *Nano Lett* 2005;5:2578–85.
- Quick KL, Ali SS, Arch R, Xiong C, Wozniak D, Dugan LL. A carboxyfullerene SOD mimetic improves cognition and extends the lifespan of mice. *Neurobiol Aging* 2008;29:117–28.

Meeting Report

Building Scientific Progress without Borders: Nanobiology and Nanomedicine in China and the U.S.

Paul C. Wang,^{1,4} Robert P. Blumenthal,⁵ Yuliang Zhao,² Julie A. Schneider,³ Nancy Miller,⁶ Piotr Grodzinski,⁷ Michael M. Gottesman,⁹ Sally Tinkle,¹⁰ Kuan Wang,⁸ Chen Wang,¹ and Xing-Jie Liang¹

¹National Center for Nanoscience and Technology of China; ²Institute of High Energy Physics, Chinese Academy of Sciences; and

³National Cancer Institute (NCI), NIH, based at the Embassy of the United States, Beijing, P.R. China; ⁴Department of Radiology,

Howard University, Washington, District of Columbia; ⁵Nanobiology Program, National Cancer Institute, NIH, Frederick,

Maryland; ⁶Office of the Director; ⁷NCI Alliance for Nanotechnology in Cancer, NCI; ⁸National Institute of Arthritis and

Musculoskeletal and Skin Disorders, NIH; and ⁹Center for Cancer Research, NCI, NIH, Bethesda, Maryland; and

¹⁰National Institute of Environmental Health Science, NIH, Research Triangle Park, North Carolina

Introduction

In recent years, growing numbers of nanomaterials and nanotechnology applications have been used as novel imaging, diagnostic, and therapeutic agents in the treatment of cancer and other diseases. The safe and effective development and use of these new nanotechnologies will require coordinated effort among diverse groups of international experts including basic scientists, toxicologists, clinical researchers, policymakers, and others. The first Joint China-U.S. Symposium on Nanobiotechnology and Nanomedicine was convened October 21 to 23, 2008, in Beijing, China, to address these and other emerging issues and opportunities (Supplementary Fig. S1). The goal of the symposium was to share experiences and exchange information pertaining to the development of nanotechnology for medical use including the prevention, detection, and treatment of disease, and ensuring the safety of the general public and of personnel working in the field. The symposium also provided a platform for exploring the development of new research collaborations among top Chinese and American scientists.

This symposium was organized in response to recent major investments in nanobiology and nanomedicine both in China and in the United States, respectively. Discussions focused on nanotechnology applications for cancer diagnostics and therapeutics, given the substantial advances in this field. The organization of the meeting was collaboratively developed by the National Center for Nanoscience and Technology of China, a leading nanotechnology research institution, and by the Chinese Academy of Sciences and Ministry of Science and Technology of China, as well as by the National Cancer Institute of the NIH and its Alliance for Nanotechnology in Cancer, and by the NIH's National Institute of Environmental Health Sciences. Additional key supporters included the NIH Office of the Director, and the Trans-NIH Nanotechnology Task Force. The meeting was initiated under the auspices of an agreement cosigned by Executive President, Dr. Chunli Bai

(Chinese Academy of Sciences, Beijing, China); Former Director, Dr. Elias A. Zerhouni (NIH, Bethesda, MD); Director, Dr. John E. Niederhuber (National Cancer Institute, Bethesda, MD); and by Former Acting Director, Dr. Samuel Wilson (National Institute of Environmental Health Services, Research Triangle Park, NC). The Symposium Organizing Committee included Dr. Yuliang Zhao (Institute of High Energy, Beijing, China), Dr. Xing-Jie Liang (National Center for Nanoscience and Technology of China, Beijing, China), Dr. Robert Blumenthal (National Cancer Institute, Bethesda, MD), Dr. Michael M. Gottesman (National Cancer Institute, Bethesda, MD), and Dr. Piotr Grodzinski (National Cancer Institute, Bethesda, MD), Dr. Sally Tinkle (National Institute of Environmental Health Services, Research Triangle Park, NC), Dr. Kuan Wang (National Institute of Arthritis and Musculoskeletal and Skin Diseases, Bethesda, MD), and Dr. Nancy E. Miller (National Cancer Institute, Bethesda, MD). Eighty scientists and research physicians attended the meeting. The U.S. delegation, composed of 30 invited leading scientists and policy experts, was led by Dr. Michael M. Gottesman, Chief, Laboratory of Cell Biology, National Cancer Institute (NCI), NIH, and Deputy Director for Intramural Research, NIH (Supplementary Fig. S2). Chinese attendees included participants from 30 universities and research institutes.

Report

Six sessions of the symposium covered topics ranging from molecular investigations of nanoparticles for medical applications, the effect of engineered nanomaterials on human health and on the environment, to the development of nanoparticles for targeted delivery in cancer therapy and imaging, and the promises and challenges of using nanomaterials in clinical applications (Supplementary Table S1). The opening session reviewed nanomedicine programs and activities in China and the U.S. Dr. Yuliang Zhao (Institute of High Energy, Beijing, China) welcomed symposium attendees and provided a brief introduction and background regarding the meeting. Dr. Chen Wang (National Center for Nanoscience and Technology of China, Beijing, China) presented an overview of nanoscience and nanotechnology research in China, touching upon the current research framework, policy concerns, progress in nanostandardization, and potential societal effects of nanotechnology. He was followed by Dr. Xiaohan Liao (Ministry of Science and Technology of China, Beijing, China) and by Drs. Minghua Liu (Chinese Academy of Sciences, Beijing, China) and

Note: Supplementary data for this article are available at Cancer Research Online (<http://cancerres.aacrjournals.org/>).

This article was approved by National Center for Nanoscience and Technology of China and the NIH Nanomedicine and Nanobiology Meeting Steering Committee.

Requests for reprints: Xing-Jie Liang, Chinese Academy of Sciences Key Laboratory for Biomedical Effects of Nanomaterials and Nanosafety, National Center for Nanoscience and Technology of China, No. 11, First North Road, Zhongguancun, Beijing, 100190, P.R. China. Phone: 86-10-82545569(O); Fax: 86-10-62656765; E-mail: liangxj@nanoctr.cn.

©2009 American Association for Cancer Research.

doi:10.1158/0008-5472.CAN-09-0563

Zhifang Chai (Institute of High Energy, Beijing, China), who voiced the support of these important Chinese scientific organizations regarding the value of promoting new discoveries in nanobiology and nanomedicine.

The first session presented an overview of key NIH-supported nanomedicine activities and highlighted national and international nano policy concerns. NCI Alliance for Nanotechnology in Cancer was introduced as a major NCI program that supports extramural investigators and a Nanotechnology Characterization Laboratory at NCI-Frederick. Research themes and team-building strategies were described in eight NIH Nanomedicine Development Centers on behalf of the NIH Roadmap Nanomedicine Implementation Team. In addition, a talk on multidrug resistance in cancer highlighted the potential for nanotechnology to accelerate progress in this area. How metallofullerenes used as nanochemotherapeutics can potentially inhibit tumor growth was also illustrated. These presentations were followed by a panel discussion addressing similarities and differences between the U.S. and China both in the structure of the field and in the conceptual approach to research.

The second session focused on the molecular basis of nanomedicine, which included examples of both basic and mechanistic studies using nanomaterials in therapeutics and diagnostics. Key topics discussed in this session included results of investigations of cell processes at the nanoscale, and recent work in applying knowledge of molecular and cell biology to design and fabricate nanoparticles that are effective for biomedical applications.

The third session addressed the molecular basis for engineered nanomaterial interactions with human health and the environment. Some of the presenters in this session described specific studies of the safety and environmental effect of specific types of nanomaterials; however, an important overarching theme addressed in this session was the need to develop novel systematic approaches for evaluating and predicting potential toxic effects of large numbers of different nanomaterials.

The fourth session focused on the development of "smart" nanoparticles for cancer therapy and imaging. Presenters reviewed recent studies of specific nanoparticles in cancer imaging and therapy, including fluorescent semiconductor quantum dots, ferromagnetic nanoparticles, and integrin-targeted liquid perfluorocarbon nanoparticles. Other presenters described overall design criteria for developing new multifunctional nanoparticles, recent advances in the use of lithography for nanoparticle fabrication, and investigations of potential toxicologic adverse effects of nanoparticles of different sizes at the genomic and proteomic level.

The fifth session addressed biomarkers and targeted delivery. Several of the presentations in this session focused on studies that targeted different types of nanoparticles to tumor cells, including conjugation with ligands to improve targeting and performance. In addition, the importance of nanoparticle standardization and characterization was discussed.

The sixth session focused on the promise and hurdles of applying nanotechnology in the clinic. Several presenters reviewed studies of different types of nanoparticles such as nano C-60, carbon nanotubes, and polymeric micelles to improve drug delivery to cancer cells. Other talks focused on developing a detailed understanding of key cell processes and pathways that influence the uptake of different types of nanoparticles.

Future Interactions

In addition to scientific presentations, members of the Symposium Steering Committee participated in two administrative meetings with representatives from the National Natural Science Foundation of China, a key Chinese scientific funding organization, and Chinese Academy of Sciences, to discuss mechanisms for encouraging future cooperation in nanobiology, nanomedicine, and other fields of biomedical research (Supplementary Fig. S3). Meeting participants discussed possible mechanisms for expanding China-U.S. cooperation, including the following: (a) developing joint research programs and grant solicitations, cooperative research agreements, and/or joint laboratories; (b) promoting additional training and exchange through predoctoral and postdoctoral fellowships, and short-term travel and training grants; and (c) supporting future joint workshops and conferences. In both administrative meetings, Chinese and U.S. representatives expressed a strong interest in developing new opportunities for cooperation, and agreed to identify research areas of mutual scientific interest based on the outcomes of the symposium.

Prospects

During a discussion at the conclusion of the symposium, participants recommended developing a web or working site or other mechanisms to facilitate sharing of key resources and contacts to enable joint progress and collaboration. Such resources and contacts could include the following: specialized equipment, databases, tools, reagents and specimens, and clinical trial participation. The importance of recognizing intellectual property and export control issues in developing mechanisms for sharing information and resources between China and the U.S. in the field of nanobiology and nanomedicine was noted.

Additional key themes identified for future research included shared interests in implementing safe design for multifunctional nanoparticles; developing cost effective, nanotechnology-based diagnostics and interventions; and exploring cross-national cooperation in nanotechnology-related clinical trials. In addition to showcasing recent scientific progress in nanobiology and nanomedicine, the symposium helped build mutual understanding regarding one another's research enterprise. In coming months, symposium participants will actively explore the possibility in nanobiology and nanomedicine research and research training, to advance scientific discovery, enhance health and optimally identify, diagnose, and treat disease.

Disclosure of Potential Conflicts of Interest

No potential conflicts of interest were disclosed.

Acknowledgments

Received 2/13/09; revised 4/28/09; accepted 5/7/09; published OnlineFirst 6/23/09.

The costs of publication of this article were defrayed in part by the payment of page charges. This article must therefore be hereby marked *advertisement* in accordance with 18 U.S.C. Section 1734 solely to indicate this fact.